# Calculations for Double Parton Distributions and Highly Boosted Hadrons




DISSERTATION ZUR ERLANGUNG DES DOKTORGRADES DER NATURWISSENSCHAFTEN (DR. RER. NAT.) DER FAKULTÄT FÜR PHYSIK

DER UNIVERSITÄT REGENSBURG

vorgelegt von

**Daniel Reitinger**

aus Regensburg

im Jahr 2026

Promotionsgesuch eingereicht am: 22.12.2025
Die Arbeit wurde angeleitet von: Prof. Dr. Andreas Schäfer

Prüfungsausschuss:
Vorsitzender: Prof. Dr. Sascha Schäfer
Erstgutachter: Prof. Dr. Andreas Schäfer
Zweitgutachter: Prof. Dr. Markus Diehl
weiterer Prüfer: Prof. Dr. Juan Diego Urbina

Datum Promotionskolloquium: 20.7.2026

**Dissertation advisor: Prof. Dr. Andreas Schäfer** **Daniel Reitinger**

# Calculations for Double Parton Distributions and Highly Boosted Hadrons


## Abstract

This thesis covers two main topics, a first-principles investigation of double parton distributions (DPDs) and improvements to the calculation of highly boosted nucleon matrix elements.

Double parton distributions (DPDs) are non-perturbative objects that contain information about the correlation of partons within a hadron. They are essential for a first-principles computation of double parton scattering (DPS) cross sections, which contribute to the Standard Model (SM) background. Combining lattice Quantum Chromodynamics (lattice QCD) and operator product expansion (OPE), their first Mellin moment can be reconstructed from Euclidean two-current correlation functions calculated on the lattice.

We present the first systematic study of leading-twist invariant functions of DPDs at zero hadron momentum, using six gauge ensembles provided by the Coordinated Lattice Simulations (CLS) collaboration with lattice spacings ranging from 0.085 fm to 0.064 fm and pion masses between 422 MeV and 214 MeV. Our analysis indicates the dominant source of systematic uncertainties to be finite volume effects, which are found to be consistent with sufficient suppression for $Lm_\pi \geq 5$.

We further discuss the skewness $\zeta$ dependence of the non-zero momentum hadronic two-current correlation functions. We find that a polynomial model used in earlier works does not predict vanishing results at $|\zeta| \to 1$, failing this physical boundary condition. Additionally, we find that the analyticity around $\zeta = 0$ assumed in this model is not physically justified and leads to artificially narrow error bands. We introduce and compare the impact of different model ansätze to this dependence on the extracted Mellin moment. The average of $\zeta^2$ is determined consistently across all considered models to be $\langle\zeta^2\rangle \approx 0.07$, while the Mellin moment at $\zeta = 0$ cannot be extracted reliably without significantly improved signal at higher hadron momenta.

We address this limitation in our study of recently proposed kinematically enhanced nucleon interpolators. As highly boosted hadronic matrix elements are of broader interest, e.g. to LaMET studies, we use the nucleon quasi-PDF matrix element at a boost momentum $P_z \approx 2.5\,\text{GeV}$ as a benchmark quantity. We compare conventional to kinematically enhanced interpolators and investigate the results for potentially increased excited state contributions, discretization and cutoff effects. To this end, we compute the nucleon quark isovector quasi-PDF matrix element on three different CLS gauge ensembles at similar pion mass $m_\pi \approx 350\,\text{MeV}$ and lattice spacings ranging from 0.085 fm to 0.064 fm. We observe a reduction in variance by an order of magnitude without increasing excited state contributions. We further detail an additional improvement in computation time by a factor of two based on a reduction in inversions of the Dirac operator.

# Contents


**1 Introduction** **1**

**2 Continuum Quantum Chromodynamics** **5**
2.1 The Dirac equation, fermions and bosons . . . . . 5
2.2 The Path integral formalism . . . . . 7
2.3 The parton model . . . . . 8
2.3.1 Deep inelastic scattering . . . . . 9
2.3.2 Hadronic scattering . . . . . 10
2.4 Parton distribution functions . . . . . 12
2.4.1 Parton correlators . . . . . 13
2.4.2 Parton distribution functions . . . . . 17
2.4.3 Double parton distribution functions . . . . . 18
2.5 Double parton scattering . . . . . 24

**3 Lattice Quantum Chromodynamics** **27**
3.1 Wick rotation . . . . . 27
3.2 Discretization of continuum physics . . . . . 29
3.2.1 The discrete Dirac operator . . . . . 29
3.2.2 The discretized action . . . . . 31
3.2.3 Symanzik improvement . . . . . 33
3.2.4 The discretized path integral . . . . . 35
3.3 Monte Carlo simulations . . . . . 36

**4 Lattice methodology** **41**
4.1 Hadronic matrix elements . . . . . 41
4.1.1 Euclidean correlation functions . . . . . 41
4.1.2 Hadron interpolating fields . . . . . 43
4.1.3 Operators . . . . . 45
4.1.4 Wick contractions . . . . . 46
4.2 Propagators . . . . . 52
4.2.1 Point sources . . . . . 52
4.2.2 Stochastic sources . . . . . 53
4.2.3 Sequential source technique . . . . . 53
4.3 Improvement techniques . . . . . 54
4.3.1 Smearing . . . . . 55
4.3.2 Hopping parameter expansion . . . . . 56

4.4 Kinematically enhanced interpolators . . . 57
4.4.1 Kinematic enhancement . . . 57
4.4.2 Interpolator kernels . . . 58
4.5 Evaluation of Wick contractions . . . 61
4.5.1 Connected three-point contractions . . . 61
4.5.2 Connected four-point contractions . . . 62
4.5.3 Disconnected contractions . . . 63
4.6 Data analysis techniques . . . 63
4.6.1 Error estimation . . . 63
4.6.2 Ground state matrix element extraction . . . 64
4.6.3 Fits and equation systems . . . 65

**5 Extracting parton distributions from lattice QCD 67**
5.1 Mellin moments of DPDs . . . 69
5.1.1 Two-current matrix elements . . . 69
5.1.2 Renormalization . . . 70
5.1.3 Mellin moments at leading twist . . . 72
5.1.4 Properties of DPD Mellin moments . . . 73
5.2 Nucleon PDFs with LaMET . . . 74
5.2.1 The unpolarized nucleon PDF . . . 77
5.2.2 Renormalization . . . 77

**6 Invariant functions of DPDs at $\omega = 0$ 79**
6.1 Lattice setup . . . 79
6.2 Excited state analysis . . . 81
6.3 Lattice artifacts . . . 85
6.3.1 Finite volume effects . . . 85
6.3.2 Discretization effects . . . 87
6.4 Lattice spacing dependence . . . 89
6.4.1 $C_1$ contributions . . . 90
6.4.2 $C_2$ contributions . . . 91
6.4.3 Flavor specific combinations . . . 91
6.5 Mass dependence . . . 92
6.5.1 $C_1$ contributions . . . 92
6.5.2 $C_2$ contributions . . . 94
6.5.3 Flavor specific combinations . . . 94

**7 Invariant functions of DPDs at $\omega \neq 0$ 97**
7.1 Lattice setup . . . 97
7.2 Modeling the lowest Mellin moment . . . 98
7.2.1 Factorization of $I(\zeta, y^2)$ . . . 99
7.2.2 Dependence on the distance $y$ . . . 99
7.2.3 Dependence on the skewness $\zeta$ . . . 101

7.3 Fit results . . . . . 104
7.3.1 Comparison of models . . . . . 105
7.3.2 Testing factorization in $\zeta$ and $y$ . . . . . 111

**8 Kinematically enhanced nucleon matrix elements 115**
8.1 Lattice measurements . . . . . 115
8.2 Kinematic enhancement results . . . . . 116
8.2.1 Excited state contamination . . . . . 117
8.2.2 Interpolator comparison . . . . . 117

**9 Conclusion 127**

**A Two-current matrix element tensor decomposition 131**

**B Spectral decomposition of correlators 133**

**C Euclidean correlation functions with open boundary conditions 135**

**Bibliography 137**

# 1 Introduction

The exploration of the structure of matter has a long history in physics. More than a century ago, the atomic nucleus was discovered by Rutherford [1] in $\alpha$-radiation scattering experiments. The nucleus was later found to consist of protons and neutrons, called nucleons. In 1953, Robert Hofstadter found in electron scattering experiments [2] that nucleons are not point-like particles but have finite size [3]. In the 1960s, Gell-Mann and Zweig [4, 5] proposed that nucleons consist of even more elementary particles. This theory was substantiated by experimental evidence towards the end of the decade [6], opening up a new field of study. To explain the observations in deep-inelastic scattering (DIS) experiments at SLAC [7], Feynman developed the parton model [8] to describe the behavior of these nucleon constituents. Much later, it became clear that they are quarks and gluons, bound together by Quantum Chromodynamics (QCD), the non-Abelian gauge theory of the strong interaction.

It has since proved to be extremely successful at describing the fundamental interactions of physics, so much so that it has been incorporated into the Standard Model (SM). The Standard Model does not describe gravity, prompting the development of Beyond the Standard Model (BSM) theories. To verify or falsify these, better experimental data are required, both at higher energies and with greater precision. The latter also necessitates an increase in the precision of theoretical predictions to analyze the experimental data.

Hadronic scattering is dominated by single parton scattering (SPS), where one parton of a hadron interacts with another parton. The probability of SPS is determined by the cross section, which in turn depends on a single parton distribution function (PDF). Considering only longitudinal momenta, the collinear parton distribution function can be interpreted as finding a parton with a specific longitudinal momentum fraction and polarization in a polarized or unpolarized hadron.

A prominent example of SPS in hadronic collisions is the Drell-Yan process [9], where one quark from each hadron interacts with the other and produces two leptons.

If the quarks carry only small momentum fractions, the parton density within the hadrons increases. This increases the probability of two quarks from each hadron interacting simultaneously, creating a double parton scattering (DPS) event, such as the double Drell-Yan process (DDY). DPS was observed four decades ago at CERN in proton-proton [10] and antiproton-proton [11–14] collisions, more recent investigations of DPS include [15–25]. DPS can occur in proton collisions, e.g. at the Tevatron, the Relativistic Heavy Ion Collider (RHIC) or the Large Hadron Collider (LHC). Of particular interest are the ATLAS and CMS experiments hosted at the LHC. Both of these experiments observe the same-sign $W$ and double $Z$ production reaction channels.

Simple models predicted that DPS could contribute at the same cross section level to these channels [26], making accurate DPS predictions crucial for future searches for BSM physics. The same sign $W$ production channel is particularly intriguing, as the SPS contribution, which otherwise overshadows DPS events, is suppressed compared to DPS. With the high-luminosity upgrade to the LHC, these will become considerably easier to observe, stressing the need for reliable DPS cross section predictions.

Although there are models to approximate DPS cross sections like the so-called pocket-formula [27] discussed in Section 2.3.2, these cannot accurately reflect all partonic correlations. Better motivated DPS approaches such as in Ref. [28] yield a very different picture. To make more accurate DPS cross section predictions, a better understanding of their underlying double parton distributions (DPDs) is required. They contain information on partonic correlations within the hadron. Again, considering only collinear momenta, they can be interpreted as probabilities of finding two partons, separated by a spatial vector $\vec{y}$, carrying longitudinal momentum fractions $x_1$ and $x_2$ inside a hadron. Both partons and the hadron can be polarized. DPDs are conceptually similar but physically distinct from PDFs. They encode correlations of partons in position, momentum, spin and color, as well as flavor interference and splitting contributions [29]. This leads to more independent functions in the case of DPDs compared to PDFs [30].

DPDs and their related quantities are non-perturbative, i.e. they cannot be calculated analytically from perturbation theory. We instead turn to lattice QCD, a non-perturbative approach that discretizes Euclidean space-time in a finite volume hypercube and can be used to compute QCD matrix elements numerically. The central limitation of this approach is that using imaginary time, we cannot access dynamical information directly. This prevents us from directly computing PDFs and DPDs alike, as they are defined on the light-cone and thus require real time. We shall discuss two strategies that have been developed to circumvent this. The first is the calculation of Mellin moments from the operator product expansion (OPE). Integrating over the longitudinal momentum fractions reduces the involved operators to local ones which can be calculated on the lattice. For quark DPDs, flavor-conserving interactions were studied in Ref. [31], while flavor interference effects were studied in Ref. [32] by the author of this thesis. In this work, we study the lowest Mellin moment of collinear DPDs and related quantities at different lattice spacings and meson masses.

In recent years several schemes [33–41] have been proposed and widely applied to extract far more information on the partonic structure of hadrons from lattice simulations than was judged possible before. One of the most popular theoretical approaches are lattice calculations in the framework of Large Momentum Effective Theory (LaMET) [42–67]. LaMET exploits Lorentz symmetry to relate light-cone distributions to matrix elements of space-like Wilson line operators computed at large but finite hadron momentum, which are then matched to the physical distributions via perturbatively calculated matching kernels.

Both approaches require the computation of lattice correlation functions at large nucleon momenta. As the signal-to-noise ratio of these decreases rapidly with momentum, this has become the principal limiting factor. In this thesis, we investigate a recently

proposed algorithmic improvement to the simulation of highly boosted hadrons [68] for nucleon correlation functions used in the LaMET framework.

The thesis is organized as follows. In chapter 2, we give a brief review of the theoretical foundations of QCD in the continuum, quarks, gluons and the path integral formalism. We introduce the parton model and the factorization of scattering processes into hard and soft parts. We define single- and double-parton distributions, and the leading-twist structure of the DPS cross section. Chapter 3 introduces Lattice QCD as a non-perturbative way to evaluate the path integral. We cover the Wick rotation to Euclidean space, the discretization of fermions and gauge fields and the Symanzik improvement program and the generation of gauge configurations by Hybrid Monte Carlo. In chapter 4 we introduce the techniques used in LQCD practice. We define hadronic correlation functions, constructed from proton interpolating fields and operators and discuss the relevant Wick contractions for two-, three-, and four-point functions. We further present practical implementations and improvements for the involved propagators and close with a section on data analysis methods used in this work. In chapter 5 we discuss two different approaches to extract parton distributions from lattice calculations, namely Mellin moments from Operator Product Expansion (OPE) and LaMET. For DPDs, we introduce Mellin moments, obtained from a Lorentz decomposition of the two-current matrix elements, and their renormalization. For PDFs, we introduce the quasi-PDFs to access the former via LaMET. We also discuss their renormalization. In chapter 6 we present the results for invariant functions of two-current matrix elements at $\omega = 0$ . We conduct a detailed analysis of finite volume effects, lattice artifacts, lattice spacing dependence, and pion-mass dependence. Chapter 7 extends the analysis to $\omega \neq 0$, introducing and investigating different fitting models for the skewness dependence. We also discuss the fit results, model dependence as well as their physical interpretation. The content of this chapter was already published in Ref. [69], where the author of this thesis was one of the lead authors. In chapter 8, we investigate kinematically enhanced nucleon interpolators for precision improvements in high-momentum matrix elements. We compare different kinematic enhancements to the nucleon interpolator, using the quasi-PDF matrix element as a benchmark observable across three CLS ensembles (H102, S400, N203) at $p_z \approx 2.5\,\text{GeV}$. We quantify the SNR improvement and investigate potential excited-state contamination. The results were published in Ref. [70], prepared for submission to JHEP. The author of this thesis is one of the lead authors of this work. We close by summarizing our findings and giving an outlook into future research areas in Chapter 9.

# 2 Continuum Quantum Chromodynamics

Since we are interested in the structure of the proton, we give a brief review of the underlying theory of strong interactions, governing the physics inside the nucleus. This theory is known as Quantum Chromodynamics and has been incorporated into the Standard Model. For the introduction of QCD, we follow [71] and [72]. We shall introduce double parton distributions later in this chapter, following [73, 74].

## 2.1 The Dirac equation, fermions and bosons

Like Quantum Electrodynamics (QED), QCD is a gauge theory. Unlike QED though, it is non-Abelian, introducing additional complexity. The QCD gauge fields are called gluons, the charge of QCD is called color. Just as QED, QCD has a Lagrangian formulation, based on fermions and gauge fields as generalized coordinates. The fermion field, generally denoted as $\psi_\mu^{f,a}(x)$, is a Dirac 4-spinor. $\psi$ has a Dirac index $\mu \in \{0,1,2,3\}$, necessary for the correct relativistic formulation, a color index $a \in \{1,2,3\}$, allowing for the appropriate color transformations, a flavor index $f \in \{u,d,s : c,b,t\}$ and a space-time position $x \in \mathbb{R}^4$. Just as in QED, the fermions fulfill a Dirac equation:

$$\left(i\not{D} - m_f\right)\psi^f(x) = 0 \tag{2.1}$$

with the notation

$$\not{D} = \gamma^\mu D_\mu \ . \tag{2.2}$$

The form of $D_\mu$ depends on the theory. For gauge theories, it is the covariant derivative containing the relevant gauge field and acting on the Dirac spinor fields in the fundamental representation of the gauge group. In the non-interacting case, where there is no gauge field, the manifold is the Minkowski plane and the Dirac operator reduces to the partial derivative, $D_\mu = \partial_\mu$. Its solutions are plane waves $\psi^f$:

$$\psi^f(x) = \begin{cases} u^{f,\lambda}(p)e^{-ixp} \\ v^{f,\lambda}(p)e^{+ixp} \end{cases} \tag{2.3}$$

with particles $u^{f,\lambda}$ and antiparticles $v^{f,\lambda}$ of flavor $f$ and helicity $\lambda$. They are both Dirac spinors, transforming in a four dimensional representation of the Lorentz group. Being

fermions, they are quantized by imposing:

$$\begin{aligned}\left\{\hat{\psi}(x), \hat{\psi}^\dagger(y)\right\}\Big|_{x^0=y^0} &= \delta^{(3)}(\vec{x}-\vec{y})\,, \\ \left\{\hat{\psi}^\dagger(x), \hat{\psi}^\dagger(y)\right\}\Big|_{x^0=y^0} &= \{\hat{\psi}(x), \hat{\psi}(y)\}\Big|_{x^0=y^0} = 0\ .\end{aligned} \tag{2.4}$$

The operators $\bar{\psi}$ ($\psi$) create (annihilate) a particle. These operators produce the corresponding fields as eigenvalues when acting on their eigenvectors: $\hat{\psi}(x)\,|\psi\rangle = \psi(x)\,|\psi\rangle$. For quarks, we introduce the operators $\bar{q}$ to create and $q$ to annihilate a quark. We will be using these later in this work.
Introducing interactions by a gauge field requires:

$$D_\mu(x) = \partial_\mu - ig_0 A^j_\mu(x) t^j\,, \tag{2.5}$$

where $g_0$ is the bare coupling constant. The vector gauge field, the gluon field, is expressed as $A^j_\mu$ with a Lorentz index just as the fermion field but linked to the $SU(3)$ generators $t^j$. These generators have two color indices instead of one. This is required as the gluons act as intermediaries for changing color charge between the fermions and thus have to be able to connect different colors. The spinor and color indices are commonly suppressed for better legibility of equations whenever possible.

In order to analyze the behavior of fermions and bosons in QCD, we first take a look at the gauge group SU(3). The generators $t^j$ of the SU(3) group form a Lie algebra with structure constants $f^{jkl}$, which are totally antisymmetric under exchange of indices:

$$\left[t^j, t^k\right] = f^{jkl} t^l\ . \tag{2.6}$$

The Gell-Mann basis is the common choice for the eight different $t^j$. These generators are $3\times 3$ hermitian and traceless matrices which span the SU(3) Lie Algebra. They also obey the extra trace orthonormality relation $\mathrm{tr}(t^i t^j) = 2\delta^{ij}$ and therefore can be used to generate all transformations $\Omega(x)$ within SU(3):

$$\Omega(x) = e^{i\theta^j(x) t^j}\,, \tag{2.7}$$

where $\theta^i(x)$ are eight position dependent parameters. The spinor fields $\psi(x)$ and $\bar{\psi}(x)$ transform in the fundamental representation:

$$\psi^c_\mu(x) \to \Omega(x)^{cc'} \psi^{c'}_\mu(x)\,, \tag{2.8}$$

$$\bar{\psi}^c_\mu(x) \to \bar{\psi}^{c'}_\mu(x) \left(\Omega^{c'c}\right)^*(x)\,, \tag{2.9}$$

where we made the color indices of the $3\times 3$ matrix $\Omega(x)$ as well as those of the spinor fields explicit. The gauge fields $A^{cc'}_\mu(x)$ are constructed as linear combinations of

coefficients $A^j_\mu(x)$ and generators $t^j$ and transform as follows:

$$\left(t^{cc'}\right)^j A^j_\mu(x) \to \Omega^{cd}(x)\left(\left(t^{de}\right)^j A^j_\mu(x) + \frac{i}{g_0}\partial_\mu \mathbb{1}^{de}_{3\times 3}\right)\left(\Omega^{ec'}\right)^*(x)\,, \tag{2.10}$$

where again we made the color indices explicit. The difference in representations and therefore transformation behavior clearly illustrates that this theory has three colors for quarks, three anti-colors for antiquarks and eight types of gluons, carrying combinations of color and anticolor. The traceless property of the generators eliminates the possibility of a color-singlet gluon, thus prohibiting long range interactions between the stable, color-singlet states of particles as observed in nature. While interactions of quarks with gluons are described by the Dirac operator (2.5), the self-interaction of gluons is described by the field strength tensor $F^a_{\mu\nu}$:

$$F^a_{\mu\nu}(x) = \partial_\mu A^a_\nu(x) - \partial_\nu A^a_\mu(x) + g_0 f^{abc} A^b_\mu(x) A^c_\nu(x)\ . \tag{2.11}$$

Comparing this to the QED equivalent, there is an additional term including the structure functions $f^{abc}$. As discussed above, it stems from the non-Abelian nature of the gauge group and gives rise to gluon self interactions. Using (2.5), while taking into account all flavors $f$, and (2.11), one arrives at the expression for the QCD Lagrangian:

$$\mathcal{L}_{\mathrm{QCD}}[A,\psi,\bar\psi](x) = \sum_f \bar\psi^f(x)\left(i\not{D} - m_f\right)\psi^f(x) - \frac{1}{4}F^{a,\mu\nu}(x)F^a_{\mu\nu}(x)\,, \tag{2.12}$$

which leads to the QCD action:

$$S_{\mathrm{QCD}}[A,\psi,\bar\psi] = \int \mathrm{d}^4x\ \mathcal{L}_{\mathrm{QCD}}[A,\psi,\bar\psi](x)\ . \tag{2.13}$$

## 2.2 The Path integral formalism

With the QCD action (2.13) we can formulate the path integral generating functional $Z[J,j,\bar j]$:

$$Z[J,j,\bar j] = \int \mathcal{D}[A]\,\mathcal{D}[\eta]\,\mathcal{D}[\bar\eta]\ \exp\left[iS_{\mathrm{QCD}}[A,\eta,\bar\eta] + i\int \mathrm{d}^4x\left(J\cdot A + \bar j\eta + \bar\eta j\right)\right]\,, \tag{2.14}$$

where the $J$ are source terms of the bosonic fields $A$. It is important to note that any pair of $\bar j, \eta, \bar\eta, j$ anticommutes, i.e. that they are Grassmann variables.

$$\eta_i\eta_j = -\eta_j\eta_i\ , \tag{2.15}$$

$$\frac{\delta}{\delta\eta_i\delta\eta_j} = -\frac{\delta}{\delta\eta_j\delta\eta_i}\ . \tag{2.16}$$

Their anticommuting property implies that the ordering of field and source terms is important. Here, we will only write $\Phi \equiv (\psi, \bar{\psi}, A_\mu)$ for fermionic and bosonic fields and $J \equiv (\bar{j}, j, J)$ for the corresponding source terms for better legibility. It is nevertheless important to keep in mind that, for the Grassmann valued variables, ordering matters, and we will point out the implications of this. Physical processes are described by expectation values of operators. These are calculable as partial derivatives of the generating functional $Z$,

$$\langle \hat{\phi}_1(x_1) \cdots \hat{\phi}_n(x_n) \rangle = \frac{1}{Z[0]} \frac{\delta^n Z[J]}{\delta J_1(x_1) \cdots \delta J_n(x_n)}\bigg|_{J=0} = \frac{i^n \int \mathcal{D}[\Phi] e^{iS[\Phi]} \phi_1(x_1) \cdots \phi_n(x_n)}{\int \mathcal{D}[\Phi] e^{iS[\Phi]}} . \tag{2.17}$$

The path integral allows a non-perturbative calculation of QCD processes. We shall use its Euclidean version later, when we have introduced lattice QCD. If the coupling $g$ is small, one can truncate the series of the exponentiated action at some power of $g$. The resulting expressions in general include ultraviolet divergences. These divergences have to be addressed and regularized, using a suitable scheme, such as dimensional regularization. These divergent terms can be isolated by a regulator, so that after the removal of the regulator, everything is finite again. The formerly divergent, now regulated, contributions can be absorbed into the constants of the theory, most notably the mass $m$ and the coupling $g$. Regulators introduce a scale dependence $\mu$, on which the renormalized constants now depend. A feature of the renormalization of $g(\mu)$, or $\alpha_s(\mu) = \frac{g^2(\mu)}{4\pi}$, is the running of the coupling:

$$\mu \frac{d\,\alpha_s(\mu)}{d\mu} = \beta(\alpha_s) . \tag{2.18}$$

For $\mu \to \infty$, $\alpha_s(\mu) \to 0$ as $\beta(\alpha_s) < 0$ in QCD. Besides making QCD asymptotically free and explaining confinement, this makes perturbation theory well suited for high energies, but it breaks down where the coupling diverges. This makes non-perturbative calculations necessary to fully understand hadron physics.

## 2.3 The parton model

The parton model was introduced by Feynman in 1969 [8] to describe the observations in deep inelastic scattering (DIS) experiments at SLAC [7]. In this model, the nucleon is treated as a collection of pointlike, non-interacting constituents he called partons. The original intuition was that a nucleon in the infinite momentum frame (IMF) is affected by time dilation so strongly that the interaction among its constituents is negligible. However, this argument was frame dependent. QCD provides the modern explanation, where the non-interaction assumption is justified by asymptotic freedom [75, 76]. At the large momentum transfers relevant for hard scattering, the QCD coupling becomes small and partons behave as quasi-free particles on the timescale of the hard interaction. These partons were then identified with the quarks and gluons of QCD.

### 2.3.1 Deep inelastic scattering

In a DIS experiment, a lepton $\ell$ scatters off a nucleon $N$ via the exchange of a virtual photon. The probability density of a given scattering outcome is given by the differential scattering cross section

$$d\sigma \sim L^{\mu\nu} W_{\mu\nu}, \tag{2.19}$$

where $L^{\mu\nu}$ is the leptonic tensor, calculable in QED, and $W_{\mu\nu}$ is the hadronic tensor, which encodes all the non-perturbative physics of the nucleon. The process is characterized by two Lorentz-invariant kinematic variables,

$$Q^2 = -q^2 > 0\,, \tag{2.20}$$

$$x = \frac{Q^2}{2p \cdot q}\,, \tag{2.21}$$

where $p^\mu$ is the nucleon four-momentum, $q^\mu$ is the momentum and $Q^2$ the virtuality of the photon, and $x \in [0, 1]$ is the Bjorken-$x$ scaling variable. In the parton model, $x$ is interpreted as the fraction of the nucleon's longitudinal momentum carried by the struck parton.

Depending on the momentum transfer $Q$, the process is called soft if $Q^2 \lesssim \Lambda^2_{\mathrm{QCD}}$, or hard if $Q^2 \gg \Lambda^2_{\mathrm{QCD}}$. Soft processes include hadronization and bound-state formation, where $\alpha_s$ is large and must be treated non-perturbatively. Hard processes can be calculated perturbatively, since $\alpha_s(Q^2) \ll 1$ for $Q^2 \gg \Lambda^2_{\mathrm{QCD}}$.

In DIS at large $Q^2$, the differential cross section factorizes into a hard part, the partonic cross section $\mathrm{d}\hat{\sigma}$, and a soft part, the parton distribution function (PDF) $f_q$, as

$$\frac{\mathrm{d}\sigma(\ell(k) + N(p) \to \ell'(k') + X)}{\mathrm{d}x} \propto \sum_q f_q(x, \mu^2)\, \mathrm{d}\hat{\sigma}(\ell(k) + q(xp) \to \ell'(k')) + \mathcal{O}\left(\frac{\Lambda^2_{\mathrm{QCD}}}{Q^2}\right). \tag{2.22}$$

This splits the complex scattering process into a simple interaction between lepton and a parton with longitudinal momentum fraction $x$, weighted with the distribution function of such a parton. As only one parton is considered in the interaction, this is called single parton scattering (SPS). The hard and soft regimes are separated by the factorization scale $\mu^2$. Contributions from momenta above $\mu^2$ are absorbed into the perturbatively calculable $\mathrm{d}\hat{\sigma}$, while those below $\mu^2$ are absorbed into the PDF $f_q$. Although $\mathrm{d}\sigma$ is formally independent of $\mu^2$, any finite-order truncation of $\mathrm{d}\hat{\sigma}$ introduces a residual dependence, which is minimized by the choice $\mu^2 \sim Q^2$.

A standard choice for the description of scattering events is the Breit frame, or brick-wall frame, where the nucleon is fast moving in the $z$-direction and the virtual photon

carries only momentum and zero energy:

$$p^\mu = \left(\sqrt{\frac{Q^2}{4x^2} + M^2},\, 0,\, 0,\, \frac{Q}{2x}\right), \tag{2.23}$$

$$q^\mu = (0,\, 0,\, 0,\, -Q)\ , \tag{2.24}$$

where $M$ is the nucleon mass. The Bjorken limit $Q^2 \to \infty$, $p \cdot q \to \infty$ with $x$ held fixed [7, 8] corresponds to the IMF, connecting to Feynman's original intuition that parton interactions are suppressed at large nucleon momenta.

### 2.3.2 Hadronic scattering

Hadronic collisions are observed at e.g. the LHC, where two highly accelerated protons interact via the strong force. In contrast to DIS, where only one nucleon interacts with one lepton, two nucleons now serve as sources of partons. For many processes, high-energy hadronic collisions ($Q^2 \gg \Lambda^2_{\mathrm{QCD}}$) can be factorized into a perturbatively calculable hard part and a soft part, i.e. non-perturbative PDFs, now one for each nucleon. As an example where factorization has been proven, we consider the Drell-Yan process, where two hadrons $A$ and $B$ collide to produce a lepton anti-lepton pair $l + \bar{l}$ and an unobserved remainder $X$. The inclusive cross section takes the form [77]:

$$\begin{aligned}\frac{\mathrm{d}\sigma(A(p_1) + B(p_2) \to l + \bar{l} + X)}{\mathrm{d}x\mathrm{d}\bar{x}} &= \\ = \sum_{q,q'} f_{A,q}(x,\mu^2)\, f_{B,q'}(\bar{x},\mu^2)\, \mathrm{d}\hat{\sigma}(q(xp_1) + q(\bar{x}p_2) \to l + \bar{l};\, \frac{\mu}{Q}, \mu^2) &+ \mathcal{O}\left(\frac{\Lambda^2_{\mathrm{QCD}}}{Q^2}\right)\ ,\end{aligned} \tag{2.25}$$

where $f_{A,q}(x,\mu^2)$ and $f_{B,q'}(\bar{x},\mu^2)$ are the PDFs of partons $q$ and $q'$ in each nucleon carrying longitudinal momentum fractions $x$ and $\bar{x}$ respectively, and $\mathrm{d}\hat{\sigma}$ is the perturbatively calculable partonic cross section for the production of the final state $l + \bar{l}$. The PDFs are the same universal objects as in DIS, their process independence is a non-trivial result guaranteed by factorization theorems [77].

At high energies and in processes with multiple hard scales, it becomes increasingly likely that two partons from each hadron undergo separate hard scatterings simultaneously. This is known as double parton scattering (DPS), and its cross section is a generalization of (2.25):

$$\frac{\sigma_{\mathrm{DPS}}}{\prod_{i=1,2}\mathrm{d}x_i\mathrm{d}\bar{x}_i} \propto \sum_{i,j,k,l}\int \mathrm{d}^2\boldsymbol{y}\ F_{ij/A}(x_1, x_2, \boldsymbol{y};\, \mu^2)\, \hat{\sigma}_{ik}\, \hat{\sigma}_{jl}\, F_{kl/B}(\bar{x}_1, \bar{x}_2, \boldsymbol{y};\, \mu^2)\,. \tag{2.26}$$

Here, $F_{ij/A}(x_1, x_2, \boldsymbol{y};\, \mu^2)$ are double parton distributions (DPDs), encoding the joint probability of finding two partons $i$ and $j$ in hadron $A$ carrying momentum fractions $x_1$ and $x_2$ at transverse separation $\boldsymbol{y}$.

The simplest phenomenological estimate of the DPS cross section is given by the

so-called pocket formula [27],

$$\sigma_{\mathrm{DPS}}^{AB} \approx \frac{1}{C}\,\frac{\sigma_A \cdot \sigma_B}{\sigma_{\mathrm{eff}}}\,, \tag{2.27}$$

where $\sigma_A$ and $\sigma_B$ are the SPS cross sections for the two subprocesses, $C$ is a combinatorial factor ($C = 1$ for distinguishable and $C = 2$ for identical subprocesses), and $\sigma_{\mathrm{eff}}$ is an effective cross section parametrizing the transverse overlap of the two parton pairs inside the colliding hadrons. This formula follows directly from the assumption that the two partons participating in the hard scatterings are uncorrelated, so that the DPD factorizes into a product of two single PDFs multiplied by a universal transverse profile $T(\boldsymbol{y})$,

$$F_{ij/A}(x_1, x_2, \boldsymbol{y};\, \mu^2) \approx f_{i/A}(x_1, \mu^2)\, f_{j/A}(x_2, \mu^2)\, T(\boldsymbol{y})\,, \tag{2.28}$$

where $T(\boldsymbol{y})$ is normalized as

$$\int \mathrm{d}^2\boldsymbol{y}\, T(\boldsymbol{y}) = 1\,. \tag{2.29}$$

The effective cross section $\sigma_{\mathrm{eff}}$ is defined as

$$\sigma_{\mathrm{eff}} = \left[\int d^2\boldsymbol{y}\ \left(T(\boldsymbol{y})\right)^2\right]^{-1}. \tag{2.30}$$

Experimentally, $\sigma_{\mathrm{eff}}$ has been measured across a range of processes at the Tevatron and the LHC. The available experimental results exhibit considerable variation, with values ranging from around 2.7 mb up to more than 26 mb [24, 25, 78–92] depending on the specific process, center-of-mass energy, and kinematic cuts, suggesting that $\sigma_{\mathrm{eff}}$ is not universal but process-dependent [93]. This directly contradicts the universality assumption underlying the pocket formula, and strongly motivates a rigorous non-perturbative treatment of DPDs.

The pocket formula (2.27) is not exact in any rigorous sense and is best understood as a rough order-of-magnitude estimate. It fails to capture several physically important features of DPS:

- **Parton correlations**: The factorized ansatz (2.28) ignores all correlations between the two partons in position, momentum, spin, and color. These correlations are in general non-negligible and carry non-trivial information about the multiparton structure of the nucleon, as demonstrated for example in model calculations [94].

- **Flavor interference**: The DPS cross section can receive contributions from flavor interference diagrams. An example is a $W$ boson exchange turning a $u$ quark into a $d$ quark and vice versa. These flavor interference contributions involve off-diagonal DPDs $F_{uddu}$ and are absent from the pocket formula (2.27), which only includes flavor-diagonal distributions.

- **Color interference**: Analogously, color interference contributions arise from color-non-singlet DPDs, which vanish in the uncorrelated limit but are present in general.

- **Perturbative splitting contributions**: At short transverse separations, one parton can split perturbatively into two, generating $1 \to 2$ splittings that are not captured by the factorized ansatz (2.28) and require careful treatment in the evolution equations [95, 96].

A rigorous theoretical framework for DPS, going beyond the pocket formula, requires the non-perturbative calculation of DPDs $F_{ij}(x_1, x_2, \boldsymbol{y};\, \mu^2)$, which can be achieved from first principles using LQCD.

## 2.4 Parton distribution functions

Parton distributions are the central non-perturbative objects of QCD factorization, encoding the soft physics of internal hadron structure. In this section, we introduce parton correlation functions as a framework to express these distributions based on hadronic matrix elements of quark and gluon operators. Within this work, we focus on (anti)quarks exclusively. Gluons can be treated in a similar fashion [30]. As factorization requires hadrons of mass $M$ accelerated to high energies $Q \gg M$, a common choice in the formulation of parton correlators and distributions is light-cone coordinates. For a fast moving hadron in $z$-direction, these are defined as

$$v^{\pm} = \frac{1}{\sqrt{2}}\left(v^t \pm v^z\right) , \qquad \boldsymbol{v} = (v^x, v^y) , \tag{2.31}$$

so that any four-vector decomposes as $v^\mu = (v^+, v^-, \boldsymbol{v})$, with the inner product

$$v \cdot w = v^+ w^- + v^- w^+ - \boldsymbol{v} \cdot \boldsymbol{w} . \tag{2.32}$$

Light-cone coordinates replace the former time-coordinate by the new light-cone time $x^+$. This naturally leads to a modification of the anticommutation relations (2.4), which now have to be fulfilled at equal light-cone time $x^+ = y^+$. This light-front or light-cone quantization [97] will be used for the remainder of this work.
A fast-moving hadron with momentum $p^\mu$ in $z$-direction has $p^+ \sim Q \gg \frac{M^2}{Q} \sim p^-$ and $\boldsymbol{p} = \boldsymbol{0}$. For the inner product with a vector $y^\nu$, this implies $p \cdot y \approx p^+ y^-$ if $y^+ = 0$. A parton carrying longitudinal momentum fraction $x$ then has $k^+ = x p^+$, with $x \in [0, 1]$. The transverse momentum is considered to be at most proportional to the hadron mass:

$$|\boldsymbol{k}| \sim M, \quad k^- \lesssim \frac{M^2}{Q} . \tag{2.33}$$

### 2.4.1 Parton correlators

For a quark of flavor $q$, the single quark correlation function is defined as

$$\Phi_{ab}^{\alpha\beta}(x, \boldsymbol{k}, \xi, \Delta) = \int \frac{\mathrm{d}^2 z \, \mathrm{d}z^-}{(2\pi)^3} \, e^{ixp^+z^-} \, e^{-i\boldsymbol{k}\cdot\boldsymbol{z}} \, \langle p + \Delta/2 | \, \bar{q}_a^\alpha(-z/2) \, q_b^\beta(z/2) \, | p - \Delta/2 \rangle \Big|_{z^+=0} \tag{2.34}$$

where

$$\xi = -\frac{\Delta^+}{2p^+} \tag{2.35}$$

parametrizes the longitudinal momentum transfer fraction.

The four-momentum transfer is $\Delta$ and the frame is chosen symmetrically. The correlator (2.34) is written without time ordering. In the derivation of the cross section via the optical theorem, the hadronic tensor involves a time-ordered product of currents. At space-like separations and the quark fields anticommute due to microcausality,

$$\left\{ \bar{q}_a^\alpha(-z/2), \, q_b^\beta(z/2) \right\} \Big|_{z^2<0} = 0 \,, \tag{2.36}$$

so the time ordering can be dropped. For $z^+ = 0$ and thus, with $\boldsymbol{z} = 0$, $z^2 = 0$, time ordering can also be dropped [98]. The restriction $z^+ = 0$ ensures that, for vanishing transverse separation, the separation is light-like and the Fourier transform in $z^-$, conjugate to $xp^+$, admits a probabilistic interpretation as a parton density. The momentum of the quark annihilated by $q$ determines the interpretation of the process. If all quark "+"-momenta are positive, a quark with momentum (fraction) $k - \Delta/2$ $(x + \xi)$ is emitted and a quark with momentum $k + \Delta/2$ $(x - \xi)$ is absorbed. If the "+"-components become negative, i.e. $\xi > x$, the quark in the wave function becomes an antiquark in the conjugate wave function. Note that this definition is not gauge invariant, as it contains open color indices at potentially different positions. It has to be made gauge invariant by including a process appropriate Wilson line. In the case of semi inclusive deep inelastic scattering (SIDIS), this would be a future-pointing, for Drell-Yan processes a past-pointing one [72, 99]. The shape of the Wilson line to be included is also generally non-trivial. If the quark lines connected by the Wilson line contain not only longitudinal but also a transverse displacement, the Wilson lines extend towards infinity at a relative offset, which is the case for transverse momentum dependent parton distribution functions (TMDPDFs or TMDs). We shall discuss examples including a Wilson line later.

This parton correlation function can be used to describe (semi-)inclusive as well as exclusive processes. The former include the measurement of only parts of the final state, the matrix elements thus involving the emission of a quark $q$ with an unresolved state of spectator partons $X$ left behind. In the squared amplitude of the total cross section, the hadronic part then takes the shape $\sum_X \langle p | \, \bar{q} \, | X \rangle \, \langle X | \, q \, | p \rangle$, which is what we obtain

from (2.34) for $\Delta = 0$. The second kind, exclusive processes, also measure the final state. If we consider those exclusive processes, where only the hadron exists in the final state, we find matrix elements $\langle p|\, \bar{q}q \,|p\rangle$ with a momentum transfer $\Delta = p - p'$. We shall consider only correlation functions for (semi-)inclusive processes. Hence we set $\Delta = 0$ in the following.

The single quark correlation function can be generalized to the n-quark correlation function [73]:

$$\begin{aligned}\Phi^{\alpha_i\beta_i}_{a_ib_i}(x_i, \boldsymbol{k}_i, \zeta_i, \boldsymbol{r}_i) &= \\ =(2p^+)^{n-1} \prod_i \int \frac{\mathrm{d}^2\boldsymbol{z}_i\, \mathrm{d}z_i^-}{(2\pi)^3} \frac{\mathrm{d}^2\boldsymbol{y}_i\, \mathrm{d}y_i^-}{(2\pi)^3}\, &e^{ix_ip^+z_i^-}\, e^{-i\boldsymbol{k}_i\cdot\boldsymbol{z}_i}\, e^{-i\zeta_ip^+y_i^-}\, e^{i\boldsymbol{r}_i\cdot\boldsymbol{y}_i}\, \delta(y_n^-)\, \delta^{(2)}(\boldsymbol{y}_n) \\ \times \langle p|\, \prod_i \bar{q}^{\alpha_i}_{i,a_i}(y_i - z_i/2)\, q^{\beta_i}_{i,b_i}(y_i + z_i/2)\, |p\rangle &\Big|_{\substack{z_i^+=0 \\ y_i^+=0}},\end{aligned} \tag{2.37}$$

where Wilson lines are omitted again. As multiple quarks are involved now, we have to account for their respective momenta $k_i$ and relative momentum differences $r_i$ w.r.t. the conjugate wave function. The Fourier conjugate to the latter are the average quark positions $y_i$. As above, we require $y^+ = z^+ = 0$. The momentum fraction $\zeta_i$ represent the quarks' relative longitudinal momentum fraction w.r.t the total hadron momentum:

$$\zeta_i = \frac{r_i^+}{p^+} \tag{2.38}$$

A generic diagram for the $n$-quark correlation function (2.37) is given in Figure 2.1. Here, all momenta have positive "+"-components. Translational invariance allows us to fix one average quark position, e.g. $y_n = 0$. Subsequently, the $n$-th relative quark momentum is set to $r_n = -\sum_{i=1}^{n-1} r_i$.

Different distributions can be extracted from the $n$-quark correlation function (2.37) by projecting onto the desired Dirac and color structures and integrating over all momenta not under consideration. Taking the forward limit ($\Delta = 0$) and integrating over transverse momentum yields the collinear distributions. Allowing a non-zero momentum transfer ($\Delta \neq 0$) gives rise to generalized parton distributions (GPDs) [100], which encode the three-dimensional spatial structure of the nucleon. Retaining the transverse momentum of the quark field yields transverse-momentum-dependent distributions (TMDs). The DPDs, which are the subject of this work, arise from a two-parton specialization of (2.37), as discussed in Section 2.4.3. In this entire work, we shall only consider quark singlet distribution functions. This is achieved by contracting the $n$-

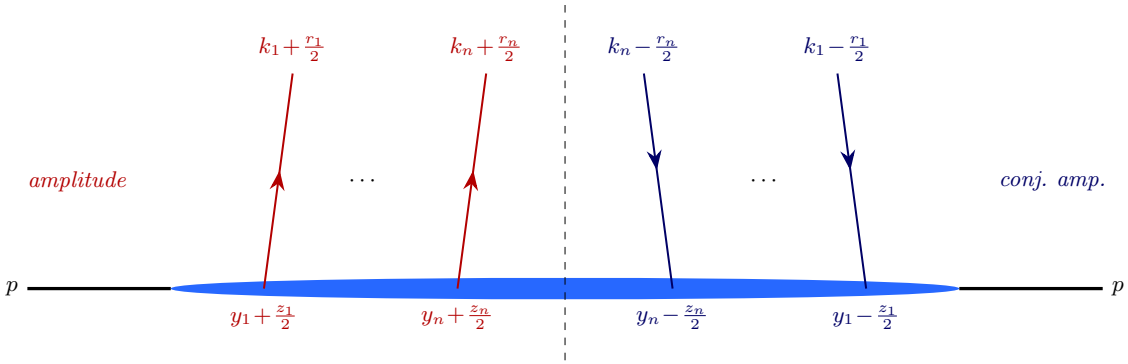



**Figure 2.1:** Diagrammatic representation of the $n$-parton correlation function (2.37). The blue blob represents the nucleon emitting and absorbing $n$ partons. Positions and their Fourier conjugate momenta are given at the end of the colored lines. Red lines (amplitude side) represent quarks, carrying momentum $k_i + r_i/2$ or emerging at position $y_i + z_i/2$. Blue lines (conjugate amplitude side, with reversed arrows) depict quarks carrying momentum $k_i - r_i/2$ or being absorbed at position $y_i - z_i/2$. The dashed vertical line indicates the cut separating the amplitude from its conjugate, with $y_i$ denoting the average position of the $i$-th quark pair. The last quark position is fixed to the origin, $y_n = 0$.

quark correlation function with a Kronecker delta in color, i.e[1].

$$\Phi^{\alpha_i\beta_i}(x_i, \boldsymbol{k}_i, \zeta_i, \boldsymbol{r}_i) = \delta_{a_i b_i} \Phi^{\alpha_i\beta_i}_{a_i b_i}(x_i, \boldsymbol{k}_i, \zeta_i, \boldsymbol{r}_i) \tag{2.39}$$

The parton polarization projectors are classified by twist, a number originating from the operator product expansion (OPE), which is detailed in e.g. [71]. In this work, we shall focus on leading twist, which is twist-2. Higher twist terms are suppressed by powers of $1/Q$ and not investigated in this work. The leading twist (2) projectors for the quark polarization are

$$\begin{aligned} \Gamma_q &= \frac{1}{2}\gamma^+ && \text{unpolarized quark,} \\ \Gamma_{\Delta q} &= \frac{1}{2}\gamma^+\gamma_5 && \text{longitudinally polarized quark,} \\ \Gamma^j_{\delta q} &= \frac{i}{2}\sigma^{j+}\gamma_5 && \text{transversely polarized quark.} \end{aligned} \tag{2.40}$$

We can contract these with the correlation function (2.39)

$$\Phi^a = (\Gamma_a)_{\alpha_i\beta_i}\Phi^{\alpha_i\beta_i}, \tag{2.41}$$

[1] While for the single parton case there is no color-octet distribution as the additional open color index would break gauge invariance, there are color-octet DPDs which were derived in Ref. [73] but are not further discussed here.

or directly with the quark and antiquark fields, yielding the twist-2 operators

$$O_a^{\perp}(y_i, z_i) = \bar{q}_i(y_i - z_i/2)\,\Gamma_a q_i(y_i + z_i/2)\Big|_{z_i^+ = y_i^+ = 0}. \tag{2.42}$$

The leading twist operators for antiquarks are defined analogously as

$$O_{\bar{a}}^{\perp}(y_i, z_i) = \bar{q}(y_i + z_i/2)\;\Gamma_{\bar{a}}\,q(y_i - z_i/2)\Big|_{z_i^+ = y_i^+ = 0} \tag{2.43}$$

with

$$\Gamma_{\bar{q}} = -\Gamma_q, \qquad \Gamma_{\Delta\bar{q}} = \Gamma_{\Delta q}, \qquad \Gamma^j_{\delta\bar{q}} = -\Gamma^j_{\delta q}. \tag{2.44}$$

Quark and antiquark operators are related by charge conjugation:

$$O_a^{\perp,\mathcal{C}}(y_i, z_i) = \bar{q}(y_i + z_i/2)\Gamma_{\bar{a}} q(y_i - z_i/2)|_{z_i^+ = y_i^+ = 0} = \eta_C^a O_a^{\perp}(y_i, -z_i) = O_{\bar{a}}^{\perp}(y_i, z_i) \tag{2.45}$$

with

$$\eta_C^a = \begin{cases} 1 & a = \Delta q\,, \\ -1 & a = q, \delta q\,. \end{cases} \tag{2.46}$$

The superscript $\perp$ implies that in general, $\boldsymbol{z} \neq 0$, thus allowing for transverse separations/moments. The operators $O_a^{\perp}(y_i, z_i)$ contain quark fields at separated space-time points that lead to divergences in hadronic matrix elements [72]. In the case of transverse momentum dependent distributions, rapidity divergences arise. As fixing the transverse momentum does not fully separate soft and collinear momentum regions, modes with widely separated rapidities but identical virtuality can contribute. The resulting divergences cannot be regularized by conventional ultraviolet methods. Integrating over the transverse momentum components, i.e. restricting to the collinear case, removes these rapidity divergences but introduces ultraviolet divergences associated with large transverse momenta. Both types of divergences require regularization. In the transverse-momentum–dependent case, a rapidity regulator is introduced, while ultraviolet divergences are regulated with a renormalization scale $\mu$. In this work, we restrict ourselves to the collinear case. As discussed in Section 2.3.1, factorization also introduces a scale $\mu$. As these two scales can be chosen to be identical, we do so, writing $\mu$ for both.

The correlation function also contains information about the additional degrees of freedom of the hadron, such as spin, which we so far suppressed in the state $|p\rangle$. We denote them as $\lambda$ in the state $|p, \lambda\rangle$. In this work, we are particularly interested in the unpolarized proton, which we obtain by averaging over the spin degrees of freedom $\lambda$ [101],

$$\Phi^a_{\text{unpol}} = \frac{1}{2}\,\text{Tr}[\Phi^a] \quad \text{unpolarized hadron.} \tag{2.47}$$

The other polarizations can be obtained by the projections

$$\begin{aligned}\Phi^a_{\text{long}} &= \frac{1}{2}\,\text{Tr}\Big[\tau_\parallel\,\Phi^a\Big] \quad \text{longitudinally polarized hadron,}\\ \Phi^{a,j}_{\text{trans}} &= \frac{1}{2}\,\text{Tr}\Big[\tau^j_\perp\,\Phi^a\Big] \quad \text{transversely polarized hadron.}\end{aligned} \tag{2.48}$$

Here, $\Phi^a$ is understood as a matrix in the hadron helicity indices, $\Phi^a_{\lambda\lambda'}$ with $\lambda, \lambda' = \pm$, and the trace runs over these indices. The matrices $\tau$ are the Pauli matrices acting on the hadron helicity index,

$$\tau^1 = \begin{pmatrix}0 & 1\\ 1 & 0\end{pmatrix}, \qquad \tau^2 = \begin{pmatrix}0 & -i\\ i & 0\end{pmatrix}, \qquad \tau^3 = \begin{pmatrix}1 & 0\\ 0 & -1\end{pmatrix}. \tag{2.49}$$

For a hadron moving in the $z$ direction, the longitudinal and transverse projectors are

$$\tau_\parallel \equiv \tau^3\,, \qquad \tau^j_\perp \equiv \tau^j \quad (j = 1, 2)\,, \tag{2.50}$$

where $j$ labels the two directions perpendicular to the hadron momentum.

### 2.4.2 Parton distribution functions

Considering only one parton in the forward limit and after integrating over transverse momentum, the correlator (2.39) reduces to the standard collinear PDF, where we suppressed spin again:

$$\Phi^a(x) = \int \frac{\mathrm{d}^2 z\,\mathrm{d}z^-}{(2\pi)^3}\mathrm{d}^2\boldsymbol{k}\, e^{ixp^+z^-}\, e^{-i\boldsymbol{k}\cdot\boldsymbol{z}}\,\langle p|\,\bar{q}(-z/2)\,\Gamma_a q(z/2)\,|p\rangle\Big|_{z^+=0}. \tag{2.51}$$

Based on the nucleon polarization, the twist-2 projectors (2.40) then yield the following PDFs [72]:

- Unpolarized quark PDF $f_q(x, \mu^2)$: this distribution can be interpreted as the probability of finding a quark of flavor $q$ with longitudinal momentum fraction $x$ in an unpolarized nucleon.

- Longitudinally polarized or helicity PDF $g_q(x, \mu^2)$: this distribution measures the difference in probability between finding a quark with spin aligned and anti-aligned with a longitudinally polarized nucleon,

- Transverse polarized or transversity PDF $h_q(x, \mu^2)$: measures the distribution in transverse spin analogously to the helicity PDF.

The probability interpretation of the unpolarized PDF for a quark of flavor $q$ in a hadron $A$ $f_{A/q}$ suggests the number sum rules [72]:

$$\int_0^1 \mathrm{d}x \left[ f_{A/q}(x,\mu^2) - f_{A/\bar{q}}(x,\mu^2) \right] = N_q \,, \tag{2.52}$$

where $N_q$ is the number of valence quarks of flavor $q$ in hadron $A$. For the proton, subtracting (2.52) for $d$-quarks from the $u$-quark version yields

$$1 = \int_0^1 \mathrm{d}x \, \left[ f_{p^+/u}(x,\mu^2) - f_{p^+/\bar{u}}(x,\mu^2) \right] - \int_0^1 \mathrm{d}x \, \left[ f_{p^+/d}(x,\mu^2) - f_{p^+/\bar{d}}(x,\mu^2) \right] \,, \tag{2.53}$$

as in the proton, $N_u = 2$ and $N_d = 1$. These sum rules hold at all scales $\mu^2$ and are preserved by DGLAP evolution, thus they make for excellent benchmark quantities for our lattice calculations later on. The scale dependence is governed by the DGLAP evolution equations [102–104],

$$\frac{\partial}{\partial \log \mu^2} f_a(x,\mu^2) = \sum_{a'} \int_{-1}^1 \mathrm{d}x' P_{aa'} \left( x, x', \alpha_s(\mu^2) \right) f_{a'} \left( x', \mu^2 \right) , \tag{2.54}$$

where $P_{aa'}\left(x, x', \alpha_s(\mu^2)\right)$ is the quark-to-quark splitting function, describing the splitting probability of quark $a$ with momentum $x$ into quark $a'$ with momentum $x'$ at scale $\mu^2$. This allows for the PDFs to be reliably evolved to another scale, serving as input for predictions at different processes and energies.

### 2.4.3 Double parton distribution functions

Double parton distributions (DPDs) are two-parton generalizations of TMDs, collinear DPDs are generalizations of PDFs. DPDs arise as hadronic matrix elements of two bilocal quark operators. For our introduction of DPDs, we follow [73]. We first obtain the more general, skewed ($\zeta \neq 0$) quark-quark leading twist singlet DPD in position space by contracting the $n$-quark correlation function (2.37) for $n = 2$ with the leading-twist projectors (2.40) and two Kronecker Deltas:

$$\begin{aligned}
{}^1F_{ab}^{\perp}\left(x_i, \boldsymbol{k}_i, \zeta, \boldsymbol{y}\right) &= \left(\Gamma_a\right)_{\alpha_1\beta_1} \left(\Gamma_b\right)_{\alpha_2\beta_2} \delta_{a_1b_1}\delta_{a_2b_2} \int \mathrm{d}^2\boldsymbol{r}\, e^{-i\boldsymbol{r}\boldsymbol{y}} \Phi_{a_ib_i}^{\alpha_i\beta_i}(x_i, \boldsymbol{k}_i, \zeta, \boldsymbol{r}) \\
&= 2p^+ \int \frac{\mathrm{d}y^-}{2\pi} e^{-i\zeta p^+ y^-} \left[ \prod_{i=1,2} \frac{\mathrm{d}^2\boldsymbol{z}_i \mathrm{d}z_i^-}{(2\pi)^3} e^{ix_i p^+ z_i^-} e^{-i\boldsymbol{z}_i\boldsymbol{k}_i} \right] \\
&\quad \times \left\langle p \middle| \mathcal{O}_a^{\perp}\left(y, z_1\right) \mathcal{O}_b^{\perp}\left(0, z_2\right) \middle| p \right\rangle \Big|_{\substack{z_i^+=0,\\ y^+=0}} \,.
\end{aligned} \tag{2.55}$$

We shall suppress the color-singlet superscript $^1$ in the following, as we focus solely on color-singlet distributions.

### Collinear DPDs

The collinear skewed quark-quark leading-twist singlet DPD in position space is obtained by integrating (2.55) over the transverse momentum components $\boldsymbol{k}$:

$$F_{ab}\left(x_1, x_2, \zeta, \boldsymbol{y}\right) := \int \mathrm{d}^2\boldsymbol{k}_1 \mathrm{d}^2\boldsymbol{k}_2 F_{ab}^{\perp}\left(x_i, \boldsymbol{k}_i, \zeta, \boldsymbol{y}\right) \tag{2.56}$$

$$= 2p^+ \int \mathrm{d}y^- e^{-i\zeta p^+ y^-} \left[\prod_{i=1,2} \frac{\mathrm{d}z_i^-}{2\pi} e^{ix_i p^+ z_i^-}\right] \left\langle p\middle|\mathcal{O}_a\left(y, z_1\right)\mathcal{O}_b\left(0, z_2\right)\middle|p\right\rangle\Big|_{\substack{z_i^+=0\\ y^+=0}} . \tag{2.57}$$

Note that we switched to operators $\mathcal{O}_a(y,z)$ without a superscript here, indicating the absence of transverse separations, i.e. $\boldsymbol{z} = 0$. Indeed,

$$\int \frac{\mathrm{d}^2\boldsymbol{k}}{2\pi} e^{-i\boldsymbol{z}_i\boldsymbol{k}_i} = \delta^{(2)}(\boldsymbol{z})\,, \tag{2.58}$$

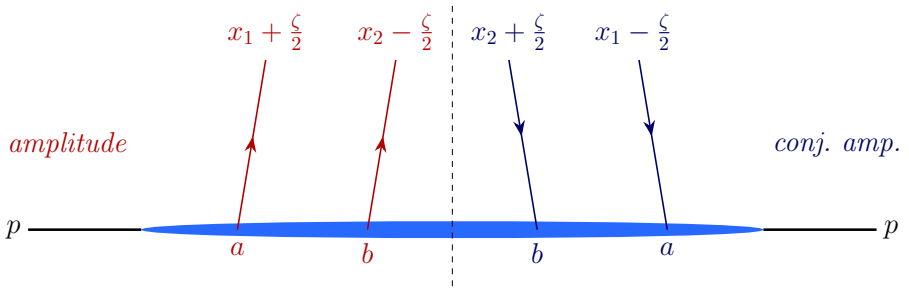
eliminating transverse separations. A Fourier transform with respect to $\boldsymbol{y}$ recovers the momentum space representation:

$$F_{ab}(x_1, x_2, \zeta, \boldsymbol{r}) = 2p^+ \int \frac{\mathrm{d}^2\boldsymbol{y}}{(2\pi)^2} e^{i\boldsymbol{r}\cdot\boldsymbol{y}} \int \frac{\mathrm{d}y^-}{2\pi} e^{-i\zeta p^+ y^-} \prod_{i=1}^{2}\left[\int \frac{\mathrm{d}z_i^-}{2\pi} e^{ix_i p^+ z_i^-}\right]$$
$$\times \left\langle p\middle|\,\mathcal{O}_a(y, z_1)\,\mathcal{O}_b(0, z_2)\middle|p\right\rangle\Big|_{\substack{z_i^+=0\\ y^+=0}} . \tag{2.59}$$

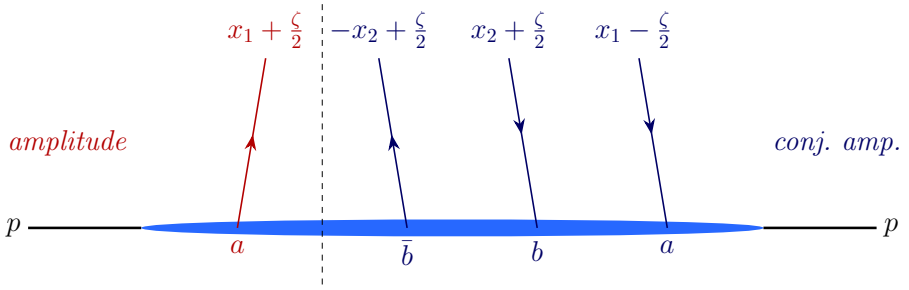
While we haven't made spin indices explicit in the DPD matrix elements so far, different hadron and parton polarizations are possible and give rise to a large number of independent distributions [105]. For spin 0 hadrons like the pion, (2.56) applies, which has been studied in previous works [106]. In this work, we focus on unpolarized hadrons, more specifically nucleons. As these are spin $\frac{1}{2}$ hadrons, we average over their spin:

$$F_{ab}\left(x_1, x_2, \zeta, \boldsymbol{y}\right) := p^+ \sum_{\lambda} \int \mathrm{d}y^- e^{-i\zeta p^+ y^-} \left[\prod_{i=1,2} \frac{\mathrm{d}z_i^-}{2\pi} e^{ix_i p^+ z_i^-}\right]$$
$$\times \left\langle p, \lambda\middle|\mathcal{O}_a\left(y, z_1\right)\mathcal{O}_b\left(0, z_2\right)\middle|p, \lambda\right\rangle\Big|_{\substack{z^+=0\\ y^+=0}} . \tag{2.60}$$

In the forward limit $\zeta = 0$ these collinear skewed quark DPDs describe quarks of flavor and polarization $a$ and $b$ with longitudinal momentum fractions $x_1$ and $x_2$ at a relative transverse distance $\boldsymbol{y}$. The skewness parameter $\zeta$ describes the difference in longitudinal momentum fraction between the amplitude and the conjugate amplitude. The emitted quarks have momenta $x_1 + \zeta/2$ and $x_2 - \zeta/2$, the absorbed ones $x_1 - \zeta/2$ and $x_2 + \zeta/2$, if all these fractions are positive. The sign of these momentum fractions determines the partonic interpretation. If $x_i \pm \zeta/2 \geq 0$, the parton corresponds to a quark emitted in the amplitude and absorbed in the conjugate amplitude as shown in Figure 2.2a. If a




**(a)** Two quarks of flavors $a$ and $b$ with total longitudinal momentum fractions $x_i \pm \zeta/2 \geq 0$ are emitted in the wavefunction amplitude and absorbed in the conjugate amplitude.




**(b)** A quark of flavor $a$ and total longitudinal momentum fraction $x_1 + \zeta/2$ is emitted in the wavefunction amplitude, an antiquark of flavor $b$ with momentum fraction $-x_2 + \zeta/2 \geq 0$ is absorbed together with two quarks of flavor $a$ and $b$ in the conjugate wavefunction amplitude.

**Figure 2.2:** Examples for kinematics included in $F_{ab}(x_1, x_2, \zeta, \boldsymbol{y})$. Contributions to the wave function amplitude are shown in red, those to the conjugate amplitude in blue. The large blue oval represents the hadronic part of the squared amplitude which for inclusive DPS processes is given by DPDs. Parton designations as quarks or antiquarks are shown beneath this.

momentum fraction becomes negative (e.g. $x_2 - \zeta/2 < 0$), this instead corresponds to an antiquark being absorbed in the conjugate amplitude, illustrated in Figure 2.2b. A change in sign of a momentum fraction swaps the interpretation between quarks and antiquarks, and between emission and absorption in the amplitude and its conjugate.

### Properties of collinear DPDs

As individual quark momentum fractions as well as their sums cannot exceed 1 due to momentum conservation, the support of skewed DPDs is restricted by

$$|x_i \pm \zeta/2| \leq 1,$$

$$|x_1| + |x_2| \leq 1, \tag{2.61}$$

which is sketched in Figure 2.3. Quarks with negative momentum fractions are in-

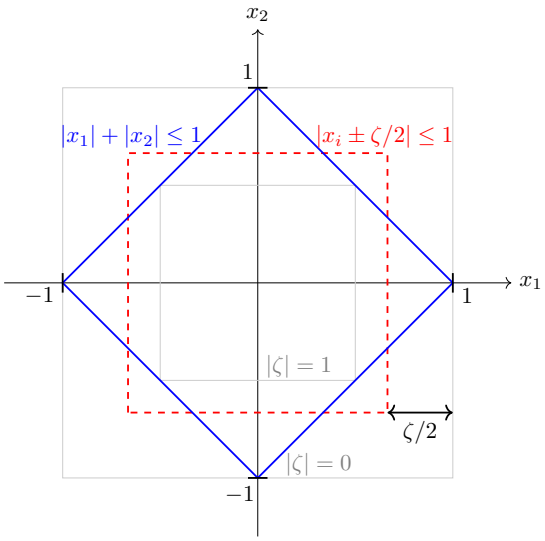



**Figure 2.3:** Support of the collinear DPDs $F_{ab}\left(x_1, x_2, \zeta, \boldsymbol{y}\right)$ at different $\zeta$, considering both individual and total momentum fraction conservation. The extreme cases for individual momentum conservation $\zeta = 0$ and $|\zeta| = 1$ are shown as gray squares. A generic situation for $0 \neq |\zeta| \neq 1$ is indicated by the red dashed square. Total momentum fraction conservation is indicated by the blue diamond. The DPD only has support where the diamond overlaps with the square for given $\zeta$.

terpreted as antiquarks with opposite, positive, momentum. This originates from the operators (2.42) and their behavior under charge conjugation. Using (2.45), one finds the following relations between quark and antiquark DPDs:

$$\begin{aligned} F_{ab}\left(x_1, x_2, \zeta, \boldsymbol{y}\right) &= \eta_C^a F_{\bar{a}b}\left(-x_1, x_2, \zeta, \boldsymbol{y}\right), \\ F_{ab}\left(x_1, x_2, \zeta, \boldsymbol{y}\right) &= \eta_C^b F_{a\bar{b}}\left(x_1, -x_2, \zeta, \boldsymbol{y}\right). \end{aligned} \tag{2.62}$$

Similarly, from $PT$ invariance one finds:

$$F_{ab}\left(x_1, x_2, \zeta, \boldsymbol{y}\right) = \eta_{PT}^a \eta_{PT}^b F_{ab}\left(x_1, x_2, -\zeta, -\boldsymbol{y}\right), \tag{2.63}$$

where

$$\eta_{PT}^a = \begin{cases} 1 & a = q, \\ -1 & a = \Delta q, \delta q. \end{cases} \tag{2.64}$$

These symmetries allow for a spin decomposition of the unpolarized DPD $F_{ab}\left(x_1, x_2, \zeta, \boldsymbol{y}\right)$. We define

$$y^2 := -\boldsymbol{y}^2\,, \quad y = \sqrt{-\boldsymbol{y}^2}\,, \tag{2.65}$$

which we will use when the function is rotationally symmetric and thus only depends on this Lorentz invariant. Both the unpolarized-unpolarized and longitudinally-longitudinally polarized DPD are parity even, i.e. scalar functions:

$$\begin{aligned} F_{qq'}\left(x_i, \zeta, \boldsymbol{y}\right) &= f_{qq'}\left(x_i, \zeta, y^2\right), \\ F_{\Delta q \Delta q}\left(x_i, \zeta, \boldsymbol{y}\right) &= f_{\Delta q \Delta q'}\left(x_i, \zeta, y^2\right). \end{aligned} \tag{2.66}$$

The unpolarized-longitudinally polarized and longitudinally polarized-unpolarized contributions are parity odd, i.e. pseudo scalar functions and cancel after the integration over transverse momenta, i.e.

$$\begin{aligned} F_{q\Delta q'}\left(x_i, \zeta, \boldsymbol{y}\right) &= 0\,, \\ F_{\Delta q q'}\left(x_i, \zeta, \boldsymbol{y}\right) &= 0\,. \end{aligned} \tag{2.67}$$

The longitudinally-transversely polarized contributions are $\mathcal{T}$-odd and thus have to vanish, as DPDs are time reversal invariant:

$$\begin{aligned} F_{\Delta q \delta q'}\left(x_i, \zeta, \boldsymbol{y}\right) &= 0\,, \\ F_{\delta q \Delta q'}\left(x_i, \zeta, \boldsymbol{y}\right) &= 0\,. \end{aligned} \tag{2.68}$$

The unpolarized-transversely polarized and transversely polarized-unpolarized contributions transform as axial vectors. In the collinear case, only the scalar contributions remain:

$$\begin{aligned} F^j_{q\delta q'}\left(x_i, \zeta, \boldsymbol{y}\right) &= \epsilon^{jl} y^l m f_{q\delta q'}\left(x_i, \zeta, y^2\right), \\ F^j_{\delta q q'}\left(x_i, \zeta, \boldsymbol{y}\right) &= \epsilon^{jl} y^l m f_{\delta q q'}\left(x_i, \zeta, y^2\right). \end{aligned} \tag{2.69}$$

Similarly, the transversely-transversely polarized DPD $F^{jk}_{\delta q \delta q'}\left(x_i, \zeta, \boldsymbol{y}\right)$ can be decomposed in the collinear case as

$$F^{jk}_{\delta q \delta q'}\left(x_i, \zeta, \boldsymbol{y}\right) = \delta^{jk} f_{\delta q \delta q'}\left(x_i, \zeta, y^2\right) + \left(2y^j y^k - \delta^{jk}\boldsymbol{y}^2\right) m^2 f^t_{\delta q \delta q'}\left(x_i, \zeta, y^2\right). \tag{2.70}$$

Using (2.63), one finds the scalar functions $f_{ab}(x_i, \zeta, y^2)$ to be even in $\zeta$:

$$f_{ab}(x_i, \zeta, y^2) = f_{ab}(x_i, -\zeta, y^2)\,. \tag{2.71}$$

In analogy to collinear PDFs, collinear DPDs include divergences as discussed in Section 2.4.1 which have to be renormalized. The two quarks evolve separately, thus it is prudent to include two different renormalization scales $\mu_1$ and $\mu_2$. These scales evolve

independently. For quark $a$ with associated scale $\mu_1$, the forward unpolarized collinear quark DPD $F(x_i, \boldsymbol{y}, \mu, \mu')$ evolves as [74]:

$$\frac{\partial}{\partial \log \mu_1^2}{}^1F_{ab}(x_1, x_2, \boldsymbol{y}, \mu_1, \mu_2) = \sum_{a'} \int_{x_1}^{1-x_2} \frac{\mathrm{d}x_1'}{x_1'} P_{aa'}\left(\frac{x_1}{x_1'}, \mu_1\right) F_{a'b}(x_1', x_2, \boldsymbol{y}, \mu_1, \mu_2)\,, \tag{2.72}$$

where $P_{aa'}\left(\frac{x_1}{x_1'}, \mu_1\right)$ is the splitting kernel. The dominant perturbative effect at small $|\boldsymbol{y}|$ is $1 \to 2$ splitting, where one parton splits into two, $a \to a'b'$:

$$F_{a'b'}(x_1, x_2, y)\Big|_{\text{splitting}} = \frac{\alpha_s}{2\pi y^2} \frac{1}{x_1 + x_2} P_{a\to a'b'}\left(\frac{x_1}{x_1 + x_2}\right) \frac{f_a(x_1 + x_2)}{x_1 + x_2}\,. \tag{2.73}$$

The singularity $y \to 0$ has to be regularized in the context of sum rules, where we integrate over the transverse distance. Analogously to the unpolarized quark PDF discussed in Section 2.4.2, in the forward case $\zeta = 0$, DPDs fulfill sum rules. These have been proposed in Ref. [95] and proven in Ref. [107, 108]. In this work, we only consider the number sum rule. For the two-quark DPD $F_{qq'}$ it can be written as [69]:

$$\begin{aligned} &2\pi \int_{y_{\text{cut}}}^{\infty} \mathrm{d}y\, y \int_{-1+|x_1|}^{1-|x_1|} \mathrm{d}x_2\, F_{qq'}(x_1, x_2, y^2) \\ &\quad = \begin{cases} (N_{q'} - \delta_{qq'})\, f_q(x_1) + \mathcal{O}\Big(\alpha_s\Big) + \mathcal{O}(\Lambda^2 y_{\text{cut}}^2) & \text{for } x_1 > 0\,, \\ -\,(N_{q'} + \delta_{qq'})\, f_{\bar{q}}(-x_1) + \mathcal{O}\Big(\alpha_s\Big) + \mathcal{O}(\Lambda^2 y_{\text{cut}}^2) & \text{for } x_1 < 0\,, \end{cases} \end{aligned} \tag{2.74}$$

where $f_q$ and $f_{\bar{q}}$ are quark and antiquark PDFs and $N_{q'}$ is the number of valence quarks $q'$. To obtain this relation, we have used the relation $F_{\bar{q}q'}(x_1, x_2, y^2) = -F_{qq'}(-x_1, x_2, y^2)$ and its counterpart for the second parton in (2.62).

The lower cutoff on the integral over $y$ regularizes the singular $1/y^2$ behavior of $F_{qq'}$ for $y \to 0$. The last term in (2.74) denotes power corrections, with $\Lambda$ representing a typical hadronic scale. One should therefore take $y_{\text{cut}}$ sufficiently small in order to keep corrections at a moderate level. We use $y_{\text{cut}} = b_0/\mu$, where $\mu$ is the renormalization scale of the DPD and $b_0 = 2e^{-\gamma} \approx 1.12$ with the Euler-Mascheroni constant $\gamma$. Taking $\mu = 2\,\text{GeV}$ we get

$$y_{\text{cut}} \approx 0.11\,\text{fm}\,. \tag{2.75}$$

When considering Mellin moments in both momentum fractions, we want to integrate (2.74) over $x_1$. This is only well defined for $q \neq q'$, because the corresponding expression for $q = q'$ includes sea quark contributions that lead to divergent results when integrated over all momentum fractions. Taking the parton combination $ud$ in (2.74) and using

the number sum rule for ordinary PDFs, we get

$$S_{ud}(y_{\text{cut}}) := 2\pi \int_{y_{\text{cut}}}^{\infty} \mathrm{d}y\, y\, I_{ud}(\zeta = 0, y^2) = 2\pi \int_{y_{\text{cut}}}^{\infty} \mathrm{d}y\, y \int_{-1}^{1} \mathrm{d}x_1 \int_{-1}^{1} \mathrm{d}x_2\, F_{ud}(x_1, x_2, y^2)$$
$$= 2 + \mathcal{O}(\alpha_s^2) + \mathcal{O}(\Lambda^2 y_{\text{cut}}^2)\,. \tag{2.76}$$

Notice that the power of $\alpha_s$ on the r.h.s. is higher than in the generic relation (2.74), because perturbative splitting for the parton combination $ud$ starts only at order $\alpha_s^2$.

## 2.5 Double parton scattering

As discussed in Section 2.3.2, double parton scattering processes involving two partons from each hadron depend on sensitive partonic correlations, encoded in the DPDs. In this section, where we follow [73], we shall focus on a leading order analysis of the DPS cross section $\sigma_{\text{DPS}}$ considering only quark color-singlet contributions. We will briefly discuss further contributions at the end of this section.
We consider two hadrons moving in opposite directions with momenta $p$ and $\bar{p}$ along the $z$ axis at a large energy scale $Q$. The hadrons emit and absorb partons with momenta $k_i - (-1)^i \frac{r_i}{2}$ and $\bar{k}_i + (-1)^i \frac{r_i}{2}$, $i \in \{1, 2\}$, at relative separation $\boldsymbol{y}$, exchanging momenta $q_i = (k_i + \bar{k}_i)$. In the center of mass frame of the collision, the different momentum components are of the order:

$$\begin{aligned} q^+ \sim k^+ \sim p^+ \sim \bar{p}^- \sim Q\,, \\ q^- \sim k^- \sim p^- \sim \bar{p}^+ \sim \frac{\Lambda^2}{Q}\,, \\ \boldsymbol{p} = \bar{\boldsymbol{p}} = 0\,. \end{aligned} \tag{2.77}$$

Momentum conservation then forces the light-cone components of $r$ to be small compared to $Q$:

$$r^+ \sim r^- \sim \frac{\Lambda^2}{Q}\,, \tag{2.78}$$

implying $\zeta = \frac{r^+}{p^+} \sim \frac{\Lambda^2}{Q^2} \approx 0$. We shall therefore only consider the forward limit $\zeta = 0$. This kinematic situation is sketched in Figure 2.4. We factorize the DPS process into a hard process, described by the hard scattering cross section $\sigma_i(q_i^2)$, and a soft process, described by the DPD $F_{ab}(x_i, \boldsymbol{k}_i, \boldsymbol{y})$. The hard scattering cross section is defined by the spin projected hard scattering matrix element $H_i$ as:

$$\sigma_{i,a\bar{b}}(x_i \bar{x}_i s) = \frac{1}{2q_i^2}\, k_i^+ \left(\Gamma_a^-\right)_{\alpha\beta} H_{i,\beta\alpha\bar{\alpha}\bar{\beta}}(q_i^2) \left(\Gamma_{\bar{b}}^+\right)_{\bar{\beta}\bar{\alpha}} \bar{k}_i^-\,, \tag{2.79}$$

where we used $q_i^+ \sim k_i^+$ and $q_i^- \sim k_i^-$ from (2.77) to express $q_i^2 \approx 2q_i^+ q_i^- \approx$

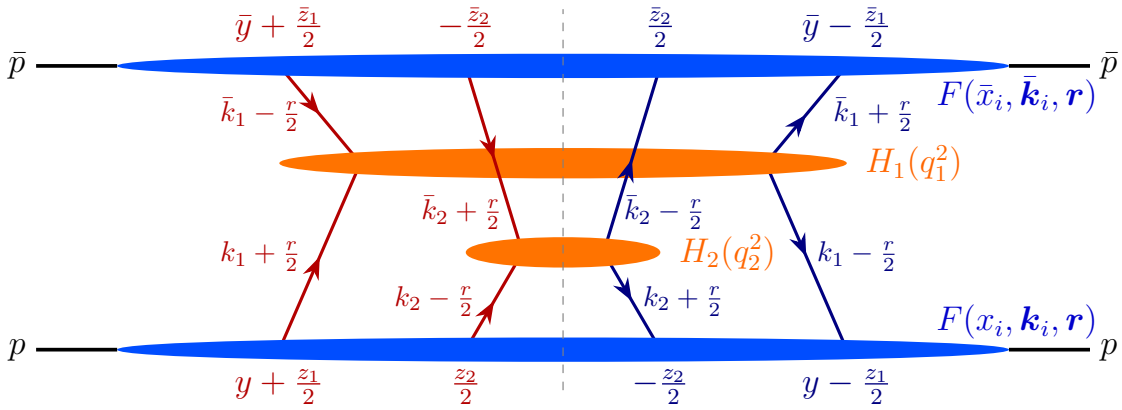



**Figure 2.4:** Illustration of leading order DPS kinematics. The soft parts of the interaction, described by the DPDs $F$, is represented by the large blue ovals. The hard part, described by the scattering matrix elements $H_i$, are shown as orange ovals. The two partons emitted from the hadrons, interacting with one parton of the other hadron each, are depicted as quark lines, connecting the soft and hard part. The dashed line in the middle represents the final state cut, separating amplitude (red) and conjugate amplitude (blue) quark lines.

$2x_i\bar{x}_i p^+\bar{p}^- \approx x_i\bar{x}_i(p+\bar{p})^2 = x_i\bar{x}_i s$, with the Mandelstam variable $s=(p+\bar{p})^2$. The leading twist spin projectors $\Gamma_a^\pm$ and $\Gamma_{\bar{a}}^\pm$ are defined similarly to the polarization projectors for parton correlation functions (2.40):

$$\Gamma_q^\pm = \frac{1}{2}\gamma^\pm, \quad \Gamma_{\Delta q}^\pm = \frac{1}{2}\gamma_5\gamma^\pm, \quad \Gamma_{\delta q}^{\pm,j} = \frac{1}{2}\gamma_5\gamma^\pm\gamma^j, \quad \Gamma_{\bar{a}}^\pm = -\eta_C^a\,\Gamma_a^\pm. \tag{2.80}$$

Combining our definition (2.55) for the quark singlet DPD ${}^1F_{ab}^\perp(x_i,\boldsymbol{k}_i,\zeta,\boldsymbol{y})$ with the hard scattering cross section (2.79), we obtain the differential DPS cross section:

$$\begin{aligned}\frac{\mathrm{d}\sigma}{\prod_{i=1}^n \mathrm{d}x_i\,\mathrm{d}\bar{x}_i\,\mathrm{d}^2\boldsymbol{q}_i} &= \frac{1}{C}\sum_{a_1a_2b_1b_2}\left[\prod_{i=1}^n\int \mathrm{d}^2\boldsymbol{k}_i\,\mathrm{d}^2\bar{\boldsymbol{k}}_i\;\delta^{(2)}(\boldsymbol{q}_i-\boldsymbol{k}_i-\bar{\boldsymbol{k}}_i)\right]\\ &\quad\times\int \mathrm{d}^2\boldsymbol{y}\;\hat{\sigma}_{a_1b_1}(x_1\bar{x}_1 s)\hat{\sigma}_{a_2b_2}(x_2\bar{x}_2 s)F_{a_1a_2}^\perp(x_1,x_2,\boldsymbol{k}_i,\boldsymbol{y})\;F_{b_1b_2}^\perp(\bar{x}_1,\bar{x}_2,\bar{\boldsymbol{k}}_i,\boldsymbol{y})\,.\end{aligned} \tag{2.81}$$

Notice that we dropped the argument $\zeta$, which is found to approximate zero within the context of DPS as discussed before. The factor $C$ is a combinatorial factor. If the two partons are identical, $C=2$, if not $C=1$. Integrating over transverse momenta reduces

the DPDs to their collinear versions:

$$\frac{\mathrm{d}\sigma}{\prod_{i=1}^{n}\mathrm{d}x_i\,\mathrm{d}\bar{x}_i} = \frac{1}{C}\sum_{a_1a_2b_1b_2}\int \mathrm{d}^2\boldsymbol{y} \\ \times \hat{\sigma}_{a_1b_1}(x_1\bar{x}_1 s)\hat{\sigma}_{a_2b_2}(x_2\bar{x}_2 s)F_{a_1a_2}(x_1,x_2,\boldsymbol{y})\; F_{b_1b_2}(\bar{x}_1,\bar{x}_2,\boldsymbol{y})\,. \tag{2.82}$$

The equations (2.82) and (2.81) were obtained using the assumption, that DPS can be factorized into hard and soft parts. For this assumption to hold, it is necessary to prove that gluons in the so-called Glauber region cancel [74]. For double Drell Yan (DDY) processes, this has been achieved in Ref. [109]. However, it does not hold for processes with hadronic final states when resolving transverse momenta [110]. We also did not include contributions from the color-octet DPD ${}^8F$ and fermion number interference. Both of these are assumed to be Sudakov suppressed [111]. In Ref. [112] it was shown that the color non-singlet distributions are suppressed at intermediate and large $y$ but cannot be neglected at small $y$, where Sudakov suppression has only a limited effect. Furthermore, we only considered leading order contributions, disregarding the effects of collinear and soft gluons. Collinear gluons are included by taking into account process-dependent Wilson lines in the same way as discussed for PDFs. Soft gluons are accounted for by multiplying the DPDs with a soft factor [113]. As discussed in Section 2.4.3, at small $y$, the DPD becomes singular due to $1 \to 2$ splitting, which are higher twist contributions. While we regularized this singularity with a cut-off in (2.74), in general, in the small $y$ regime, an SPS contribution has to be added by the DPS contribution in a suitable manner to avoid double counting [114].

# 3 Lattice Quantum Chromodynamics

At low energy scales $Q$, perturbation theory breaks down as $\alpha_s(Q)$ becomes large. To access low energy or soft quantities like PDFs, non-perturbative calculations are necessary. To perform non-perturbative QCD calculations, we have to evaluate the full path integral (2.17) to compute matrix elements like

$$\langle O \rangle = \frac{1}{Z} \int \mathcal{D}[\psi]\mathcal{D}[\bar{\psi}]\mathcal{D}[A_\mu]\, O(\psi, \bar{\psi}, A_\mu)\, e^{iS_{\mathrm{QCD}}(\psi,\bar{\psi},A_\mu)}\,, \tag{3.1}$$

where $O$ is the expression of interest, $Z$ is the partition function and $S_{\mathrm{QCD}}$ is the QCD action:

$$\begin{aligned} Z &= \int \mathcal{D}[\psi]\mathcal{D}[\bar{\psi}]\mathcal{D}[A_\mu]\, e^{iS_{\mathrm{QCD}}(\psi,\bar{\psi},A_\mu)}\,, \\ S_{\mathrm{QCD}}[A,\psi,\bar{\psi}] &= \int \mathrm{d}^4x\; \mathcal{L}_{\mathrm{QCD}}[A,\psi,\bar{\psi}](x)\;. \end{aligned} \tag{3.2}$$

In this section, we will introduce Lattice QCD as a non-perturbative tool to do so. The basic idea is to switch from real to imaginary time so that the exponentiated action becomes a weight instead of a phase factor, which allows one to evaluate the path integral using numerical methods like Monte Carlo sampling techniques. To evaluate integrals over space-time coordinates numerically, we will discretize the theory, including fermions and bosons. In this chapter, we follow [115].

## 3.1 Wick rotation

To obtain a real weight $e^{-S_{\mathrm{QCD}}}$, we want to replace Minkowski time $t$ by Euclidean time $t_E = -it$. This is achieved by performing the Wick rotation. The Wick rotation analytically continues the time coordinate to imaginary values,

$$t \to -it_E\,, \tag{3.3}$$

$$\mathrm{d}t \to -i\mathrm{d}t_E\,. \tag{3.4}$$

This rotates the integration contour from the real to the imaginary axis. Assuming the integrand to be analytic, the contour can be deformed back to the real axis, yielding

$$\int_{-\infty}^{\infty} \mathrm{d}t = i \int_{-\infty}^{\infty} \mathrm{d}t_E\,. \tag{3.5}$$

We introduce Euclidean space-time coordinates

$$x_E^\mu = (x_1, x_2, x_3, x_4) = (\vec{x}, t_E)\,, \qquad \mu = 1, \ldots, 4\,. \tag{3.6}$$

The Minkowski distance

$$x^2 = t^2 - \vec{x}^{\,2} \tag{3.7}$$

translates to

$$x^2 \to -\left(t_E^2 + \vec{x}^{\,2}\right) = -x_E^2\,, \tag{3.8}$$

where

$$x_E^2 = x_E^\mu x_E^\nu \, g_{E,\mu\nu}\,, \tag{3.9}$$

with the Euclidean metric

$$g_{E,\mu\nu} = \delta_{\mu\nu}\,. \tag{3.10}$$

As the metric is encoded in the anti-commutation relations of the Dirac gamma matrices,

$$\begin{aligned} \{\gamma_\mu^M, \gamma_\nu^M\} &= 2g_{\mu\nu}\,, \\ \{\gamma_\mu^E, \gamma_\nu^E\} &= 2\delta_{\mu\nu}\,, \end{aligned} \tag{3.11}$$

these also differ between Minkowski ($\gamma_\mu^M$) and Euclidean ($\gamma_\mu^E$) space. In this work, we follow the convention [115]:

$$\gamma_4^E = \gamma_0^M\,, \tag{3.12}$$

$$\begin{aligned} \gamma_k^E &= -i\gamma_k^M\,, \qquad k = 1, 2, 3\,, \\ \gamma_5^E &= \gamma_1^E \gamma_2^E \gamma_3^E \gamma_4^E\,, \end{aligned} \tag{3.13}$$

which fulfills (3.11).

The Euclidean gamma matrices obey $\gamma_\mu^E = \gamma_\mu^{E\,\dagger} = \gamma_\mu^{E\,-1}$. Applying the Wick rotation to the QCD action,

$$S_{\mathrm{QCD}} = \int \mathrm{d}^4x \, \mathcal{L}_{\mathrm{QCD}}(x)\,, \tag{3.14}$$

continues the Minkowski action analytically to the Euclidean action $S_E$,

$$iS_{\mathrm{QCD}} \to -S_E\,, \tag{3.15}$$

where

$$S_E = \int \mathrm{d}^4x_E \, \mathcal{L}_E(x_E) \tag{3.16}$$

is a real valued quantity.

We can write the expectation value of an operator $O$ in Euclidean space-time as

$$\langle O \rangle = \frac{1}{Z_E} \int \mathcal{D}[\psi]\mathcal{D}[\bar{\psi}]\mathcal{D}[A_\mu] \; O(\psi, \bar{\psi}, A_\mu)\, e^{-S_E(\psi, \bar{\psi}, A_\mu)}\,, \tag{3.17}$$

$$Z_E = \int \mathcal{D}[\psi]\mathcal{D}[\bar{\psi}]\mathcal{D}[A_\mu] \; e^{-S_E(\psi, \bar{\psi}, A_\mu)}\,. \tag{3.18}$$

The generating functional of the Euclidean path integral can be thought of as a statistical partition function with a real and positive weight. This allows us to evaluate the Euclidean path integral numerically, using Monte Carlo methods.

In the following, we only consider Euclidean expressions unless explicitly noted differently.

## 3.2 Discretization of continuum physics

We define the lattice $\Omega$ as a four-dimensional hypercube:

$$\Omega := \{n \mid n_\mu \in \{0, 1, \ldots, N_s - 1\},\ \mu = 1, 2, 3;\ n_4 \in \{0, 1, \ldots, N_t - 1\}\}\ . \tag{3.19}$$

The lattice $\Omega$ has $N_s$ ($N_t$) points, spaced by the lattice spacing $a$, in spatial (temporal) directions and spans a spatial volume of $(N_s a)^3$. Fermionic fields exist now only on these lattice sites. We denote the vector connecting two neighboring lattice sites along the $\mu$-axis as $\hat{\mu}$. Replacing the continuum infinite volume with this hypercube reduces the symmetry from the full Poincaré group to the hypercubic group, $H(4)$. To ensure that (spatial) momentum remains a good quantum number, we have to maintain momentum conservation. This is achieved by restoring discrete translational invariance by choosing periodic boundary conditions in space, i.e. $f(x + L\hat{\mu}) = f(x)$ for any function $f$ on $\Omega$. We will discuss artifacts associated with this finite volume later. Common choices for temporal boundary conditions include (anti) periodic as well as open boundaries. Periodic (anti-periodic) boundary conditions for bosonic (fermionic) fields preserve time translation invariance and thus energy, allowing for a straightforward spectral interpretation of correlation functions. However, at fine lattice spacings they lead to so-called topological freezing, i.e. the Monte Carlo evolution becomes trapped in a fixed topological sector due to large action barriers separating configurations of different topological charge. This results in long auto-correlation times and poor sampling of the path integral. Open boundary conditions in time explicitly break time translation invariance, but allow the topological charge to flow continuously through the boundaries, thereby alleviating topological freezing. For (anti)periodic boundary conditions, the full volume can be used to extract physical observables. On open temporal boundary lattices, only the bulk region sufficiently far from the temporal boundaries yields physical results, where boundary effects are exponentially suppressed [116].

### 3.2.1 The discrete Dirac operator

The free part of the action in Euclidean space can be discretized as

$$\int \mathrm{d}^4x\ \bar{\psi}(x)\left(\partial_\mu \gamma^\mu + m\right)\psi(x)\ \longrightarrow\ a^4 \sum_{x,y\in\Lambda} \bar{\psi}(x) D_{\text{free}}(x|y)\psi(y) \tag{3.20}$$

by replacing the integral with a sum and defining the free Dirac operator

$$D_{\text{free}}(x|y) = \sum_{\mu} \frac{\gamma_\mu}{2a} \left(\delta_{x,y+\hat{\mu}} - \delta_{x,y-\hat{\mu}}\right) + m\,\delta_{x,y}\,, \tag{3.21}$$

where the derivative was replaced by a symmetric differential quotient. This expression is not gauge covariant, as the fermion fields at different positions $x$ and $y \pm \hat{\mu}$ transform independently, as defined in (2.8). This can be amended by connecting the fermion fields with a gauge transporter, i.e. a Wilson line of length $a$:

$$U_\mu(x) = \mathcal{P} \exp\left(ig \int_x^{x+a\hat{\mu}} A_\mu(s)\, ds\right), \tag{3.22}$$

where $\mathcal{P}$ denotes path ordering. These Wilson lines are called gauge links and represent the bosonic degrees of freedom, living on the lattice edges. They transform as

$$U_\mu(x) \to \Omega(x)\, U_\mu(x)\, \Omega^\dagger(x+\hat{\mu})\,, \tag{3.23}$$

forming a naively discretized covariant Dirac operator:

$$(D_{\text{naive}})^{ab}_{\alpha\beta}(x|y) = \frac{1}{2a} \sum_{\mu} \gamma_{\mu,\alpha\beta} \Big[U^{ab}_\mu(x)\, \delta_{x,\,y+\hat{\mu}} - U^{\dagger\,ab}_\mu\,(x-\hat{\mu})\, \delta_{x,\,y-\hat{\mu}}\Big] + m\,\delta_{x,\,y}, \tag{3.24}$$

where we made both color $(a, b)$ and spinor $(\alpha, \beta)$ indices explicit.

In the free, massless, non-interacting case where $U_\mu = \mathbb{1}$, we can obtain the propagator, i.e. the Green's function of the Dirac operator (3.24), analytically. For convenience, we switch to momentum space by using a discrete Fourier transformation. The finite lattice size limits the momentum to $p^\mu \in (-\pi/a, \pi/a]$. In momentum space, the naive discretized propagator takes the following form:

$$(D_{\text{naive}})^{-1}(p) = -\frac{i}{a} \sum_{\mu} \gamma_\mu \frac{\sin(p_\mu a)}{\sum_\nu \sin^2(p_\nu a)}\,. \tag{3.25}$$

In continuum theory, the propagator of a massless particle has exactly one pole at $p = 0$. The naive discretized propagator (3.25) has additional singularities at $p^\mu = \pi/a$. In four dimensions, this corresponds to 16 poles, 15 of which are unphysical so-called doublers. These can be decoupled from the physical pole by introducing the Wilson term

$$T_{\text{Wilson}}(x|y) = -\frac{1}{2a} \sum_{\mu} \Big(U_\mu(x)\, \delta_{x+\hat{\mu},y} - 2\,\delta_{x,y} + U^\dagger_\mu(x-\hat{\mu})\, \delta_{x-\hat{\mu},y}\Big)\,, \tag{3.26}$$

which adds a mass $\propto a^{-1}$ to the doublers. Note that the gauge links are added here, not subtracted as in the naive Dirac operator (3.24). This produces a symmetric Fourier transform $\propto 1 - \cos(p_\mu a)$, which splits the zero momentum pole from the doublers. Notice also the absence of $\gamma_\mu$ in the Wilson term, making it independent of the spinor structure, particularly momentum. Adding (3.26) to (3.24) yields the Wilson-Dirac

operator:

$$D_{\text{Wilson}}[U_\mu](x|y) = \frac{1}{2a\kappa}\Big[\mathbf{1}\,\delta_{x,y} - \kappa\, H_W[U_\mu](x|y)\Big]\,, \tag{3.27}$$

where $\kappa$ is the hopping parameter

$$2am = \frac{1}{\kappa} - \frac{1}{\kappa_c} \tag{3.28}$$

and $H_W[U_\mu](x|y)$ is the hopping term

$$H_W[U_\mu](x|y) := \sum_\mu \Big[(1-\gamma_\mu)\,U_\mu(x)\,\delta_{x+\hat{\mu},y} + (1+\gamma_\mu)\,U_\mu^\dagger(x-\hat{\mu})\,\delta_{x-\hat{\mu},y}\Big]\,. \tag{3.29}$$

The critical hopping parameter $\kappa_c$ is the value of $\kappa$ at which the quark becomes massless, i.e. $m = 0$. It is determined numerically, e.g. by using the chiral relation $m_\pi^2 \propto m$ and extrapolating the squared pion mass $m_\pi^2$ to zero as a function of $1/\kappa$. In the free field case, $\kappa_c = 1/8$. In the interacting case, the quark mass has to be renormalized, becoming scale dependent, so that $\kappa_c$ depends on the lattice spacing $a$.

While the Wilson term (3.26) effectively removes doublers by acting as an extra mass term, it explicitly breaks chiral symmetry. A chiral transformation (rotation) of a fermion is defined as

$$\begin{aligned}\psi &\to e^{i\alpha\gamma_5}\psi\,,\\ \bar{\psi} &\to \bar{\psi}e^{i\alpha\gamma_5}\,.\end{aligned} \tag{3.30}$$

From this it becomes evident that any form of mass term breaks chiral symmetry, as the phases do not cancel. These two properties, chiral symmetry and no doublers, cannot be reconciled at $a \neq 0$, which is known as the Nielsen-Ninomiya theorem [117].

### 3.2.2 The discretized action

The free gauge action in the continuum is

$$S_g = \int \mathrm{d}^4x\, F^{a\ \mu\nu}(x) F^a_{\mu\nu}(x)\,. \tag{3.31}$$

To discretize this expression, we have to reformulate it in terms of gauge links $U_\mu$. For small $a$, the gauge links defined in (3.23) can be approximated as

$$\begin{aligned}U_\mu(x) = \mathcal{P}\exp\left(ig\int_x^{x+a\hat{\mu}} A_\mu(s)\,ds\right) &\overset{a\ll 1}{\approx} \exp\Big(igaA_\mu(x)\Big)\\ &= 1 + igaA_\mu(x) - \frac{1}{2}g^2a^2A_\mu^2(x) + \mathcal{O}(a^3)\,.\end{aligned} \tag{3.32}$$

Inserting (3.32) into the definition of the naively discretized Dirac operator (3.24) and taking the continuum limit $a \to 0$ recovers the continuum formulation (2.5). Considering the smallest possible loop of gauge links on the lattice, the so-called plaquette $U_{\mu\nu}$, one arrives at the following expression:

$$U_{\mu\nu}(x) = U_\mu(x) U_\nu(x + a\hat{\mu}) U_\mu^\dagger(x + a\hat{\nu}) U_\nu^\dagger(x) \,. \tag{3.33}$$

Using the approximation (3.32) and expanding the gauge fields around $x$,

$$A_\nu(x + a\hat{\mu}) = A_\nu(x) + a\partial_\mu A_\nu(x) + \mathcal{O}(a^2) \,, \tag{3.34}$$

the individual link variables can be written as

$$\begin{aligned} U_\mu(x) &= 1 + igaA_\mu(x) - \frac{1}{2} g^2 a^2 A_\mu^2(x) + \mathcal{O}(a^3) \,, \\ U_\nu(x + a\hat{\mu}) &= 1 + iga\Big(A_\nu(x) + a\partial_\mu A_\nu(x)\Big) - \frac{1}{2} g^2 a^2 A_\nu^2(x) + \mathcal{O}(a^3) \,. \end{aligned} \tag{3.35}$$

Using (3.35) to evaluate (3.33), keeping terms up to $\mathcal{O}(a^2)$, one obtains

$$U_{\mu\nu}(x) = 1 + iga^2\Big(\partial_\mu A_\nu - \partial_\nu A_\mu\Big) - g^2 a^2\Big(A_\mu A_\nu - A_\nu A_\mu\Big) + \mathcal{O}(a^3) \,, \tag{3.36}$$

where the $\mathcal{O}(a^2)$ terms can be identified with the field strength tensor (2.11):

$$U_{\mu\nu}(x) = 1 + iga^2 F_{\mu\nu}(x) + \mathcal{O}(a^3) = \exp\Big(iga^2 F_{\mu\nu}(x)\Big) + \mathcal{O}(a^3) \,. \tag{3.37}$$

The $\mathcal{O}(a^3)$ and $\mathcal{O}(a^5)$ contributions vanish similarly to the $\mathcal{O}(a)$ ones [115], so that the exponential can be expanded to second order in $a^2$,

$$U_{\mu\nu}(x) = 1 + iga^2 F_{\mu\nu}(x) - \frac{1}{2} g^2 a^4 F_{\mu\nu}^2(x) + \mathcal{O}(a^6) \,. \tag{3.38}$$

Taking the trace w.r.t color and using $\mathrm{tr}(F_{\mu\nu}) = 0$, one obtains

$$\mathrm{tr}\Big(U_{\mu\nu}(x)\Big) = \mathrm{tr}(\mathbb{1}) - \frac{1}{2} g^2 a^4 \,\mathrm{tr}\Big(F_{\mu\nu}^2(x)\Big) + \mathcal{O}(a^6) \,. \tag{3.39}$$

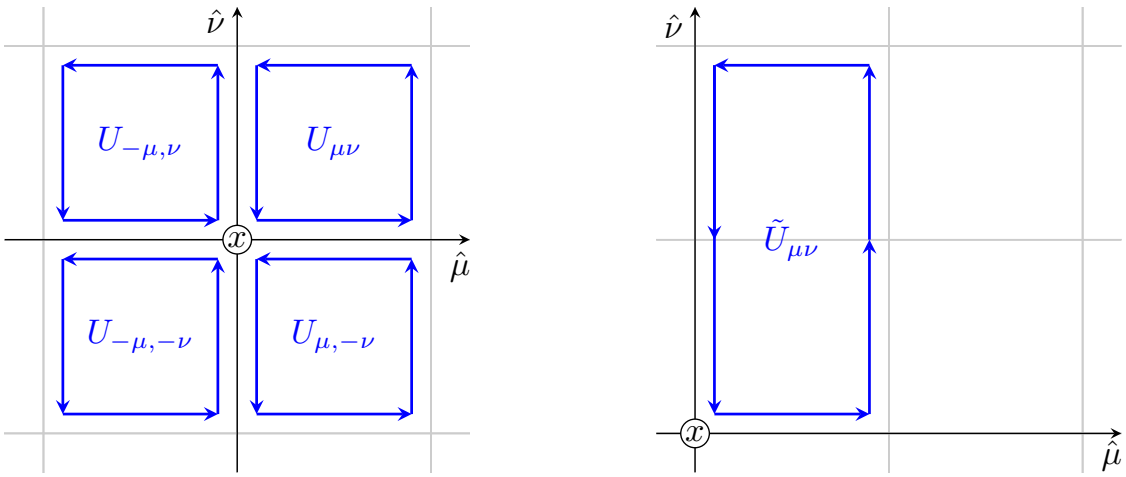
Now, we can evaluate (3.31) by replacing the integral with a sum over all lattice sites $\int \mathrm{d}^4x \to a^4 \sum_x$. This defines the Wilson gauge action

$$S_g = \frac{\beta}{3} \sum_{x,\mu<\nu} \Re \,\mathrm{tr}\Big(\mathbb{1} - U_{\mu\nu}(x)\Big) \,, \tag{3.40}$$

where $\beta = \frac{6}{g^2}$. Higher order contributions to $U_{\mu\nu}$, which vanish in the continuum, can contain imaginary contributions. To ensure the action is always real, the real part of the trace is taken.

### 3.2.3 Symanzik improvement

The discretization of QCD introduces artifacts proportional to powers of the lattice spacing $a$. For the Wilson fermions, defined by the Wilson-Dirac operator (3.27), the leading discretization effects are of $\mathcal{O}(a)$. For the Wilson gauge action (3.40) they are of $\mathcal{O}(a^2)$. While in the continuum, all discretization effects vanish, taking the continuum limit is laborious and computationally expensive. Thus, it is desirable to reduce discretization effects by removing the leading order contributions. This can be done systematically by following the Symanzik improvement program which makes use of the fact that our discretization is not unique. Combining terms from different discretizations, which have different discretization errors, enables us to remove leading order discretization effects. The core idea is to find alternative discretizations that include terms of the order to be removed. These terms are then added to the original with a suitable weight as to precisely cancel the leading discretization error contribution.




**(a)** Clover term summands **(b)** Rectangular plaquette

**Figure 3.1:** Comparison of the lattice plaquette structures. Left: the summands of the clover term $Q_{\mu\nu}$. Right: The rectangular plaquette $\tilde{U}_{\mu\nu}$ used to obtain the Lüscher-Weisz action.

Wilson fermions suffer from $\mathcal{O}(a)$ discretization errors stemming from the Wilson term. They can be $\mathcal{O}(a)$ improved by the addition of the clover term as proven by Sheikholeslami and Wohlert [118]:

$$C[U_\mu](x|y) := -\frac{i}{16a^2}\sigma_{\mu\nu}Q_{\mu\nu}(x)\,\delta_{xy}\,, \tag{3.41}$$

where

$$Q_{\mu\nu}(x) := U_{\mu,\nu}(x) + U_{\nu,-\mu}(x) + U_{-\mu,-\nu}(x) + U_{-\nu,\mu}(x) \tag{3.42}$$

is the sum over all plaquettes in the $(\mu,\nu)$-plane including the lattice site $x$, forming a four-leaf clover. This is illustrated in Figure 3.1a. Adding (3.41) to (3.27) yields the $\mathcal{O}(a)$ improved Wilson Dirac operator

$$D_{\mathrm{SW}}[U_\mu](x|y) = \frac{1}{2a\kappa}\Big[\delta_{xy} - \kappa H_W[U_\mu](x|y)\Big] + a c_{\mathrm{SW}}\, C[U_\mu](x|y)\,, \tag{3.43}$$

where $c_{\mathrm{SW}}$ is the Sheikholeslami-Wohlert coefficient. It can be determined non-perturbatively, which for $n_f = 3$ was done in Ref. [119].

The $\mathcal{O}(a)$-improved Dirac operator (3.43) still breaks chiral symmetry explicitly. However, it satisfies the important symmetry property of so-called $\gamma_5$-Hermiticity:

$$\gamma_5\,[D_{\mathrm{SW}}[U_\mu](x|y)]^\dagger\,\gamma_5 = D_{\mathrm{SW}}[U_\mu](y|x)\,. \tag{3.44}$$

This relation follows from the unitarity of the gauge links, $U_\mu(x)^\dagger = U_{-\mu}(x)$, and the fact that $\gamma_5$ anticommutes with the Dirac matrices, $\{\gamma_5,\gamma_\mu\} = 0$. It holds separately for both the Wilson hopping term and the clover term.

As a consequence, the eigenvalues of the Dirac operator occur in complex conjugate pairs, implying that its determinant is real-valued. This ensures a well-defined fermionic measure in the path integral.

The Wilson gauge action (3.40) is subject to $\mathcal{O}(a^2)$ discretization errors. These arise from higher-order terms in the expansion (3.38), which contribute at order $a^6$ to the plaquette. Upon summation over lattice sites, these terms correspond to $\mathcal{O}(a^2)$ corrections in the continuum limit.

The absence of $\mathcal{O}(a)$ discretization errors can already be observed in the explicit expansion of the plaquette (3.36), where odd powers in $a$ cancel due to the symmetry of the closed loop. More generally, an $\mathcal{O}(a)$ contribution would correspond to a dimension-five operator. While these occur in the Wilson-Dirac operator (3.27), they are forbidden by gauge invariance and hypercubic symmetry in the pure gauge theory.

The Wilson gauge action $S_g$ can be improved to $\mathcal{O}(g^2a^2)$ by the addition of a rectangular plaquette term $\tilde{U}_{\mu\nu}$ to (3.31). This is the so-called Lüscher-Weisz action [120]:

$$S_{\mathrm{LW}}[U_\mu] = c_0\, S_g[U_\mu] + \frac{c_1\beta}{6}\sum_x\sum_{\mu\neq\nu}\Re\ \mathrm{tr}\left(\mathbb{1} - \tilde{U}_{\mu\nu}(x)\right), \tag{3.45}$$

where $\tilde{U}_{\mu\nu}$ is

$$\begin{aligned}\tilde{U}_{\mu\nu}(x) := {}& U_\mu(x)\,U_\nu(x+\hat{\mu})\,U_\nu(x+\hat{\mu}+\hat{\nu})\,U_\mu^\dagger(x+2\hat{\nu}) \\ & \times U_\nu^\dagger(x+\hat{\nu})\,U_\nu^\dagger(x)\,,\end{aligned} \tag{3.46}$$

illustrated in Figure 3.1b. Note that this expression represents one orientation of a $1 \times 2$ rectangular Wilson loop in the $(\mu, \nu)$-plane. The sum over $\mu \neq \nu$ includes all orientations related by lattice symmetries.

Combining (3.43) and (3.45), we obtain the LQCD action used for all simulations in this work:

$$S[\psi, \bar{\psi}, U_\mu] = a^4 \sum_f \sum_x \bar{\psi}_f(x)\, D_{\mathrm{SW}}[U_\mu]\, \psi_f(x) + S_{\mathrm{LW}}[U_\mu]\,. \tag{3.47}$$

### 3.2.4 The discretized path integral

We can now formulate the Euclidean path integral (3.17) on a discrete lattice. One can split the expectation value of some operator $\langle O \rangle$ into a fermionic and a gauge component, i.e. $\langle O \rangle = \langle \langle O \rangle_F \rangle_G$. We shall focus on the fermionic part first, i.e. the integration over the Grassmann valued fields, which we denote here by $\eta$ and $\bar{\eta}$. We split the action accordingly,

$$S_E = S_F[\eta, \bar{\eta}, U_\mu] + S_G[U_\mu]\,. \tag{3.48}$$

We can now write

$$\langle O \rangle = \frac{1}{Z} \int \mathcal{D}[U_\mu] e^{-S_G[U_\mu]} Z_F[U_\mu] \underbrace{\frac{1}{Z_F[U_\mu]} \int \mathcal{D}[\eta, \bar{\eta}] e^{-S_F[\eta, \bar{\eta}, U_\mu]} O[\eta, \bar{\eta}, U_\mu]}_{\langle O \rangle_F}\,, \tag{3.49}$$

where

$$Z_F[U_\mu] = \int \mathcal{D}[\bar{\eta}] \mathcal{D}[\eta]\, e^{-S_F[\eta, \bar{\eta}, U_\mu]}\,. \tag{3.50}$$

We express the fermionic part of the action as

$$S_F[\eta, \bar{\eta}, U_\mu] = \sum_{i,j} \bar{\eta}_i A_{ij} \eta_j \tag{3.51}$$

to evaluate $Z_F$ as a Gaussian integral

$$Z_F = \int \mathcal{D}[\bar{\eta}] \mathcal{D}[\eta]\, \exp\left[\sum_{i,j} \bar{\eta}_i A_{ij} \eta_j\right] = \det[A]\,, \tag{3.52}$$

where we can choose $A_{ij} = -D_{ij}$ to arrive at the fermionic determinant.

Analogous to the continuum (2.14), we can define a generating functional for fermions

$$W[j, \bar{j}] = \int \mathcal{D}\eta \mathcal{D}\bar{\eta}\, \exp[\bar{\eta} A \eta] + \bar{j}\eta + j\bar{\eta} = \det[A] \exp\left[-\bar{j} A^{-1} j\right]\,, \tag{3.53}$$

where we completed the square and used (3.52) to arrive at the final expression. We can use this to compute fermionic expectation values, e.g.

$$\langle \eta\bar{\eta}\rangle_F = \frac{1}{Z_F}\frac{\partial}{\partial j}\frac{\partial}{\partial \bar{j}} W[j,\bar{j}]\bigg|_{j=\bar{j}=0} = -A^{-1}\,. \tag{3.54}$$

Explicitly evaluating this formula for expectation values of multiple operators, we arrive at Wick's theorem,

$$\begin{aligned}\langle \eta_{i_1}\bar{\eta}_{j_1}\cdots\eta_{i_n}\bar{\eta}_{j_n}\rangle_F &= \frac{1}{Z_f}\int \mathcal{D}[\eta]\mathcal{D}[\bar{\eta}]\eta_{i_1}\bar{\eta}_{j_1}\cdots\eta_{i_n}\bar{\eta}_{j_n}\exp\left[\bar{\eta}A\eta\right] \\ &= (-1)^n \sum_{P\in S_n}\operatorname{sign}(P)(A^{-1})_{i_1 j_{P(1)}}\cdots(A^{-1})_{i_1 j_{P(n)}}\,.\end{aligned} \tag{3.55}$$

## 3.3 Monte Carlo simulations

The Euclidean version of the path integral (3.17) can be evaluated numerically using the Monte Carlo method. This method allows us to approximate the numerical result of an integral by evaluating the integrand at stochastically selected points within the integrands support region and averaging over the corresponding values. For a simple, one dimensional integral, this means

$$\int_a^b \mathrm{d}x\, f(x) = \lim_{N\to\infty}\frac{b-a}{N}\sum_{x_i\in[a,b]} f(x_i)\,. \tag{3.56}$$

The error associated with a truncation at some large $N$ is proportional to $1/\sqrt{N}$. If the integrand receives most contributions from a small subset of its support, convergence of the sampling can be increased by biasing the sampling points with a suitable probability distribution so that support regions with larger contributions are sampled more frequently. This can be achieved by decomposing the integrand $f$ into a product of some function $g$ and a real and positive weight $w$ which share their support with $f$, i.e. $\forall_{x\in[a,b]} : f(x) = g(x)w(x)$. The weight $w$ defines the probability distribution which governs the choice of the sampling points $x_i$:

$$Z_w = \int_a^b \mathrm{d}x\, w(x)\,, \quad \mathrm{d}P = \frac{w(x)}{Z_w}\mathrm{d}x\,. \tag{3.57}$$

This allows us to rewrite the original integration and sampling as

$$\frac{1}{Z_w}\int_a^b \mathrm{d}x\, f(x) = \int_a^b \mathrm{d}P\, g(x) = \lim_{N\to\infty}\frac{1}{N}\sum_{x_i\in[a,b]} g(x_i)\,, \tag{3.58}$$

where the points $x_i$ were distributed according to $\mathrm{d}P$.

We can evaluate general expectation values of operators (3.49) by using Wick's theorem (3.55) for the fermionic part, then integrating over the gauge links:

$$\begin{aligned}\left\langle \hat{\psi}^{f_1}_{\alpha_1 a_1}(x_1)\, \hat{\bar{\psi}}^{f'_1}_{\beta_1 b_1}(x'_1) \cdots \hat{\psi}^{f_n}_{\alpha_n a_n}(x_n)\, \hat{\bar{\psi}}^{f'_n}_{\beta_n b_n}(x'_n) \right\rangle &= \frac{(-1)^n}{Z} \sum_{P\in S_n} \operatorname{sign}(P) \int \mathcal{D}\left[U_\mu\right] \\ &\times \left(M^{f_1}\left[U_\mu\right]\right)^{a_1 b_{P(1)}}_{\alpha_1 \beta_{P(1)}} \left(x_1 \mid x'_{P(1)}\right) \cdots \left(M^{f_n}\left[U_\mu\right]\right)^{a_n b_{P(n)}}_{\alpha_n \beta_{P(n)}} \left(x_n \mid x'_{P(n)}\right) \\ &\times \delta_{f_1 f'_{P(1)}} \cdots \delta_{f_n f'_{P(n)}} e^{-S_{\mathrm{LW}}[U_\mu]} \prod_f \det\left\{D^f_{\mathrm{SW}}\left[U_\mu\right]\right\}, \end{aligned} \tag{3.59}$$

where we made all spinor (greek) and color (latin) indices explicit, $f_i$ denote the flavor of the corresponding quark field. We introduced the fermionic propagator $M^f\left[U_\mu\right]$, which is defined as the solution of $D^f_{\mathrm{SW}}\left[U_\mu\right] M^f\left[U_\mu\right] = \mathbb{1}$. The exponentiated Lüscher-Weisz gauge action $e^{-S_{\mathrm{LW}}[U_\mu]}$ provides a suitable real and positive weight for Monte Carlo integration, the fermion determinant $\det\left\{D^f_{\mathrm{SW}}\left[U_\mu\right]\right\}$ appearing in (3.59) can be absorbed into this Monte-Carlo weight as

$$\mathcal{D}P[U_\mu] = \frac{e^{-S_{\mathrm{LW}}[U_\mu]}}{Z} \left[\prod_f \det\left\{D^f_{\mathrm{SW}}[U_\mu]\right\}\right] \mathcal{D}\left[U_\mu\right] . \tag{3.60}$$

The determinant is always real due to $\gamma_5$-hermiticity (3.44). In practice, it can become negative due to gauge fluctuations. This becomes more likely for lighter quark masses. Due to its considerably larger mass it is unlikely for the strange quark determinant to become small or even negative. Violations of this assumption were found in Ref. [121], particularly for coarser lattices. The corresponding sign can be included during reweighting, which we shall discuss below.

For the light quarks it is useful to choose $m_u = m_d$, i.e. consider them as mass degenerate. As their Dirac operators are now identical, the product of their determinants is always non-negative. To avoid instabilities caused by near-zero eigenvalues of the Wilson Dirac operator, a small twisted-mass term $\mu_0$ is introduced into the simulated action, shifting all eigenvalues away from zero. It is added to the hermitian Dirac operator $Q := \gamma_5 D$ and ensures $\det(Q^2 + \mu_0^2) > 0$. The resulting mismatch with the target theory has to be corrected by reweighting every observable with a configuration dependent reweighting factor [122, 123], which will be discussed in more detail below:

$$W_0 = \det\left[\frac{(\hat{Q}^2 + 2\mu_0^2)\hat{Q}^2}{(\hat{Q}^2 + \mu_0^2)^2}\right] . \tag{3.61}$$

We can now use (3.60) to evaluate the Euclidean path integral over the gauge links for an operator $\mathcal{O}$ as

$$\langle O \rangle_U = \frac{1}{Z_E} \int \mathcal{D}[U_\mu]\; O(U_\mu)\, e^{-S_E(\psi,\bar{\psi},U_\mu)} \approx \frac{1}{N} \sum_i O[U_i] . \tag{3.62}$$

To obtain the gauge configurations $U_i$ distributed in accordance with (3.60), we employ a Markov chain Monte Carlo algorithm. A Markov chain is a stochastic process that generates a new configuration $U_i$ based on an existing one $U_{i-1}$ by performing random updates with transition probability $T(U_i|U_{i-1})$ which satisfies

$$0 \leq T(U_i|U_{i-1}) \leq 1\,, \quad \sum_{U_i} T(U_i|U_{i-1}) = 1\,. \tag{3.63}$$

Each update depends only on the current configuration. Starting from a random configuration, the chain requires a number of initial updates to lose memory of the starting point, which is called thermalization. In equilibrium, the transition probability $T$ must satisfy detailed balance

$$T(U_i|U_{i-1})P(U_{i-1}) = T(U_{i-1}|U_i)P(U_i)\,, \tag{3.64}$$

which guarantees convergence to the target distribution $P(U)$, provided the chain is also ergodic, i.e. any configuration will be encountered in the chain at some point, independent on the initial configuration. At small lattice spacings, ergodicity can be violated by topological freezing, which can be avoided by using open boundary conditions in time as discussed in Section 3.2. Subsequent configurations are obtained by continuing the Markov chain without the need to thermalize again.

A possible choice for the transition probability $T$ is the Metropolis-Hastings algorithm, $T = \min(1, \exp(-\Delta S))$, where $\Delta S = S(U_i) - S(U_{i-1})$. The handling of fermions is numerically expensive due to the non-local nature of the fermionic determinant. A suitable solution is presented by the Hybrid Monte Carlo (HMC) algorithm [124], where fermions are replaced by pseudofermion fields $\phi$ via the identity

$$\det(D^\dagger D) \propto \int \mathcal{D}[\phi^\dagger]\mathcal{D}[\phi]\, e^{-\phi^\dagger (D^\dagger D)^{-1}\phi}\,, \tag{3.65}$$

reducing the light quark determinants to a bosonic integral. The HMC then evolves the gauge field via fictitious molecular dynamics equations of motion, with the Metropolis step at the end of each trajectory correcting for the finite step size of the numerical integration and ensuring detailed balance.

The reformulated fermionic determinant requires an inversion of the Dirac operator product $D^\dagger D$. This inversion becomes particularly expensive when the condition number $\kappa = \lambda_{\max}/\lambda_{\min}$ is large, where $\lambda_{\max}$ and $\lambda_{\min}$ are the largest and smallest eigenvalues of $D^\dagger D$, respectively. For light quark masses, $\lambda_{\min}$ is small and $\kappa$ becomes large, significantly increasing the cost of the inversion. This is known as critical slowing down, a phenomenon, where the increase in computational cost does not follow the naive scaling of the system size but exceeds it. It occurs when approaching the critical point of a theory due to increased auto-correlation times [125].

To reduce $\kappa$, the light quark determinant is factored into a tower of determinant ratios with increasing auxiliary masses $\mu_0 < \mu_1 < \cdots < \mu_{N_{mf}}$ via Hasenbusch mass preconditioning [126, 127], where each ratio is significantly better conditioned than the

full operator, considerably reducing the computational cost. This does not influence reweighting, as the additional ratios of determinants are exact.

The strange quark contributes a single unpaired determinant which, after even-odd preconditioning, requires the evaluation of $\sqrt{\det \hat{Q}_s^2}$. This cannot be expressed directly as a bosonic pseudofermion integral. It is therefore treated via the RHMC algorithm [128, 129], where the square root is approximated by a rational function whose deviation from the exact result is corrected by another reweighting factor $W_1$. This factor can also be used to absorb the sign of possible real negative eigenvalues of the Dirac operator mentioned above [121]. Combining $W_0$ and $W_1$, expectation values of any observable $O$ are then recovered via

$$\langle O \rangle = \frac{\langle O \cdot W_0 W_1 \rangle_{\mu_0}}{\langle W_0 W_1 \rangle_{\mu_0}} \,. \tag{3.66}$$

Both RHMC and twisted-mass reweighting can be further improved by Low-mode deflation [130], more details on the techniques used to generate gauge configurations in this work can be found in Ref. [131–133].

# 4 Lattice methodology

In this section we summarize the methods employed to compute hadronic observables on the lattice. We begin by introducing hadronic matrix elements constructed from $n$-point correlation functions of interpolating fields and the operators of interest. We then apply Wick's theorem to evaluate the correlation functions. In the context of this work, we have to consider two-, three-, and four-point functions. Following this, we introduce the improvement strategies used to increase the SNR of the correlation functions. Finally, we present the data analysis techniques we employ to extract reliable physics results from our lattice data.

## 4.1 Hadronic matrix elements

We first introduce Euclidean correlation functions to access Euclidean matrix elements on the lattice. We then proceed to define hadronic interpolating fields and operators considered in this work. We end this subsection with an overview of the resulting Wick contractions for the matrix elements defined in Chapter 5.

### 4.1.1 Euclidean correlation functions

In this section, we define Euclidean correlation functions following [115]. These expectation values $\langle O_n(t_n) \dots O_1(0) \rangle$ are called $n$-point functions. To evaluate the role of imaginary time, we consider a theory described by a Euclidean Hamiltonian $H$ with an orthonormal set of energy eigenstates $|n\rangle$ and corresponding energy eigenvalues $E_n$ so that $E_n \leq E_{n+1}$, where we set the vacuum energy $E_0 = 0$ without loss of generality. All other energy levels are now considered w.r.t the vacuum energy level.

The theory can be discretized by time-slicing and introducing intermediate fields. To make this explicit, we discretize the Euclidean time extent $T$ into $N$ slices of spacing $a$, such that $T = Na$. The partition function $Z_E$ then takes the form

$$Z_E = \int \prod_{k=1}^{N} \mathcal{D}\phi_k \prod_{k=1}^{N} \langle \phi_{k+1} | e^{-aH} | \phi_k \rangle, \tag{4.1}$$

where $|\phi_k\rangle$ denotes a field eigenstate on the $k$-th time slice. For periodic boundary conditions in time, the fields satisfy

$$\phi_{N+1}(\mathbf{x}) = \phi_1(\mathbf{x}), \tag{4.2}$$

such that the product of transfer matrix elements forms a closed chain. This closure implies

$$Z_E = \int \mathcal{D}\phi_1 \, \langle \phi_1 | e^{-TH} | \phi_1 \rangle, \tag{4.3}$$

which, using the completeness relation $\int \mathcal{D}\phi \, |\phi\rangle\langle\phi| = \mathbb{1}$, yields the trace representation

$$Z_E = \mathrm{tr}\Big(e^{-TH}\Big) \, . \tag{4.4}$$

For a two-point correlation function with operators $O_1$ and $O_2$ at Euclidean times 0 and $t$, we can write:

$$\langle O_2(t) O_1(0) \rangle = \frac{\mathrm{tr}\Big(e^{-(T-t)H} \, O_2(0) \, e^{-tH} \, O_1(0)\Big)}{\mathrm{tr}(e^{-TH})} \, , \tag{4.5}$$

where we used the Heisenberg picture to evolve $O_2(t) = e^{tH} O_2(0) e^{-tH}$. Using the trace identity $\mathrm{tr}(O) = \sum_n \langle n | \, O \, | n \rangle$, inserting a complete set of energy eigenstates $\mathbb{1} = \sum_m |m\rangle\langle m|$ and evaluating the exponentiated Hamiltonians, one obtains the spectral decomposition

$$\begin{aligned} \langle O_2(t) O_1(0) \rangle &= Z_E^{-1} \sum_{n,m} \langle n | O_2 | m \rangle \langle m | O_1 | n \rangle e^{-(T-t)E_n} e^{-tE_m} \\ &\xrightarrow{T \to \infty} \sum_m \langle 0 | O_2 | m \rangle \langle m | O_1 | 0 \rangle e^{-tE_m} \, , \end{aligned} \tag{4.6}$$

where we used $Z_E \to 1$ in the limit of $T \to \infty$.

When using open boundary conditions, the initial and final state can be different. The chain of transfer matrix elements cannot be reformulated into a trace in this case. This leads to boundary state contributions which are exponentially suppressed in the bulk [123]. If we use operators at times $t_1$ and $t_2$ sufficiently far from the boundary, i.e. $T \gg t_2 \geq t_1 \gg a$, we recover the spectral decomposition (4.6) for $T \to \infty$:

$$\langle O_2(t_2) O_1(t_1) \rangle_{\mathrm{OBC}} \xrightarrow[\text{bulk}]{} \sum_m \langle 0 | \, O_2(0) \, | m \rangle \, \langle m | \, O_1(0) \, | 0 \rangle \; e^{-E_m (t_2 - t_1)} \, , \tag{4.7}$$

where we used $Z_{\mathrm{OBC}} \to 1$ for $T \to \infty$. This is sketched in more detail in appendix C.

We conclude that both boundary conditions in time, open and periodic, yield the same result in the bulk as $T \to \infty$. In the following, we shall thus no longer distinguish between them. For notational convenience, the times $t_1$ and $t_2$ can be shifted by $-t_1$, so that the correlator can again be written as $\langle O_2(t = t_2 - t_1) O_1(0) \rangle$. We also do not explicitly denote the time, if it is equal to zero, i.e. $O_i(0) \equiv O_i$.

Including an additional operator, usually at an intermediate time $0 \leq \tau \leq t$, yields

three-point functions:

$$\langle O_3(t)O_2(\tau)O_1(0)\rangle \overset{T\to\infty}{=} \sum_{m,n} \langle 0|\, O_3\, |m\rangle \, \langle m|\, O_2\, |n\rangle \, \langle n|\, O_1\, |0\rangle \, e^{-E_m(t-\tau)} e^{-E_n\tau} \,. \tag{4.8}$$

For large temporal separations $t-\tau$ and $\tau$, the lowest energy eigenstate dominates. This can be used to extract the ground state matrix element $\langle m|\, O_2\, |n\rangle$, provided operators $O_1(t)$ and $O_2(0)$ are found that have sufficiently large overlap with the ground states of the particle of interest. For hadronic matrix elements, these are called hadron interpolating fields, which we shall discuss next.

### 4.1.2 Hadron interpolating fields

To find operators that create and annihilate a specific hadron, we have to find operators that share its quantum numbers. For hadron physics, these are spin, parity and flavor. These operators are called hadron interpolators and are often inspired by the valence quark model. We shall denote these as $\mathcal{J}(\vec{x},t)$ for the annihilation and $\overline{\mathcal{J}}(\vec{x},t)$ for the creation of hadrons at time $t$ and position $\vec{x}$. We suppress additional indices, e.g. open spin or flavor indices, for the moment. Mesons can be created as quark-antiquark pairs while baryons are simulated as three-quark states. The important aspect of the interpolators is to have maximum overlap $\alpha_0$ with the hadronic ground state $|h\rangle$ and ideally as little overlap $\alpha_n$ as possible with other states, e.g. excited states of said hadron or multi-particle states, which we summarize as $|h^n\rangle$:

$$\overline{\mathcal{J}}\,|0\rangle = \alpha_0\,|h\rangle + \sum_n \alpha_n\,|h^n\rangle \;. \tag{4.9}$$

To create/annihilate a hadron with momentum $\vec{p}$, the interpolators $\mathcal{J}, \overline{\mathcal{J}}$ have to be projected onto said momentum by a discrete Fourier transform on the lattice:

$$\begin{aligned} \mathcal{J}(\vec{p},t) &= a^3 \sum_{\vec{x}} e^{-i\vec{p}\cdot\vec{x}}\, \mathcal{J}(\vec{x},t), \\ \overline{\mathcal{J}}(\vec{p},t) &= a^3 \sum_{\vec{x}} e^{i\vec{p}\cdot\vec{x}}\, \overline{\mathcal{J}}(\vec{x},t)\,. \end{aligned} \tag{4.10}$$

We can now formulate hadronic two-point functions as

$$C_{\mathrm{2pt}}(\vec{p},t) = \langle 0|\, \mathcal{J}(\vec{p},t)\overline{\mathcal{J}}(\vec{p},0)\,|0\rangle \tag{4.11}$$

and three-point functions as

$$C_{\mathrm{3pt}}(\vec{p},t,\tau) = \langle 0|\, \mathcal{J}(\vec{p},t)O(\tau)\overline{\mathcal{J}}(\vec{p},0)\,|0\rangle \;, \tag{4.12}$$

by introducing the operator $O(\tau)$. The spectral decompositions (4.7) and (4.8) then yield

$$C_{\text{2pt}}(\vec{p},t) = \sum_n \frac{|Z_n|^2}{2E_n} e^{-E_n t}\,, \tag{4.13}$$

and

$$C_{\text{3pt}}(\vec{p},t,\tau) = \sum_{m,n} \frac{Z_m Z_n^*}{4E_m E_n} \langle m|\, O(\tau)\, |n\rangle\, e^{-E_m(t-\tau)} e^{-E_n \tau}\,, \tag{4.14}$$

where

$$\begin{aligned} Z_n &= \langle 0|\, \mathcal{J}(\vec{p},t)\, |n\rangle\ , \\ Z_n^* &= \langle n|\, \overline{\mathcal{J}}(\vec{p},t)\, |0\rangle\ , \end{aligned} \tag{4.15}$$

and we used the relativistic normalization of states and subsequently $\mathbb{1} = \sum_n \frac{1}{2E} |n\rangle \langle n|$. Note that the interpolators have no overlap with the vacuum, so that the lowest energy state is no longer the vacuum but the ground state of the simulated hadron. To extract the ground state matrix element, we have to cancel the overlap terms, e.g. by dividing the three-point function by the two-point function. This is only possible if the overlap terms are scalars, which they are not if we have e.g. open Lorentz indices. We introduce the label $\lambda$ to denote these degenerate states, e.g. spin for the nucleon, with the ground state $|\vec{p},\lambda\rangle$. To obtain scalar terms, we have to project the matrix elements onto e.g. a certain polarization, using a suitable projection $\mathcal{T}$. For an unpolarized nucleon, this $\mathcal{T} = \mathbb{1}$:

$$\frac{1}{2}\sum_\lambda \langle \vec{p},\lambda|\, O\, |\vec{p},\lambda\rangle|_{\text{latt}} = \left.\frac{\left\langle \text{tr}\Big[\mathcal{T}\, \mathcal{J}(\vec{p},t)\, O(\tau)\, \overline{\mathcal{J}}(\vec{p},0)\Big]\right\rangle}{\left\langle \text{tr}\Big[\mathcal{T}\, \mathcal{J}(\vec{p},t)\, \overline{\mathcal{J}}(\vec{p},0)\Big]\right\rangle}\right|_{0\ll\tau\ll t}\,. \tag{4.16}$$

This formula has to be adjusted in case of different initial and final state momenta to obtain the desired overlap cancellation. A more sophisticated extraction of ground state matrix elements taking into account one excited state is presented in Section 4.6.2. To obtain the continuum matrix element from the lattice matrix element (4.16), the latter has to be multiplied by a factor of $2EV$, where $V = (La)^3$ is the spatial lattice volume:

$$\langle \vec{p},\lambda|\, O\, |\vec{p},\lambda\rangle\,\Big|_{\text{cont}} = 2EV\, \langle \vec{p},\lambda|\, O\, |\vec{p},\lambda\rangle\,\Big|_{\text{latt}}\,. \tag{4.17}$$

The factor $2EV$ originates in the normalization of the external states, where each external state introduces a factor $\sqrt{2EV}$. As we have two states of identical energy, this simplifies to $2EV$. Using $\mathcal{P} = \mathcal{P}^2$ and the cyclic property of the trace, the projectors can be absorbed into the definition of the interpolating fields, which we define for the

proton as

$$\begin{aligned}\mathcal{J} &= \mathcal{P}\epsilon_{abc}u_a\left(u_b\Gamma' d_c^T\right)\,,\\ \overline{\mathcal{J}} &= \epsilon_{abc}\bar{u}_a\gamma_4\mathcal{P}^\dagger\gamma_4\left(\bar{u}_b\gamma_4\Gamma'^*\gamma_4\bar{d}_c^T\right)\,.\end{aligned} \tag{4.18}$$

These proton interpolators consist of a diquark, containing the diquark kernel $\Gamma'$, and a free quark, which carries the free Lorentz index of the proton and is thus projected onto the desired polarization by the projector $\mathcal{P}$. At zero momentum, parity is a good quantum number, which we project onto using

$$\mathcal{P} = \mathcal{P}_+ := \frac{\gamma_t + \mathbb{1}}{2}\,, \quad \Gamma' = C\gamma_5\,, \tag{4.19}$$

where $C$ is the charge conjugation matrix. This diquark kernel $C\gamma_5$ yields spin 0, combining with the free quark to spin 1/2, as required for the proton. Recently, kinematically enhanced interpolators [68] for the interpolation of hadrons with high momenta have been proposed, which employ other Dirac structures. These not only offer improved overlap with the boosted ground state, but also computational advantages. We shall discuss them in Section 4.4 after introducing lattice calculation techniques.

### 4.1.3 Operators

In the following, we discuss the operators we use in this work to obtain hadronic matrix elements (4.16) on the lattice. These are local quark bilinear operators, which are defined at a single lattice site, and non-local operators involving purely spatial Wilson lines. The latter are required to maintain gauge invariance of the final matrix element for extended quark field separations.

**Local operators** on the lattice are defined as

$$O^i_{q_1q_2}(\vec{x}_{\text{ins}}) = \bar{q}_1(\vec{x}_{\text{ins}},\tau)\Gamma^i q_2(\vec{x}_{\text{ins}},\tau)\,, \tag{4.20}$$

where $\Gamma^i$ is a product of Dirac matrices. If $q_1 = q_2$, we only denote the flavor $q_1$. The following Dirac structures are of particular interest for our investigation of DPDs:

$$\begin{aligned} V^\mu_{qq'}(y) &= \bar{q}(y)\,\gamma^\mu\,q'(y) && \text{(vector)},\\ A^\mu_{qq'}(y) &= \bar{q}(y)\,\gamma^\mu\gamma_5\,q'(y) && \text{(axial vector)},\\ T^{\mu\nu}_{qq'}(y) &= \bar{q}(y)\,\sigma^{\mu\nu}\,q'(y) && \text{(tensor)}. \end{aligned} \tag{4.21}$$

In Minkowski space-time, these operators obey the symmetries

$$\begin{aligned} O^{i,\mathcal{C}}_{qq'}(y) &= \eta^i_{\mathcal{C}}O^i_{q'q}(y)\,,\\ O^{i,\mathcal{PT}}_{qq'}(y) &= \eta^i_{\mathcal{PT}}O^i_{q'q}(-y)\,, \end{aligned} \tag{4.22}$$

where

$$\eta_C^j \in \begin{cases} 1 & j = A \\ -1 & j = V, T \end{cases}, \tag{4.23}$$

and

$$\eta_{PT}^j \in \begin{cases} 1 & j = V \\ -1 & j = A, T \end{cases}. \tag{4.24}$$

For the hermitian conjugate, it holds that

$$\left(O^i_{qq'}(y)\right)^\dagger = O^j_{q'q}(y)\,. \tag{4.25}$$

This implies that all flavor-conserving operators are hermitian. Note the different definitions of Minkowski and Euclidean $\gamma$-matrices in (3.12). We will discuss the implications in Chapter 5.

**Non-local operators** include quark fields at different lattice sites, which have to be connected with a Wilson line to maintain gauge invariance. Along a lattice axis, which we choose to be the $z$-axis, they are commonly defined as

$$O^i_q(y,z) = O^i_q(\vec{y},z;\tau) = \bar{q}(\vec{y}+z\hat{z};\tau)\Gamma^i\mathcal{W}[\vec{y}+z\hat{z},\vec{y};\tau]q(\vec{y};\tau)\,, \tag{4.26}$$

where the discretized version of the Wilson line is

$$\mathcal{W}[\vec{y}+z\hat{z},\vec{y};\tau] = \prod_{k=0}^{z-1} U_z(\vec{y}+(z-k-1)\hat{z};\tau)\,, \tag{4.27}$$

where $\hat{z}$ is the unit vector in $z$-direction of length $a$.

### 4.1.4 Wick contractions

We can now combine the hadronic interpolators (4.18) into two-point functions and with the operators defined in Section 4.1.3 into three- and four-point functions. These are now expectation values of quark fields, contracted with the Dirac structure and gauge links contained in the interpolators and operators. The fermionic expectation value can be evaluated using Wick's theorem for the interacting case (3.59), where the path integral is used to replace a quark and an antiquark operator by one flavor-conserving quark propagator:

$$q^a_\alpha(y)\bar{q}^b_\beta(x) \to M^{ab}_{\alpha\beta}(y|x)\,. \tag{4.28}$$

We will now use the nucleon interpolators (4.18) with the kernels defined in (4.19) to calculate the Wick contraction for two-point function explicitly. We give only a dia-

grammatic overview over the kinds of Wick contractions for the higher $n$-point functions. For brevity, we use Euclidean four-vectors, thus setting the source position to $0 = (\vec{0}, 0)$ and the sink position to $x = (\vec{x}, t)$.

**Two-point functions** contain only the two interpolators:

$$\begin{aligned} C_{\text{2pt}}(\vec{p}, t) &= a^6 \sum_{\vec{x}, x^4 = t} e^{-i\vec{p}\vec{x}} \left\langle \text{tr}\left( \mathcal{J}(x) \overline{\mathcal{J}}(0) \right) \right\rangle \\ &= a^6 \sum_{\vec{x}, x^4 = t} e^{-i\vec{p}\vec{x}} \epsilon_{abc} \epsilon_{a'b'c'} (\mathcal{P}_+)_{\alpha\alpha'} \left(C\gamma_5\right)_{\beta\gamma} \left(C\gamma_5\right)_{\beta'\gamma'} \\ &\times D_{cc'}^{\gamma\gamma'}(x, 0) \left( U_{ab'}^{\alpha\beta'}(x, 0)\, U_{ba'}^{\beta\alpha'}(x, 0) \right. \\ &\left. - U_{aa'}^{\alpha\alpha'}(x, 0)\, U_{bb'}^{\beta\beta'}(x, 0) \right), \end{aligned} \tag{4.29}$$

where $D$ is the down-quark propagator and $U$ is the up-quark one. As there are two up-quarks, there are two possible Wick contractions, which are shown in Figure 4.1. The permutation of indices results in the cross term having negative sign.

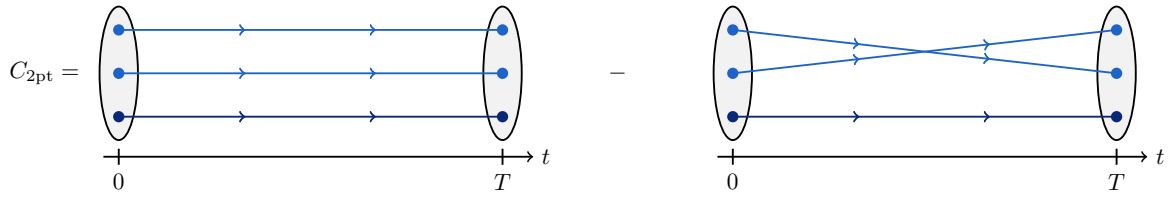



**Figure 4.1:** Overview of two-point function Wick contractions. Up quark propagators are shown in light blue, down quark propagators in dark blue.

**Three-point functions** contain two interpolators and the operator of interest. We use the local operators (4.21), inserted at $y = (y, \vec{\tau})$,

$$C_{\text{3pt},q}^{i}(\vec{p}, t, \tau) = a^6 \sum_{\vec{x}, x^4 = t, \vec{y}, y^4 = \tau} e^{-i\vec{p}\cdot(\vec{x} - \vec{y})} \left\langle \text{tr}\left( \mathcal{J}(x) O_q^i(y) \overline{\mathcal{J}}(0) \right) \right\rangle . \tag{4.30}$$

The two kinds of Wick contractions, $C_{\text{3pt},u}^{i}$ and $C_{\text{3pt},d}^{i}$, are shown in Figure 4.2.

Three-point functions include disconnected contributions, which occur when the operator is contracted with itself, forming a loop. The remaining two interpolators yield the regular two-point function. These disconnected contributions cancel when considering $C_{\text{3pt},u-d}^{i} = C_{\text{3pt},u}^{i} - C_{\text{3pt},d}^{i}$ for degenerate masses $m_u = m_d$. We shall only consider the isovector combination for non-local operators, which can be accessed by using $\Gamma^i = \gamma_t$ and subtracting the $d$ from the $u$ contribution. The expression for non-local operators

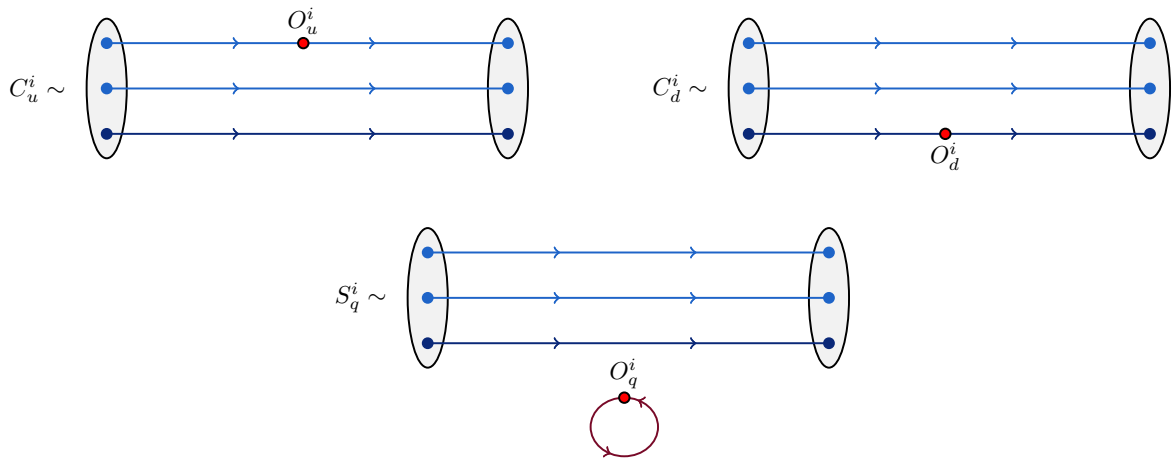



**Figure 4.2:** Overview of three-point function Wick contractions up to quark line permutations. Up quark propagators are shown in light blue, down quark propagators in dark blue, quark lines that can be of any flavor are shown in red. Connected contributions are shown on top, the disconnected one at the bottom.

(4.26) is

$$C^i_{3\mathrm{pt},q}(\vec{p},t,\tau,z) = a^6 \sum_{\vec{x},x^4=t,\vec{y},y^4=\tau} e^{-i\vec{p}\cdot(\vec{x}-\vec{y})} \left\langle \mathrm{tr}\left(\mathcal{J}(x)O^i_q(y,z)\overline{\mathcal{J}}(0)\right)\right\rangle , \tag{4.31}$$

where the two connected contributions relevant for this work are shown in Figure 4.3. The three-point matrix elements can be extracted according to (5.8), where $z = 0$

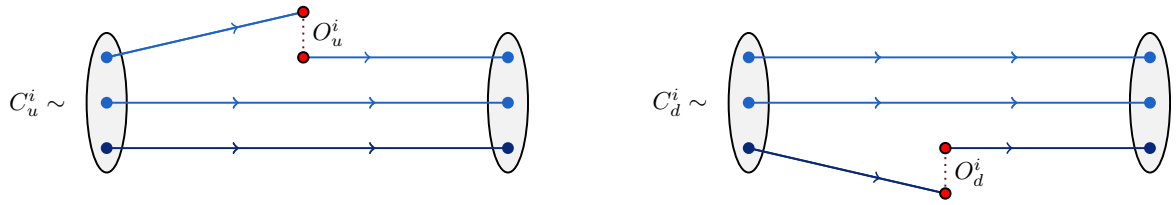



**Figure 4.3:** Overview of three-point function Wick contractions with non-local operators up to quark line permutations. Up quark propagators are shown in light blue, down quark propagators in dark blue. The Wilson line is represented by a red dotted line. Only connected contributions are shown.

recovers the local quark bilinear case:

$$C^i_q(\vec{p},z) = \langle\vec{p}|\, O^i_q(\vec{y},z;\tau)\,|\vec{p}\rangle = 2EV\ \left.\frac{C^i_{3\mathrm{pt},q}(\vec{p},t,\tau,z)}{C_{2\mathrm{pt}}(\vec{p},t)}\right|_{0\ll\tau\ll t} . \tag{4.32}$$

For the isovector case we are interested in, the matrix element of interest is

$$\begin{aligned}&\langle\vec{p}|\, O_u^t(\vec{y},z;\tau) - O_d^t(\vec{y},z;\tau)\,|\vec{p}\rangle = \langle\vec{p}|\, O_u^t(\vec{y},z;\tau)\,|\vec{p}\rangle - \langle\vec{p}|\, O_d^t(\vec{y},z;\tau)\,|\vec{p}\rangle \\ &= C_u^t(\vec{p},z) + S_u^t(\vec{p},z) - C_d^t(\vec{p},z) - S_d^t(\vec{p},z) \overset{m_u=m_d}{=} C_u^t(\vec{p},z) - C_d^t(\vec{p},z) = C_{u-d}^t(\vec{p},z)\,.\end{aligned} \tag{4.33}$$

If the operator is positioned on the $d$-quark line, there are again two possible Wick contractions due to interchange in the $u$-quark lines:

$$\begin{aligned}C_{3\mathrm{pt},d}^i(\vec{p},t,\tau) = a^6 \sum_{\vec{x},x^4=t,\vec{y},y^4=\tau} & e^{-i\vec{p}\cdot(\vec{x}-\vec{y})}\,\epsilon_{abc}\,\epsilon_{a'b'c'}(\mathcal{P}_+)_{\alpha\alpha'}(C\gamma_5)_{\beta\gamma}(C\gamma_5)_{\beta'\gamma'} \\ \times \Big[ & U_{aa'}^{\alpha\alpha'}(x,0)\,U_{bb'}^{\beta\beta'}(x,0)\,D_{cd}^{\gamma\delta'}(x,y)\Gamma_{\delta'\delta}^i D_{dc'}^{\delta\gamma'}(y,0) \\ & - U_{ab'}^{\alpha\beta'}(x,0)\,U_{ba'}^{\beta\alpha'}(x,0)\,D_{cd}^{\gamma\delta'}(x,y)\Gamma_{\delta'\delta}^i D_{dc'}^{\delta\gamma'}(y,0)\Big] \\ & + \text{disconnected terms.}\end{aligned} \tag{4.34}$$

For an operator on the $u$-quark line, there are four Wick contractions, as the operator can be positioned on either quark line:

$$\begin{aligned}C_{3\mathrm{pt},u}^i(\vec{p},t,\tau) = a^6 \sum_{\vec{x},x^4=t,\vec{y},y^4=\tau} & e^{-i\vec{p}\cdot(\vec{x}-\vec{y})}\,\epsilon_{abc}\,\epsilon_{a'b'c'}(\mathcal{P}_+)_{\alpha\alpha'}(C\gamma_5)_{\beta\gamma}(C\gamma_5)_{\beta'\gamma'} \\ & \times D_{cc'}^{\gamma\gamma'}(x,0) \\ & \times \Big[ U_{ad}^{\alpha\delta'}(x,y)\Gamma_{\delta'\delta}^i\,U_{da'}^{\delta\alpha'}(y,0)\,U_{bb'}^{\beta\beta'}(x,0) \\ & - U_{ad}^{\alpha\delta'}(x,y)\Gamma_{\delta'\delta}^i\,U_{db'}^{\delta\beta'}(y,0)\,U_{ba'}^{\beta\alpha'}(x,0) \\ & + U_{bd}^{\beta\delta'}(x,y)\Gamma_{\delta'\delta}^i\,U_{db'}^{\delta\beta'}(y,0)\,U_{aa'}^{\alpha\alpha'}(x,0) \\ & - U_{bd}^{\beta\delta'}(x,y)\Gamma_{\delta'\delta}^i\,U_{da'}^{\delta\alpha'}(y,0)\,U_{ab'}^{\alpha\beta'}(x,0)\Big] \\ & + \text{disconnected terms.}\end{aligned} \tag{4.35}$$

**Four-point functions** include two interpolators and two operators at potentially different spatial insertion positions. Here, we position the source at $x_{\mathrm{src}} = (\vec{x}_{\mathrm{src}}, 0)$, the sink at $x_{\mathrm{snk}} = (\vec{x}, t)$ and the operators of interest at $(\vec{0},\tau)$ and $(\vec{y},\tau)$. We shall restrict ourselves to local operators here which we defined in (4.21). As two operators could each change the quark flavor, still resulting in a proton, this case has to be included as well. We only consider four-point functions where the operators are inserted at identical time to obtain equal time matrix elements, necessary for extraction of the lowest Mellin

moment of DPDs:

$$C^{ij}_{4\mathrm{pt},q_1q_2q_3q_4}(\vec{p},\vec{y},t,\tau) = \\ = a^6 \sum_{\vec{x}_{\mathrm{src}},\vec{x}_{\mathrm{snk}}} e^{-i\vec{p}\cdot(\vec{x}_{\mathrm{snk}}-\vec{x}_{\mathrm{src}})} \left\langle \mathrm{tr}\left(\mathcal{J}(\vec{x}_{\mathrm{snk}},t)O^i_{q_1q_2}(\vec{y},\tau)O^j_{q_3q_4}(\vec{0},\tau)\overline{\mathcal{J}}(\vec{x}_{\mathrm{src}},0)\right)\right\rangle , \tag{4.36}$$

We do not give all Wick contractions explicitly, instead, we give a diagrammatic overview of the different kinds of contractions in Figure 4.4, making quark flavor explicit. The computation of the contractions follows the same recipe in all cases. First, one considers all 6 possible connections of source and sink quark operators by quark lines, including the signs of the respective permutations. Next, one places the operators relevant for the flavor combination under consideration on the suitable quark lines, taking all possible different combinations into account (e.g. which $u$-quark line to choose for $C^{ij}_{1,uudd}$). For disconnected diagrams, the various possible combinations for the quark loop flavors also have to be considered. Finally, one adds up the contractions using the correct signs obtained above. This procedure together with the explicit Wick contractions of all four-point functions considered in this work has been documented in Ref. [134] and the appendix of Ref. [31]. The two-current matrix elements for local quark bilinears, only taking into account light quarks, are then

$$\begin{aligned}
\langle\vec{p}|\, O^{uu}_i(\vec{0})\; O^{dd}_j(\vec{y})\,|\vec{p}\rangle &= C^{ij,\vec{p}}_{1,uudd}(\vec{y}) + S^{ij,\vec{p}}_{1,u}(\vec{y}) + S^{ji,\vec{p}}_{1,d}(-\vec{y}) + D^{ij,\vec{p}}(\vec{y}) \,, \\
\langle\vec{p}|\, O^{uu}_i(\vec{0})\; O^{uu}_j(\vec{y})\,|\vec{p}\rangle &= C^{ij,\vec{p}}_{1,uuuu}(\vec{y}) + C^{ij,\vec{p}}_{2,u}(\vec{y}) + C^{ji,\vec{p}}_{2,u}(-\vec{y}) \\
&\quad + S^{ij,\vec{p}}_{1,u}(\vec{y}) + S^{ji,\vec{p}}_{1,u}(-\vec{y}) + S^{ij,\vec{p}}_{2}(\vec{y}) + D^{ij,\vec{p}}(\vec{y}) \,, \\
\langle\vec{p}|\, O^{dd}_i(\vec{0})\; O^{dd}_j(\vec{y})\,|\vec{p}\rangle &= C^{ij,\vec{p}}_{2,d}(\vec{y}) + C^{ji,\vec{p}}_{2,d}(-\vec{y}) + S^{ij,\vec{p}}_{1,d}(\vec{y}) + S^{ji,\vec{p}}_{1,d}(-\vec{y}) \\
&\quad + S^{ij,\vec{p}}_{2}(\vec{y}) + D^{ij,\vec{p}}(\vec{y}) \,, \\
\langle\vec{p}|\, O^{ud}_i(\vec{0})\; O^{du}_j(\vec{y})\,|\vec{p}\rangle &= C^{ij,\vec{p}}_{1,uddu}(\vec{y}) + C^{ij,\vec{p}}_{2,u}(\vec{y}) + C^{ji,\vec{p}}_{2,d}(-\vec{y}) + S^{ij,\vec{p}}_{2}(\vec{y}) \,,
\end{aligned} \tag{4.37}$$

where the matrix elements of the individual contractions are extracted as in (5.8):

$$C^{ij,\vec{p}}_{q_1q_2q_3q_4}(\vec{y}) = \langle\vec{p}|\, O^i_{q_1q_2}(\vec{y},\tau)O^j_{q_3q_4}(\vec{0},\tau)\,|\vec{p}\rangle = 2EV\; \left.\frac{C^{ij}_{4\mathrm{pt},q_1q_2q_3q_4}(\vec{p},\vec{y},t,\tau)}{C_{2\mathrm{pt}}(\vec{p},t)}\right|_{0\ll\tau\ll t} . \tag{4.38}$$

Similar to the two-current matrix elements discussed in Section 5.1.1 and DPDs discussed in Section 2.4.3, the individual contractions possess symmetries under $\mathcal{PT}$, $\mathcal{C}$ and $\mathcal{P}$ transformations:

$$\begin{aligned}
G^{ij,\vec{p}}(y) &= \eta^{ij}_{PT} G^{ij,\vec{p}}(-y) && \text{for } G = C_{1,uudd}, C_{1,uuuu}, S_{1,u}, S_{1,d}, S_2, D \,, \\
G^{ij,\vec{p}}(y) &= \eta^{ij}_{PT} G^{ji,\vec{p}}(y) && \text{for } G = C_{2,u}, C_{2,d} \,,
\end{aligned} \tag{4.39}$$

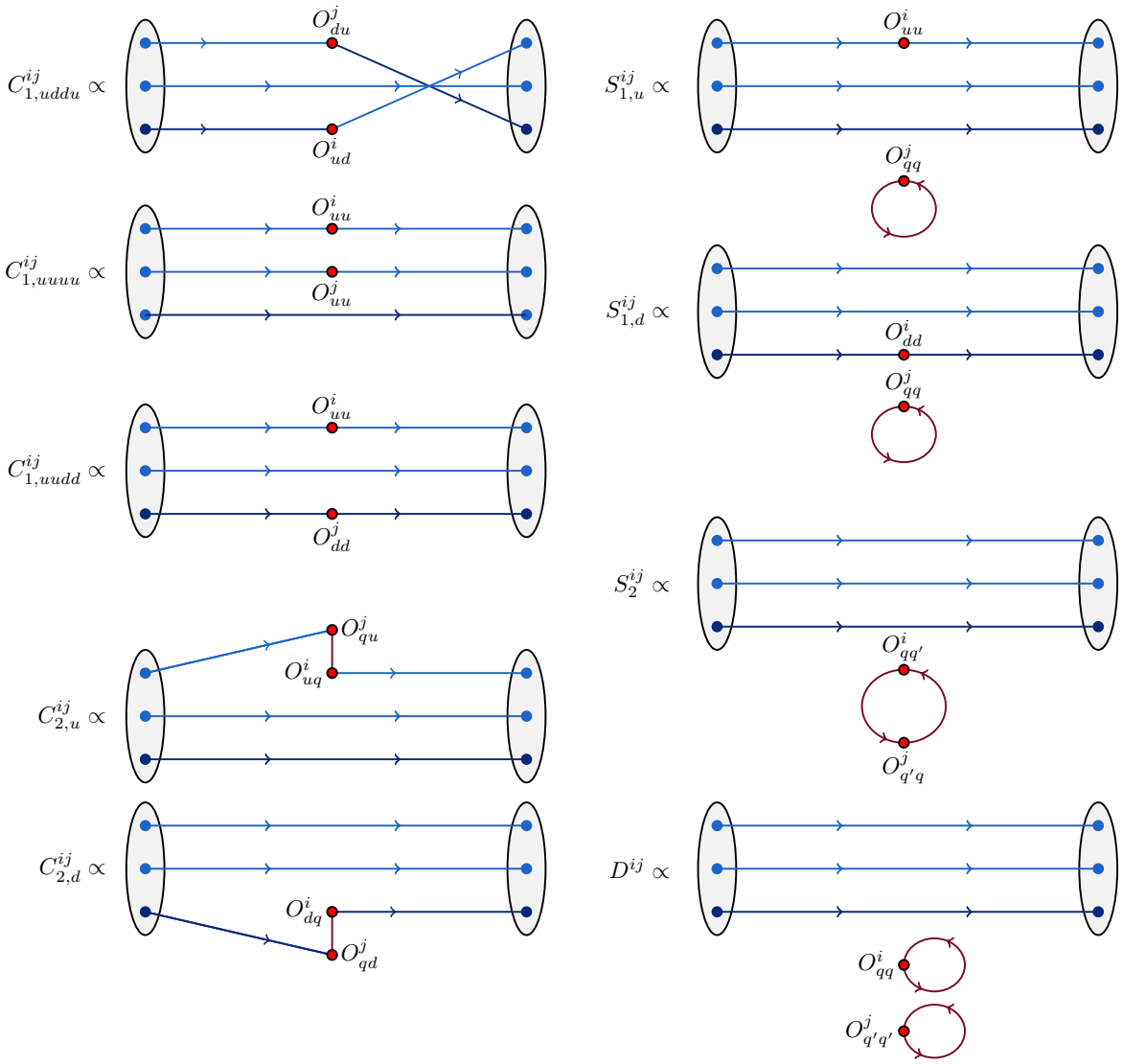



**Figure 4.4:** Overview of four-point function Wick contractions up to quark line permutations. Connected contractions are shown on the left, while contractions involving disconnected contributions (loops) are shown on the right. Up quark lines are shown in light blue, down quark ones in dark blue. Red lines can have any quark flavor.

where $\eta^{ij}_{PT}$ is the same as in (2.64). Taking into account the symmetries of the operators discussed in Section 4.1.3 and the Wick contractions, it can furthermore be shown [31] that

$$\left[G^{ij,\vec{p}}(y)\right]^* = \eta_4^{ij}\eta_{PT}^{ij}G^{ij,\vec{p}}(-y) \ , \tag{4.40}$$

where

$$\eta_4^i = \begin{cases} 1 & i = V, T \\ -1 & i = A \end{cases}, \qquad \eta_4^{ij} = \eta_4^i \eta_4^j \,. \tag{4.41}$$

For the channels investigated in this work, $\eta_4^{ij} = 1$, as all collinear DPDs containing exactly one axial current are identical to zero, as shown in (2.67) and (2.68).
The symmetries (4.40) and (4.39) imply that all kinds of contractions except $C_{1,duud}$ and $C_{2,q}$ are real valued. For the latter, we find

$$\begin{aligned} 2\Re\left\{C_{2,q}^{ij,\vec{p}}(y)\right\} &= C_{2,q}^{ij,\vec{p}}(y) + C_{2,q}^{ji,\vec{p}}(-y) \\ 2i\Im\left\{C_{2,q}^{ij,\vec{p}}(y)\right\} &= C_{2,q}^{ij,\vec{p}}(y) - C_{2,q}^{ji,\vec{p}}(-y)\,. \end{aligned} \tag{4.42}$$

Comparing with (4.37), we find that all flavor-conserving two-current matrix elements have to be real valued, while the flavor interference contribution may have non-zero imaginary part.

## 4.2 Propagators

To evaluate the Wick contractions, we have to calculate the quark propagators. Propagators are obtained by solving the Dirac equation, i.e. inverting the Dirac operator (3.43). This inversion is the computationally most expensive step of the lattice calculation and so resource intensive that obtaining the full all-to-all propagator is not feasible. In the following, we present the techniques employed for propagator computation in this work. We only briefly review the techniques employed, for a detailed calculation of all quantities relevant in the context of four-point functions, we again refer the reader to [31] and [134].

### 4.2.1 Point sources

Instead of inverting the Dirac equation on the entire lattice, it is inverted only on one lattice site, this point source is zero everywhere else:

$$S_{x_{\mathrm{src}}}^{ab,\alpha\beta}(y) = \delta^{\alpha\beta}\delta^{ab}\delta_{y,x_{\mathrm{src}}}\,. \tag{4.43}$$

The resulting propagator is called the point-to-all propagator, fulfilling

$$D(y|z)M(z|x_{\mathrm{src}}) = S_{x_{\mathrm{src}}}(y)\,. \tag{4.44}$$

To obtain the point-to-all propagator, 12 inversions have to be performed, one for each spin-color index, here $\beta, b$. In contractions, e.g. (4.29) for the two-point function, momentum conservation or translational invariance, respectively, allow us to skip the momentum projecting sum over the source position. Thus, we can evaluate two-point

functions using only point-to-all propagators.

### 4.2.2 Stochastic sources

It is possible to approximate the all-to-all propagator by sufficiently many stochastic propagators, obtained from stochastic sources [135]. These stochastic sources $\eta_t$ are defined on one time slice $t$ only as

$$\left(\eta_t^{(\ell)}\right)_{\alpha a}(y) = \frac{1}{\sqrt{2}}(\pm 1 \pm i)\ \delta_{y^4,t} \tag{4.45}$$

and decompose the unit matrix:

$$\frac{1}{N_{\mathrm{st}}} \sum_{\ell}^{N_{\mathrm{st}}} \eta_t^{(\ell)} \otimes \eta_t^{\dagger(\ell)} \xrightarrow{N_{\mathrm{st}}\to\infty} \mathbb{1}_t\ . \tag{4.46}$$

The stochastic propagator $\psi_t^{(\ell)}$ fulfills

$$D\,\psi_t^{(\ell)} = \eta_t^{(\ell)}\ , \tag{4.47}$$

thereby approximating the full propagator from any spatial lattice site on the time slice $t$ to any other site on the lattice in the limit $l \to \infty$. This allows the calculation of contractions including disconnected loops like $S$, $S_1$, $S_2$ and $D$. Using these propagators introduces considerable noise in the contractions which is reduced $\propto 1/\sqrt{N_{\mathrm{st}}}$, thus we will only use it when there is no better alternative like the sequential source technique, which we shall discuss next.

### 4.2.3 Sequential source technique

Contractions involving operators, e.g. $C_d^i$, (4.34), contain not only source and sink, but also the operator insertion, which is averaged over. To obtain a propagator connecting the operator of interest inserted at $y = (\vec{y}, \tau)$ with the sink at $x = (\vec{x}, t)$, without employing stochastic sources, we can use the sequential source technique [136], which was originally developed for three-point functions in pions, e.g.

$$\langle \pi^-(x)|\, O_d^i\, |\pi^-(0)\rangle \sim \langle \bar{d}(x)\gamma_5 u(x)\, \bar{d}(y)\Gamma^i d(y)\, \bar{u}(0)\gamma_5 d(0)\rangle\,, \tag{4.48}$$

where we used the pion interpolator $\mathcal{J}_{\pi^-}(x) = \bar{u}(x)\gamma_5 d(x)$ and the local operator from (4.20). The key idea is that in a product of propagators, one propagator can be used as a source to compute the other. We demonstrate this on the example of the connected

three-point function necessary to obtain the matrix element (4.48)

$$C^{\pi,i}_{\text{3pt},d}(\vec{p},\tau,t) = a^6 \,\text{tr}\left(\sum_{\vec{y};y^4=\tau} e^{i\vec{p}\cdot\vec{y}} M(0|y)\Gamma^i \underbrace{\sum_{\vec{x};x^4=t} e^{-i\vec{p}\cdot\vec{x}} M(y|x)\gamma_5 M(x|0)\gamma_5}_{X(y|0)}\right)$$
$$= a^6 \,\text{tr}\left(\sum_{\vec{y};y^4=\tau} e^{i\vec{p}\cdot\vec{y}} M(0|y)\Gamma^i X(y|0)\right) , \tag{4.49}$$

where we kept the source position fixed and denoted all light quarks propagators as $M$ due to their degenerate masses. Here, $X(y|0)$ is the sequential propagator. Applying the Dirac operator to it yields

$$\sum_y D(z,y)X(y|0) = e^{-i\vec{p}\cdot\vec{z}}\gamma_5 M(z|0)\gamma_5\Big|_{z^4=0} . \tag{4.50}$$

The r.h.s. is called the sequential source, as we can use it as a source for another inversion of the Dirac operator. This allows us to calculate three-point functions cost efficiently, as we only have to invert the Dirac operator on a point source twice. A visual representation of the above equations is given in Figure 4.5.

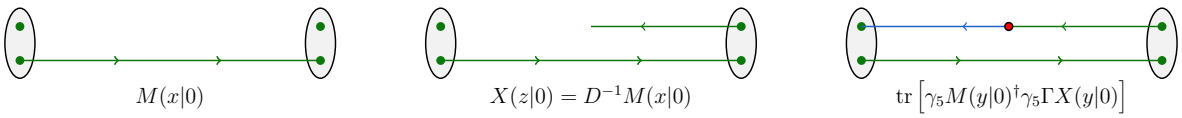



**Figure 4.5:** The pion three-point function obtained via the sequential source technique. Quark propagators contributing to the sequential propagator are shown in green, other point-to-all propagators are shown in blue and the inserted operator of interest is shown as a red dot. From left to right we show the sequential source, the sequential propagator and the full contraction. The corresponding mathematical expressions are given below the respective illustrations.

## 4.3 Improvement techniques

To access more subtle effects or simply improve precision, it is highly desirable to improve the SNR of observables obtained from lattice calculations. The main sources of noise in the propagators introduced in the previous section are poor overlap with the spatial wave function of the proton ground state and considerable statistical fluctuations from the stochastic sources. In this section, we will introduce improvements to both of these.

### 4.3.1 Smearing

To improve the signal quality of practical quark propagators, we use momentum smearing [137] which is based on Wuppertal smearing [138]. Wuppertal smearing extends the point source by summing over neighboring lattice sites in a gauge covariant way, so that the source receives a gaussian profile. As the gauge links are subject to UV-fluctuations, they are smoothed beforehand using APE-smoothing [139]. This is done iteratively, where the next iteration of gauge fields is obtained as a sum of the current gauge field and the shortest staple connecting its origin to end point. As this sum of SU(3) matrices is not necessarily again a SU(3) matrix, it has to be projected back into the group:

$$U_\mu^{(n+1)}(x) = P_{SU(3)}\left[\alpha_{\mathrm{APE}}\, U_\mu^{(n)}(x) + S_\mu^{(n)}(x)\right], \tag{4.51}$$

$$S_\mu^{(n)}(x) = \sum_{\nu\neq\mu} U_\nu(x)\, U_\mu(x+a\hat{\nu})\, U_\nu^\dagger(x+a\hat{\nu}+a\hat{\mu}), \tag{4.52}$$

where $\alpha_{\mathrm{APE}}$ is a weight factor and

$$P_{SU(3)}(V) = \arg\max_{X\in SU(3)} \Re\,\mathrm{tr}\left(XV^\dagger\right) \tag{4.53}$$

is a projection back to $SU(3)$. These smoothed gauge fields $U_\mu^{\mathrm{sm}}$ can now be used to calculate the quark momentum smearing function $(\Phi_0^{\vec{p}})_{x,y}$:

$$(\Phi_0^{\vec{p}})_{x,y} = \frac{1}{1+6\epsilon}\left[\delta_{x,y} + \epsilon\sum_{\mu=1}^{3}\left(\delta_{x+\hat{\mu},y}U_\mu^{\mathrm{sm}}(x)e^{ib\vec{p}\hat{\mu}} + \delta_{y+\hat{\mu},x}U_\mu^{\mathrm{sm},\dagger}(y)e^{-ib\vec{p}\hat{\mu}}\right)\right], \tag{4.54}$$

where the smearing parameter $\epsilon$ is another weight factor. Applying the smearing function $\Phi_0$ $n-$times gradually extends the source over the neighboring lattice sites. The inclusion of a momentum phase $b\vec{p} \neq 0$, which was introduced as quark momentum smearing [137], improves the signal for non-zero momenta immensely. This can be understood by considering the extended source in momentum space. A Fourier transformed Gaussian is still a Gaussian, which gets shifted to a target momentum $b\vec{p}$ in momentum space by the momentum phase, thus increasing overlap with the boosted ground state of the nucleon, leading to an improved signal-to-noise ratio (SNR).

Sources and propagators can be smeared by left multiplication, i.e.

$$\begin{aligned} S^\Phi &= \Phi^n S \quad \text{source smearing}, \\ M^\Phi &= \Phi^n M \quad \text{sink smearing}. \end{aligned} \tag{4.55}$$

This technique can be used to greatly enhance the signal of propagators connected to the source or the sink, i.e. where they are projected onto definite momentum. This is due to the increased overlap $\alpha_0$ of the interpolator with the ground state (4.9). Propagators that have no connection to neither the source nor the sink cannot benefit from it, as

their sources do not mimic the spatial wave function of the nucleon ground state. This applies to the stochastic propagators used to simulate the all-to-all propagator between operator insertions. The momentum phase could bias them when they are used to simulate propagators in disconnected graphs, where the momentum is not known.

### 4.3.2 Hopping parameter expansion

To enhance the signal of stochastic propagators, we use the hopping parameter expansion (HPE). The idea is to rewrite the Dirac operator $D = (1 - H)/(2a\kappa)$ so that its inverse forms a geometric series:

$$D^{-1} = \frac{2a\kappa}{1-H} = 2a\kappa \sum_{n=0}^{\infty} H^n \,. \tag{4.56}$$

Rewriting $D_{\mathrm{SW}}$ from (3.43), we find for the hopping term $H$:

$$H[U_\mu] = \kappa H_{\mathrm{W}}[U_\mu](x|y) - 2a^2\kappa c_{\mathrm{SW}} C[U_\mu](x|y) \;. \tag{4.57}$$

There is a minimal number $N(y)$ of hops that are needed to connect to points separated by $\vec{y}$. Hence, terms with less hops in the HPE do not contribute for given $\vec{y}$. In the case of stochastic propagators this is only true in the stochastic limit. We can remove these terms, which for finite $N_{\mathrm{st}}$ contain only noise, by rewriting the series

$$\begin{aligned} D^{-1} = 2a\kappa \sum_{n=0}^{\infty} H^n &= 2a\kappa \sum_{n=0}^{N-1} H^n + 2a\kappa \sum_{n=N}^{\infty} H^n \\ &= 0 + 2a\kappa \sum_{n=N}^{\infty} H^n = H^N 2a\kappa \sum_{n=0}^{\infty} H^n = H^N D^{-1} \;. \end{aligned} \tag{4.58}$$

We can thus remove all $N$ noisy neighbors by replacing $D^{-1}$ by $H^N D^{-1}$. As (4.57) connects a site only with a neighboring one, the maximum number of zero entries equals the one-norm of the separation $|\vec{y}|_1 = \sum_{i=1}^{3} \frac{y_i}{a}$. Taking into account the periodicity of the lattice, the exact definition of $N(y)$ is:

$$N(y) = \sum_{i=1}^{3} \min\left( \frac{|y_i|}{a}, L - \frac{|y_i|}{a} \right) \,. \tag{4.59}$$

Altogther, the stochastic propagator can be improved by left multiplication:

$$\xi_\tau^{(\ell),N}(y) = H^N \psi_\tau^{(l)}(y) \,. \tag{4.60}$$

## 4.4 Kinematically enhanced interpolators

As explained in Section 4.3.1, it is possible to increase the SNR of lattice calculations by improving the overlap $\alpha_0$ of the sources with the ground state (4.9) through manipulation of the spatial profile of the source. Likewise, one can increase the overlap of the sources with the ground state by altering the Dirac structure of the interpolators, as mentioned in Section 4.1.2. We shall address this in this section, following [68]. This section was already published in Ref. [70], the lead author of which is also the author of this thesis.

### 4.4.1 Kinematic enhancement

To have non-vanishing overlap with the ground state we want to approximate, the interpolating operator $\mathcal{J}$ must transform in the same irreducible representation. In a boosted system, the spatial lattice symmetry group is reduced from the cubic group $O_h^D$ ($O_h$) to the little group $\mathrm{Dic}_4$ ($C_{4v}$) corresponding to the 4-fold rotation around the longitudinal direction[1]. Thus the hadron has non-vanishing overlap with a larger set of Fock states. Among them, the leading component at large momentum, or near the light-cone, is described by the leading-twist wave function of the hadron. This is related to the fact that the "+" component $\psi_+ = \frac{1}{\sqrt{2}}\gamma_-\gamma_+\psi$ is the only dynamic degree of freedom on the lightcone. Here $\gamma_\pm = \frac{1}{\sqrt{2}}(\gamma_t^M \mp \gamma_z^M)$ (assuming the hadron is moving in the $\hat{z}$ direction) in Minkowski spacetime, which is related to the Euclidean definition through $\gamma_4 = \gamma_t^M$ and $\gamma_{\{1,2,3\}} = \mathbf{i}\gamma^M_{\{x,y,z\}}$. On a Euclidean lattice, although the lightcone does not exist, the "+" components still dominate at large but finite momentum in the form of a kinematical enhancement. For a leading-twist interpolator $J_+$ constructed with $n$ "+"-component quarks, the overlap with the hadron $h(p)$ moving at momentum $p$ is kinematically enhanced as,

$$\langle 0|\mathcal{J}_+|h(p)\rangle \propto p_+^{n/2}, \tag{4.61}$$

where $p_+ = (E + p_z)/\sqrt{2}$. As a result, the amplitude of the corresponding two-point correlation function is enhanced as

$$|Z_n|^2 = |\langle 0|\mathcal{J}_+|h(p)\rangle|^2 \propto p_+^n\,. \tag{4.62}$$

The fluctuation of the measurement is determined by the variance operator [140, 141],

$$\begin{aligned}\mathrm{Var}(C_{2\mathrm{pt}}) &= \frac{1}{2}\langle|C_{2\mathrm{pt}}|^2\rangle + \frac{1}{2}\langle C_{2\mathrm{pt}}^2\rangle - \langle C_{2\mathrm{pt}}\rangle^2, \\ &= \frac{1}{2}\langle\mathcal{J}^\dagger(t)\mathcal{J}(t)\mathcal{J}^\dagger(0)\mathcal{J}(0)\rangle + \frac{1}{2}\langle\mathcal{J}^\dagger(t)\mathcal{J}^\dagger(t)\mathcal{J}(0)\mathcal{J}(0)\rangle - \langle\mathcal{J}^\dagger(t)\mathcal{J}(0)\rangle^2,\end{aligned} \tag{4.63}$$

[1]Note that the little group will be different if the hadron's momentum is not pointing in direction of an axes, but this does not affect the following discussion.

where the first term is the two-point correlation for a static or scattering state with zero total quantum number and momentum, and the second term is for a two-particle state with momentum $2p$. At large Euclidean times, the variance is dominated by the lowest-energy state, corresponding to $n$ static pions. Thus the fluctuation of the correlator does not get a kinematic enhancement, resulting in an improved SNR,

$$\frac{C_{2\mathrm{pt}}(t\to\infty)[\mathcal{J}_+]}{\sqrt{\mathrm{Var}[C_{2\mathrm{pt}}(t\to\infty)]}} \propto p_+^n e^{E_0 - n m_\pi/2}. \tag{4.64}$$

In comparison with the static system, except for the exponential decay, the SNR from the overlap factor $|Z_n|^2$ is enhanced by the factor $\frac{p_+^n}{M^n}$. Since $p_+ \propto E + p_z$, both the $\mathcal{J}_4$ and $\mathcal{J}_{\hat{p}}$ components get enhanced by the factor $\frac{E^n}{M^n}$ and $\frac{p_z^n}{M^n}$, respectively. The $\mathcal{J}_4$ component has non-vanishing overlap with the hadron ground-state at rest, and thus has already been well studied for static hadrons in the literature.

### 4.4.2 Interpolator kernels

We begin by restating the definition (4.18) for proton interpolators:

$$\begin{aligned}\mathcal{J} &= \mathcal{P}\epsilon_{abc} u_a \left(u_b \Gamma' d_c^T\right) ,\\ \overline{\mathcal{J}} &= \epsilon_{abc}\bar{u}_a \gamma_4 \mathcal{P}^\dagger \gamma_4 \left(\bar{u}_b \gamma_4 \Gamma'^* \gamma_4 \bar{d}_c^T\right) ,\end{aligned} \tag{4.65}$$

where $\mathcal{P}$ project onto the desired degrees of freedom. We use $\mathcal{P}_+$ for projection onto positive parity. $\Gamma'$ is the diquark kernel. Both the two-point and the three-point function include a contraction of the respective free-quarks in the source and sink interpolators. We summarize the contraction of the projectors as $\mathcal{T}$, the free-quark kernel. The two-point function $C_{2pt}$ reads

$$\begin{aligned} C_{2pt}(\mathbf{p},t) &= \langle 0|\mathcal{J}(\mathbf{p},t)\,\overline{\mathcal{J}}(\mathbf{p},0)|0\rangle \\ &= a^3 \sum_{\mathbf{x}} e^{-i\mathbf{p}\cdot\mathbf{x}}\, \epsilon_{abc}\,\epsilon_{a'b'c'} \\ &\quad \times \left\langle 0\right| \mathrm{tr}\left[\bar{u}_{a'}(0)\, \underbrace{\gamma_4\mathcal{P}^\dagger\gamma_4\mathcal{P}}_{\mathcal{T}}\, u_a(x) (u_b(x)\,\Gamma'\,d_c^T(x)) (\bar{u}_{b'}(0)\,\gamma_4\Gamma'^*\gamma_4\,\bar{d}_{c'}^T(0))\right] \left|0\right\rangle \\ &= a^3 \sum_{\mathbf{x}} e^{-i\mathbf{p}\cdot\mathbf{x}}\, \epsilon_{abc}\,\epsilon_{a'b'c'} \left\langle 0\right| \mathrm{tr}\left[\underbrace{\bar{u}_{a'}(0)\,\mathcal{T} u_a(x)}_{\text{free quarks}} (u_b(x)\,\Gamma'\,d_c^T(x)) (\bar{u}_{b'}(0)\,\gamma_4\Gamma'^*\gamma_4\,\bar{d}_{c'}^T(0))\right] \left|0\right\rangle . \end{aligned} \tag{4.66}$$

Kinematic enhancement can be applied to both the diquark and the free quark. Previously, the parity projection $\mathcal{P}_+$ was commonly used, as it has maximum overlap with the proton ground state at zero momentum. However, as pointed out in Ref. [68], parity is no longer a good quantum number at non-zero momenta, particularly at large ones.

More specifically, before projection, the nucleon two-point correlation function constructed with the interpolator $\hat{J}$ can be expressed as [142, 143],

$$\langle 0|\hat{J}^\dagger(t)\hat{J}|0\rangle = \sum_i |\lambda_{i,+}|^2 \frac{\gamma\cdot p + M_i^+}{2E_i^+} e^{-E_i^+ t} + \sum_i |\lambda_{i,-}|^2 \frac{\gamma\cdot p - M_i^-}{2E_i^-} e^{-E_i^- t}, \tag{4.67}$$

where $\lambda_{i,\pm}$ are the overlap of the interpolator with the $i$-th positive (negative) parity states, and $E_i^\pm$ and $M_i^\pm$ are the corresponding energies and masses. At rest, the projectors $\mathcal{P}_\pm$ can eliminate the entire sector of negative (positive) parity states. But when boosted, this is not possible. On the other hand, for a general spin matrix $\mathcal{T}$,

$$\mathcal{T} = b + c_i\gamma_i + d_{ij}\sigma_{ij} + e\gamma_5 + f_i\gamma_5\gamma_i, \tag{4.68}$$

the projection of the two-point correlator is

$$\begin{aligned}\mathrm{tr}[\mathcal{T}\langle 0|\hat{J}^\dagger(t)\hat{J}|0\rangle] = &\sum_i |\lambda_{i,+}|^2 \frac{c_3 p_z + c_4 E_i^+ + bM_i^+}{2E_i^+} e^{-E_i^+ t} \\ &+ \sum_i |\lambda_{i,-}|^2 \frac{c_3 p_z + c_4 E_i^- - bM_i^-}{2E_i^-} e^{-E_i^- t}.\end{aligned} \tag{4.69}$$

Thus the requirement of a positive-definite spectral expansion results only in constraints for its coefficients

$$c_4 \geq |b|, \qquad c_3 \geq 0. \tag{4.70}$$

The coefficients $d_{ij}$ and $f_i$ are related to the polarization, which does not contribute to the spin-averaged two-point correlation functions. The coefficient $e$ will not contribute unless $\hat{J}^\dagger_{\mathrm{snk}}$ and $\hat{J}_{\mathrm{src}}$ operators are defined with opposite parities to each other, for example, when an extra $\gamma_5$ is inserted into only one of the diquarks.

This opens up other possibilities for $\mathcal{T}$ as well as the option to include linear combinations of multiple "projectors" at no additional computational cost like mixed parity, $\mathcal{T} = \mathcal{P}_+ - \mathcal{P}_- = \gamma_t$, which already provides kinematic enhancement. Another option which we shall explore in this work is $\mathcal{T} = \gamma_+$, which is not a projector as $\gamma_+^2 = 0$, but also provides kinematic enhancement.

In the following, we considered different choices for both kernels, namely $\Gamma' = C\gamma_5\Gamma$ with $\Gamma \in \{\mathbb{1}, \gamma_t, \gamma_+\}$ and $\mathcal{T} \in \{\mathcal{P}_+, \gamma_t, \gamma_+\}$.

When using $\Gamma' = C\gamma_5\gamma_+$, the quarks forming the diquark are projected onto their "+"-components. The free quark is projected likewise with $\mathcal{T} = \gamma_+$. This choice creates an additional improvement by a factor of 2 in variance compared to $(\mathcal{T}, \Gamma) = (\gamma_t, \gamma_t)$ or $(\mathcal{T}, \Gamma) = (\gamma_t, \gamma_z)$, as both information is used. In addition, this reduces the original degrees of freedom by projecting onto the "+"-components only. This cancels all "-"-components of the propagators in contractions, e.g. a nucleon three-point function,

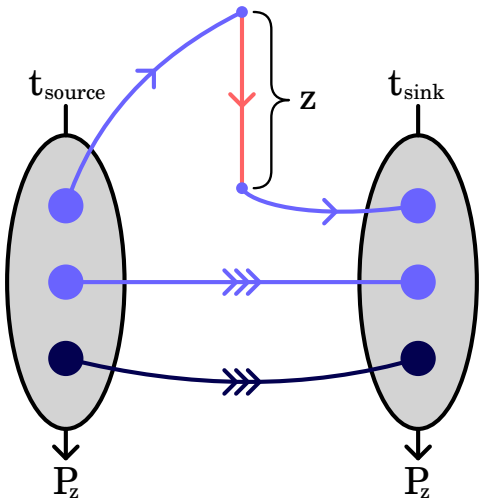



**Figure 4.6:** A nucleon 3pt contraction. Quark lines are colored blue and dark blue for the up- and down quarks, respectively. The Wilson line is colored red. Source and sink are placed at $t_{\text{source}}$ and $t_{\text{sink}}$, respectively. Both source and sink are boosted by $p_z$, which is also the direction of the inserted Wilson link.

where the operator $O(x_{\text{ins}}) = \bar{u}^{\delta'}_{d'}(x_{\text{ins}}) K^{d'd}_{\delta'\delta} u^{\delta}_{d}(x_{\text{ins}})$ has been inserted:

$$
\begin{aligned}
C^{u}_{\text{3pt},K}(\vec{p},\, t_{\text{ins}},\, t_{\text{sep}},\, z) &= a^6 \sum_{\vec{x}_{\text{snk}},\, \vec{x}_{\text{ins}}} e^{-i\vec{p}\cdot(\vec{x}_{\text{snk}} - \vec{x}_{\text{src}})}\, \epsilon_{abc}\, \epsilon_{a'b'c'} (\mathcal{T})_{\alpha\alpha'} (C\gamma_5\gamma_+)_{\beta\gamma} (C\gamma_5\gamma_-)_{\beta'\gamma'} \\
&\times \Big\langle u^{\alpha}_{a}(x_{\text{snk}})\, u^{\beta}_{b}(x_{\text{snk}})\, d^{\gamma}_{c}(x_{\text{snk}})\, \bar{u}^{\delta'}_{d'}(x_{\text{ins}})\, K^{d'd}_{\delta'\delta}\, u^{\delta}_{d}(x_{\text{ins}})\, \bar{u}^{\beta'}_{b'}(x_{\text{src}})\, \bar{d}^{\gamma'}_{c'}(x_{\text{src}})\, \bar{u}^{\alpha'}_{a'}(x_{\text{src}}) \Big\rangle . \\
&= a^6 \sum_{\vec{x}_{\text{snk}},\, \vec{x}_{\text{ins}}} e^{-i\vec{p}\cdot(\vec{x}_{\text{snk}} - \vec{x}_{\text{src}})}\, \epsilon^{abc}\, \epsilon^{a'b'c'} (\mathcal{T})_{\alpha\alpha'} (C\gamma_5\gamma_+)_{\beta\gamma} (C\gamma_5\gamma_-)_{\beta'\gamma'} \\
&\times D^{cc'}_{\gamma\gamma'}(x_{\text{snk}}, x_{\text{src}}) \\
&\times \Big[ U^{\alpha\delta'}_{ad'}(x_{\text{snk}}, x_{\text{ins}})\, K^{d'd}_{\delta'\delta}\, U^{\delta\alpha'}_{da'}(x_{\text{ins}}, x_{\text{src}})\, U^{\beta\beta'}_{bb'}(x_{\text{snk}}, x_{\text{src}}) \\
&\quad - U^{\alpha\delta'}_{ad'}(x_{\text{snk}}, x_{\text{ins}})\, K^{d'd}_{\delta'\delta}\, U^{\delta\beta'}_{db'}(x_{\text{ins}}, x_{\text{src}})\, U^{\beta\alpha'}_{ba'}(x_{\text{snk}}, x_{\text{src}}) \\
&\quad + U^{\beta\delta'}_{bd'}(x_{\text{snk}}, x_{\text{ins}})\, K^{d'd}_{\delta'\delta}\, U^{\delta\beta'}_{db'}(x_{\text{ins}}, x_{\text{src}})\, U^{\alpha\alpha'}_{aa'}(x_{\text{snk}}, x_{\text{src}}) \\
&\quad - U^{\beta\delta'}_{bd'}(x_{\text{snk}}, x_{\text{ins}})\, K^{d'd}_{\delta'\delta}\, U^{\delta\alpha'}_{da'}(x_{\text{ins}}, x_{\text{src}})\, U^{\alpha\beta'}_{ab'}(x_{\text{snk}}, x_{\text{src}}) \Big] .
\end{aligned}
\tag{4.71}
$$

When projecting all quarks in the source onto their "+"-components via $(\mathcal{T}, \Gamma) = (\gamma_+, \gamma_+)$, all "−"-component contractions of the resulting propagators with the source kernels become exactly 0, only the "+"-components contribute. This allows us to reduce the number of inversions to obtain the propagator connecting source and sink, in our case from a point source, by half. This reduction also applies to the propagator connecting the inserted operator to the sink, if it is obtained via the sequential source technique [136], even if the sink interpolator does not project its quarks onto their "+"-components. The propagators obtained from the "+"-projected source interpolator ensure that in the

contraction with the sink, only "+"-components contribute, making all "−"-components in the sequential source obsolete. This reduction in inversions also applies to polarized hadrons and partons, as polarization does not mix "+" and "-" components. Explicitly, "−"-components obtained as $q_- = \frac{1}{\sqrt{2}}\gamma_+\gamma_- q$ still cancel after combining $\gamma_+$ with the helicity or transversity projector:

$$\begin{aligned} \gamma_+\gamma_5\gamma_+\gamma_- &= 0\,, \\ \gamma_+\gamma_5\gamma_\perp\gamma_+\gamma_- &= 0\,. \end{aligned} \tag{4.72}$$

This applies neither at the source nor the sink if $(\mathcal{T}, \Gamma) = (\gamma_t, \gamma_+)$ is chosen, as contractions in general involve the free quark and thus mix "+" and "−"-components. An example of this is shown in (4.71), where the propagators connecting the operator with the sink that contract with the free quark kernel require all 12 indices. One such contraction, the first summand, is presented in Figure 4.6, with the down quark propagator shown in dark blue, and the up quark ones in light blue. To fully exploit this additional improvement in computation time, we consider only $(\mathcal{T}, \Gamma) = (\gamma_+, \gamma_+)$ for the case of $\gamma_+$-improvement. We summarize all tuples of kernels for our investigation in Table 4.1. The results of our investigation are presented in Chapter 8.

| Kernels $(\mathcal{T}, \Gamma)$ | Name |
|---|---|
| $(\mathcal{P}_+, \mathbb{1})$ | Conventional |
| $(\gamma_+, \gamma_+)$ | $\gamma_+$ enhanced |
| $(\gamma_t, \gamma_t)$ | $\gamma_t$ enhanced |

**Table 4.1:** Choices of interpolator kernels $(\mathcal{T}, \Gamma)$ used in this work.

## 4.5 Evaluation of Wick contractions

The techniques introduced in the previous sections allow us to evaluate the Wick contractions defined in Section 4.1.4 in a cost efficient way, which we review schematically in this section. Details on all these computations as well as explicit formulas can be found in Ref. [134] and the appendix of Ref. [31].

### 4.5.1 Connected three-point contractions

We first discuss the connected Wick contractions, the simplest of which are those occurring in two-point functions. They are calculated using point sources and their point-to-all propagators exclusively, no additional techniques are required.

The connected contractions of three-point functions, regardless of inserted operators of interest (see Figure 4.2 for local and 4.3 for non-local operators), are evaluated using the sequential source technique. Note that in our introduction of the sequential source

technique for the pion, the sequential propagator connects the source with the insertion in a forward manner, as the antiquark propagator faces in the opposite direction of the quark propagator. When inverting on the sink, the resulting propagator contains the information on propagation from the source through the sink to another lattice site, i.e. it will always point away from the sink. For the nucleon, all propagators are quark propagators and have to point towards the sink. We thus have to change the heading of the propagators accordingly. This is sketched in Figure 4.7.

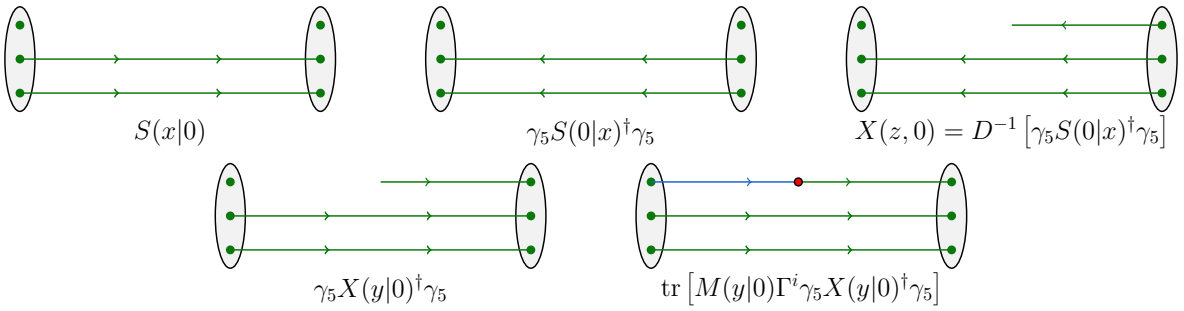


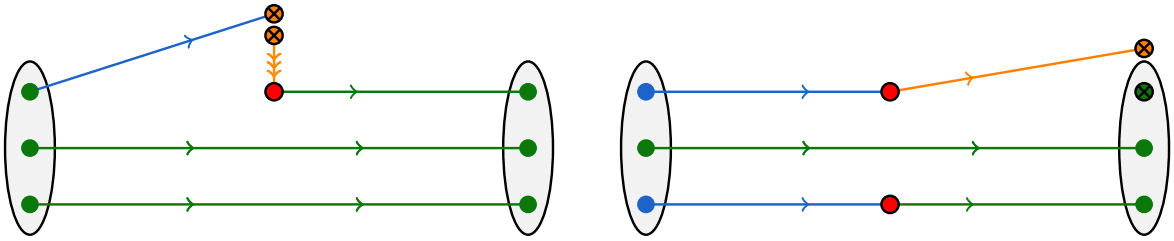

**Figure 4.7:** The sequential source technique for a nucleon three-point function. All expressions are given below the contraction sketch. Quark propagators contributing to the sequential propagator are shown in green, other point-to-all propagators are shown in blue and the inserted operator of interest is shown as a red dot. We present the computation from top left to bottom right. We begin with a product of point-to-all propagators named $S$, connecting source to sink. We then use $\gamma_5$-hermiticity (3.44) to reverse the propagator directions and obtain the sequential source. Next, we invert the Dirac operator in the sequential source to obtain the sequential propagator $X$. We then reverse the direction of the sequential propagator again using $\gamma_5$-hermiticity. Finally, we contract the reversed sequential propagator with the kernel $\Gamma^i$ of the operator of interest and the point-to-all propagator. The corresponding mathematical expressions are given below the respective illustrations.

### 4.5.2 Connected four-point contractions

The connected four-point Wick contractions $C_1$ and $C_2$ can be calculated in similar fashion. We shall first discuss the $C_2$ contraction. The sequential propagator is identical to the one for three-point functions, the only difference is the operator of interest. In this instance, we can consider the two operators as one non-local operator, that includes a quark propagator [144]. As this propagator has to connect any lattice site to any other lattice site, we approximate it by a stochastic propagator, improved by HPE. This is sketched in Figure 4.8a.

The $C_1$ contraction contains two operators on different quark lines. Using the quark line without operator insertions to invert the Dirac operator on the sink indices alone would increase the required inversions by a factor of 12 due to the additional open sink

indices. This can be avoided by contracting said open index with a stochastic source. The result can then be used as a sequential source. This is illustrated in Figure 4.8b.



**(a)** Details on the $C_2$ contraction. **(b)** Details on the $C_1$ contraction.

**Figure 4.8:** Schematic representation of techniques used in the calculation of connected four-point contractions. The sequential propagator is shown in green, other point-to-all propagators are shown in blue and the inserted operators of interest are shown as red circles. The stochastic propagator is shown as an orange line, stochastic sources as circles with crosses. Three consecutive arrows indicate HPE has been used to enhance the stochastic propagators signal.

### 4.5.3 Disconnected contractions

The loops occurring in disconnected contractions are computed separately, using point- and stochastic sources. They are combined with the remaining two-point (for $S_2$ and $D$) or three-point (for $S_1$) functions afterwards.

## 4.6 Data analysis techniques

In this section, we give a brief overview of the techniques we used to analyze the lattice data. We begin with the preprocessing of the data by binning and resampling, then include the extraction of ground state matrix elements from correlator data.

### 4.6.1 Error estimation

To reduce correlations in our data, we bin our data by averaging over $N_{\text{bin}}$ neighboring data points:

$$A_i^{\text{binned}} = \frac{1}{N_{\text{bin}}} \sum_{j=iN_{\text{bin}}}^{(i+1)N_{\text{bin}}-1} A_j^{\text{raw}} \,. \tag{4.73}$$

In the context of lattice calculations, neighboring data points are measurements performed on subsequent configurations from the same Markov chain. To estimate the underlying probability distribution of our data, extract accurate errors and propagate

errors properly through our subsequent analysis, we use jackknife resampling. This technique resamples our binned data $A_i^{\text{binned}}$ by subtracting each data point once to form exactly as many samples $A_j^{\text{jackknife}}$ as initial data points:

$$A_j^{\text{jackknife}} = \frac{1}{N-1} \sum_{i \neq j} A_i^{\text{binned}} , \tag{4.74}$$

where $N$ is the number of resampled data points. The mean of the jackknife samples is identical to the original dataset one:

$$\langle A^{\text{jackknife}} \rangle = \langle A^{\text{binned}} \rangle . \tag{4.75}$$

The Jackknife variance is related to the variance of the original data points before resampling by a factor of $N-1$:

$$\text{Var}\left(A^{\text{binned}}\right) = (N-1)\,\text{Var}\left(A^{\text{jackknife}}\right) . \tag{4.76}$$

### 4.6.2 Ground state matrix element extraction

Multiple techniques exist to extract the ground state matrix element from lattice data, see e.g. [145]. We shall discuss two approaches, the ratio method and a two-state fit. When the source-sink separation time $t_{\text{sep}}$ is large enough, excited states are sufficiently suppressed and we can extract the ground state matrix element from the correlator ratio as the weighted average over the central points, neglecting $d$ points close to the boundary:

$$R_n = \left\langle \frac{C_{n-\text{point}}(\tau, t_{\text{sep}})}{C_{2\text{pt}}(t)} \right|_{d \leq \tau \leq t_{\text{sep}}-d} \Bigg\rangle_{\tau} . \tag{4.77}$$

When the separation times are smaller or a more thorough investigation of excited state effects is necessary, we use a two state fit to extract the ground state matrix element. This is more robust, as we include at least one excited state in our approximation of the spectral decomposition. This additional state is not equivalent to the actual first excited state but instead acts as a garbage collector, its overlap indicating the strength of excited state contamination. For a three-point function, this leads to the following fit ansatz:

$$R_3(\vec{p}, t, \tau) = \frac{c_0 + c_1\, e^{-\Delta E \frac{t}{2}} \cosh\left(\Delta E \left(\tau - \frac{t}{2}\right)\right) + c_2\, e^{-\Delta E t}}{1 + c_3\, e^{-\Delta E t}} , \tag{4.78}$$

where the parameters $c_3$ and $\Delta E$ are obtained from a simultaneous two-state fit to the two-point function data:

$$C_2(\mathbf{p}, t) = A_0\, e^{-E_0 t} \left[1 + c_3\, e^{-\Delta E t}\right] . \tag{4.79}$$

The same fit function could be applied to four-point functions if the operators are inserted at identical insertion times, which is the case for our equal time matrix elements. A derivation of this is given in appendix B.

### 4.6.3 Fits and equation systems

To perform fits of functions to our data, we use $\chi^2$ minimization. Let $A_i$ be data points with mean $A = \langle A_i \rangle$ and variance $\sigma_i^2 = \mathrm{Var}(A_i)$ with position index $i$. Neglecting correlations, we have to minimize the expression

$$\chi^2(\vec{p}) = \sum_i \frac{\left(f_i(\vec{p}) - A_i\right)^2}{\sigma_i^2} \tag{4.80}$$

w.r.t. the vector of parameters $\vec{p}$. In this work, we use the iminuit library for python [146], that provides a python wrapper for the MINUIT algorithms [147].

To fit a linear ansatz to data points $A_i$, we write

$$f_i(\vec{p}) = \sum_j a_{ij} p_j \,, \tag{4.81}$$

where $a_{ij}$ are known coefficients. Inserting (4.81) into (4.80), we find

$$\chi^2(\vec{p}) = \sum_i \sigma_i^{-2} \left( \sum_j a_{ij} p_j - A_i \right)^2 , \tag{4.82}$$

which is differentiable, allowing us to analytically solve for its minimum:

$$\begin{aligned} 0 \overset{!}{=} \frac{\partial \chi^2}{\partial p_k} &= 2 \sum_i \sigma_i^{-2} a_{ik} \left( \sum_j a_{ij} p_j - A_i \right) = 2 \sum_i \left( \sum_j \sigma_i^{-2} a_{ik} a_{ij} p_j - \sigma_i^{-2} a_{ik} A_i \right) \\ &= 2 \sum_j \left( \underbrace{\sum_i \sigma_i^{-2} a_{ik} a_{ij}}_{=:\alpha_{kj}} p_j \right) - \underbrace{\sum_i \sigma_i^{-2} a_{ik} A_i}_{=:\gamma_k} = 2 \sum_j \alpha_{kj} p_j - \gamma_k \,. \end{aligned} \tag{4.83}$$

We can thus fit our data with a linear function by solving

$$\sum_j \alpha_{kj} p_j = \gamma_k \,. \tag{4.84}$$

# 5 Extracting parton distributions from lattice QCD

The parton correlation function (2.37) matrix elements include light-like separations, which are subsequently also present in all derived distribution functions like the PDFs (2.51) and collinear DPDs (2.56). These light-like separations are inherently Minkowskian, as they explicitly depend on real time, which is inaccessible on a Euclidean lattice. One approach is the calculation of Mellin moments via matrix elements of local twist-two operators on the lattice. This is possible, as for local operators the temporal separation of 0 is identical in real and imaginary time. The $n$-th Mellin moment of a single PDF $\Phi^a(x)$ is defined as

$$I_n^a = \int_0^1 dx\, x^{n-1}\, \Phi^a(x)\,. \tag{5.1}$$

The Operator Product Expansion (OPE) allows to express Mellin moments of PDFs in terms of matrix elements of local operators for the relevant hadron states:

$$\begin{aligned} I_1^a &= \int_0^1 dx \int \frac{d^2\mathbf{z}\, dz^-}{(2\pi)^3}\, d^2\mathbf{k}\; e^{ixp^+z^-}\, e^{-i\mathbf{k}\cdot\mathbf{z}}\, \langle p|\, O_a(z)|p\rangle\Big|_{z^+=0} \\ &= \frac{1}{p^+}\langle p|\, O_a(z=0)|p\rangle\,. \end{aligned} \tag{5.2}$$

This matrix element now no longer has an explicit time dependence and thus can be evaluated on a Euclidean lattice using local operators. Higher Mellin moments can be accessed by adding derivatives to the local operator, which we will discuss in more detail below. Roughly speaking, in principle, knowledge of sufficiently many Mellin moments determines the full distribution, although practical reconstruction from a finite set of moments is challenging. This was e.g. done using the first three Mellin moments of the pion and kaon in Ref. [148]. Calculating higher Mellin moments comes at considerable computational cost, as operators with derivatives have much smaller SNR than those without. Additionally, beyond the third non-trivial Mellin moment, an unavoidable power law mixing long made accessing higher Mellin moments impossible. Recent techniques allow the calculation of higher Mellin moments by using the gradient flow for fermion and gauge fields [41], already applied to the pion and kaon [149, 150], or using momentum space derivatives instead of position space [151].

Another possibility to access PDFs on the light-cone is presented by LaMET [37,

49], which has become one of the most successful approaches, yielding competitive phenomenological results [42–67]. This approach builds on Feynman's original intuition, that for hadron momenta approaching infinity, the partons behave as free particles. A consequence of this is that hadron structure eventually becomes independent of the actual hadron momentum, provided it is large enough. As time dilation effectively freezes any dynamics at infinite momentum, there must be a time independent matrix element that can be used to access hadron structure. Now using that hadron structure is independent of the hadron momentum $P$ at $P \gg \Lambda_{\mathrm{QCD}}$, the physical distributions at all $x$ can be extracted. The idea is thus to calculate time independent, non-local matrix elements at finite hadron momenta and then extrapolate towards infinite hadron momentum. Physically, this corresponds to applying a boost to the hadronic matrix element, illustrated in Figure 5.1.

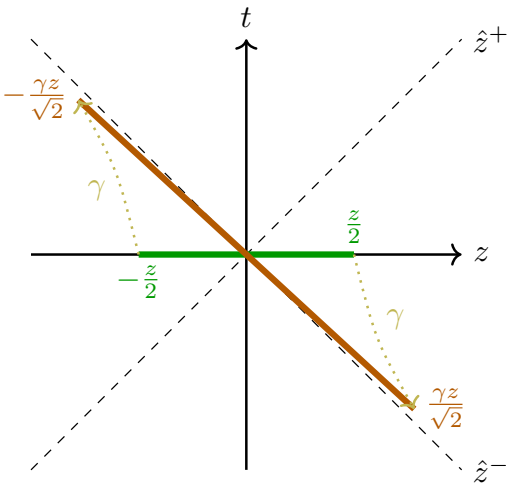



**Figure 5.1:** Illustration of a space-like separation (green bar) and its Lorentz-boosted counterpart (orange bar). The boost is indicated by the golden arrows and characterized by the Lorentz factor $\gamma$. In the rest frame of the hadron, the separation approaches the light-cone, while in a highly boosted frame, it is space-like. The endpoints of each segment are labeled by their $z$-components, and the total length of the boosted segment scales as $\gamma z$.

As discussed in Section 2.3, factorization introduces a scale dependence to regularize UV-divergences. Such a UV-cutoff $\Lambda_{\mathrm{UV}}$ has to be adjusted with larger momenta. In general, the infinite UV-cutoff limit and infinite momentum limit do not commute. Feynman's model takes the limit $(P \gg \Lambda_{\mathrm{UV}}) \to \infty$, while the physical limit is $(P \ll \Lambda_{\mathrm{UV}}) \to \infty$. This difference is reconciled by the introduction of matching functions which are calculated perturbatively and correct the UV-behavior.

In the following, we introduce the lowest Mellin moment for DPDs as well as how

PDFs are calculated using the LaMET formulation.

## 5.1 Mellin moments of DPDs

Multiparton distributions have multiple momentum fractions. We thus define the $(n, m)$-th Mellin moment of the skewed collinear DPD $F_{ab}(x_1, x_2, \zeta, \mathbf{y})$ as

$$I_{ab}^{(n,m)}(\zeta, \mathbf{y}) = \int_{-1}^{1} \mathrm{d}x_1 \, x_1^{n-1} \int_{-1}^{1} \mathrm{d}x_2 \, x_2^{m-1} F_{ab}(x_1, x_2, \zeta, \mathbf{y}) \,. \tag{5.3}$$

In analogy to the PDF case, the integration over the momentum fractions turns the non-local operators (2.60) into local ones:

$$I_{ab}^{(n,m)}(\zeta, \mathbf{y}) = (p^+)^{1-n-m} \sum_{\lambda} \int \mathrm{d}y^- \, e^{-i\zeta p^+ y^-} \langle p, \lambda | O_a^{n-1}(y) \, O_b^{m-1}(0) | p, \lambda \rangle \tag{5.4}$$

$$= 2(p^+)^{1-n-m} \int \mathrm{d}y^- \, e^{-i\zeta p^+ y^-} \mathcal{M}_{ab}^{(n-1,m-1)}(p, y) \Big|_{y^+=0, \, \mathbf{y}=0} \,, \tag{5.5}$$

where the local operators $O^n$ include $n$ derivatives:

$$O_n^q(y) := \bar{q}_1(y) \, \Gamma_a \, \left( i \overleftrightarrow{D}^+ \right)^n q_2(y) \,. \tag{5.6}$$

We include the possibility of $q$ being a pair of quarks of different flavor to account for flavor interference. We also define the spin averaged matrix element

$$\mathcal{M}_{ab}^{(n-1,m-1)}(p, y) := \frac{1}{2} \sum_{\lambda} \langle p, \lambda | O_a^{n-1}(y) \, O_b^{m-1}(0) | p, \lambda \rangle \,. \tag{5.7}$$

### 5.1.1 Two-current matrix elements

The light-like separations $y^-$ cannot be resolved on the lattice. To access the matrix elements nevertheless, we exploit the matrix element's Lorentz symmetry. We define spin averaged equal time two-current matrix elements with purely space-like separation $y$, i.e. $y^0 = 0$:

$$M_{ab}(p, y) = \frac{1}{2} \sum_{\lambda} \langle p, \lambda | O_a(y) \, O_b(0) | p, \lambda \rangle \Big|_{y^0=0} \,, \tag{5.8}$$

where we used the local operators on the lattice (4.21). These are precisely the matrix elements occurring in our four-point functions (4.37).

As $y$ is spacelike, the operators $O$ commute, which implies

$$M_{a_1 a_2 b_1 b_2}(p, y) = M_{b_1 b_2 a_1 a_2}(p, -y) \,. \tag{5.9}$$

Furthermore, if $a_1 = a_2$ and $b_1 = b_2$, the local operators $O$ conserve flavor and are

hermitian, implying

$$[M_{a_1a_2b_1b_2}(p,y)]^* = M_{a_2a_1b_2b_1}(p,y)\,. \tag{5.10}$$

Combining these two properties, the matrix element is guaranteed to be real for flavor-conserving currents.

To transfer the results from Euclidean to Minkowski space, the matrix elements have to be multiplied by powers of $i$ in accordance with (3.12), one for every spatial gamma matrix included in their operators.

### 5.1.2 Renormalization

For this section, we follow [115]. Physical matrix elements include divergences which have to be renormalized properly. Matrix elements obtained on the lattice are regularized by the lattice spacing $a$, which introduces a hard $\pi/a$ momentum UV-cutoff, while in the continuum the most frequently used scheme is dimensional regularization, followed by renormalization within the $\overline{\text{MS}}$ scheme. To extract results comparable with continuum physics from the lattice, these differences have to be resolved. At a renormalization scale $\mu$, usually 2 GeV, local quark bilinear operators can be renormalized multiplicatively:

$$O^{\text{ren}}_{\Gamma,\mu^2} = Z_\Gamma(\mu^2) O^{\text{bare}}_\Gamma\,. \tag{5.11}$$

To obtain the renormalization constants $Z_\Gamma(\mu^2)$, one must fix a renormalization condition first. This condition relates lattice to continuum results from which $Z_\Gamma(\mu^2)$ can be extracted. Thus, one has to choose a scheme, that can be applied both on the lattice and in the continuum. This also explains the common choice of $\mu = 2\,\text{GeV}$, as $\alpha_s(2\,\text{GeV}) \approx 0.3$ so that perturbation theory at sufficiently high order produces accurate results while at the same time, $\mu \ll \pi/a$, so that discretization artifacts from the lattice calculation remain small at typical lattice spacings. One such scheme is the RI' scheme [152], based on the RI scheme [153].

The renormalization condition in the RI' scheme is

$$Z_\Gamma^{\text{RI}'} \langle p|\, O_\Gamma\, |p\rangle \Big|_{p^2=\mu^2} = \langle p|\, O_\Gamma\, |p\rangle_0 \Big|_{p^2=\mu^2}\,, \tag{5.12}$$

where the l.h.s includes the interacting case with renormalization factor $Z_\Gamma^{\text{RI}'}$ and the r.h.s. describes the non-interacting, tree-level result. Here, $|p\rangle$ signifies a quark "state". At tree level,

$$\langle p|\, O_\Gamma\, |p\rangle_0 = \Gamma\,, \tag{5.13}$$

with $\Gamma$ being the Dirac structure under investigation, e.g. from (4.21). The renormalized

matrix element

$$Z_q^{\mathrm{RI}'} \langle p| O_\Gamma |p\rangle = \Lambda_\Gamma \tag{5.14}$$

where $Z_q^{\mathrm{RI}'}$ is the quark field renormalization constant, is equal to the amputated Green's function $\Lambda_\Gamma$ which can be calculated on the lattice as

$$\Lambda_\Gamma(p) = S^{-1}(p) G_\Gamma(p) S^{-1}(p)\,, \tag{5.15}$$

where

$$\begin{aligned} G_\Gamma(p) &= \frac{1}{V}\sum_{xyz} e^{-ip(x-y)} M(x|z)\Gamma M(z|y)\,, \\ S(p) &= \frac{1}{V}\sum_{xy} e^{-ip(x-y)} M(x|y)\,, \\ M(x|y) &= \langle q(x)\bar{q}(y)\rangle\,. \end{aligned} \tag{5.16}$$

As $\Lambda_\Gamma$ is gauge variant, the gauge has to be fixed, usually to the Landau gauge. The quark field renormalization constant $Z_q^{\mathrm{RI}'}$ is obtained by comparing the quark propagator $S$ with the free lattice propagator $S^{\mathrm{free}}$:

$$Z_q^{\mathrm{RI}'}(\mu^2) = \frac{1}{12}\,\mathrm{tr}\Big[S^{-1}(p)\, S^{\mathrm{free}}(p)\Big]\Big|_{p^2=\mu^2}\,. \tag{5.17}$$

We can now rearrange (5.12) to the l.h.s. and take the trace, yielding

$$Z_\Gamma^{\mathrm{RI}'} \frac{1}{12}\,\mathrm{tr}\left(\langle p| O_\Gamma |p\rangle \langle p| O_\Gamma |p\rangle_0^{-1}\right)\Big|_{p^2=\mu^2} = 1\,. \tag{5.18}$$

Inserting (5.14) and (5.13), we obtain

$$Z_\Gamma^{\mathrm{RI}'}(\mu^2) = \frac{12\, Z_q^{\mathrm{RI}'}}{\mathrm{tr}[\Lambda_\Gamma(p)\,\Gamma^{-1}]}\Big|_{p^2=\mu^2}\,. \tag{5.19}$$

In the continuum, the RI' renormalization factor $Z_\Gamma^{\mathrm{RI}'}(\mu^2)$ obtained from perturbation theory is related to $Z_\Gamma^{\overline{\mathrm{MS}}}(\mu^2)$ by a conversion factor $R_\Gamma(\mu^2)$:

$$Z_\Gamma^{\overline{\mathrm{MS}}}(\mu^2) = R_\Gamma(\mu^2) Z_\Gamma^{\mathrm{RI}'}(\mu^2)\,. \tag{5.20}$$

While the individual renormalization factors might be divergent when approaching the continuum limit, $R_\Gamma(\mu^2)$ is not. The non-perturbatively determined $Z_\Gamma^{\mathrm{RI}'}(\mu^2)$ is related to $Z_\Gamma^{\overline{\mathrm{MS}}}(\mu^2)$ via a perturbatively computed finite ratio $R_\Gamma(\mu^2)$, so that the full renormalization factor $Z_\Gamma(\mu^2) = R_\Gamma(\mu^2)\, Z_\Gamma^{\mathrm{RI}'}(\mu^2)$ converts bare lattice results directly to the $\overline{\mathrm{MS}}$ scheme. This has been done for local quark-bilinears without derivatives up to four-loop order in perturbation theory [154], the results of which we will be using later in this

work.

### 5.1.3 Mellin moments at leading twist

For the parton polarization channels of interest identified in Section 2.4.3, the matrix element obtained from the lattice (5.8) can be decomposed into Lorentz covariant tensors and Lorentz scalars [106]:

$$
\begin{aligned}
M^{\mu\nu}_{VV,qq'} - g^{\mu\nu}\frac{1}{4}\,\mathrm{tr}\Big\{M^{\mu\nu}_{VV,qq'}\Big\} &= u^{\mu\nu}_{VV,A}\,A_{qq'} + \nu^{\mu\nu}_{VV,B}\,m^2 B_{qq'} + \nu^{\mu\nu}_{VV,C}\,m^4 C_{qq'}\,,\\
M^{\mu\nu\rho}_{TV,qq'} + g_{\lambda\sigma}g_{\rho[\mu}M^{\nu]\lambda\sigma}_{TV,qq'} &= u^{\mu\nu\rho}_{TV,A}\,m A_{q\delta q'} + \nu^{\mu\nu\rho}_{TV,B}\,m^3 B_{q\delta q'}\,,\\
\frac{1}{2}\left[M^{\mu\nu\rho\sigma}_{TT,qq'} + M^{\rho\sigma\mu\nu}_{TT,qq'}\right] &= u^{\mu\nu\rho\sigma}_{TT,A}\,A_{\delta q\delta q'} + u^{\mu\nu\rho\sigma}_{TT,B}\,m^2 B_{\delta q\delta q'} + u^{\mu\nu\rho\sigma}_{TT,C}\,m^2 C_{\delta q\delta q'}\\
&\quad + u^{\mu\nu\rho\sigma}_{TT,D}\,m^2 D_{\delta q\delta q'} + u^{\mu\nu\rho\sigma}_{TT,E}\,m^4 E_{\delta q\delta q'}\,.
\end{aligned}
\tag{5.21}
$$

We subtract trace contributions to reduce the number of degrees of freedom. The tensors $u$ include all Lorentz covariant four-vectors ($y^\mu$, $p^\mu$) and are given in the appendix A. The decompositions of $M^{\mu\nu}_{AA,qq'}$ is identical to $M^{\mu\nu}_{VV,qq'}$, the decomposition of $M^{\rho\mu\nu}_{VT,qq'}$ is obtained from interchanging the indices $\mu\nu$ and $\rho$ on the l.h.s of the decomposition of $M^{\mu\nu\rho}_{TV,qq'}$. To extract the invariant functions from the four-point matrix elements according to (5.21), we have to solve an overdetermined system of linear equations. We use the additional information to estimate the errors involved in our extraction and obtain the invariant functions via $\chi^2$ minimization as detailed in Section 4.6.3. The invariant functions depend solely on the Lorentz scalars $y^2$ and the Ioffe time $\omega = p\cdot y$, which is the Fourier conjugate of $\zeta$. With the time separation $y^0$ between the two currents being zero, the Lorentz invariants are given by

$$
y^2 = -\vec{y}^{\,2}\,, \qquad\qquad \omega = -\vec{p}\,\vec{y}\,, \tag{5.22}
$$

so that the Ioffe time is limited to

$$
|\omega| \le |\vec{p}\,|\,|\vec{y}\,|\,. \tag{5.23}
$$

At leading twist, only the invariant functions $A_{XqYq'}$, where $X$ and $Y$ signifies any combination of contributing channels, and $B_{\delta q\delta q'}$ contribute [106]:

$$
\begin{aligned}
M^{++}_{VV,qq'}(p,y) &= 2\left(p^+\right)^2 A_{qq'}\left(\omega, y^2\right)\,,\\
M^{++}_{AA,qq'}(p,y) &= 2\left(p^+\right)^2 A_{\Delta q\Delta q'}\left(\omega, y^2\right)\,,\\
M^{j++}_{TV,qq'}(p,y) &= 2\left(p^+\right)^2 y^j m A_{\delta qq'}\left(\omega, y^2\right)\,,
\end{aligned}
$$

$$M^{+j+}_{VT,qq'}(p,y) = 2\left(p^+\right)^2 y^j m A_{\delta qq'}\left(\omega, y^2\right),$$
$$M^{j+l+}_{TT,qq'}(p,y) = 2\left(p^+\right)^2 \left[\delta^{jl} A_{\delta q\delta q'}\left(\omega, y^2\right) - \left(2y^j y^l + \delta^{jl} y^2\right) m^2 B_{\delta q\delta q'}\left(\omega, y^2\right)\right]. \quad (5.24)$$

Note the difference in operator definitions in the continuum (2.40) and on the lattice (4.21). They are related by multiplication with an appropriate factor:

$$\begin{aligned}
\mathcal{M}_{qq} &= \frac{1}{4} M^{++}_{VV,qq'},\\
\mathcal{M}_{\Delta q\Delta q} &= \frac{1}{4} M^{++}_{AA,qq'},\\
\mathcal{M}^{jl}_{\delta q\delta q} &= -\frac{1}{4}\epsilon^{jk}\epsilon^{lm} M^{k+m+}_{TT,qq'},\\
\mathcal{M}^{l}_{q\delta q} &= \frac{i}{4}\epsilon^{lm} M^{+m+}_{VT},\\
\mathcal{M}^{j}_{\delta qq} &= \frac{i}{4}\epsilon^{jk} M^{k++}_{TV}.
\end{aligned} \quad (5.25)$$

Inserting the leading twist contributions (5.24) into (5.4) and using the factors (5.25) for $n = m = 1$ in the $VV$ case yields

$$\begin{aligned}
I^{(1,1)}_{qq'}(\zeta, \mathbf{y}) &= p^+ \int \mathrm{d}y^-\, e^{-i\zeta p^+ y^-} \mathcal{M}_{qq'}(p,y)\Big|_{y^+=0,\,\mathbf{y}=0}\\
&= \int \mathrm{d}\omega\, e^{-i\zeta\omega} M^{++}_{VV,qq'}(p,y)\Big|_{y^+=0,\,\mathbf{y}=0}.
\end{aligned} \quad (5.26)$$

This extends to all polarizations:

$$I_{qq'}(\zeta, y^2) = \int_{-\infty}^{\infty} \mathrm{d}\omega\, e^{-i\zeta\omega}\, A_{qq'}(\omega, y^2), \quad (5.27)$$
$$I^t_{qq'}(\zeta, y^2) = \int_{-\infty}^{\infty} \mathrm{d}\omega\, e^{-i\zeta\omega}\, B_{qq'}(\omega, y^2). \quad (5.28)$$

Note that (5.28) is only defined for transverse polarization of $q$ and $q'$, i.e. $B_{\delta q\delta q'}$.

Applying the inverse Fourier transform to (5.27), we obtain

$$A_{qq'}(\omega, y^2) = \frac{1}{2\pi}\int_{-1}^{1} \mathrm{d}\zeta\, e^{i\zeta\omega}\, I_{qq'}(\zeta, y^2). \quad (5.29)$$

### 5.1.4 Properties of DPD Mellin moments

To obtain the lowest Mellin moment of DPDs, $I_{qq'}(\zeta = 0, y^2)$, according to (5.27), we have to integrate $A_{qq'}(\omega, y^2)$ over the Ioffe time $\omega$. As we can only access finite $\omega$ on the lattice, we have to solve this inverse problem using a suitable model ansatz to approximate $I_{qq'}(\zeta, y^2)$. The functional form of $I_{qq'}(\zeta, y^2)$ is mostly unknown. The only

constraint we introduced so far is that they are even functions of $\zeta$, wherefore we only consider positive $\zeta$ in this section.

To narrow the field for possible ansätze, we follow [69] and consider the support of the DPDs in the extreme case of $\zeta \to 1$, where it reduces to the central square $|x_1|, |x_2| \leq \frac{1}{2}\zeta$ in Figure 2.3. In this context, the moment $I_{qq'}(\zeta = 1, y^2)$ for flavor-conserving currents $(qq') \in \{(ud), (uu), (dd)\}$ describes the extraction of a color-singlet pair $q\bar{q}$ that carries all longitudinal momentum of the proton. The remaining spectator partons have zero longitudinal momentum. It is plausible, that the probability of such an event is zero and that $\lim_{\zeta\to 1} I_{qq'}(\zeta, y^2) = 0$ similarly fast as the proton quark PDFs approach their $\lim_{x\to 1} f_q(x) = 0$.

Furthermore, $I_{qq'}(\zeta, y^2)$ is in general not an analytic function of $\zeta$ around $\zeta \in 0, 1$. This is shown in Ref. [69] by considering the $g \to q\bar{q}$ contribution to the skewed DPD $F_{q\bar{q}}$ at leading order in $\alpha_s$ in the short distance limit, which exhibits a singular behavior when approaching $\zeta = 0$. While a polynomial model produced stable fits the data for $A_{qq'}(\omega, y^2)$ in Ref. [155], it does not vanish when approaching $\zeta = 1$ and enforces analyticity around $\zeta = 0$. We will compare different ansätze to extrapolate the lattice data that respect the boundary condition at $\zeta = 1$ and investigate the effects of enforced analyticity on the extracted information in Chapter 7.

## 5.2 Nucleon PDFs with LaMET

For the introduction of LaMET, we follow [37]. The nucleon quark PDF defined in (2.51) contains light-like distances which cannot be resolved on the lattice. In LaMET, the problem of light-like separations is circumvented by again exploiting Lorentz symmetry. As discussed above, PDFs can equivalently be expressed through their Mellin moments via the twist-2 operators

$$O^{\mu_1\cdots\mu_n} = \bar{\psi}\,\gamma^{\{\mu_1} iD^{\mu_2}\cdots iD^{\mu_n\}}\psi - \text{trace}\,, \tag{5.30}$$

where the indices of the derivatives are symmetrized and the trace terms contain at least one trace over momenta. The contracted pairs of momenta are replaced by $g^{\mu\nu}$. The proton matrix element of these operators yields

$$\langle P|\, O^{\mu_1\cdots\mu_n}(\mu^2)\,|P\rangle = 2\,a_n(\mu^2)\,(P^{\mu_1}\cdots P^{\mu_n} - \text{trace})\ , \tag{5.31}$$

where the coefficients $a_n(\mu^2)$ are proportional to the Mellin moments of the PDF,

$$\int \mathrm{d}x\, x^{n-1} f(x, \mu^2) = a_n(\mu^2)\,. \tag{5.32}$$

Selecting all "+"-components recovers time dependence, i.e. $\langle P|O^{+\cdots+}|P\rangle = 2a_n(\mu^2)(P^+)^n$, which is kinematically connected to the "+"component of the nucleon momentum. Now, instead of considering the "+"-component, one can also isolate the spatial momentum

direction, which in our framework is chosen to be the $z$-direction:

$$\langle p_z|\ \bar{\psi}\,\gamma^z\, iD^z \cdots iD^z\,\psi\ |p_z\rangle = 2\,a_n(\mu^2)\,(p^z)^n \times \left[1 + \mathcal{O}\left(\frac{\Lambda^2_{\rm QCD}}{(p^z)^2},\ \frac{M^2}{(p^z)^2}\right)\right]. \tag{5.33}$$

Lorentz symmetry dictates that the trace terms of lower power in $p_z$ are proportional to $\Lambda^2_{\rm QCD}$ or $M^2$ at most, making them power-suppressed in the large $p_z$ limit. The Taylor expansion around $z = 0$ of the non-local, space-like Wilson line is

$$\begin{aligned}\bar{\psi}(z/2)\,\gamma^z\,W(z/2,-z/2)\,\psi(-z/2) &= \bar{\psi}(z/2)\,\gamma^z\,\mathcal{P}\exp\left(-ig\int_{-z/2}^{z/2} dz'\,A_z(z')\right)\psi(-z/2)\\ &= \sum_{n=0}^{\infty}\frac{z^n}{n!}\bar{\psi}(0)\,\gamma^z\,(D^z)^n\psi(0) + \text{traces}\,. \end{aligned}\tag{5.34}$$

One can use (5.33) to evaluate the r.h.s of (5.34), then use (5.32) and invert the result to obtain a non-local, time-independent expression, the quasi-PDF

$$\tilde{f}(x,p_z) = \int\frac{\mathrm{d}z}{4\pi}\,e^{ixzp_z}\,\langle p_z|\ \bar{\psi}(z)\,\gamma^z\,\mathcal{W}[z,0]\,\psi(0)\ |p_z\rangle + \mathcal{O}\left(\frac{\Lambda^2_{\rm QCD}}{(p^z)^2},\ \frac{M^2}{(p^z)^2}\right), \tag{5.35}$$

which includes an equal-time matrix element which is only non-local in the $z$ direction. As $p_z \to \infty$, its kinematic structure approaches that of a light-cone correlation in the infinite-momentum limit. A spacelike separation remains spacelike under Lorentz transformations; however, in the infinite-momentum limit its projection onto the light-cone becomes dominant.

The distribution defined by this correlator is referred to as the quasi-PDF (qPDF). It can be related to the light-front (LF) PDF by the LaMET factorization theorem [156]:

$$f(x,\mu) = \int_{-\infty}^{\infty}\frac{dy}{|y|}\tilde{C}\left(\frac{x}{y},\frac{\mu}{yp_z}\right)\tilde{f}\,(y,p_z,\mu) + \mathcal{O}\left(\frac{\Lambda^2_{\rm QCD}}{(xp_z)^2},\frac{\Lambda^2_{\rm QCD}}{((1-x)p_z)^2}\right), \tag{5.36}$$

where $f(x,\mu)$ is the PDF, $\tilde{f}\,(y,p_z,\mu)$ is the qPDF at longitudinal momentum $p_z$ and $\tilde{C}\left(\frac{x}{y},\frac{\mu}{yp_z}\right)$ is the corresponding matching kernel. The latter can be calculated in perturbation theory, at leading [37], one loop (NLO) [157] and two loop (NNLO) [158] accuracy. It was later shown that errors can be greatly reduced by renormalization group resummation (RGR) [159] and leading renormalon resummation (LRR) [160, 161].

The higher twist and trace contributions in (5.36) are suppressed by powers of $xp_z$ and $(1-x)p_z$ which will vanish in the infinite momentum limit. In practice, only finite momenta are accessible on the lattice, which imposes limitations on the validity of the factorization formula:

$$x \gg \frac{\Lambda_{\rm QCD}}{p_z} \quad \text{and} \quad x \ll 1 - \frac{\Lambda_{\rm QCD}}{p_z}\,. \tag{5.37}$$

Currently achievable momenta for nucleons are $\approx 2.5\,\text{GeV}$, corresponding to a momentum fraction range of $0.08 \ll x \ll 0.92$. This implies that for very small or large $x$, power corrections are considerable. LaMET results thus are only considered reliable within a more restricted range $0.2 \leq x \leq 0.8$. It is highly desirable to increase this range by increasing hadron momentum.

For the quasi-PDF matrix element to be well-resolved on the lattice, the lattice spacing $a$ must be sufficiently small to support the momentum modes of the boosted nucleon. Concretely, the nucleon carries longitudinal momentum $p_z$, and the Wilson line correlator defining the quasi-PDF probes distances $z \sim 1/p_z$. For the lattice to faithfully represent these short-distance correlations, one requires

$$a \ll \frac{1}{p_z}\,, \tag{5.38}$$

or equivalently $ap_z \ll 1$, so that discretization errors of order $(ap_z)^2$ remain small. Using $\hbar c \approx 0.197\,\text{GeV} \cdot \text{fm}$, a target momentum of $p_z = 2.5\,\text{GeV}$ constrains

$$a \ll \frac{0.197\,\text{GeV} \cdot \text{fm}}{2.5\,\text{GeV}} \approx 0.08\,\text{fm}\,, \tag{5.39}$$

and for $p_z = 5\,\text{GeV}$ the requirement tightens to $a \ll 0.04\,\text{fm}$. These are significantly more demanding than the condition $a \ll \Lambda_{\text{QCD}}^{-1} \approx 1\,\text{fm}$, required to resolve the nonperturbative structure in a hadron at rest, and they set the practical upper limit on the nucleon momenta accessible in current calculations. Lattice spacings below $\sim 0.04\,\text{fm}$ are at the frontier of what is currently feasible, due both to the computational cost and to the severe topological charge freezing that afflicts fine ensembles [125]. Consequently, $p_z = 5\,\text{GeV}$ has not yet been reached in LaMET calculations, and current state-of-the-art results use $p_z \approx 2.5 - 3.0\,\text{GeV}$ for the nucleon [162] and $p_z \approx 1.7 - 2.0\,\text{GeV}$ for mesons [163].

The core principle of LaMET is to make matrix elements of light-cone operators accessible by considering matrix elements of purely spatial separations with highly boosted external states. As illustrated in Figure 5.1, a spatial separation in the frame of a highly boosted nucleon approximates a light-cone separation in a zero momentum frame. The PDF can be thought of in the rest frame, probed by a light-like probe, the quasi-PDF corresponds to a static probe acting on a nucleon boosted to large momentum $p_z$, ideally approaching the speed of light. In the following, we define the unpolarized quark isovector quasi PDF as a suitable test quantity to investigate the improvement of lattice SNR, as performed in Chapter 8.

### 5.2.1 The unpolarized nucleon PDF

The nucleon light-cone PDF was defined in (5.36). We now define the quasi-PDF:

$$\begin{aligned}\tilde{f}\left(x,p^z,\mu\right) &= p^z\int\frac{dz}{2\pi}e^{iz(xp^z)}\tilde{h}_R\left(z,p^z,\mu\right),\\ \tilde{h}_R\left(z,p^z,\mu\right) &= \frac{1}{2E}\langle P|\bar{\psi}(z)\gamma^t\psi(0)|P\rangle\,.\end{aligned} \tag{5.40}$$

Note that we choose $\gamma^t$ here instead of $\gamma^z$ for the Dirac structure to reduce effects from operator mixing [164]. This changes the matching kernel and influences renormalization. The quasi-PDF matrix elements $\tilde{h}_R\left(z,p^z,\mu\right)$ are renormalized matrix elements, obtained by renormalizing the bare matrix elements, calculated on the lattice:

$$\tilde{h}(z,p_z,1/a) = \frac{1}{2E}\langle P|\bar{\psi}(z)\gamma^t\mathcal{W}[z,0]\psi(0)|P\rangle, \tag{5.41}$$

where $\mathcal{W}[z,0]$ is the straight Wilson line running from 0 to $z$. As $\gamma_t$ is identical in Euclidean and Minkowski space-time, we do not have to multiply these results by any powers of $i$.

### 5.2.2 Renormalization

The bare correlation function (5.41) suffers from linear divergences due to the Wilson self-energy and logarithmic UV divergences stemming from the UV regulating lattice spacing. Both need to be removed correctly for a proper renormalization. We choose the hybrid scheme [165] which renormalizes short distances $z$ in a ratio scheme [38, 166, 167] and long ones via self-renormalization [168]:

$$\tilde{h}_R(z,p_z,\mu) = \frac{\tilde{h}(z,p_z,1/a)}{\tilde{h}(z,p_z=0,1/a)}\theta(z_s-|z|)+\eta_s\frac{\tilde{h}(z,p_z,1/a)}{Z_R(z,1/a)}\theta(|z|-z_s)\,. \tag{5.42}$$

The short-distance scale $z_s$ is introduced as an artificial separator between short and long distances, which will be canceled by the $z_s$ dependence in the corresponding perturbative matching kernel. It can be varied in the analysis to reduce bias associated with its choice. $\eta_s$ is a normalization factor that guarantees the continuity of renormalization at $z = z_s$ during the transition from the perturbative to the non-perturbative region. At small $z \leq z_s$, we divide the correlation functions at large momenta by the same correlation functions in the rest frame. At large distances, the self-renormalization factor $Z_R(z,1/a)$ is used to remove UV divergences while preserving IR physics. The UV physics can be extracted from the short distance bare matrix elements in the rest frame $\tilde{h}(z,p_z=0,1/a)$ at multiple lattice spacings. Motivated by perturbation theory,

it is assumed to be of functional form

$$\ln \tilde{h}(z, p_z = 0, 1/a) = \frac{kz}{a \ln(a\Lambda_{\mathrm{QCD}})} + g(z) + f(z)a^2 + \frac{3C_F}{11 - 2N_f/3} \ln \left[ \frac{\ln\left[1/(a\Lambda_{\mathrm{QCD}})\right]}{\ln\left[\mu/\Lambda_{\mathrm{QCD}}\right]} \right] + \ln \left[ 1 + \frac{d}{\ln(a\Lambda_{\mathrm{QCD}})} \right] . \tag{5.43}$$

The first term includes the linear divergence stemming from the Wilson line self-energy. The second term, $g(z)$, contains the non-perturbative information necessary for renormalization as well as a renormalon ambiguity term, which we will have to remove later. The third term, $f(z)a^2$, accounts for discretization errors. The last two terms result from the resummation of leading and sub-leading logarithms, affecting normalization at different lattice spacings. As higher order effects and further lattice artifacts cannot be removed entirely, $\Lambda_{\mathrm{QCD}}$ and $d$ are treated as fit parameters as well [169]. The normalized long distance renormalization coefficient $Z_R(z, 1/a)/\eta_s$ is defined as

$$\frac{Z_R(z, 1/a)}{\eta_s} = \tilde{h}(z_s, p_z = 0, 1/a) \exp \left[ -\frac{k(|z| - z_s)}{a \ln(a\Lambda_{\mathrm{QCD}})} - m_0(|z| - z_s) \right] , \tag{5.44}$$

where the renormalon mass $m_0$ is extracted via a linear fit to the difference of the continuum perturbative $\overline{\mathrm{MS}}$ result $C^{\overline{\mathrm{MS}}}_{0,\mathrm{NLO}}(z)$ and $g(z)$ obtained from (5.43)

$$g(z) - \ln(C^{\overline{\mathrm{MS}}}_{0,\mathrm{NLO}}(z)) = m_0 z \, . \tag{5.45}$$

The fixed order (NLO) result was obtained in Ref. [156] and is given as

$$C^{\overline{\mathrm{MS}}}_{0,\mathrm{NLO}}(z) = 1 + \frac{\alpha_s C_F}{2\pi} \left( \frac{3}{2} \ln \left( z^2 \mu^2 e^{2\gamma_{\mathrm{E}}}/4 \right) + \frac{5}{2} \right) . \tag{5.46}$$

Note that the determination of $m_0$ is not unique due to the renormalon ambiguity, and needs to be properly regularized when matched to the lightcone PDF to avoid introducing extra linear corrections in $1/p_z$ [161]. However, the scope of this work only focuses on the statistical uncertainties of quasi-PDF lattice data, not including the perturbative matching to the lightcone PDFs. It makes no difference if we simply use the fixed-order NLO result from (5.46), as the ambiguity does not affect the relative statistical errors of the lattice data.

# 6 Invariant functions of DPDs at $\omega = 0$

In this chapter, we present our results for the lattice spacing and mass dependence of the invariant functions of DPDs at $\omega = 0$. We first present the lattice setup of our calculation, then proceed to analyze the results. First, we probe for excited state contributions within our data on one exemplary ensemble. Second, we examine the dependence of lattice artifacts observed in the past [31, 32] on lattice parameters. Third, we present our results for the lattice spacing dependence of leading twist invariant functions, followed by their mass dependence as fourth point. The calculations on the H102 ensemble, the results of which will be used in the $a$-dependence analysis, have already been published in Ref. [31] and [32]. The simulations on the S100 ensemble were performed in the context of Ref. [170] and have been reused for this work. By the time of the publication of this thesis, the contents of this chapter have already been published in Ref. [171]. In the following, we shall only discuss data for the connected contractions $C_1$ and $C_2$. The contributions by the disconnected contractions $S_1$ and $S_2$ were found to be small in the considered region of distances $\vec{y}$ (see [31, 32] and section 6.3). The contribution of doubly disconnected contractions $D$ cannot be determined at this point in time due to statistical uncertainties in our data. We can neglect them as we expect the ratio $D : S_1$ to be of similar size as the ratio $S_1 : C_1$, which is small [172].

## 6.1 Lattice setup

Our goal is to investigate the physical limit of the lattice observables in the context of DPDs. To this end, we perform the simulations on several gauge ensembles, varying both the lattice spacing and light and strange quark masses. Moreover, the different physical volumes realized by the employed ensembles allow us to estimate finite volume effects. All simulations for this investigation are performed on ensembles provided by the CLS Collaboration [131], including reweighting factors [132, 133], which for some configurations of the S400 ensemble were sign corrected [121, 130]. The ensembles used in this work have open boundary conditions in time direction except for B452 and B451, where antiperiodic boundary conditions are realized. The ensembles were generated using the tree level improved Lüscher-Weisz action and $n_f = 2 + 1$ non-perturbatively $\mathcal{O}(a)$-improved Sheikholeslami-Wohlert fermions, as discussed in Section 3.3. A brief overview of the pion masses and lattice spacings of the ensembles used in this work is given in Figure 6.1, details on all ensembles can be found in Table 6.1.

We use momentum smearing [174] with APE-smoothed gauge links [139] for both sources and sinks to improve the signal as introduced in Section 4.3.1. APE smoothing is iterated $n_{\mathrm{APE}} = 25$ times with $\alpha_{\mathrm{APE}} = 2.5$. Momentum smearing is performed using $b =$

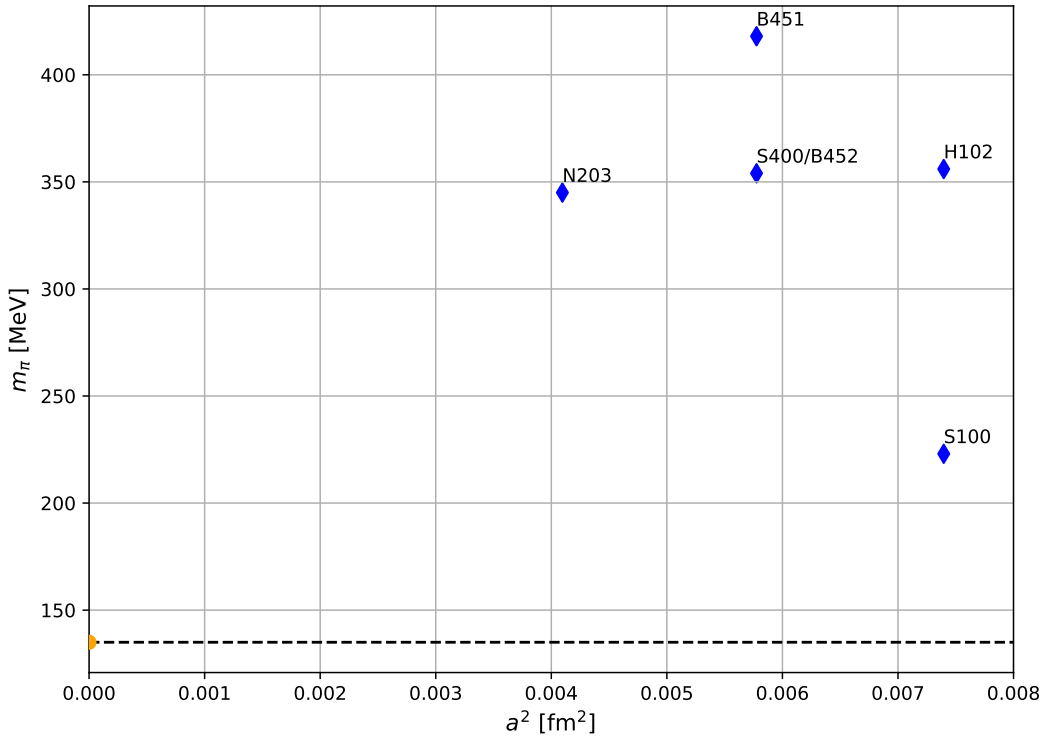



**Figure 6.1:** Lattice spacing and pion masses of the CLS ensembles used in this work (blue diamonds) compared to the physical pion mass (dashed line) and the physical point (orange circle in the bottom left corner).

| id | $\beta$ | $a$[fm] | $L^3 \times T$ | $\kappa_l$ | $\kappa_s$ | $m_{\pi,K}$[MeV] | $m_\pi L$ | $La$ [fm] |
|---|---|---|---|---|---|---|---|---|
| H102 | 3.4 | 0.085 | $32^3 \times 96$ | 0.136865 | 0.136549339 | 354, 442 | 4.89 | 2.72 |
| S100 | 3.4 | 0.085 | $32^3 \times 128$ | 0.137030 | 0.136222041 | 214, 476 | 2.95 | 2.72 |
| S400 | 3.46 | 0.075 | $32^3 \times 128$ | 0.136984 | 0.136702387 | 354, 445 | 4.33 | 2.41 |
| B452 | 3.46 | 0.075 | $32^3 \times 64$ | 0.1370455 | 0.136378044 | 352, 548 | 4.31 | 2.41 |
| B451 | 3.46 | 0.075 | $32^3 \times 64$ | 0.136981435679729 | 0.136408545268417 | 422, 577 | 5.16 | 2.41 |
| N203 | 3.55 | 0.064 | $48^3 \times 128$ | 0.137080 | 0.136840284 | 348, 445 | 5.39 | 3.06 |

**Table 6.1:** Details of the CLS ensembles used in this work [173].

0.45 and $\epsilon = 0.25$ at different iterations $n_{\text{mom}}$, accounting for different lattice spacings and pion masses, see Table 6.3. The Wick contractions are evaluated as discussed in Section 4.5. The matrix elements and invariant functions extraction are detailed in Section 4.6. The number of configurations and separation times used in this work are presented in Table 6.2. All simulations for DPDs in this work have been performed using the Chroma software package [175].

The renormalization constants for all operators and ensembles analyzed in this work are shown in Table 6.4, extracted from table XXIX in Ref. [154].

| id | $t_{\mathrm{sep}}[a]$ | $t_{\mathrm{sep}}$[fm] | #cnfgs. used |
|---|---|---|---|
| H102 | 12 | 1.020 | 990 |
| S100 | 8 | 0.68 | 890 |
| | 10 | 0.850 | 890 |
| | 12 | 1.02 | 890 |
| S400 | 11 | 0.825 | 100 |
| | 13 | 0.975 | 1000 |
| | 16 | 1.2 | 500 |
| B451/B452 | 13 | 0.975 | 750 |
| N203 | 16 | 1.024 | 300 |

**Table 6.2:** Summary of ensembles, source-sink separations and number of configurations used for the investigation of the lattice spacing and mass dependence at momentum $\vec{p} = \vec{0}$. The results of the calculations on the H102 ensemble were already published in [31] and [176].

| | H102 | S100 | S400 | B451 | B452 | N203 |
|---|---|---|---|---|---|---|
| $n_{\mathrm{mom}}$ | 250 | 350 | 310 | 270 | 310 | 445 |

**Table 6.3:** Number of momentum smearing iterations $n_{\mathrm{mom}}$ per CLS ensemble.

| | $\beta = 3.40$ | $\beta = 3.46$ | $\beta = 3.55$ |
|---|---|---|---|
| $Z_V$ | 0.7115(5)(15) | 0.7206(2)(13) | 0.7327(3)(9) |
| $Z_A$ | 0.7510(4)(14) | 0.7580(3)(13) | 0.7683(4)(9) |
| $Z_T$ | 0.8294(4)(26) | 0.8429(2)(27) | 0.8619(3)(27) |

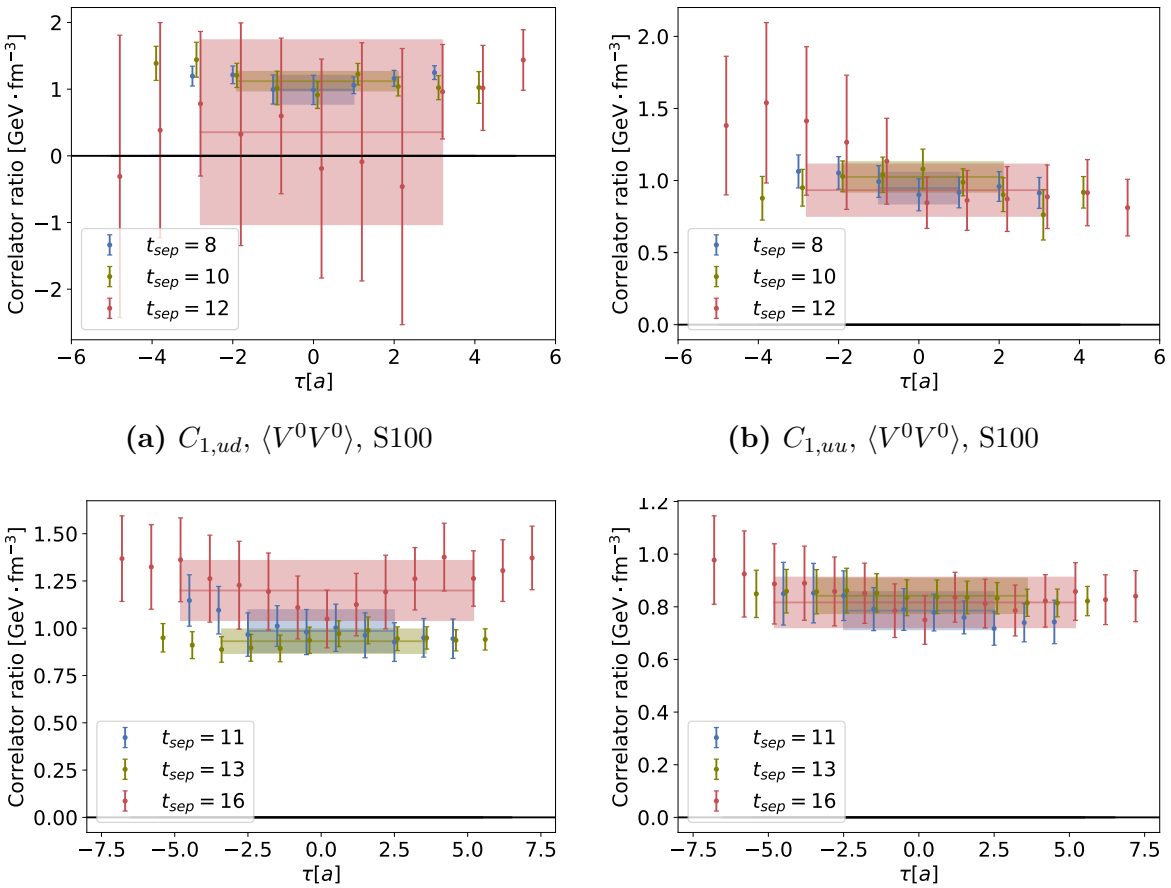
**Table 6.4:** Renormalization constants for the local currents on the ensembles used in the analysis at the renormalization scale $\mu = 2$ GeV [154] (table XXIX therein). For the analysis of the mass dependence, only the center column is required.

## 6.2 Excited state analysis

Before extracting the matrix elements according to eq. (4.38), we examine the plateau behavior of the correlators (4.36) to assess potential excited-state contamination as well as signal strength and quality. Due to computation time limits, the only four-point contractions calculated for all intermediate insertion timeslices are the $C_1$ graphs, which we analyze in the following.

To evaluate the validity and stability of the extraction, the calculations are repeated at different source-sink separations for the S400 and S100 ensembles, details given in table 6.2.

The results are shown in Figure 6.2, where we show the ratios $R_{4\mathrm{pt}}$ to compare the




**(a)** $C_{1,ud}$, $\langle V^0 V^0 \rangle$, S100

**(b)** $C_{1,uu}$, $\langle V^0 V^0 \rangle$, S100

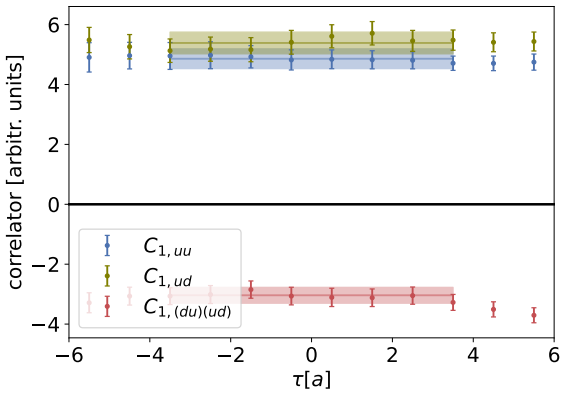
**(c)** $C_{1,ud}$, $\langle V^0 V^0 \rangle$, S400

**(d)** $C_{1,uu}$, $\langle V^0 V^0 \rangle$, S400

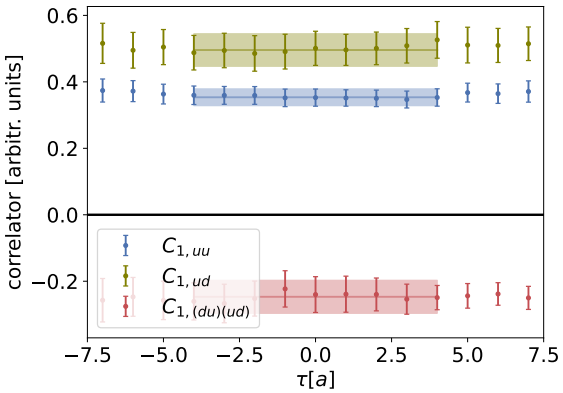
**Figure 6.2:** Plateaus for the $C_{1,ud}$ (left column) and $C_{1,uu}$ (right column) correlators on S100 (top row) and S400 (bottom row). All matrix elements are evaluated at $\vec{y} = (3,3,3)a$ and $\vec{p} = (0,0,0)$.

results of different separation times. Only the data at $\vec{y} = (3,3,3)a$ with zero momentum are shown. We find that the plateaus obtained at different separations are consistent with each other within the statistical uncertainties. This implies that contamination by excited states is moderate. We thus extract the matrix elements by fitting a constant to the data around the central region in $\tau$ (4.77). The differences in statistical precision arise from both the varying separation times and, in the case of S400, the different numbers of configurations analyzed as listed in table 6.2. We attribute the irregular shape present in the data with $t_{\text{sep}} = 11$ to the considerably decreased statistics, while the increasing errors at large $t_{\text{sep}}$ are due to a decreasing SNR at larger timescales. In the following analysis, we focus on the data for $t = 10a$ (S100) or $t = 13a$ (S400), respectively, where we obtain a reasonable SNR, while excited state contamination is expected to be under control. For the ensembles B451, B452 and N203, all calculations are performed at only one separation time close to 1 fm, details can be found in table 6.2.

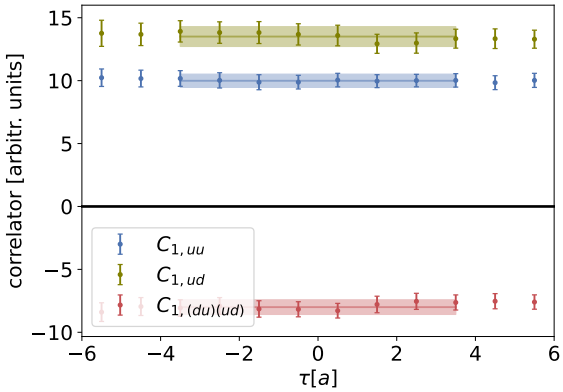
Figure 6.3 depicts the plateaus for the $C_1$ correlators for the $V^0V^0$ matrix element on the ensembles newly analyzed for this work. For the $V^0V^0$ channel, we observe plateaus extending over all insertion times. While the data for the other matrix elements is noisier than in the case of $V^0V^0$, we find no definite curvature in any of them either. We exclude points near the source and sink where residual excited-state effects may persist for added robustness of the extraction.



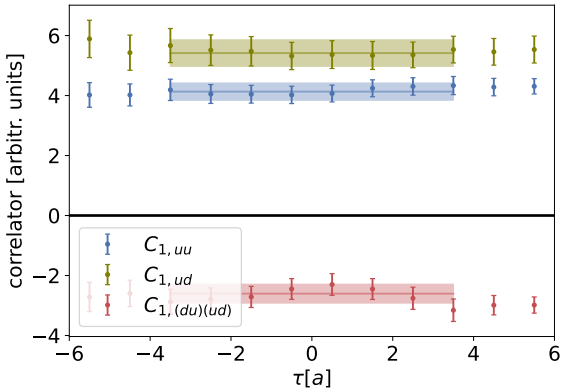

**(a)** S400, $\langle V^0 V^0 \rangle$



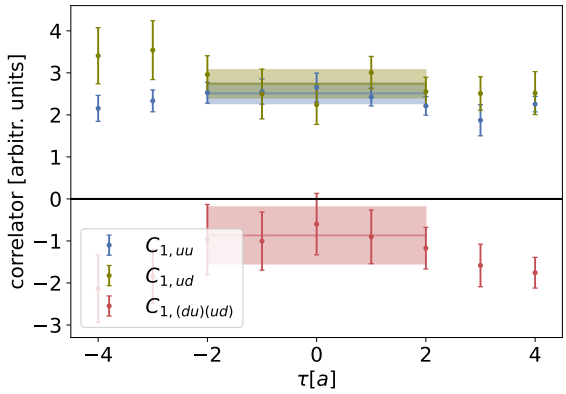

**(b)** N203, $\langle V^0 V^0 \rangle$




**(c)** B451, $\langle V^0 V^0 \rangle$




**(d)** B452, $\langle V^0 V^0 \rangle$




**(e)** S100, $\langle V^0 V^0 \rangle$

**Figure 6.3:** Comparison of the $C_1$ plateaus at $\vec{y} = (3,3,3)a$ for the $\langle V^0 V^0 \rangle$ channel on the ensembles S400, N203, B451, B452 and S100 (from top left to bottom right). The best fit is presented as a straight line with errors, its extension indicating the subset of points used in the fit.

## 6.3 Lattice artifacts

As the target quantities of our investigation are Lorentz invariant functions, they depend only on Lorentz invariants, i.e. $y^2$ and $p \cdot y = \omega$. This allows us to average the matrix element over all separations $\vec{y}$ of identical $(\omega, y^2)$[1], provided that symmetry breaking effects due to discretization are small. In order to have these effects under control, we investigate our data for artifacts stemming from both discretization and finite volume.

### 6.3.1 Finite volume effects

To investigate our data for finite volume effects, we analyze the dependence of the matrix elements and invariant functions on the direction of the separation $\vec{y}$. Specifically, we consider the angle $\theta$ enclosed between the vector $\vec{y}$ and the closest spatial diagonal $\hat{n}$, i.e. $\cos(\theta) = \vec{y} \cdot \hat{n}/|\vec{y}|$. This has already been done in Ref. [31, 69, 176].

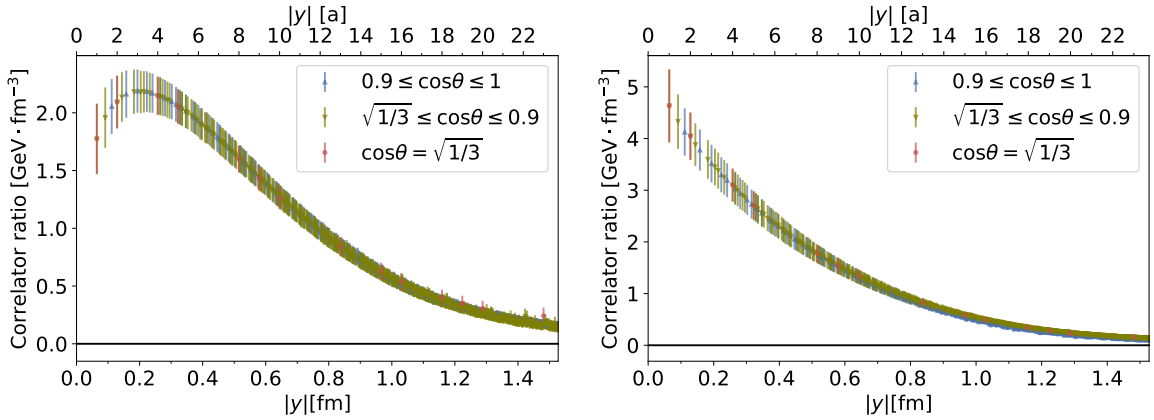
A set of rotationally invariant matrix elements obtained from the N203 ensemble is shown in Figure 6.4. In the case of N203, the $C_1$ contraction exhibits no significant anisotropy effects at large $|y|$. This is in contrast to the case of H102, where a saw tooth pattern is clearly observable in Figure 7 in Ref. [31]. In all cases, including H102 [31, 176], the $C_2$ contraction has a pronounced anisotropy at smaller $|\vec{y}|$, independent of lattice spacing and extension.

Figure 6.5 shows selected leading twist invariant functions of the $ud$ flavor combination, with the Lorentz decomposition being performed solely on data from the $C_1$ contraction at hadron momentum $\vec{p} = \vec{0}$. The anisotropy effects observed on the S400 ensembles are very similar to those found in Ref. [31] for H102 in all channels, exhibiting a clear saw tooth pattern at large separations $|\vec{y}|$. The ensembles S400 and H102 have smaller spatial extent and finite volume parameter than N203, see Table 6.1. For the N203 ensemble with $Lm_\pi = 5.39$ and $La = 3.06\,\mathrm{fm}$, finite volume effects are strongly suppressed, particularly in the vector-vector channel (first row). This can be explained by the increased distance between mirror images introduced by the periodic boundary conditions in space. Despite this, even on N203 residual finite volume effects remain, see e.g. Figure 6.5d, necessitating an exclusion of all points with $\cos\theta < 0.9$.

The same saw-tooth anisotropy pattern is also observed when comparing data obtained on the S100 and H102 ensembles, presented in Figure 6.6. Both ensembles have the same lattice spacing and spatial extension $La$, but the pion mass on S100 (214 MeV) is considerably smaller than on H102 (354 MeV), leading to their considerably different values of $Lm_\pi$.

Figure 6.7 highlights the diminishing signal-to-noise ratio of the invariant functions $A_{ud}$ and $A_{duud}$ at separations considerably larger than $La/2$. The apparent discrepancy between the olive and blue data points at large separation $|\vec{y}|$ and the deviation of the red data point at $|\vec{y}| = La/2$ clearly demonstrate the influence of finite volume effects. While the signal decays close to the lattice diagonal towards zero, it appears to reach a

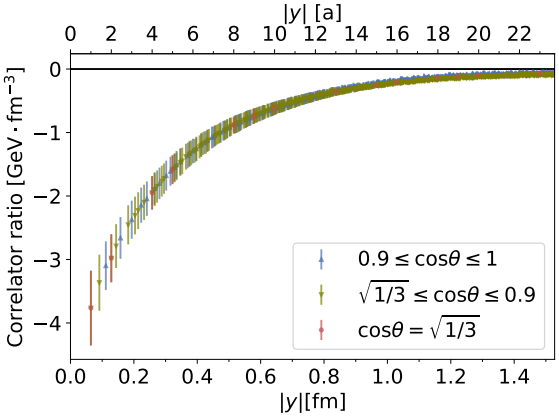
[1] For ease of writing, we henceforth write $y$ for the distance $\sqrt{-y^2} = |\vec{y}|$ when there is no risk of confusion.




**(a)** $\langle V_u^0 V_u^0 \rangle$ anisotropy for $C_{1,uuuu}$




**(b)** $\langle V_u^0 V_d^0 \rangle$ anisotropy for $C_{1,uudd}$

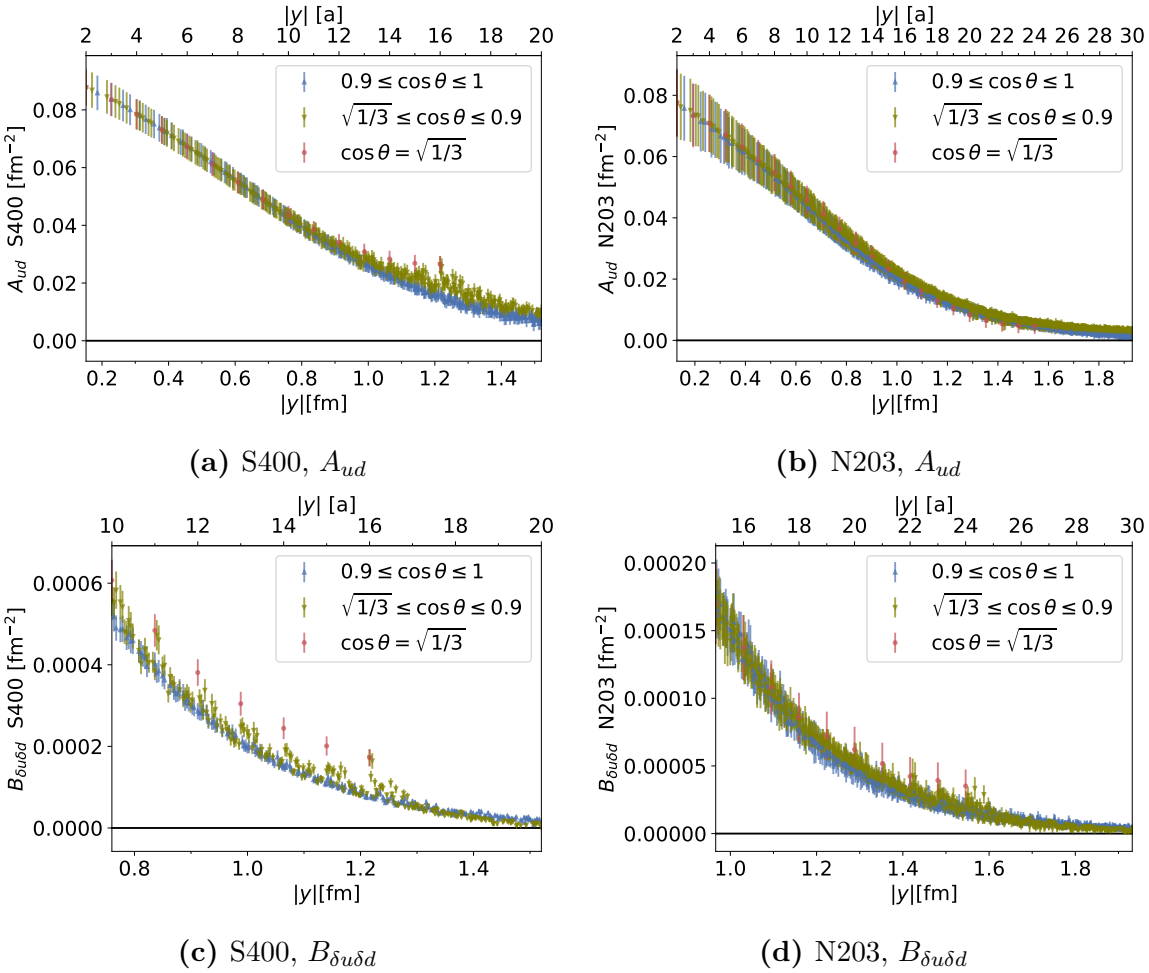



**(c)** $\langle V_{du}^0 V_{ud}^0 \rangle$ anisotropy for $C_{1,duud}$

**Figure 6.4:** Anisotropy for $\langle V^0 V^0 \rangle$ matrix elements from $C_1$ contractions on the N203 ensemble.

plateau and even arch slightly away from zero again when considering data closer to the lattice axis. The largest separation along these axes, the red data point at $|\vec{y}| = 16a$, exceeds the value of the data along the lattice diagonals by a factor of almost two. Both these observations prove the presence of considerable finite volume effects caused by mirror charges. The degradation of the signal quality and eventual end of the line of olive and red data points is due to the cones, defined by their respective angles enclosed with the lattice diagonals, gradually leaving the cubic volume of the lattice. This leads to a reduction in the number of points included in the Lorentz decomposition, increasing the error, until eventually, there are no more points left at the chosen separation and angles.

To account for this, we limit the region of included separations for our analysis to $|\vec{y}| \leq La/2$, i.e. the upper boundary of included separations is set at half the lattice extension in space. We close this subsection on finite volume effects with the conclusion that the two-current matrix elements required for our DPD analysis are affected by finite




**(a)** S400, $A_{ud}$

**(b)** N203, $A_{ud}$

**(c)** S400, $B_{\delta u \delta d}$

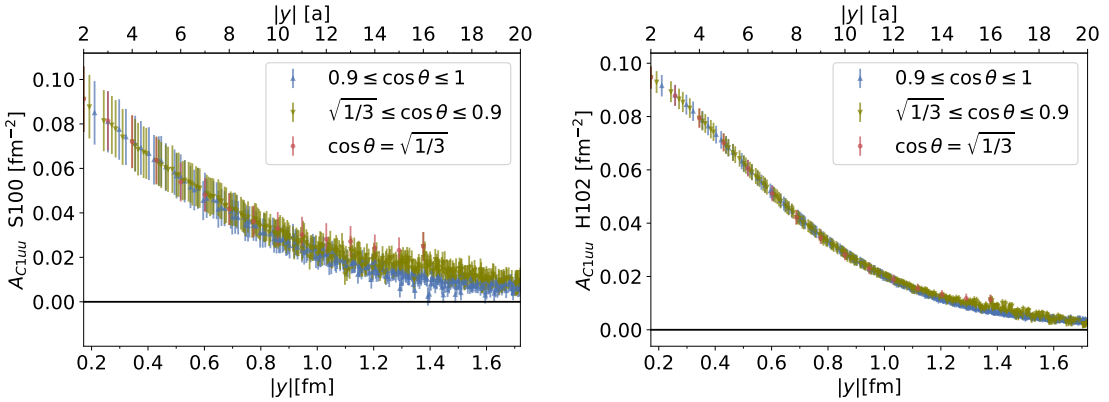
**(d)** N203, $B_{\delta u \delta d}$

**Figure 6.5:** Anisotropy comparison of $ud$ leading twist invariant functions $A$ and $B$ at $\vec{p} = \vec{0}$, only considering $C_1$ contraction contributions calculated on S400 (left column) and N203 (right column). $A$ for the vector-vector channel is shown in the top row, $B$ for the tensor-tensor channel is depicted in the bottom row. The included $|\vec{y}|$ [a] range has been adapted to the spatial geometry of the ensembles.

volume artifacts depending on $Lm_\pi$. In particular, this holds for the contraction $C_1$, which has a large contribution for long distances. Hence, finite volume effects should be considered carefully when taking physical limits. Similar findings have been published for the pion [177, 178].

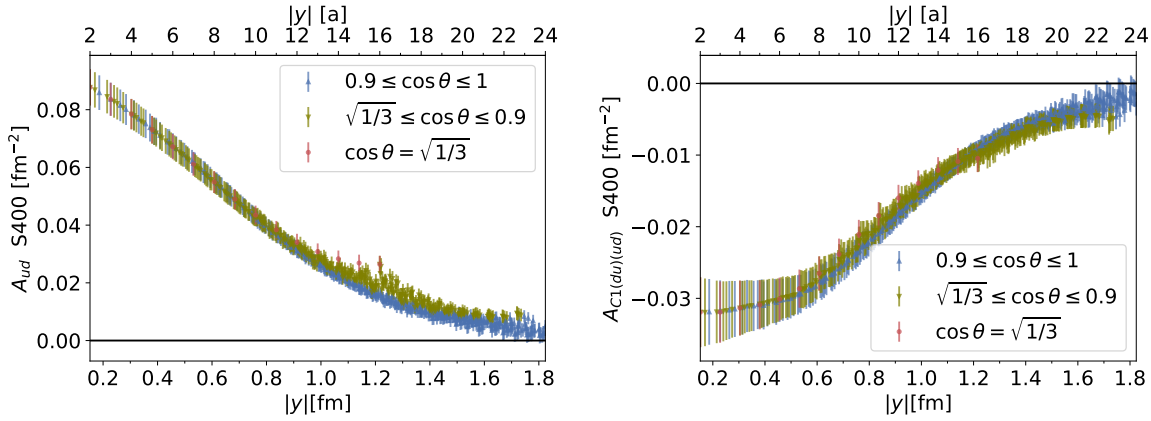
### 6.3.2 Discretization effects

We proceed in similar fashion to 6.3.1 for finite volume effects. The same selection of invariant functions presented in Figure 6.5 is shown here again for the $uu$ flavor combination, only taking into account data from the $C_2$ contraction in Figure 6.8. As can be observed there, the data shows a strong anisotropic behavior at very small




**(a)** S100, $Lm_\pi = 2.95$ **(b)** H102, $Lm_\pi = 4.89$

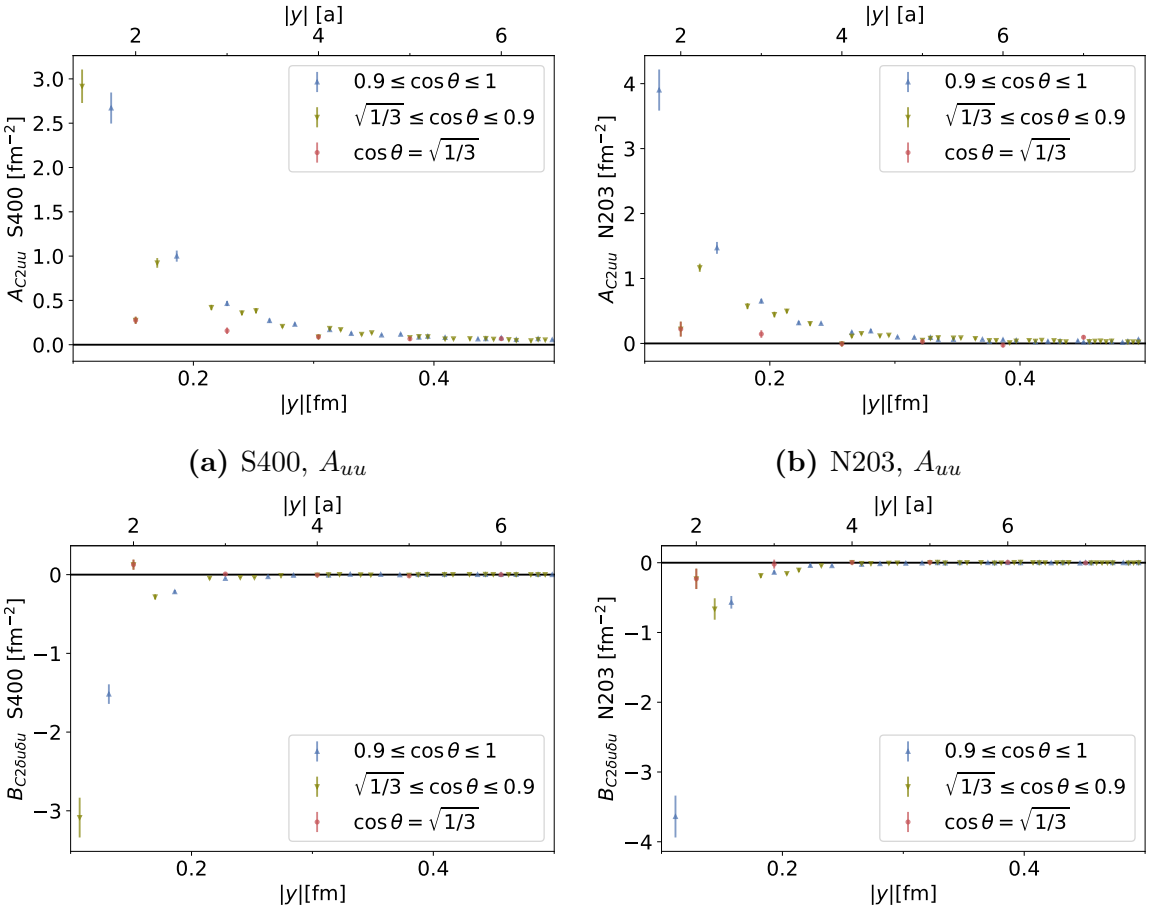
**Figure 6.6:** Comparison of invariant functions $A_{uu}$, considering only the $C_1$ contraction, on the S100 (left) and H102 (right) with separations $\vec{y}$ enclosing different angles $\theta$ with the diagonals.




**(a)** $A_{ud}$, $C_1$ **(b)** $A_{duud}$, $C_1$

**Figure 6.7:** Comparison of invariant functions $A_{ud}$ (left) and $A_{duud}$ (right) including separations $\vec{y}$ enclosing different angles $\theta$ with extended range towards the boundary. Data is obtained by computations on the S400 ensemble.

distances. This can be explained by discretization artifacts in the Dirac propagator for Wilson fermions. This has been discussed in e.g. [179, 180]. The contribution of the $C_2$ contraction decays very fast with increasing distance. We therefore expect finite volume effects to play a minor role. Indeed no evidence for finite volume effects can be found in Figure 6.8.




**(a)** S400, $A_{uu}$

**(b)** N203, $A_{uu}$

**(c)** S400, $B_{\delta u\delta u}$

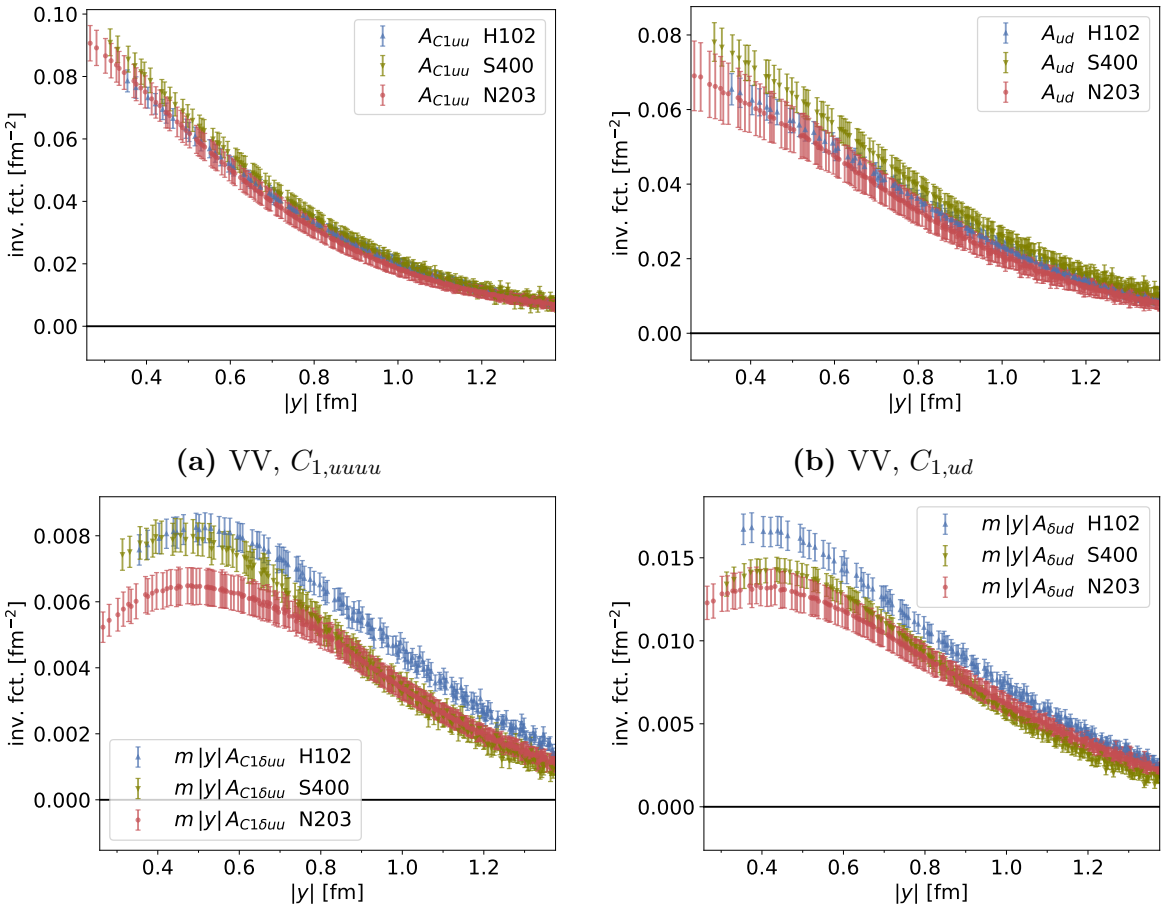
**(d)** N203, $B_{\delta u\delta u}$

**Figure 6.8:** Anisotropy comparison of $uu$ leading twist invariant functions $A$ and $B$ at $\vec{p} = \vec{0}$, only considering $C_2$ contraction contributions calculated on S400 (left column) and N203 (right column). $A$ for the vector-vector channel is shown in the top row, $B$ for the tensor-tensor channel is depicted in the bottom row. The limits of the physical distance $|y|$ [fm] have been kept constant across all four subfigures.

## 6.4 Lattice spacing dependence

In this section we investigate the lattice spacing dependence of the leading twist invariant functions. We adhere to the data selection criteria established in Section 6.3, namely that the angle $\theta$ enclosed by the separations $\vec{y}$ with the closest lattice diagonal has to fulfill $\cos\theta > 0.9$ and $4a \leq |\vec{y}| \leq La/2$. We thus account for discretization effects and finite volume artifacts discussed in the previous section. We will first discuss our findings for single contractions before considering the overall contribution for specific flavor combinations.

### 6.4.1 $C_1$ contributions



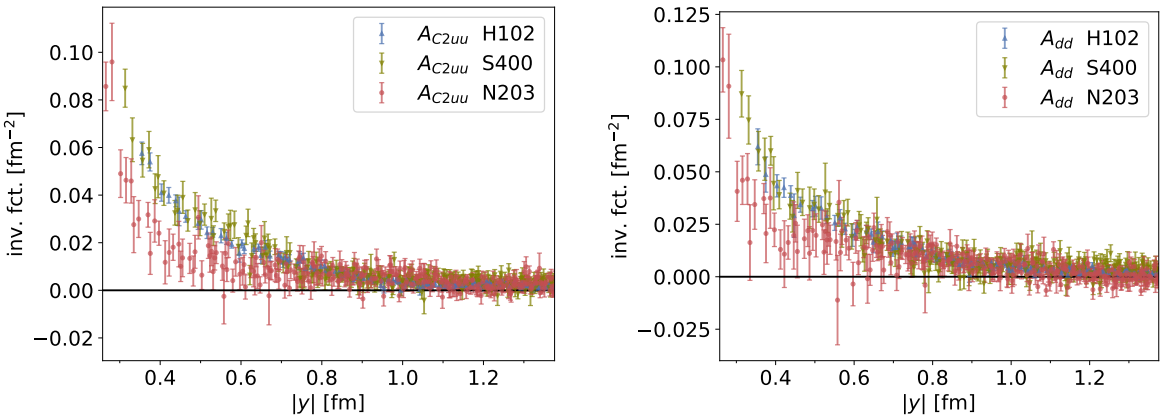

**(a)** VV, $C_{1,uuuu}$ **(b)** VV, $C_{1,ud}$

**(c)** TV, $C_{1,uuuu}$ **(d)** TV, $C_{1,ud}$

**Figure 6.9:** Leading twist invariant functions for selected channels. We plot the vector-vector (first row) and tensor-vector (second row) channels for the flavor combinations $C_{1,uuuu}$ (left column) and $C_{1,ud}$ (right column). Results are shown for the H102, S400, and N203 ensembles at $\vec{p} = (0, 0, 0)$ and $\cos\theta > 0.9$, only including data from the $C_1$ contraction.

Figure 6.9 shows a selection of invariant functions of leading twist based solely on data from $C_1$ contractions. The $A_{q\delta q'}$ signal is very similar to the one in $A_{\delta qq'}$ while the $A_{\Delta q\Delta q'}$ signal is primarily dominated by noise and thus not presented. We observe no clear $a$-dependence in the vector-vector and tensor-tensor channels, as data from the coarsest and finest ensembles studied coincide within $1\sigma$. In the tensor-vector channel, where we used (5.9) to enhance the signal in the $uu$ case, we observe a slight lattice spacing dependence.

### 6.4.2 $C_2$ contributions



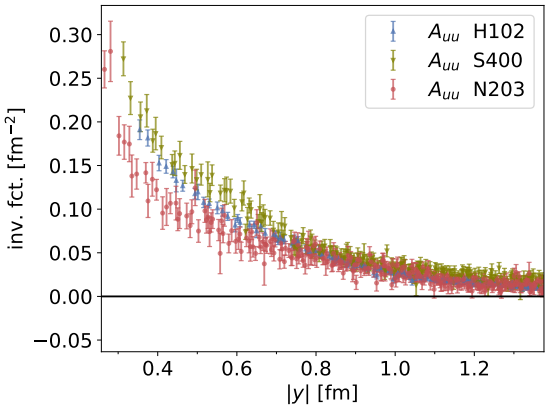

**(a)** VV, $C_{2u}$ **(b)** VV, $dd$

**Figure 6.10:** Leading twist invariant functions in the vector-vector channel for the flavor combinations $C_{2u}$ (left) and $dd$ (right). Results are shown for the H102, S400, and N203 ensembles at $\vec{p} = (0, 0, 0)$ and $\cos\theta > 0.9$.

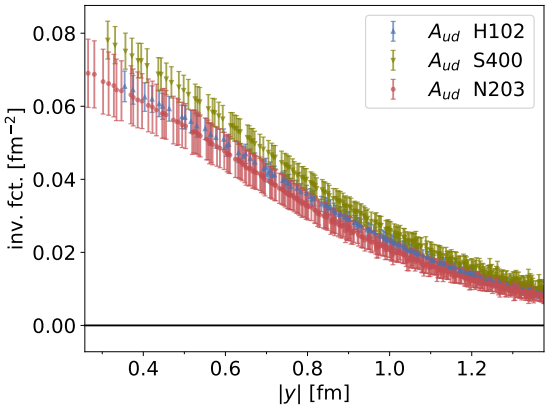
Similarly to the previous subsection, Figure 6.10 contains the flavor combinations $uu$ and $dd$, but obtained from data of $C_2$ contractions only. In the $A_{qq'}$ data, one can observe a dependence on the lattice spacing for small distances. For the finest lattice spacing $a = 0.064\,\text{fm}$, we find values smaller by up to around $2\sigma$ compared to the results obtained from our coarsest lattice with $a = 0.085\,\text{fm}$, in particular for $A_{C_{2u}}$ (Figure 6.10a) and $A_{C_2,dd}$ (Figure 6.10b). In the case of other channels, like $A_{C_2,\delta qq}$, the dependence on lattice spacing is less significant and uncertainties are larger, preventing a closer inspection.

### 6.4.3 Flavor specific combinations

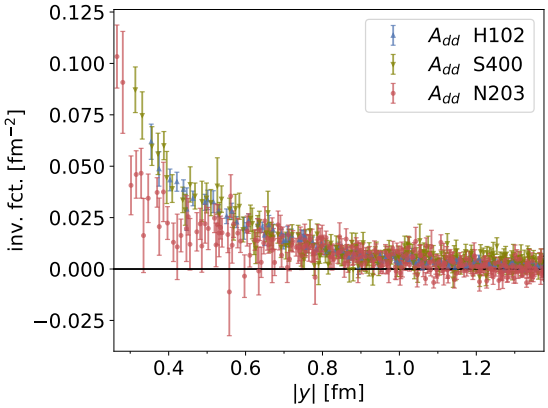
The resulting leading twist invariant functions $A_{qq'}$ obtained from physical data combinations are presented in Figure 6.11. The lattice spacing dependence of the $C_2$ contraction are well visible in Figure 6.11a for the $uu$ flavor combination. The $ud$ flavor combination in Figure 6.11b is the same as in the $C_1$ contraction only case. Likewise, the $dd$ combination has no $C_1$ contribution and is thus the same as in 6.10. The flavor interference combination $duud$ in Figure 6.11d exhibits no observable lattice spacing dependence within errors. It is unclear if the zero-crossing observed for H102 [32] remains after taking the continuum limit, since the larger statistical error prevents us from drawing any conclusions in this direction.



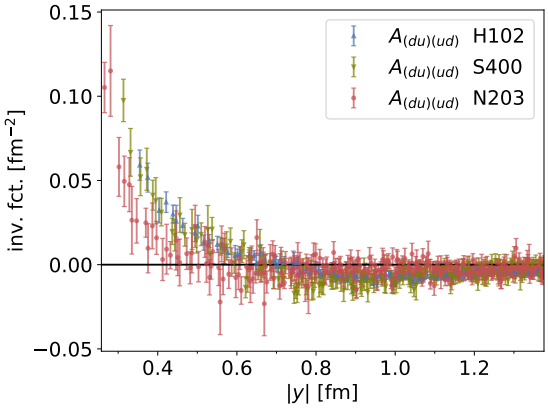

**(a)** VV, $uu$




**(b)** VV, $ud$




**(c)** VV, $dd$




**(d)** VV, $duud$

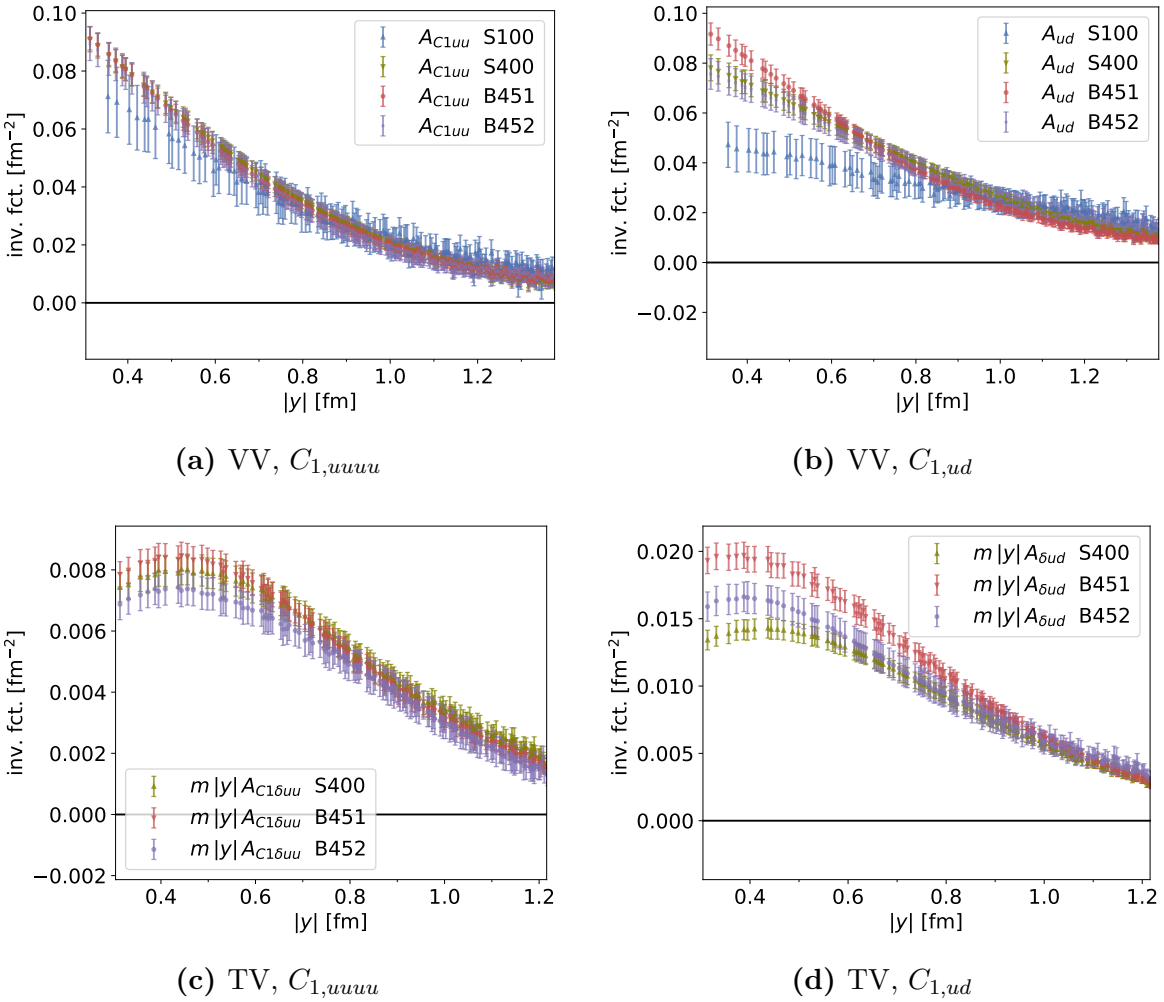
**Figure 6.11:** Leading twist invariant functions in the VV channel for the flavor combinations $uu$, $ud$, $dd$, and $duud$ (arranged left to right, top to bottom). Results are shown for the H102, S400, and N203 ensembles at $\vec{p} = (0, 0, 0)$ and $\cos\theta > 0.9$.

## 6.5 Mass dependence

In this section we investigate the meson mass dependence of the leading twist invariant functions. We adhere to the data selection criteria established in Section 6.3, namely that the angle $\theta$ enclosed by the separations with the closest lattice diagonal has to fulfill $\cos\theta > 0.9$ and $4a \leq |\vec{y}| \leq La/2$. Just as for the lattice spacing dependence, we will first discuss the results from single contractions. Finally, we give a comparison of all physical flavor combinations.

### 6.5.1 $C_1$ contributions

Figure 6.12 contains the leading twist invariant functions $A_{qq'}$ and $A_{\delta qq'}$ extracted from $C_1$ contraction data for all flavors. It is structured the same way as for the lattice




**(a)** VV, $C_{1,uuuu}$ **(b)** VV, $C_{1,ud}$

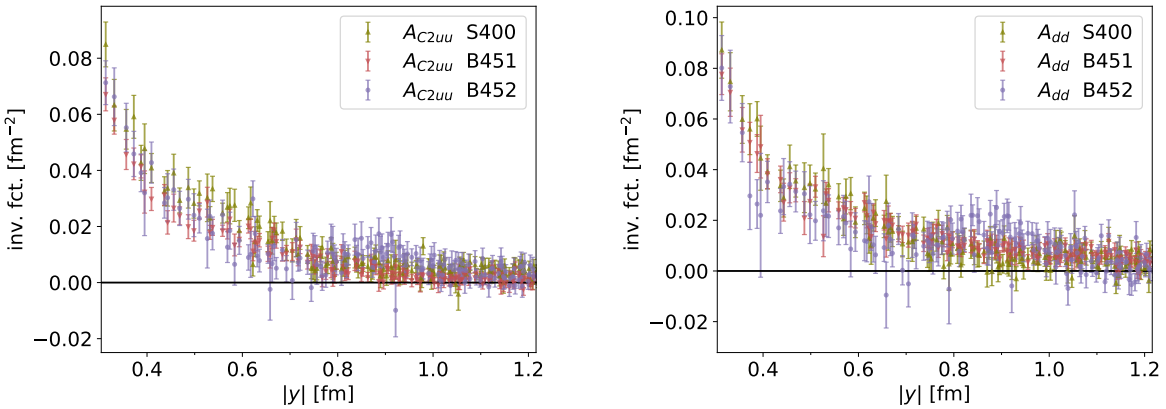
**(c)** TV, $C_{1,uuuu}$ **(d)** TV, $C_{1,ud}$

**Figure 6.12:** Leading twist invariant functions illustrating the mass dependence in the vector-vector (top row) and tensor-vector (bottom row) channel for the flavor combinations $C_{1,uuuu}$ (left column) and $C_{1,ud}$ (right column). Results are displayed at $\vec{p} = (0,0,0)$ and $\cos\theta > 0.9$, including only data from the $C_1$ contraction. The ensembles S100, S400, B451, and B452 are used to probe the pion-mass dependence. For the vector-vector channel, data from all four ensembles are shown, while for the tensor-vector channel, the comparison includes S400, B451, and B452.

spacing dependence case. For $A_{qq'}$ (first) row, data obtained from the S100 ensemble is presented additionally, where the pion mass is $m_\pi = 214\,\text{MeV}$. Notice that the lattice spacing of S100 is coarser than that of the other ensembles used in this plot. This is not an issue, since there is no significant dependence on the lattice spacing in the case of $A_{qq}$ (see section 6.4.1). While this widens the range of the mass dependence investigation, S100 sharing the same geometry with S400 and being of the same lattice spacing as H102 means it has a very small $Lm_\pi \approx 2.95$. As already discussed in Section 6.3.1, we expect finite volume effects to be larger in this case. We find a definite mass dependence in

multiple cases, e.g. in $A_{ud}$ (Figure 6.12b) and $A_{duud}$ (not shown), consistently following the trend of reducing the absolute value of the signal as the light quark masses decrease. This decrease is most prominent when comparing data of ensembles of different pion mass in descending order, here B451, S400 and S100. While the signals from the S400 and B452 data, which differ only in strange quark mass, agree in most cases, distinct differences $\approx 2\sigma$ can be observed in $A_{\delta ud}$ (Figure 6.12d) and $A_{\delta(du)ud}$ (not shown), hinting at potential sea quark effects. For the flavor combination $uu$, we find no mass dependence in any channel.

### 6.5.2 $C_2$ contributions



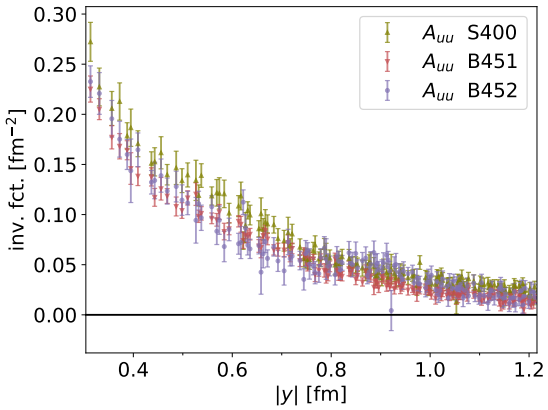

**(a)** VV, $C_{2u}$ **(b)** VV, $dd$

**Figure 6.13:** Leading twist invariant functions illustrating the mass dependence in the vector-vector channel for the flavor combinations $C_{2u}$ (left) and $dd$ (right). Results are displayed for the S400, B451, and B452 ensembles at $\vec{p} = (0, 0, 0)$ and $\cos\theta > 0.9$.

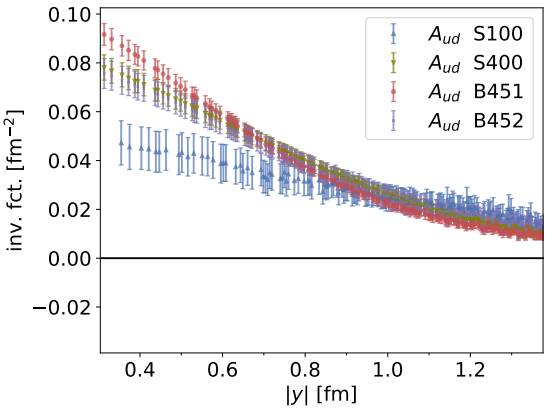
The leading twist invariant functions for the vector-vector, tensor-vector and vector-tensor channel extracted form $C_2$ contraction exhibit no mass dependence in any channel. As an example, $A_{qq'}$ is depicted in Figure 6.13. As in the lattice spacing case, $A_{\Delta q \Delta q'}$ and $A_{\delta q \delta q'}$ data is too beset with noise as to lead to any sensible conclusions and is thus excluded.

### 6.5.3 Flavor specific combinations

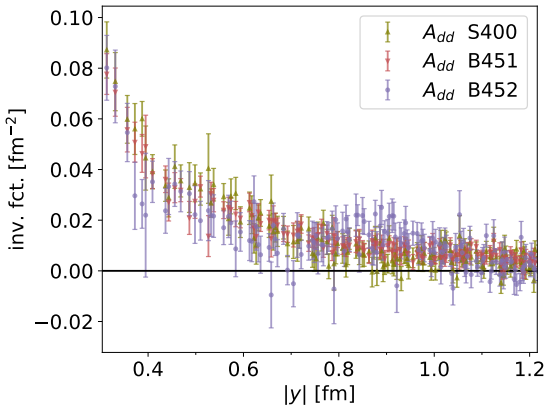
The resulting leading twist invariant functions $A_{qq'}$ obtained from physical data combinations are presented in Figure 6.14. The $uu$ and $dd$ combinations exhibit no observable mass dependence. The $ud$ flavor combination data is the same as in Figure 6.12b, as it contains no $C_2$ contribution, exhibiting a clear mass dependence. All other combinations include contributions from $C_2$ contractions, which exhibit a definite $a$-dependence, thus the S100 data is not included in their comparison. We find no evidence for mass dependence in any channel for the combinations $uu$, $dd$ and $duud$.



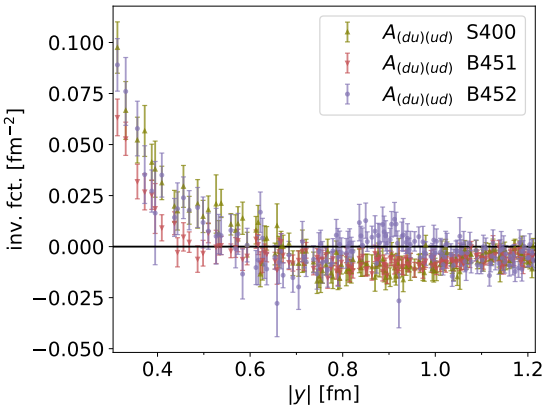

**(a)** VV, $uu$




**(b)** VV, $ud$




**(c)** VV, $dd$




**(d)** VV, $duud$

**Figure 6.14:** Leading twist invariant functions illustrating the mass dependence in the VV channel for the flavor combinations $uu$, $ud$, $dd$, and $duud$ (arranged left to right, top to bottom). Results are shown at $\vec{p} = (0, 0, 0)$ and $\cos\theta > 0.9$. For $uu$, $dd$, and $duud$ the ensembles S400, B451, and B452 are included, while for the $ud$ case additional data from the S100 ensemble are shown.

# 7 Invariant functions of DPDs at $\omega \neq 0$

Calculating the lowest Mellin moment of DPDs requires us to integrate the invariant functions w.r.t. $\omega$. As the $\omega$-range accessible on the lattice is limited, it is necessary to extrapolate the invariant functions towards infinity to evaluate the integral. In Ref. [31], the limit $\zeta = 0$ was used to extract this information out of the lowest Mellin moment of skewed DPDs (5.27) by assuming a simple functional form for the $\zeta$ dependence and determining its parameters by fits to the lattice data.

In this chapter, most of which was already published in Ref. [69], we take a closer look at this approach, considering a broader range of physically motivated ansätze for the $\zeta$ dependence and investigating the corresponding fit results. Using several models, we study the impact of this model dependence on extracting moments of double parton distributions from existing lattice data that have been generated in the context of Ref. [155]. The author of this thesis is one of the lead authors of Ref. [69], from which this chapter is reproduced. They performed the numerical analysis of the lattice data and developed two alternative ansätze. The physically motivated integral model was originally thought of by Markus Diehl, with Oskar Grocholski performing unpublished pilot work.

## 7.1 Lattice setup

The simulation includes 990 configurations of the H102 ensemble provided by the CLS Collaboration as discussed in Section 6.1[1], where we also give an overview of the techniques used in the calculation of the results.

The renormalization factor for the vector current has been determined in [183] and can be found in table XXIX therein. For $\beta = 3.4$ it is equal to $Z_V = 0.7115$.

In this chapter, we limit ourselves to the matrix element for the flavor combination $ud$. The other two combinations, $uu$ and $dd$, include the $C_2$ graph, which involves a propagator connecting the two current insertions and has considerably larger statistical errors than $C_1$. This would reduce the stability of the fits we will perform. With the lattice data we have at hand, we therefore refrain from performing fits for the equal-flavor combinations.

Again, we neglect the disconnected contributions for the same reasons as in Chapter 6.

[1] We take $a = 0.0856\,\text{fm}$ for the lattice size in order to be consistent with our previous study [155]. More recent determinations [181, 182] differ from this value by up to 1%, which is of no practical relevance in the present context.

| $\vec{P}$ | $\lvert\vec{p}\rvert$[GeV] | $(t_{\mathrm{snk}} - t_{\mathrm{src}})[a]$ |
|---|---|---|
| $(0,0,0)$ | 0 | 12 |
| $(-1,-1,-1)$ | 0.78 | 10 |
| $(-2,-2,-2),\ (2,2,-2),\ (2,-2,2),\ (-2,2,2)$ | 1.57 | 10 |

**Table 7.1:** Summary of momenta and source-sink separations in our lattice data.

The invariant functions were obtained as discussed in Section 5.1.3 and the results investigated for discretization and finite size artifacts as in Chapter 6. In addition, we tested for a dependence on the size of the proton momentum (frame dependence) when $y$ and $\omega$ were kept fixed. It was found in Ref. [155] that lattice artifacts were smallest for $\vec{y}$ close to the space diagonals of the lattice, limiting data extraction to distance vectors for which the angle $\theta$ between $\vec{y}$ and the nearest lattice diagonal satisfies

$$\cos\theta > 0.9\,, \tag{7.1}$$

just as we found in 6. To maximize the reach in $\omega$, the proton momenta were aligned with the lattice diagonals, see Table 7.1, where $\vec{p} = \frac{2\pi}{La}\vec{P}$.

To limit discretization and finite size effects, we will consider data only in the region.

$$4a \leq y \leq 16a\,, \tag{7.2}$$

which in physical units approximately corresponds to $0.34\,\mathrm{fm} < y < 1.37\,\mathrm{fm}$. The upper limit on $y$ corresponds to half the lattice size. It is not too relevant in the sense that for $y$ close to $16a$ statistical uncertainties become rather large, so that this region has little impact on our fits.

## 7.2 Modeling the lowest Mellin moment

Our strategy for evaluating Mellin moments $I_{q_1q_2}(\zeta, y^2)$ is to make a model (in the sense of an ansatz) for their functional dependence. For a given model the Fourier transform (5.29) can readily be evaluated. The parameters of the model are then fitted to the data on $A_{q_1a_2}(\omega, y^2)$, which have been extracted from our lattice simulations as described in the preceding section.

To obtain stable fits, we proceed in two steps. We first make an ansatz for the function

$$K_{q_1q_2}(y^2) = A_{q_1q_2}(\omega = 0, y^2) \tag{7.3}$$

and fit its parameters to the data for $\omega = 0$, which has by far the highest statistical precision because it includes the case of zero proton momentum. With this function

fixed, we perform fits to the normalized quantity

$$\hat{A}_{q_1q_2}(\omega, y^2) = \frac{A_{q_1q_2}(\omega, y^2)}{A_{q_1q_2}(0, y^2)} \tag{7.4}$$

with the numerator taken from the data and the denominator from the fit of (7.3).

### 7.2.1 Factorization of $I(\zeta, y^2)$

We assume that in the $y$ range specified in 7.2, i.e. $4a \leq |y| \leq 16a$ the $\zeta$ and $y$ dependence of $I(\zeta, y^2)$ factorizes as

$$I_{q_1q_2}(\zeta, y^2) = J_{q_1q_2}(\zeta)\, K_{q_1q_2}(y^2)\,, \tag{7.5}$$

where $K_{q_1q_2}$ is given in (7.3) and $J_{q_1q_2}$ is an even function of $\zeta$. Fourier transforming (7.5) w.r.t. $\zeta$ and comparing with (5.29), we obtain the relation

$$\frac{1}{2\pi}\int_{-1}^{1} \mathrm{d}\zeta\, e^{i\zeta\omega}\, J_{q_1q_2}(\zeta) = \hat{A}_{q_1q_2}(\omega)\,, \tag{7.6}$$

where $\hat{A}_{q_1q_2}$ defined in (7.4) is now $y$ independent. This implies the normalization condition

$$\int_{0}^{1} \mathrm{d}\zeta\, J_{q_1q_2}(\zeta) = \pi\,. \tag{7.7}$$

The different models used for the functional dependence of $J_{q_1q_2}$ are specified below.

We will validate the factorization hypothesis (7.5) by performing fits to (7.6) in narrow bins of $y$ and monitoring to which extent the functions $J_{q_1q_2}$ obtained in this way depend on $y$. Details are given in Section 7.3.2.

### 7.2.2 Dependence on the distance $y$

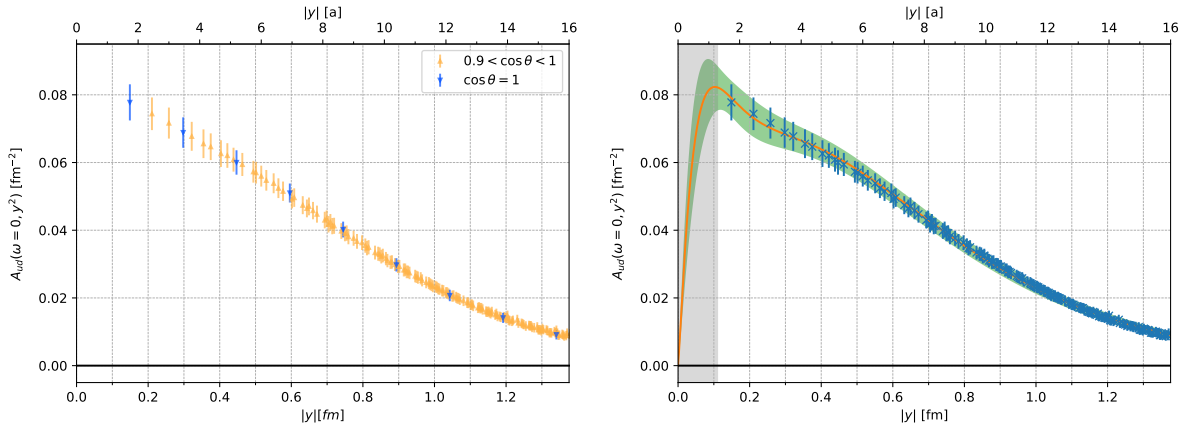
From now on we focus on the quark flavor combination $(q_1, q_2) = (ud)$ so that we may compare our results with (2.76). Our data for $A_{ud}(\omega = 0, y^2) = K_{ud}(y^2)$ is quite precise. Figure 7.1a shows that there is no systematic difference between data points with $0.9 < \cos\theta < 1$ and data points with $\cos\theta = 1$. This suggests that within the range $0.9 < \cos\theta$ of our data selection, possible anisotropy effects are smaller than statistical errors for this observable.

For the function $K_{ud}(y^2)$ we adapt the fit previously performed in [155], which has the form

$$K_{ud}(y^2) = A_1\,(\eta_1 y)^\delta\, e^{-\eta_1(y-4a)} + A_2\,(\eta_2 y)^\delta\, e^{-\eta_2(y-4a)} \qquad \text{for } \sqrt{3}a \leq y \leq 16a \tag{7.8}$$

with $\delta = 1.2$. The fitted parameters $A_i$ and $\eta_i$ are

$$A_1 = (3.49 \pm 2.37) \times 10^{-4}\ \mathrm{fm}^{-2}\,, \qquad A_2 = (5.14 \pm 0.04) \times 10^{-2}\ \mathrm{fm}^{-2}\,,$$




**(a)** **(b)**

**Figure 7.1:** Lattice data of the invariant function $A_{ud}$ for $\omega = 0$, together with the fit (7.8). The shaded region $y \leq 0.11\,\text{fm}$ is not used in our analysis.

$$\eta_1 = (17.6 \pm 2.8)\,\text{fm}^{-1}\,, \qquad \eta_2 = (3.53 \pm 0.03)\,\text{fm}^{-1}\,. \tag{7.9}$$

In Figure 7.1b we show the fit together with the data. We emphasize that the $y$ region where the function (7.8) increases with $y$ due to the factor $y^\delta$ is never used in our analysis.

At this stage we include data below $y = 4a$ for the following reason. In order to evaluate the number sum rule (2.76), we need values of $y$ down to $0.11\,\text{fm} \approx 1.29a$. Fitting the form (7.8) down to $y = 4a$ would entail a substantial extrapolation error at smaller $y$. By contrast, a fit down to $y = \sqrt{3}a \approx 1.73a$, which corresponds to the lattice points closest to the origin along the space diagonals, requires only moderate extrapolation.

Together with the factorization assumption (7.5), our fit of $K_{ud}$ relates $J_{ud}$ with the number sum rule as

$$S_{ud}(y_{\text{cut}}) = f(y_{\text{cut}})\, J_{ud}(\zeta = 0) \tag{7.10}$$

with

$$f(y_{\text{cut}}) = 2\pi \int_{y_{\text{cut}}}^{\infty} \text{d}y\, y\, K_{ud}(y^2) \approx 0.215\,, \tag{7.11}$$

where we take $y_{\text{cut}} = 0.11\,\text{fm}$ from (2.75).

The proportionality factor $f$ decreases by about 16% if we integrate over $y$ up to the upper limit $16a$ of our fit, rather than up to $\infty$. In turn, it decreases by about 11% if we integrate over $y$ from $4a$ to $\infty$. These numbers may be taken as upper limits (or very conservative estimates) for the uncertainty on $f$ due to $(i)$ extrapolating the fit (7.8) to

$y \geq 16a$, and due to $(ii)$ including the region $y \leq 4a$ where discretization effects in our data may be substantial. We also recall from Section 2.4.3 that the value of $y_{\text{cut}}$ in the sum rule integral itself is a matter of choice. Multiplying or dividing $y_{\text{cut}}$ by 2 changes the $f$ by less than 5%.

### 7.2.3 Dependence on the skewness $\zeta$

The main purpose of this work is to explore different forms for the dependence of Mellin moments on $\zeta$. We now present our models for this dependence.

For ease of notation, we assume that $|\zeta| \leq 1$ throughout this section, bearing in mind that $J_{q_1q_2}(\zeta)$ is zero for $|\zeta| > 1$. The Fourier transform of $J_{q_1q_2}$ is hence to be understood as in (5.29). We will also omit the quark flavor labels henceforth, given that we only perform fits for $(q_1q_2) = (ud)$ as explained above.

**The polynomial model** is what we used in our previous work [155]. For a given integer $N$ it is given by

$$J_{\text{poly}}(\zeta) = \pi \sum_{n,m=0}^{N} \zeta^{2n} \left(T^{-1}\right)_{nm} c_m \qquad \text{with } c_0 = 1\,, \tag{7.12}$$

where the $(N+1) \times (N+1)$ matrix $T$ is defined by

$$T_{mn} = 1\Big/(1 + 2n + 2m)\,. \tag{7.13}$$

The condition $c_0 = 1$ ensures the normalization condition (7.7), as shown in Section 4.4 of [155]. The model thus has $N$ free parameters, $c_1$ to $c_N$. The normalized Fourier transform of (7.12) reads

$$\hat{A}_{\text{poly}}(\omega) = \sum_{n,m=0}^{N} h_n(\omega) \left(T^{-1}\right)_{nm} c_m\,, \tag{7.14}$$

with the functions $h_n$ given by

$$h_n(\omega) = \frac{1}{2}\int_{-1}^{1} \mathrm{d}\zeta\, e^{i\zeta\omega}\, \zeta^{2n} = \sin(\omega)\, s_n(\omega) + \cos(\omega)\, c_n(\omega) \tag{7.15}$$

and

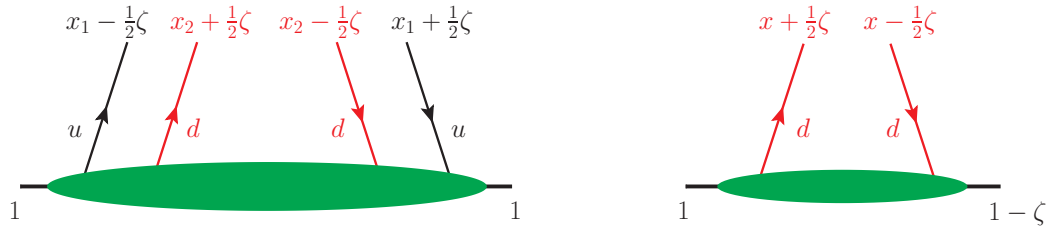
$$s_n(\omega) = \sum_{m=0}^{n} \frac{(-1)^m\,(2n)!}{(2n-2m)!}\,\frac{1}{\omega^{1+2m}}\,, \quad c_n(\omega) = \sum_{m=0}^{n-1} \frac{(-1)^m\,(2n)!}{(2n-2m-1)!}\,\frac{1}{\omega^{2+2m}}\,. \tag{7.16}$$

We note that the singular behavior of $s_n(\omega)$ and $c_n(\omega)$ for $\omega \to 0$ cancels in the combination (7.15), such that the function $h(\omega)$ is finite at $\omega = 0$, as is obvious from its integral representation.

in Ref. [155] we carried out fits with $N = 2$ and $N = 3$ and found their results to be quite close to each other. No clear improvement was observed in the description of the data for $N = 3$, and we regard that version as close to overfitting the data. In the present work we hence restrict ourselves to the case $N = 2$.

The polynomial model does not satisfy the properties we derived in Section 5.1.4: the form (7.12) does not vanish for $\zeta \to 1$ (unless one introduces an additional constraint on the polynomial coefficients), nor does it allow for a non-analytic behavior at $\zeta = 0$ or $\zeta = 1$.

When making this ansatz in our previous work, we had in mind the case of generalized single-parton distributions (GPDs).[2] Their Mellin moments *are* in fact polynomials in the skewness parameter $\zeta$, as a consequence of Lorentz invariance [42]. Moreover, they do not generally vanish for $\zeta \to 1$, which already follows from the fact that the lowest moments of quark GPDs are $\zeta$ independent. We note that the limit $\zeta \to 1$ is peculiar for GPDs, because for a given invariant momentum transfer $t$ it is always outside the physical region $-t \geq m_p^2 \zeta^2/(1-\zeta)$ in which the proton states are on shell. Despite the apparent similarity between the role of $\zeta$ in DPDs and GPDs (see Figure 7.2), the $\zeta$ dependence of these distributions and their Mellin moments is therefore very different.




**(a)** **(b)**

**Figure 7.2:** Comparison between a skewed DPD $F_{ud}\,(x_i, \zeta, y^2)$ in the region $x_i \pm \zeta/2 > 0$ (a) and a generalized (a.k.a. skewed) single-parton distribution (b). The notation in [184] uses the variable $X = x + \frac{1}{2}\zeta$ instead of $x$. All momentum fractions refer to the incoming proton.

The following three models are new and have been designed to fulfill the properties discussed in Section 5.1.4, i.e. they ensure $I \to 0$ for $\zeta \to 1$, and they allow for a nonanalytic behavior of $I$ at $\zeta = 0$ and $\zeta = 1$.

**The power-law model** is a rather direct generalization of the polynomial model, given by

$$J_{\text{pow}}(\zeta) = \pi(a+1)\left(1 - |\zeta|\right)^a \qquad \text{with } a > 0\,. \tag{7.17}$$

[2] The following statements hold for both for the skewness parameter $\zeta$ of Radyushkin [184] and for the parameter $\xi$ of Ji [42], given their relation $\xi = \zeta/(2-\zeta)$.

Its normalized Fourier transform reads

$$\hat{A}_{\text{pow}}(\omega) = {}_1F_2\left(1; \frac{a+2}{2}, \frac{a+3}{2}; -\frac{\omega^2}{4}\right), \tag{7.18}$$

where ${}_1F_2$ is the hypergeometric function.

The function (7.17) has a spike (i.e.ã discontinuous first derivative) at $\zeta = 0$ for all admissible values of $a$.

**The integral model** has the form

$$J_{\text{int}}(\zeta) = \pi \frac{\Gamma(a+b+1)}{\Gamma(a+1)\Gamma(b)} \int_{|\zeta|}^1 \mathrm{d}z\, z^{a-1}(1-z)^{b-1} \qquad \text{with } a > 0 \text{ and } b > 0\,, \tag{7.19}$$

and its normalized Fourier transform is given by

$$\hat{A}_{\text{int}}(\omega) = {}_2F_3\left(\frac{a+2}{2}, \frac{a+1}{2}; \frac{3}{2}, \frac{a+b+2}{2}, \frac{a+b+1}{2}; -\frac{\omega^2}{4}\right) \tag{7.20}$$

with the generalized hypergeometric function ${}_2F_3$. The ansatz (7.19) is inspired by the leading-order splitting formula for $g \to q\bar{q}$ in conjunction with a gluon PDF behaving as $f_g(z) \sim z^{-1+\alpha}(1-z)^\beta$ with $-1 < \alpha < 0$ without trying to emulate its detailed features, which are specific to $I_{qq}$ and not directly applicable to $I_{ud}$.

For $a \leq 1$ the function (7.19) has a spike at $\zeta = 0$, whereas for $a > 1$ it is smooth at that point (with a vanishing first derivative but possible discontinuities of higher odd derivatives).

**The cosine model** is inspired by the shape of the integral model, but allows for a more direct interpretation of the parameters. It is given by

$$J_{\cos}(\zeta) = \mathcal{N}_{a,b} \cos^b\left(\frac{\pi}{2}|\zeta|^a\right) \text{ with } a > 0 \text{ and } b > 0\,, \tag{7.21}$$

where $\mathcal{N}_{a,b}$ is determined by the normalization condition (7.7). We have not found a closed form for its Fourier transform, which is computed numerically in our fit to the lattice data. Important features of the function $J_{\cos}(\zeta)$ are:

- the parameter $a$ controls the width of the central maximum around $\zeta = 0$,
- the parameter $b$ controls the speed of approaching zero for $|\zeta| \to 1$,
- for $a \leq 1/2$ it has a spike at $\zeta = 0$ and is very sensitive to even small changes in $a$, whilst for $a > 1/2$ it is smooth at that point,
- for positive half integer $a$, the function is analytic at $\zeta = 0$.

## 7.3 Fit results

We now discuss the results of fitting the above models to our lattice data. We performed global fits to the data in the range

$$4a \leq y \leq 14a\,, \qquad -2.72\,y\big/(4a) \leq \omega \leq 2.72\,y\big/(4a)\,, \tag{7.22}$$

where the second condition follows from the bound (5.23) and from the range of proton momenta in our simulations. The highest value of $|\omega|$ in the data thus selected is about 9.5. Since statistical errors increase with the proton momentum *and* with the distance $y$ between the currents, the uncertainty on the data is smallest around $\omega = 0$ and grows rather quickly with $|\omega|$. We omit distances $y > 14a$ from the fit because some of the corresponding data points have very large errors.

The fitted data are shown in Figure 7.3. They are obtained by dividing the data for $A(\omega, y^2)$ in the range (7.22) by the function $K(y^2)$, which is evaluated with the fit specified in (7.8) and (7.9). The errors on the data points are obtained with the jackknife method.

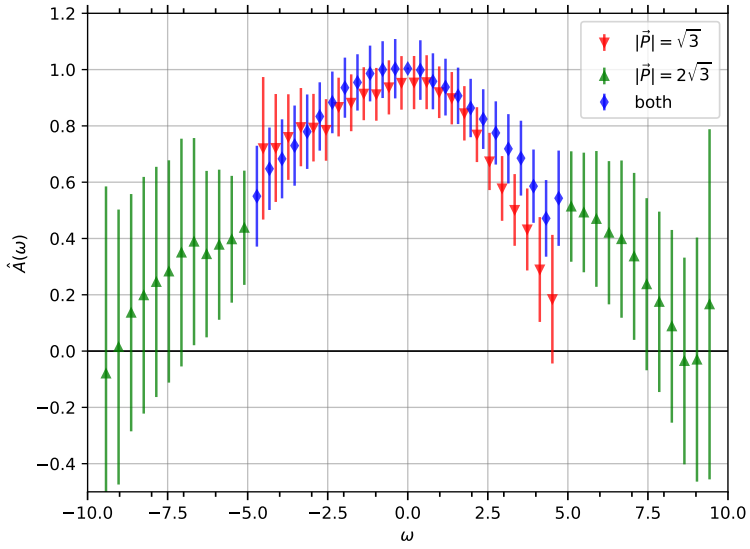



**Figure 7.3:** Data for the normalized invariant function $\hat{A}(\omega)$, obtained as described in the text. The different symbols and colors indicate whether a data point receives contributions from proton momenta with $|P| = \sqrt{3}$, $|P| = 2\sqrt{3}$, or from both.

Each data point in Figure 7.3 results from combining all pairs of $\vec{y}$ and $\vec{p}$ that give the same $\omega$. Even with this combination the result is still statistics limited, especially for larger values of $|\omega|$. Averaging only over pairs of $\vec{y}$ and $\vec{p}$ that are related by lattice symmetries would give points with yet larger statistical errors and not permit us to assess the size of lattice artifacts in the $\omega$ dependence.

| model | parameters | | $\chi^2$/ d.o.f. |
|---|---|---|---|
| polynomial | $c_1 = (9.84 \pm 4.41) \times 10^{-2}$ | $c_2 = (6.16 \pm 4.57) \times 10^{-2}$ | 0.38 |
| power-law | $a = 2.95 \pm 1.10$ | — | 0.36 |
| integral | $a = 0.37 \pm 2.83$ | $b = 2.04 \pm 3.97$ | 0.35 |
| integral | $a = 0.5$ fixed | $b = 1.23 \pm 1.84$ | 0.35 |
| integral | $a = 4$ fixed | $b = 7.36 \pm 2.67$ | 0.40 |
| cosine | $a = 0.29 \pm 1.14$ | $b = 1.92 \pm 3.33$ | 0.35 |
| cosine | $a = 1$ fixed | $b = 5.42 \pm 1.78$ | 0.38 |

**Table 7.2:** Fit results for our models of the $\zeta$ dependence. The low values of $\chi^2$/ d.o.f. are explained in the text. The models are specified in Section 7.2.3.

The figure shows that data points receiving only contributions from $|\vec{P}| = \sqrt{3}$ tend to deviate systematically from those with contributions from $|\vec{P}| = \sqrt{3}$ and $2\sqrt{3}$. We recall that we have only one momentum with $|\vec{P}| = \sqrt{3}$, whereas the data with $|\vec{P}| = 2\sqrt{3}$ includes four momenta and thus benefits from averaging over different spatial directions. We also note that time reversal (which flips the sign of $\vec{p}$ but not of $\vec{y}$) implies that the $\omega$ distribution must be symmetric, whilst the central values of the $|\vec{P}| = \sqrt{3}$ data are slightly asymmetric in $\omega$. We shall not investigate this issue further, because the observed deviations are not significant within statistical errors.

In Table 7.2 we list the results of the fits that will be discussed in the following. We note that the $\chi^2$ of the data was computed *without* taking into account the statistical correlations between data points at different $\omega$. This is because the corresponding correlation matrix is very close to singular, such that its inversion would be affected by severe instabilities. With correlations between data points being neglected, the resulting values of $\chi^2$ per degree of freedom are significantly below 1 in all our fits.

In the left panels of the following figures, we show the fits of $\hat{A}(\omega)$ with their error bands, together with the fitted data points. In the right panels of the same figures, we show the resulting value of $J(\zeta)$, multiplied by the factor $f$ from (7.11). We recall that, according to the number sum rule (2.76), one should have $fJ(\zeta = 0) = 2$ up to corrections of parametric order $\alpha_s^2$ or $(\Lambda y_{\rm cut})^2$.

### 7.3.1 Comparison of models

The fit results for the polynomial and the power-law model are shown in Figure 7.4. Both fits give a good description of the data. We note that at large $|\omega|$ they both yield rather narrow error bands compared with the errors on the data points. We observe that the two models behave rather differently in the $|\omega|$ region where we have no data (or data with huge errors), with pronounced oscillations occurring in the polynomial model.[3] In the Fourier conjugate space, these differences are reflected by pronounced differences between the fit results around $\zeta = 0$. Whereas the polynomial model is

[3]Such oscillations could be anticipated from the functional form in (7.15).

smooth at that point by construction, the power-law model exhibits a clear spike. At $|\zeta| \to 1$ the polynomial model results in a nonzero value of the Mellin moment, at least within $1\sigma$ uncertainties. Based on our arguments in Section 5.1.4, we hence disfavor this fitting ansatz on physical grounds.

Figure 7.5 shows that the two fits agree within their uncertainties for $\hat{A}$ up to $|\omega| \sim 7$. They yield similar results for the Mellin moment at intermediate $|\zeta|$ but differ qualitatively for $|\zeta|$ close to 0 or to 1. Already at this stage we can conclude that in $\zeta$ space the uncertainty bands of an individual fit can significantly misrepresent the actual uncertainty on the Mellin moment. At $\zeta = 0$, both fits are consistent with the sum rule value of 2, although for the power-law model this value is at the lower end of the uncertainty band.

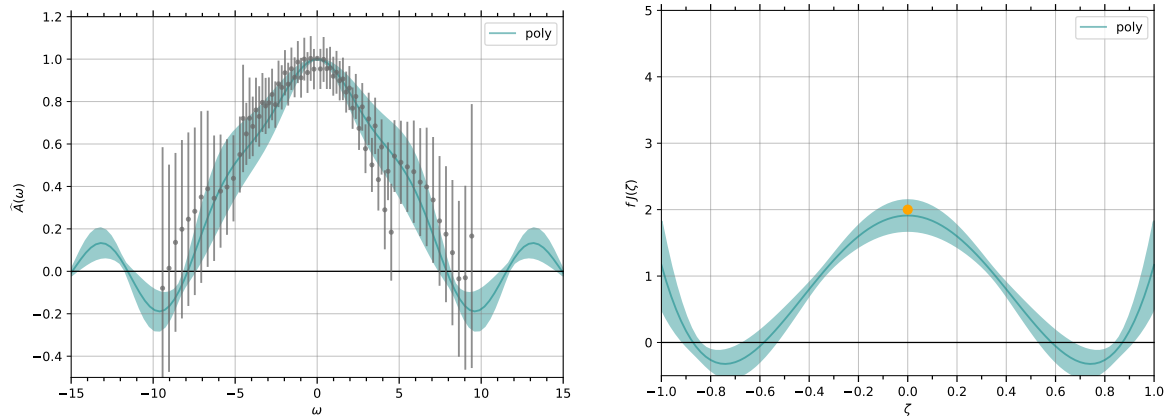
It is interesting to note that, broadly speaking, the two fits have error bands of similar size, both in $\omega$ and in $\zeta$ space, despite the fact that the polynomial model has two and the power-law model one free parameter. This shows that the amount of flexibility of the functional form is crucial for the behavior of the fit, at least with data of the quality we are working with.

The fit results for the integral and cosine models are shown separately in Figure 7.6 and together in Figure 7.7. Quite remarkably, both the central values and the error bands agree almost perfectly between the two fits, despite the apparent difference between the functional forms (7.19) and (7.21).

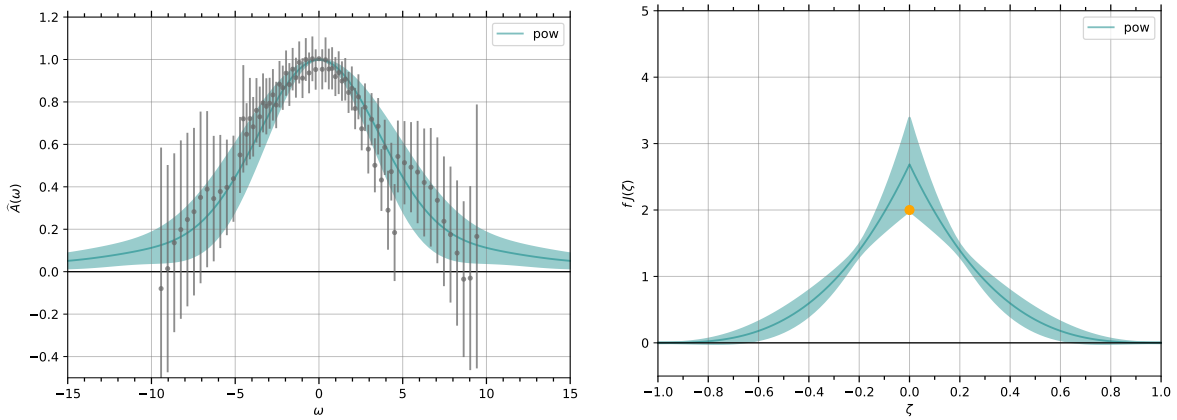
The fits describe the data well. Their error bands become broad at large $|\omega|$, at variance with the polynomial and power-law fits. Correspondingly, we find a *huge* uncertainty on the Mellin moment around $\zeta = 0$ in the right panels of Figure 7.6. If we accept that these fits adequately represent the uncertainty of our lattice data at large $|\omega|$, we must conclude that the data does not permit a reconstruction of the Mellin moments at the point $\zeta = 0$ without further theory input. Interestingly, the fit uncertainty on the Mellin moment is extremely large only in a narrow range $|\zeta| \lesssim 0.05$, whereas for larger skewness it is of moderate size.

**Constrained fits.** For the flavor combination $ud$ (but not for equal quark flavors) one may opt to *use* the number sum rule (2.76) as a theory input to the fit. To explore this option, we performed a series of fits to the integral and cosine models with their respective parameters $a$ fixed to a prior value. We find that the fit results for $fJ(\zeta = 0)$ are close to the sum rule value 2 if we impose $a = 4$ in the integral model (7.19) and $a = 1$ in the cosine model (7.21). In Table 7.2 we see that both constrained fits have a slightly higher $\chi^2$ than their two-parameter counterparts, but still provide a good description of the data. This is also seen in Figure 7.8a, which additionally shows that the two constrained fits are quite similar in their central values and error bands. The bands are significantly reduced with respect to the two-parameter fits, as is evident from the comparison with Figure 7.7.

For the integral model we also performed a constrained fit with fixed $a = 0.5$, which is close to the fitted value of $a$ in the two-parameter fit. The result is compared with the case $a = 4$ in Figure 7.8b. We see that the two fits differ noticeably at large $|\omega|$




**(a)** polynomial model




**(b)** power-law model

**Figure 7.4:** Fit results for the polynomial and power-law models. Left panels show the fit and data vs. Ioffe time $\omega$ and right panels show the fit results after a Fourier transformation to the skewness $\zeta$. The plots on the right are normalized such that the number sum rule requires the value 2 at $\zeta = 0$, which is indicated by an orange dot. Further explanations are given in the text.

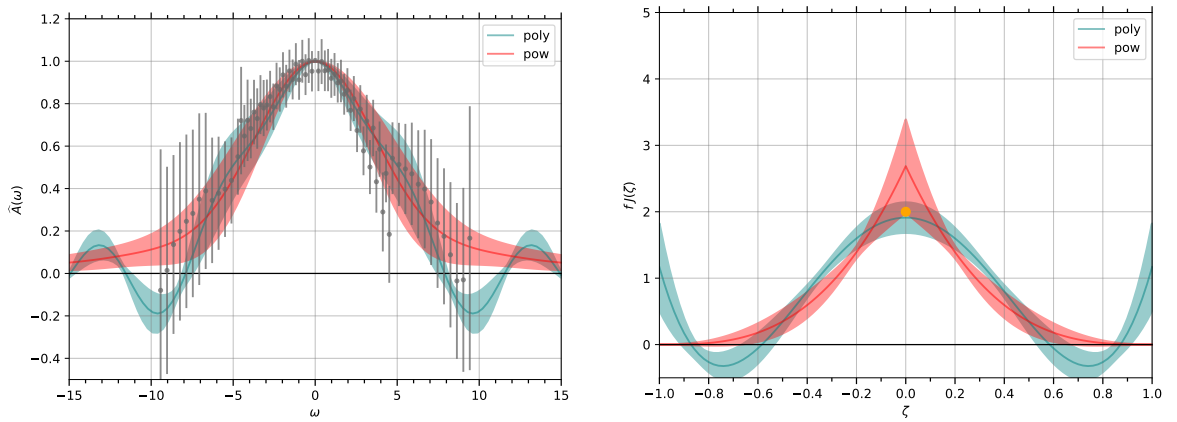
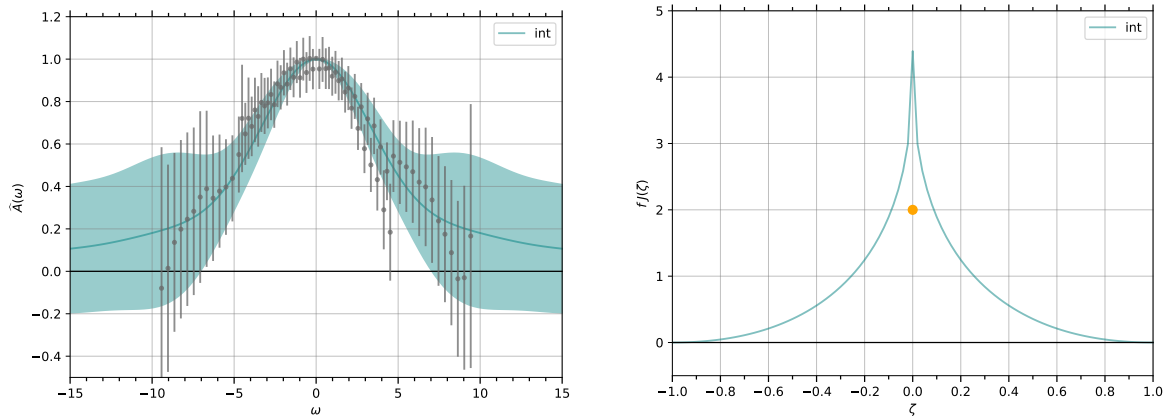
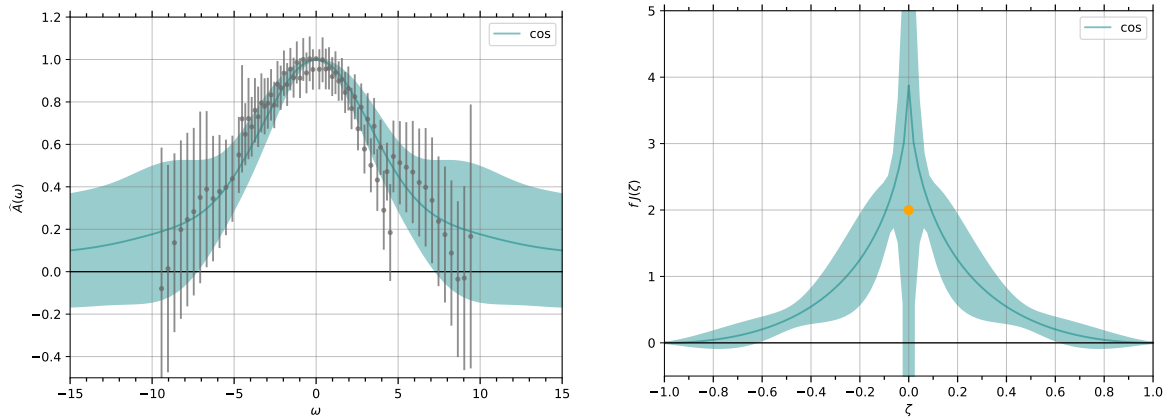



**Figure 7.5:** Comparison of the fit results shown in Figure 7.4. The polynomial model is shown in blue and the power-law model in red.




**(a)** integral model




**(b)** cosine model

**Figure 7.6:** As Figure 7.4, but for the integral and cosine models.

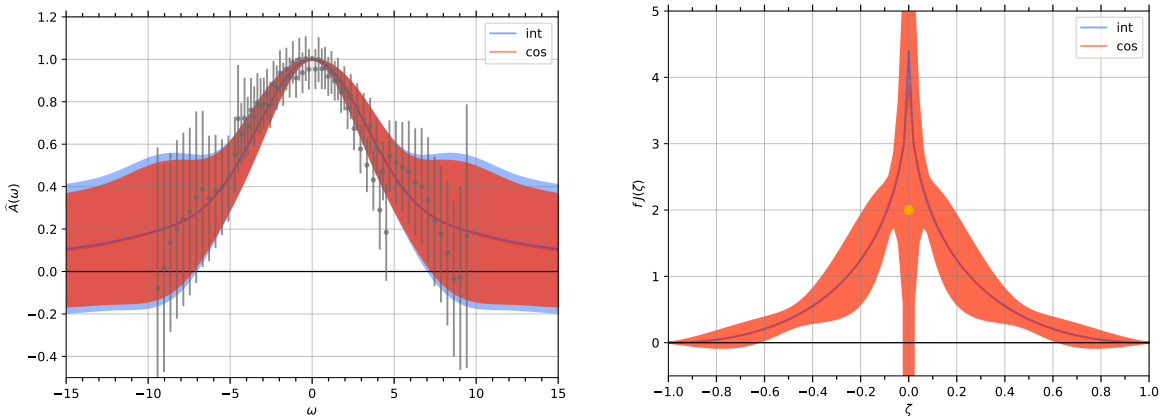
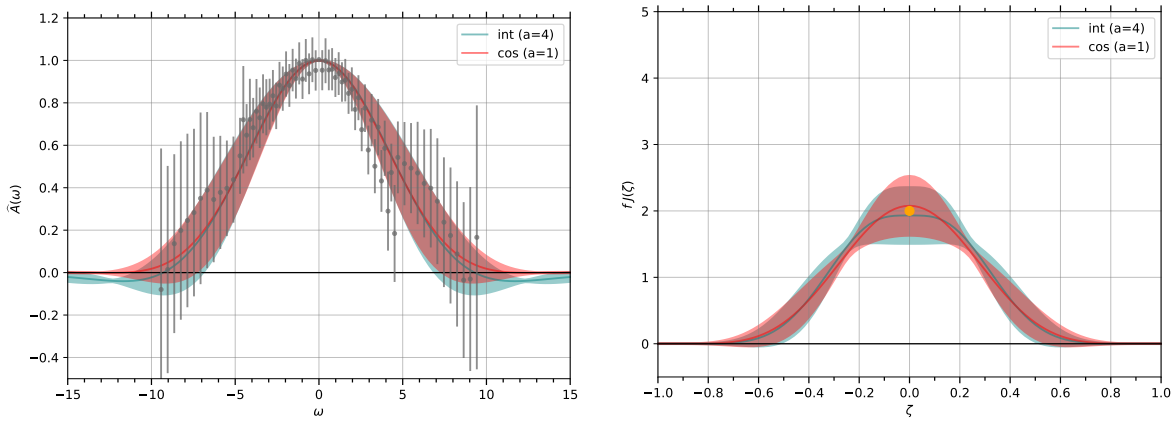
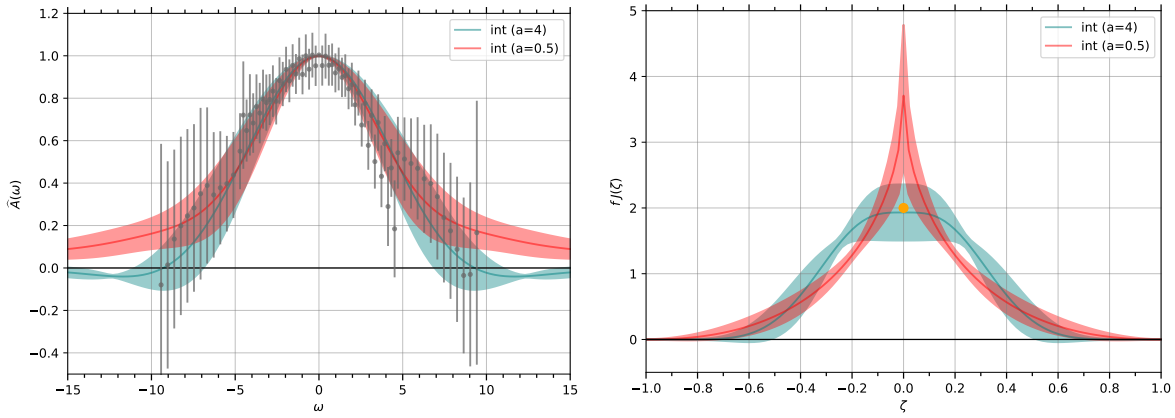



**Figure 7.7:** Comparison of the fit results shown in Figure 7.6. The blue and red curves for the central values are barely distinguishable.




**(a)** integral and cosine models with fixed $a$




**(b)** integral model with fixed $a$

**Figure 7.8:** As Figure 7.6, but for fits with one fixed and one free parameter.

| model | fixed params. | $S_{ud} = fJ_{ud}(\zeta = 0)$ | $100\langle\zeta^2\rangle$ | $\chi^2$ / d.o.f. |
|---|---|---|---|---|
| polynomial | — | 1.91 ± 0.22 | 9.67 ± 3.93 | 0.38 |
| power-law | — | 2.67 ± 0.70 | 6.84 ± 2.58 | 0.36 |
| integral | — | 4.4 ± 938.4 | 7.30 ± 3.14 | 0.35 |
| integral | $a = 0.5$ | 3.69 ± 1.06 | 7.14 ± 2.67 | 0.35 |
| integral | $a = 4$ | 1.92 ± 0.42 | 6.13 ± 2.36 | 0.40 |
| cosine | — | 3.9 ± 262.2 | 7.30 ± 3.08 | 0.35 |
| cosine | $a = 1$ | 2.07 ± 0.45 | 6.34 ± 2.49 | 0.38 |

**Table 7.3:** Results of the fits in Table 7.2 for the value $S_{ud}$ of the number sum rule and for the average value of $\zeta^2$ defined in (7.23).

and result in a quite different behavior of the Mellin moment for central values of $\zeta$. The fit with $a = 0.5$ has a spike at $\zeta = 0$ and misses the sum rule value within its $1\sigma$ uncertainties.

The results of our fits for the sum rule value $fJ(\zeta = 0)$ are collected in Table 7.3, where we see again the huge uncertainties on this value obtained with the two-parameter versions of the integral and cosine models.

Also shown in that table are the fit results for another quantity of physical interest, namely

$$\langle\zeta^2\rangle = \frac{\int_0^1 \mathrm{d}\zeta\ \zeta^2\, I(\zeta, y^2)}{\int_0^1 \mathrm{d}\zeta\ I(\zeta, y^2)} = -\frac{\partial^2}{\partial\omega^2}\,\hat{A}(\omega, y^2)\bigg|_{\omega=0}, \tag{7.23}$$

which may be interpreted as the average [4] value of $\zeta^2$. In general $\langle\zeta^2\rangle$ depends on the distance $y$, but this dependence is absent if we adopt the factorization hypothesis (7.5).

We see in the table that the results for $\langle\zeta^2\rangle$ agree within uncertainties for all our fits, much better than the results for the sum rule value $fJ(\zeta = 0)$. To understand this, we observe in Equation (7.23) that $\langle\zeta^2\rangle$ depends on the behavior of $\hat{A}(\omega, y^2)$ around $\omega = 0$, where our lattice data is quite precise. By contrast, the Mellin moment at $\zeta = 0$ corresponds an integral over all $\omega$ and is sensitive to $\hat{A}$ at large $\omega$, where the data becomes increasingly noisy or is missing altogether.

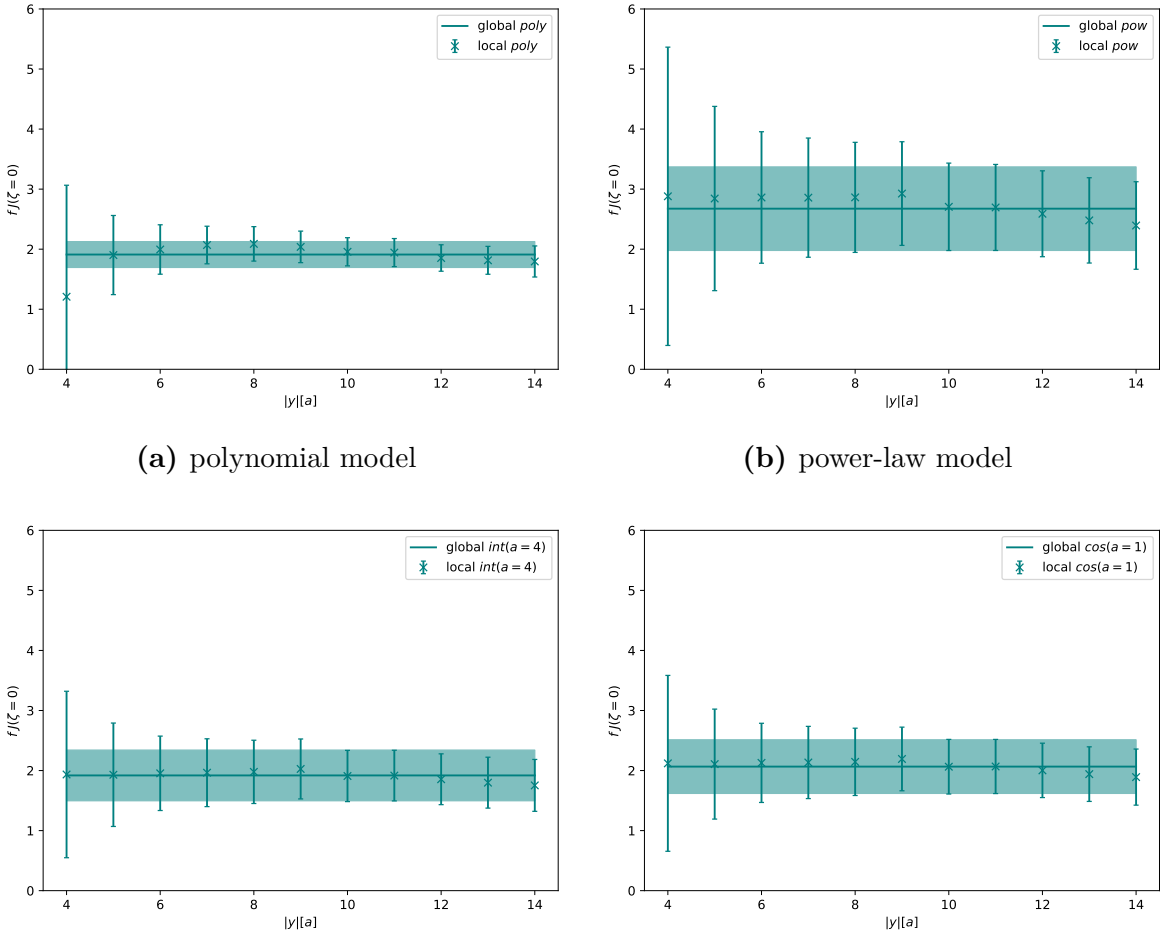
The grand average of $\langle\zeta^2\rangle$ over all fits is around 0.07 (with the largest deviation from the polynomial model) and thus quite small. This is consistent with our argument from Section 5.1.4 that $I(\zeta, y^2)$ should decrease rather quickly for $\zeta \to 1$ and makes this statement more quantitative.

[4] Strictly speaking, the interpretation as an "average" in the statistical sense requires $I(\zeta, y^2) \geq 0$, which is the case for the central values of all our fits, except for the polynomial model.

### 7.3.2 Testing factorization in $\zeta$ and $y$

To test whether the hypothesis (7.5) of a factorized dependence of $I(\zeta, y^2)$ on $\zeta$ and $y$ is adequate, we perform "local" fits of the $\zeta$ dependence in narrow bins of $y$. Specifically, we group the lattice data into intervals $(i - 0.5)\,a \leq |y| \leq (i + 0.5)\,a$ with $i = 4$ to 14 and fit them to the same models for the $\zeta$ dependence as before.

The resulting values and errors for $fJ(\zeta = 0)$ and $\langle \zeta^2 \rangle$ are shown respectively in Figures 7.9 and 7.10 for those fits where the value of $fJ(\zeta = 0)$ has an acceptable uncertainty and is consistent with the number sum rule.




**(a)** polynomial model

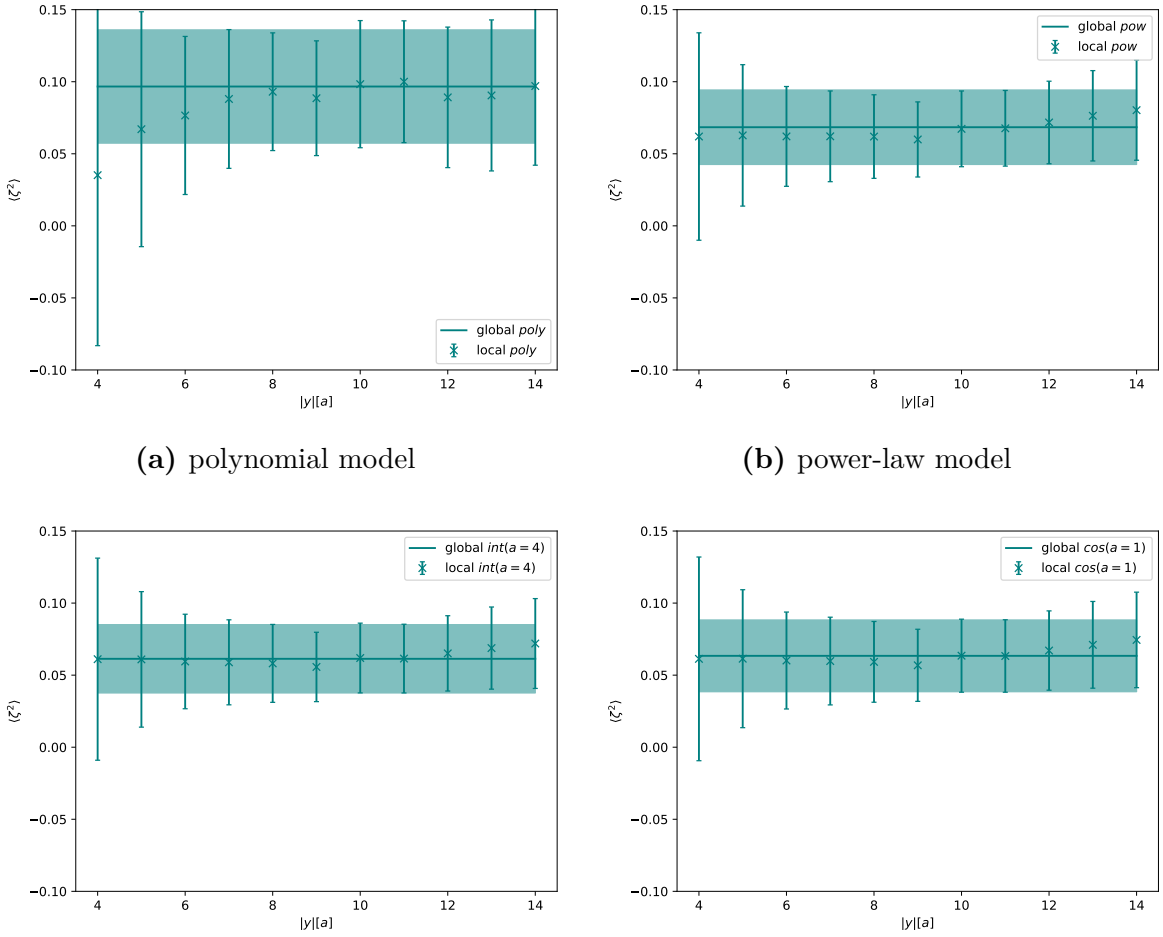
**(b)** power-law model

**(c)** integral model with fixed $a = 4$

**(d)** cosine model with fixed $a = 1$

**Figure 7.9:** Results for $S_{ud} = fJ_{ud}(\zeta = 0)$ from fits restricted to bins in $y$ of width $a$. The bands indicate the results of the global fits over all $y$ from $4a$ to $14a$.

We see that there is no significant indication for a $y$ dependence of either quantity. The errors of the local fits tend to increase when $y$ becomes small, which is due to the decreasing range of $\omega$ in that limit. We conclude that our factorized ansatz for the




**(a)** polynomial model

**(b)** power-law model

**(c)** integral model with fixed $a = 4$

**(d)** cosine model with fixed $a = 1$

**Figure 7.10:** As Figure 7.9, but for $\langle \zeta^2 \rangle$.

$\zeta$ and $y$ dependence is good enough for data of the quality we have analyzed. Note that this is equivalent to a factorized form of the $\omega$ and $y$ dependence of the invariant function $A(\omega, y^2)$.

# 8 Kinematically enhanced nucleon matrix elements

As we saw in the previous chapter, an accurate lattice determination of the $\omega$-dependence of the invariant functions is currently not feasible due to the high computational cost of obtaining high quality matrix elements at large momenta. This issue affects not only the Mellin moments of DPDs but also all matrix elements obtained using the LaMET approach introduced in Chapter 5. In fact, any improvement in this direction would benefit lattice studies of strongly boosted hadrons, in general.

in Ref. [68] such an algorithmic improvement was presented. This and practical applications thereof are discussed in Ref. [65, 66, 162, 185–190]. While these publications presented results mostly for two-point functions and effective energies, we investigate the improvement for nucleon matrix elements. To quantify the improvement, we compute the unpolarized isovector nucleon quark qPDF matrix elements (5.41). We furthermore investigate the results for possible increased excited-state overlap as well as discretization and cutoff artifacts. To this end, we make a direct comparison of qPDF matrix elements obtained using conventional and kinematically enhanced interpolators at different lattice spacings at similar momenta.

The results presented in this chapter are reproduced almost verbatim, with minor modifications, from Ref. [70], prepared for submission to JHEP, whose lead author is also the author of this thesis. They co-developed the lattice simulation code in collaboration with Tobias Sizmann and performed the analysis of the lattice data. Rui Zhang contributed his expertise on kinematic enhancement and its implementation, while Yong Zhao and Andreas Schäfer supervised the project.

## 8.1 Lattice measurements

We use three ensembles with open boundary conditions in time generated by the CLS collaboration, namely H102, S400 and N203. Details about the ensembles can be found in Section 6.1 and Table 6.1 therein, taken from [181]. We perform calculations for two different momenta. For renormalization in the hybrid scheme (5.42), it is necessary to extract the matrix elements at nucleon momentum $p_z = 0\,\mathrm{GeV}$. In this case, the conventional interpolator is the superior choice. We, therefore, calculate the matrix element in the rest frame using it exclusively. The interpolator comparison is made at a nucleon momentum of $p_z \approx 2.5\,\mathrm{GeV}$, for details on the run parameters see Table 8.1. We repeat this calculation, using otherwise identical parameters, for three different

combinations of interpolator kernels as specified in Table 4.1. For N203, we work with a single source per configuration, while for H102 and S400, we use two sources per configuration to increase statistics.

In order to improve the signal, two smearing techniques are applied. First, we prepare two APE-smoothed gauge fields with $\alpha_{\mathrm{APE}} = 0.25$, one for the calculation of the Wilson line and one for quark smearing [139]. For the calculation of the Wilson line, we only apply two steps of APE-smoothing to preserve the UV fluctuations of the gauge field. This is crucial for the correct long range renormalization. To obtain the quark propagators, we apply source-sink momentum smearing [174] ($b = -0.45$, $\epsilon = 0.25$, $n_{\mathrm{steps}} = \{250, 310, 445\}$ for H102, S400 and N203 respectively) where we use 25 APE-smoothing steps. Here, the APE smoothed gauge field is used only to maintain covariance of the source, sink and propagator and not for its physical content. Thus, we can afford more smoothing steps to reduce noise stemming from gauge field fluctuations. We use point-to-all propagators to evaluate the two-point function and the sequential source technique for the three-point function [136] as discussed in Section 4.5. Details on the chosen separation times, Wilson line lengths and numbers of measurements for the different momenta and ensembles can be found in Table 8.1.

Most lattice operations, including IO, smearing, and inversions, are performed using the `QUDA` library [191, 192]. In order to use `QUDA` in our scripts we made use of the `QUDA`-Python bindings package `PyQUDA` [193].

| Ensemble | $t_{\mathrm{sep}}/a$ | $z_{\mathrm{max}}/a$ | $p_{\mathrm{z}}$ [GeV] : $N_{\mathrm{meas}}$ | #cnfgs. used |
|---|---|---|---|---|
| H102 | {6, 8, 10} | 20 | {0: 400, 2.7: 800} | 400 |
| S400 | {7, 9, 11} | 20 | {0: 400, 2.5: 800} | 400 |
| N203 | {8, 11, 13} | 20 | {0: 200, 2.4: 200} | 200 |

**Table 8.1:** Run parameters, numbers of measurements per momentum and number of configurations used in the calculations. The number $N_{\mathrm{meas}}$ indicates the number of measurements taken, a number twice as large as the number of configurations used implies two sources placed on each configuration, separated spatially by a diagonal vector $(La/2, La/2, La/2)$.

## 8.2 Kinematic enhancement results

In this section, we present our numerical results obtained for nucleon observables using different interpolating operators, focusing on the impact of kinematic enhancements. We begin by examining excited-state contamination (ESC), a good understanding of which is crucial for a reliable determination of ground-state matrix elements. In Ref. [68], the ESC was suspected to become more pronounced when using kinematic enhancement. We start by determining their size for the nucleon. Finally, we present a direct comparison of results obtained with different nucleon interpolators, both kinematically enhanced

and conventional. This comparison allows us to quantify the potential gain in precision or signal-to-noise ratio (SNR).

### 8.2.1 Excited state contamination

For a realistic comparison of data obtained via different nucleon interpolators, we perform a two-state fit (4.78) to $C_{3pt}/C_{2pt}$ ratio data to extract the ground state matrix element. For an adequate comparison of our results for the isovector charges with the continuum limit, we multiply our results with the renormalization factors obtained for local quark bilinears obtained in Ref. [181].

In Figure 8.1, we compare the two-state fit results of different free quark and diquark kernel choices (top to bottom) for both the unpolarized nucleon quark isovector local current (left column) and a non-local current with Wilson line length $z = 8a$ (right column). Within uncertainties, we do not observe any increase in curvature within the data and hence the two-state fit, indicating no considerable enhancement of ESC. However, we do observe a considerably improved SNR in the case of the kinematically enhanced interpolators, which we will discuss in detail in 8.2.2. The results of all three interpolators are in good agreement.

This is to be expected, as $\mathcal{O}(a^2p^2)$ cutoff effects become more pronounced for large momentum data when using ensembles with $\mathcal{O}(a)$ improved action. A linear extrapolation in $a^2p_z^2$, presented in Figure 8.2, shows that the correct physical result is obtained in the continuum limit, supporting that the extracted ground state matrix elements do not suffer from further ESC.

Summarily, we find that the kinematically enhanced interpolators do not produce uncontrollably large ESC and meaningful results for the ground state matrix element can still be obtained by regular two-state fits.

### 8.2.2 Interpolator comparison

In this section, we compare our results obtained using different interpolators. We will first present the two-point and three-point functions used in the $C_{3pt}/C_{2pt}$ ratio separately, before turning to the latter. Finally, we present our results for renormalized matrix elements.

The two-point functions for the ensembles studied in this work are shown in Figure 8.3. The results obtained using kinematically enhanced interpolators show a stronger signal and increased SNR, providing high precision results for larger times than the conventional interpolator. This is crucial for ground state matrix element extraction. At identical statistics (number of measurements), the maximum usable sink time $t$ is increased by $\approx 50\%$. The SNR is improved considerably at smaller $t$, where both the signal from the conventional and the kinematically enhanced interpolators is usable, as found already in Ref. [68]. Both these facts contribute to an improved $C_{3pt}/C_{2pt}$ signal even before considering the potential enhancement to the three-point function.

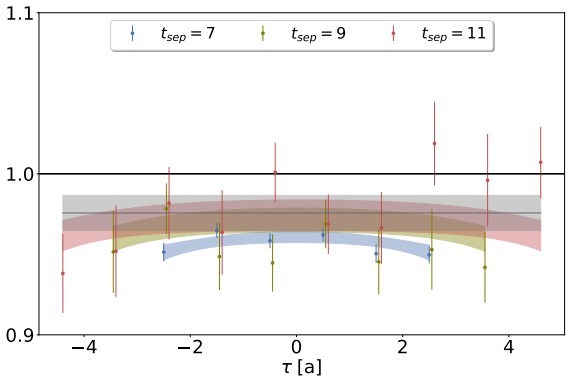
An improvement similar to the one shown in Figure 8.3 is observed for the three-point function $C_{3pt}$, presented in Figure 8.4. As the numerical values of the overlap factors, which later will be canceled in the $C_{3pt}/C_{2pt}$ ratio, differ vastly, we divided the data points by the weighted average of the central points for better comparison of the error bars. Clearly, the SNR is improved when using the kinematically enhanced interpolators, particularly at larger separation times.

We present the bare unpolarized nucleon quark isovector matrix elements w.r.t. $\lambda = zp_z$ at $p_z \approx 2.5\,\text{GeV}$ in Figure 8.5 for all three ensembles used in this work. Here, we used the normalization $\tilde{h}(z, p_z) = \tilde{h}(z, p_z)/\tilde{h}(z = 0, p_z)$ as $\tilde{h}(z = 0, p_z) = 1$ in the continuum. We will also use this normalization for the renormalization of the matrix elements. All calculations were performed at the same number of measurements; see table 8.1. A clear improvement in SNR by an order of magnitude in variance is evident when using the kinematically enhanced interpolators. Across the three lattice ensembles, we observe an $\mathcal{O}(10)$ improvement of the variance for the kinematically enhanced interpolators compared to the conventional one.

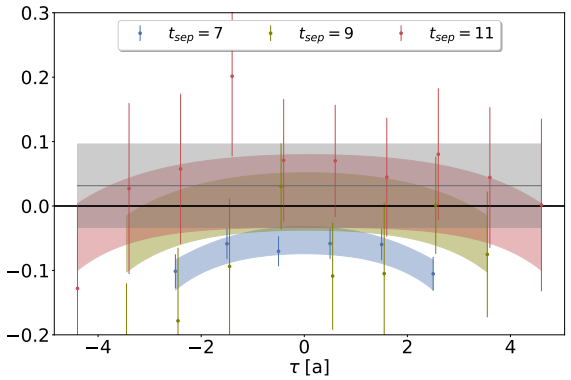
We renormalize the normalized matrix elements non-perturbatively using the hybrid renormalization scheme [49] as discussed in Subsection 5.2.2. We shall not elaborate on this further as it is not the focus of this work, instead referring the reader to recent works like [55, 56, 59, 194–197]. The required correlation functions in the rest frame were calculated with the conventional nucleon interpolator, as the kinematically enhanced ones are suboptimal choices at zero momentum. The ground state matrix elements at zero and large momenta were extracted, normalized by the local current results and their ratio taken subsequently. The linear divergence and renormalon term were extracted from a combined fit to the zero momentum ground state matrix elements on all three ensembles simultaneously [161, 198, 199]. The results for the renormalized, unpolarized nucleon quasi PDF obtained with different interpolators are shown in Figure 8.6. As for the bare matrix elements, we find an $\mathcal{O}(10)$ improvement of the variance for the kinematically enhanced interpolators compared to the conventional one for all lattice spacings.

We can also observe the additional improvement of the $\gamma_+$-enhancement over the $\gamma_t$-enhancement. Both the variance and the computational cost are cut in half, yielding further, multiplicative improvement by a factor of 4 at equal computational cost.

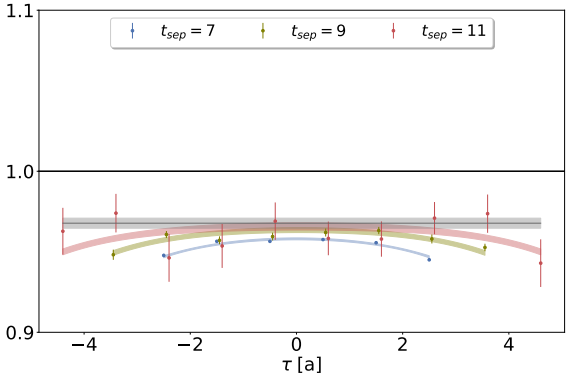
In Figure 8.7, we compare the same renormalized matrix elements shown in Figure 8.6 with identical interpolators across three lattice spacings: H102 ($a = 0.085$ fm), S400 ($a = 0.075$ fm), and N203 ($a = 0.064$ fm). While the value of $p_z$ is not exactly identical on all these ensembles, see Table 6.2, no statistically significant lattice spacing dependence is observed for any of the considered interpolators. This indicates that discretization effects remain moderate even at large momentum. A full quantification of the uncertainties associated with LaMET calculations requires taking both the infinite momentum $p_z \to \infty$ and continuum $a \to 0$ limit. The existence of a well-defined continuum limit is demonstrated by our precise results obtained with the kinematically enhanced interpolating operators. This is an important foundation for future precision calculations with LaMET.



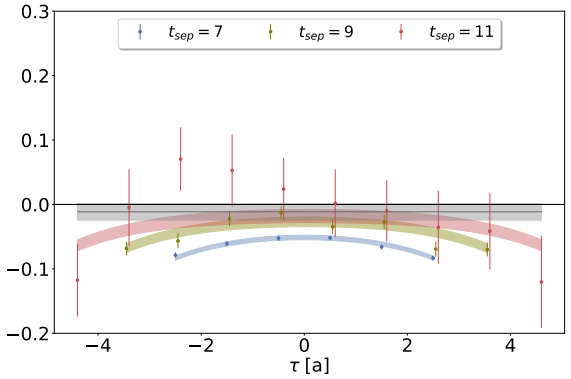

**(a)** $z = 0$, $\mathcal{T} = P_+$, $\Gamma = \mathbb{1}$



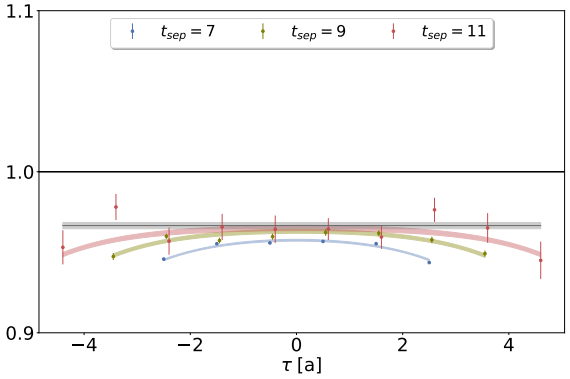

**(b)** $z = 8a$, $\mathcal{T} = P_+$, $\Gamma = \mathbb{1}$



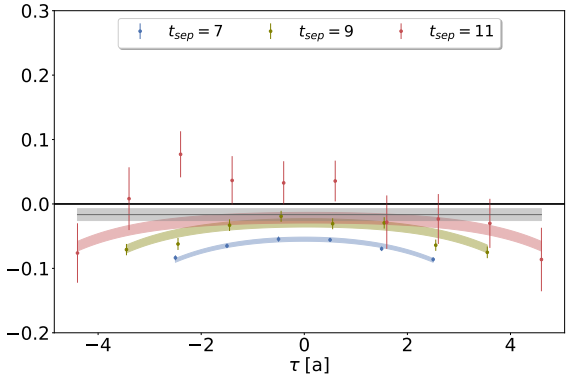

**(c)** $z = 0$, $\mathcal{T} = \gamma_t$, $\Gamma = \gamma_t$




**(d)** $z = 8a$, $\mathcal{T} = \gamma_t$, $\Gamma = \gamma_t$




**(e)** $z = 0$, $\mathcal{T} = \gamma_+$, $\Gamma = \gamma_+$




**(f)** $z = 8a$, $\mathcal{T} = \gamma_+$, $\Gamma = \gamma_+$

**Figure 8.1:** Two-state fit results (gray bands) for the isovector local ($z = 0$, left column) and non-local ($z = 8a$, right column) current at different separation times, locally normalized. Different interpolators are presented in rows, from top to bottom: conventional interpolator, $\gamma_t$ enhanced, $\gamma_+$ enhanced. The data was obtained from 400 measurements on the S400 ensemble at $p_z = 2.5\,\text{GeV}$. $\tau$ is the insertion time relative to $t_{\text{sep}}/2$

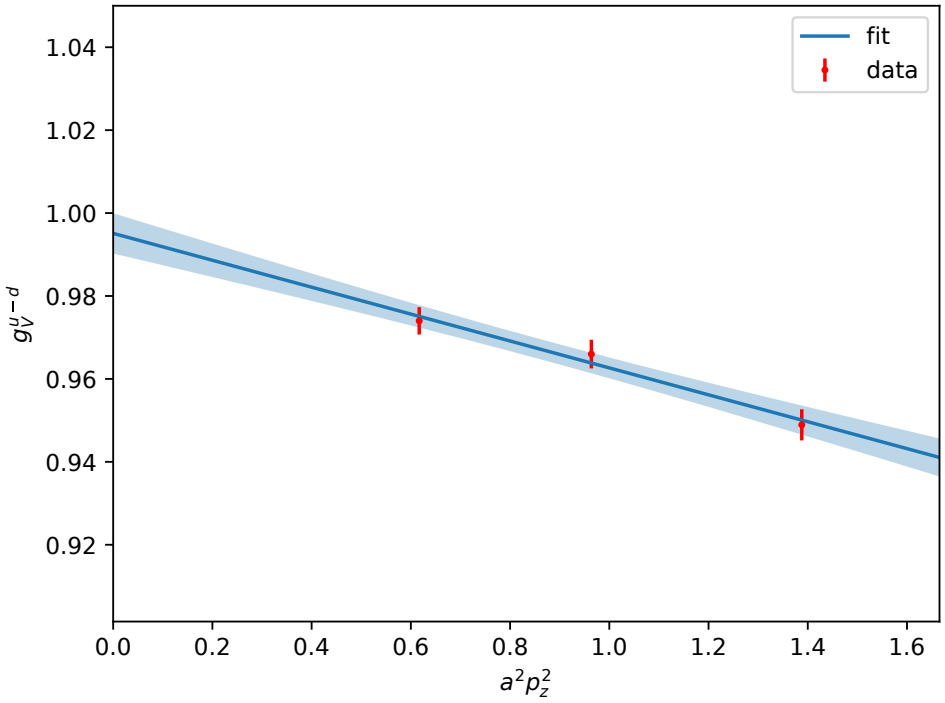
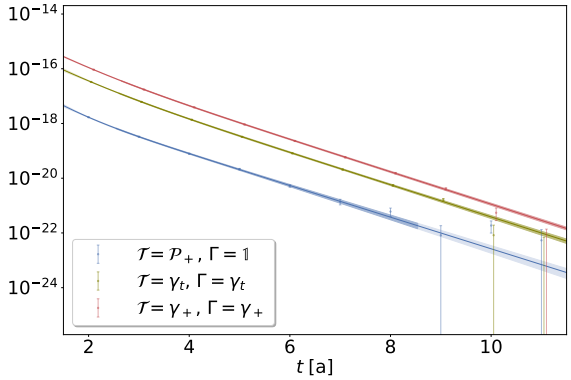
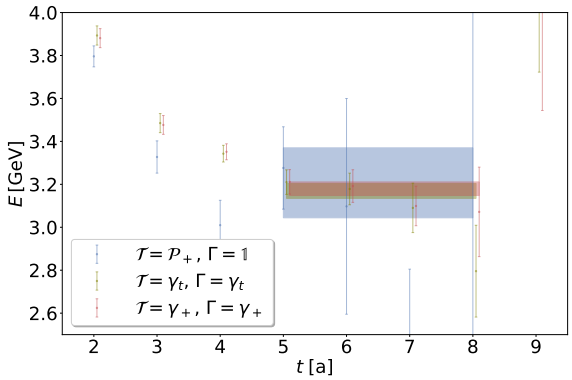


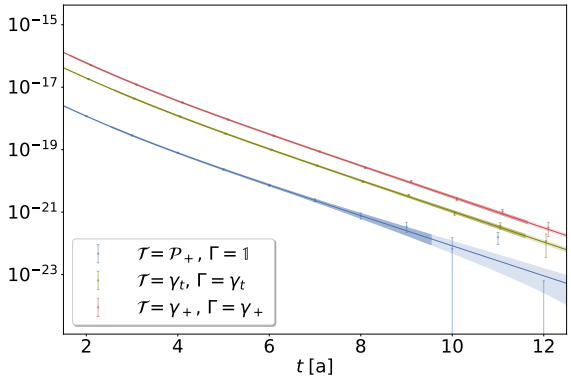

**Figure 8.2:** Renormalized local vector charge $g_V^{u-d}$, extrapolated linearly in $(ap_z)^2$.



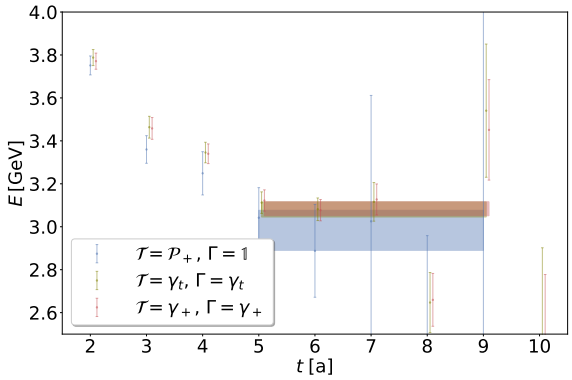

**(a)** H102, $C_{2pt}$



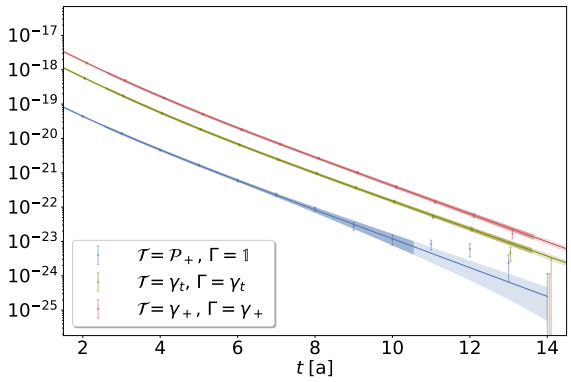

**(b)** H102, $E_{\text{eff}}$



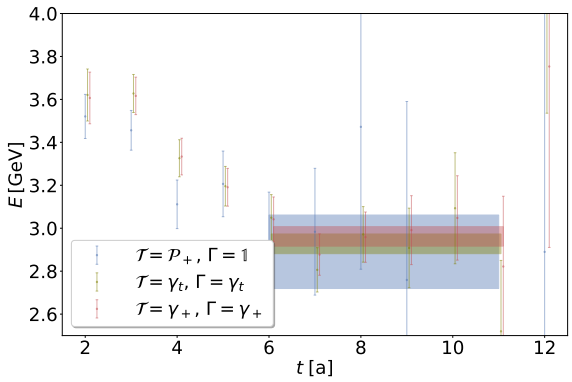

**(c)** S400, $C_{2pt}$




**(d)** S400, $E_{\text{eff}}$




**(e)** N203, $C_{2pt}$




**(f)** N203, $E_{\text{eff}}$

**Figure 8.3:** Two-state fit results to the 2pt correlation functions (left column) and the corresponding effective ground state energy ($E_{\text{eff}}$) plateaus (right column) for the H102 (top row), S400 (middle row) and N203 (bottom row) ensembles.

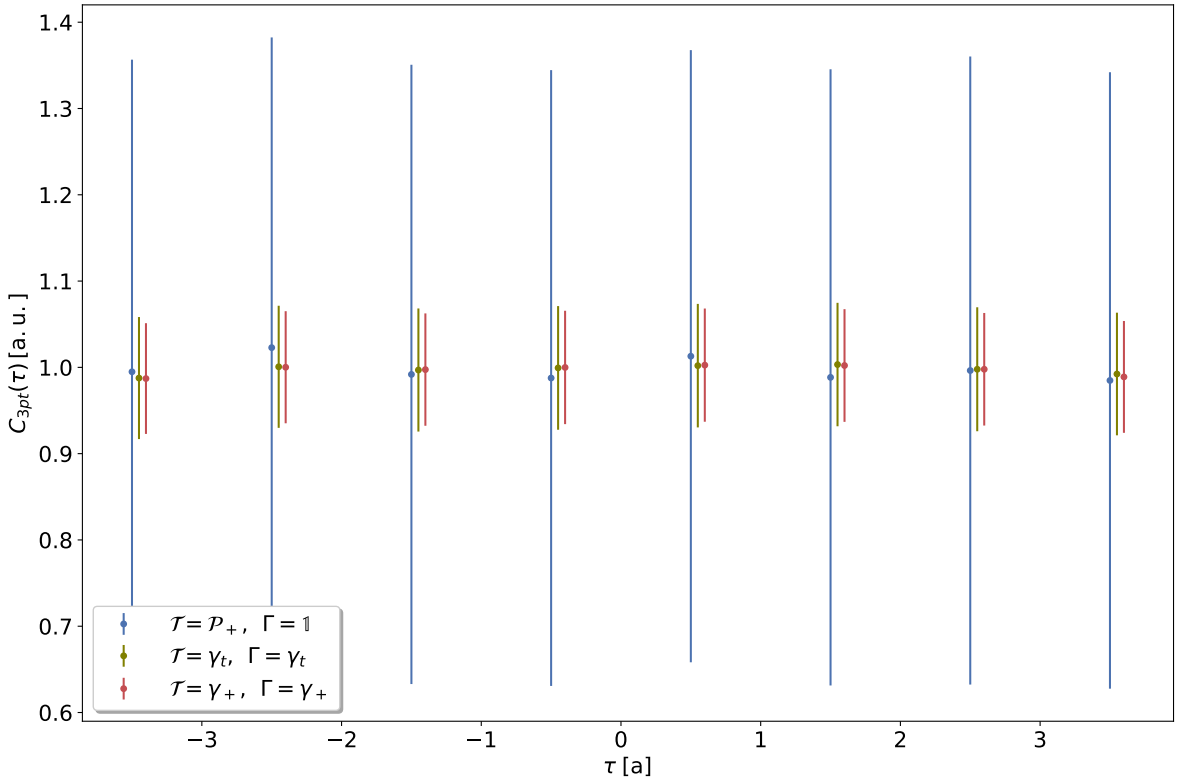
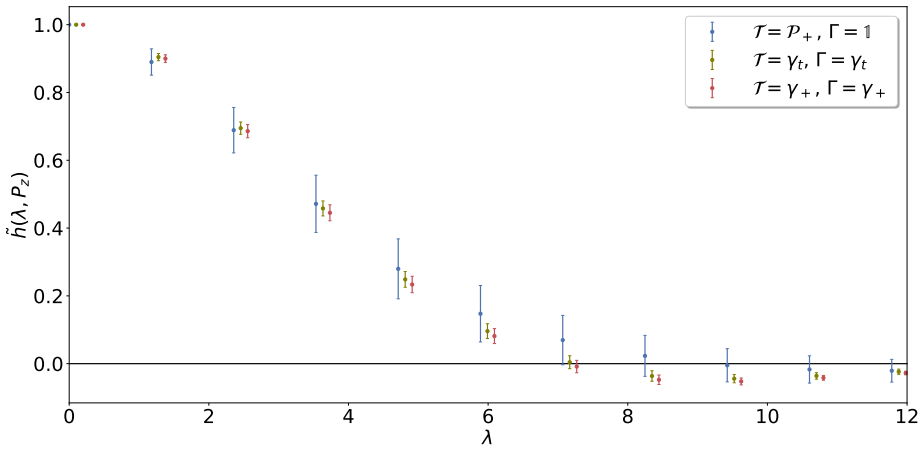
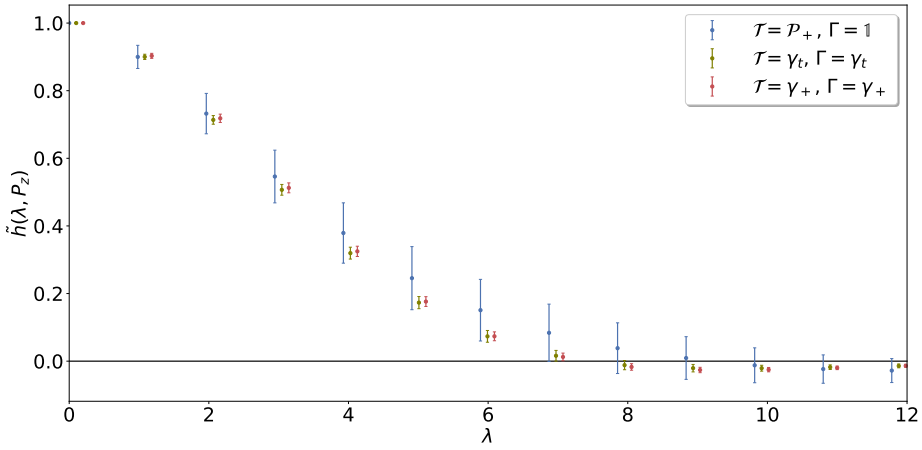


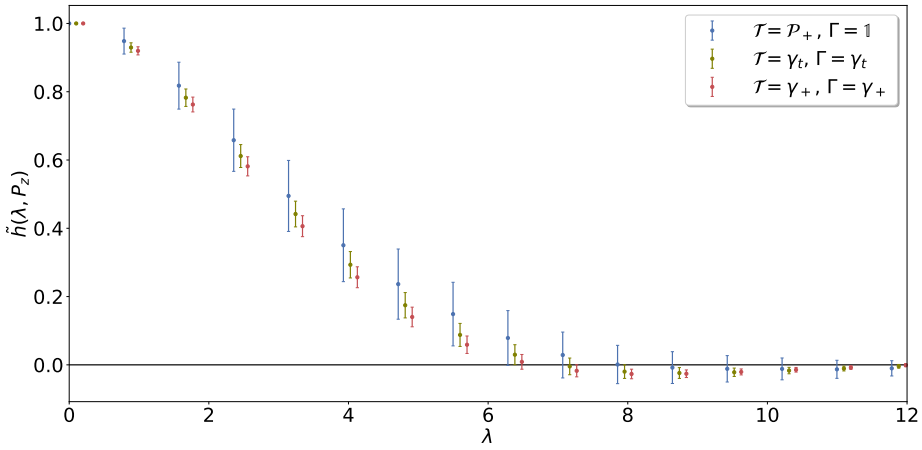

**Figure 8.4:** Bare, normalized unpolarized nucleon isovector three-point function for different interpolators, obtained from 400 measurements on the S400 ensemble at $|p_z| = 2.5\,\mathrm{GeV}$, $z = 0$ and $t_{\mathrm{sep}} = 9$. $\tau$ is the insertion time relative to $t_{\mathrm{sep}}/2$.




**(a)** H102

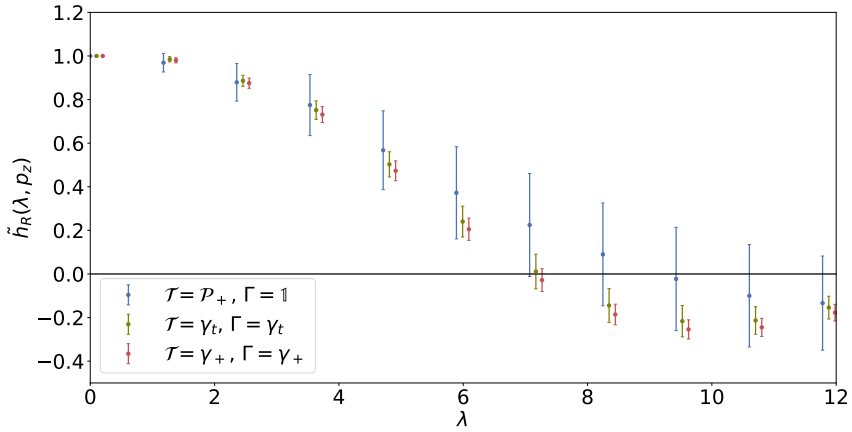



**(b)** S400

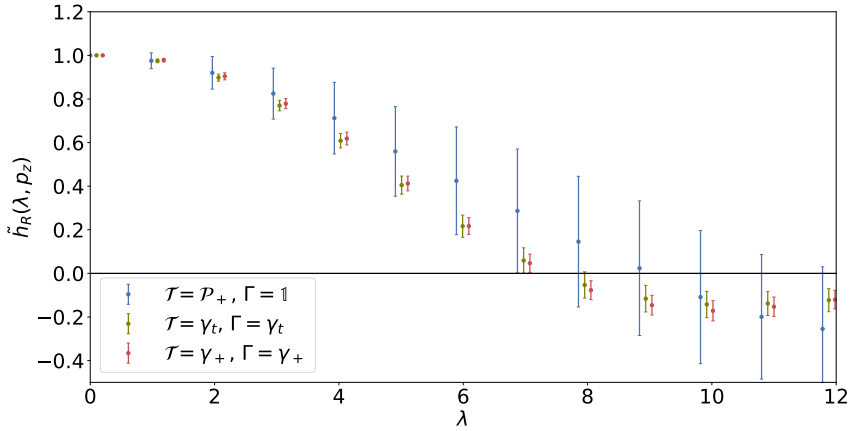



**(c)** N203

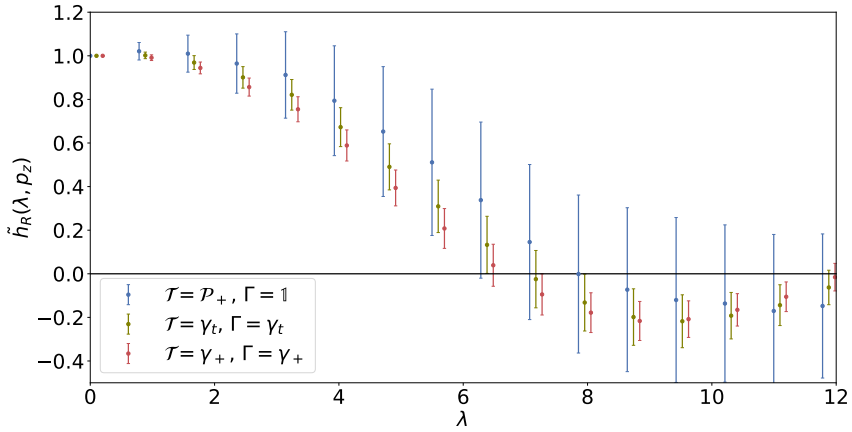
**Figure 8.5:** Comparison of normalized bare matrix elements from different interpolators on H102, S400, and N203 ensembles (left to right) at momenta close to $p_z = 2.5\,\mathrm{GeV}$.




**(a)** H102

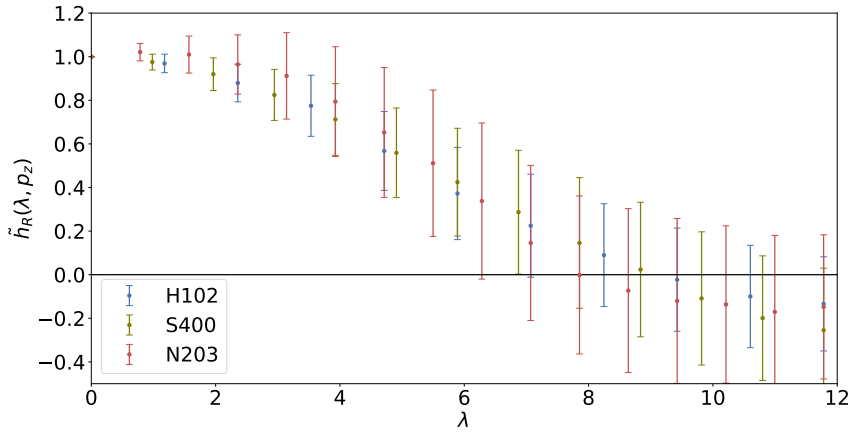



**(b)** S400

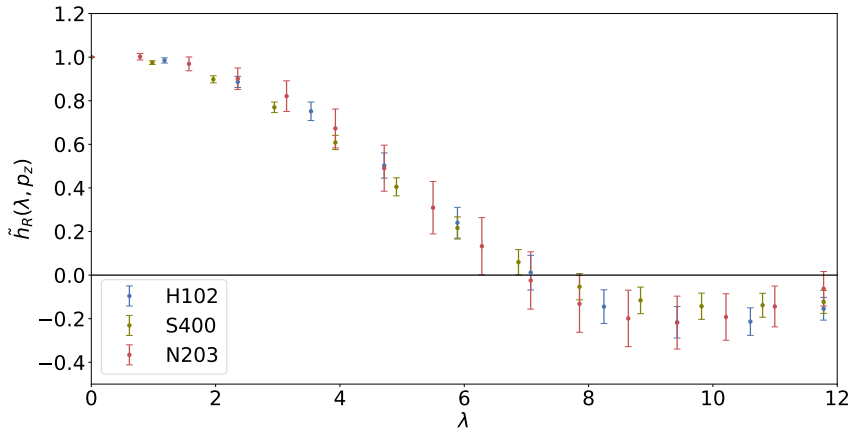



**(c)** N203

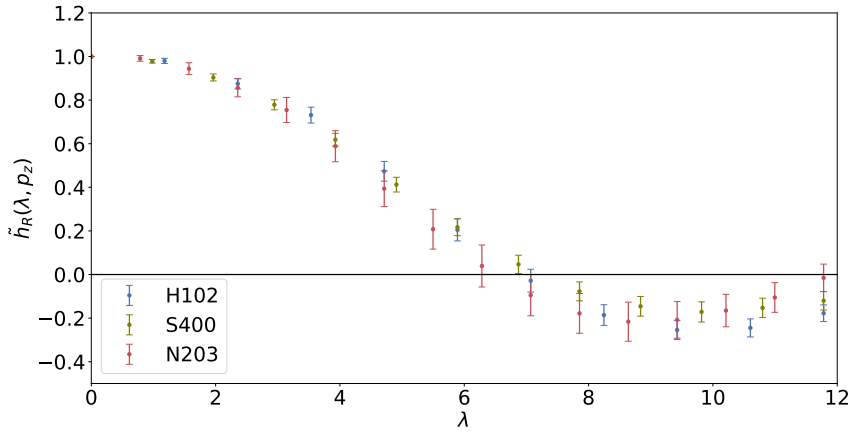
**Figure 8.6:** Renormalized nucleon quark isovector matrix elements on calculated on three ensembles for different interpolator structures $\Gamma$ and $\mathcal{T}$.




**(a)** $(\mathcal{T}, \Gamma) = (P_+, \mathbb{1})$




**(b)** $(\mathcal{T}, \Gamma) = (\gamma_t, \gamma_t)$




**(c)** $(\mathcal{T}, \Gamma) = (\gamma_+, \gamma_+)$

**Figure 8.7:** Renormalized nucleon quark isovector matrix elements at $p_z \approx 2.5\,\text{GeV}$ calculated on three ensembles of similar $m_\pi \approx 350\,\text{MeV}$ but different lattice spacing $a \in [0.064, 0.085]\,\text{fm}$ for the different interpolator structures $\Gamma$ and $\mathcal{T}$.

# 9 Conclusion

In this work, we studied the lowest Mellin Moment of DPDs from a Euclidean lattice and investigated kinematic enhancement for nucleon matrix elements.

We performed the first systematic study of the lattice spacing and meson mass dependence of leading-twist DPD invariant functions in Chapter 6 using six CLS ensembles. We analyzed lattice spacings $a \in \{0.085, 0.075, 0.064\}\,\text{fm}$ and pion masses $m_\pi \in [422, 214]\,\text{MeV}$.

We find the dominant systematic uncertainty to be finite volume effects. We assessed them by comparing the anisotropy of data from ensembles with different values of $Lm_\pi \in [2.95, 5.39]$. For the lower values, we observed a clear saw-tooth pattern, whereas for the largest value the pattern disappeared. Comparing the data points at large separations $|\vec{y}|$, we observe agreement within errors, indicating that finite volume effects at large separations are sufficiently under control after the cut in $\cos\theta$.

We found no significant lattice spacing dependence in vector-vector and tensor-tensor channels for the $C_1$ contraction. In the tensor-vector channel, we observe a mild $a$-dependence. We observe a clear $a$-dependence in the vector-vector channel for the $C_2$ contraction at small separations $y$, consistent with known discretization effects of the Wilson-fermion propagators at short distances. In the other channels and at larger separations, uncertainties are too large to draw firm conclusions.

Our investigation of results from ensembles of different meson mass revealed clear mass dependencies in several channels. For the $C_1$ contractions, we find the invariant functions $A_{ud}$ and $A_{duud}$ to decrease with decreasing pion masses consistent across $m_\pi \in \{422, 354, 214\}$. In addition, we observe a $\approx 2\sigma$ difference in $A_{ud}$ and $A_{duud}$ when comparing data from two ensembles of nearly identical pion mass $m_\pi \approx 350\,\text{MeV}$ but different kaon mass $m_K \in \{445, 577\}\,\text{MeV}$, hinting at potential sea quark effects. No mass dependence is observed for the $C_2$ contractions.

We performed a systematic study of different ansätze for the skewness dependence of the lowest skewed Mellin moment $I(\zeta, y^2)$ of DPDs in Chapter 7. We introduce arguments motivating additional constraints of the functional form of $I(\zeta, y^2)$. Based on the support properties of skewed DPDs, we argue that $\lim_{|\zeta|\to 1} I(\zeta, y^2) \to 0$ rapidly. We also found no grounds to require analyticity around $\zeta = 0$. We find that the polynomial ansatz used in past works produced artificially narrow error bands while not respecting the constraint at $|\zeta| \to 1$, thereby not faithfully representing the uncertainties in the data. We introduce three new models that obey our boundary conditions, the power-law, cosine and integral model. The first one was a direct improvement over the

polynomial model which provided the correct limiting behavior but failed to capture the full uncertainty in the data. The expectation value $\langle\zeta^2\rangle$, which is related to the curvature of our lattice data $\hat{A}(\omega)$ around $\omega = 0$, was described by all four models equally well at $\langle\zeta^2\rangle \approx 0.07$.

The cosine and integral model satisfy the correct limiting behavior and were able to account for the uncertainties in the data but introduce uncertainties well beyond 100% for $I(\zeta = 0, y^2)$. This led to results compatible with the number sum rule $S_{ud} = 2 + \mathcal{O}(\alpha_s^2)$, although they remain largely unconstrained without additional theory input. Using the number sum rule to fix one of the two parameters in these models produced well behaved results with considerably narrower error bands at large $\omega$, signaling a fundamental limitation of the current dataset. Finally, we validated our factorization assumption of $I(\zeta, y^2)$ into separate $y^2$- and $\zeta$- dependent parts by comparing local to global fits. We conclude that a physically reliable extraction of the lowest Mellin moment of DPDs requires significantly improved data quality at large $\omega$ and therefore calculations at larger momenta.

This bottleneck is addressed in Chapter 8. We investigated possible SNR improvements in nucleon correlation functions by altering the Dirac structure of hadron interpolators. We compared the conventional interpolator to kinematically enhanced alternatives that couple preferentially to the energy or "+"-components of the nucleon wave function. As a benchmark observable, we calculated the unpolarized nucleon isovector quasi-PDF matrix element at $p_z \approx 2.5\,\text{GeV}$ across three different CLS ensembles of similar pion mass $m_\pi \approx 350\,\text{MeV}$ at lattice spacings $a \in \{0.085, 0.075, 0.064\}\,\text{fm}$. We find an improvement of one order of magnitude to the variance of the data for all lattice spacings. The $\gamma_+$-enhancement is found to be most advantageous, providing two improvements over $\gamma_t$ enhancement. By including information from both $t$ and $z$ components, it reduces the variance by a factor of 2. Furthermore, by projecting all quarks onto their "+"-components, it reduces the number of inversions and therefore computational cost per measurement by 50%. In total, this yields a fourfold improvement in variance at identical computational resources.

We investigate our results for excited state contamination (ESC) via a two-state fit, that incorporates three different source-sink separation times. No increase in ESC due to kinematic enhancement is observed. Residual discretization effects were found to be of $\mathcal{O}((ap_z)^2)$ and extrapolate linearly to the correct continuum limit.

In summary, we find the invariant functions of DPDs at $\omega = 0$ to be stable against variations in lattice spacing while exhibiting flavor and channel dependent mass dependencies. Our analysis of the skewness dependence of lowest DPD Mellin moment reveals that a reliable extraction is not possible with currently available data due to insufficient data at large $|\omega|$. Our study of kinematic enhancement for highly boosted nucleon matrix elements suggests this limitation can be overcome in the near future.

We conclude this chapter with an outlook on future research directions. In this

work, we studied only collinear, color-singlet DPDs. Further quantities of interest for future research include color-octet DPDs, DPDs of polarized nucleons (although these are not directly accessible in LHC experiments) and non-valence quark DPDs. For the kinematically enhanced interpolators, we found they significantly extend the accessible momentum- and thus $\omega$ range, without introducing additional systematic uncertainties. This improvement can be used not only to extract the lowest Mellin moment accurately but also, using LaMET for qDPDs [200], to directly extract the full color-singlet collinear DPD. This appears to be the most promising avenue of research we intend to pursue in the near future. This approach will yield the lowest Mellin moment as an intermediate result, providing an important cross check with the number sum rule. This would have to be followed by a continuum extrapolation, building on the results obtained within this thesis, which is the final objective.

# A Two-current matrix element tensor decomposition

We give the tensors $u$ used in the Lorentz decomposition of two-current matrix elements (5.21) channel by channel. For the vector-vector and axial-axial channel, these are identical:

$$\begin{aligned} u^{\mu\nu}_{VV,A}(p,y) &:= 2p^\mu p^\nu - \frac{m^2}{2}\, g^{\mu\nu}, \\ u^{\mu\nu}_{VV,B}(p,y) &:= 2p^{\{\mu} y^{\nu\}} - \frac{p\cdot y}{2}\, g^{\mu\nu}, \\ u^{\mu\nu}_{VV,C}(p,y) &:= 2y^\mu y^\nu - \frac{y^2}{2}\, g^{\mu\nu}. \end{aligned} \tag{A.1}$$

The tensors for the tensor-vector and vector-tensor channel are

$$\begin{aligned} u^{\mu\nu\rho}_{TV,A}(p,y) &:= 4y^{[\mu}p^{\nu]}p^\rho + \frac{4m^2}{3}\, g^{\rho[\mu}y^{\nu]} - \frac{4\,p\cdot y}{3}\, g^{\rho[\mu}p^{\nu]}, \\ u^{\mu\nu\rho}_{TV,B}(p,y) &:= 4y^{[\mu}p^{\nu]}y^\rho + \frac{4\,p\cdot y}{3}\, g^{\rho[\mu}y^{\nu]} - \frac{4y^2}{3}\, g^{\rho[\mu}p^{\nu]}\,. \end{aligned} \tag{A.2}$$

For the tensor-tensor channel, we use the following tensors:

$$\begin{aligned} u^{\mu\nu\rho\sigma}_{TT,A}(p,y) &:= -8\,p^{[\nu}g^{\mu][\rho}p^{\sigma]}, \\ u^{\mu\nu\rho\sigma}_{TT,B}(p,y) &:= -16\,y^{[\mu}p^{\nu]}y^{[\rho}p^{\sigma]} + 8\,y^{[\nu}p^{\mu]}g^{[\rho\sigma]}, \\ u^{\mu\nu\rho\sigma}_{TT,C}(p,y) &:= -4\,p^{[\nu}g^{\mu][\rho}y^{\sigma]} - 4\,y^{[\nu}g^{\mu][\rho}p^{\sigma]}, \\ u^{\mu\nu\rho\sigma}_{TT,D}(p,y) &:= -8\,y^{[\nu}g^{\mu][\rho}y^{\sigma]}, \\ u^{\mu\nu\rho\sigma}_{TT,E}(p,y) &:= 2\,g^{\mu[\rho}g^{\sigma]\nu}. \end{aligned} \tag{A.3}$$

We use the following notation for (anti)commutators:

$$\begin{aligned} a^{[\mu_1\dots\mu_n]} &= \frac{1}{n!}\sum_{P\in S_n} \mathrm{sign}(P) a^{\mu_{P(1)}\cdots\nu_{P(n)}}, \\ a^{\{\mu_1\dots\mu_n\}} &= \frac{1}{n!}\sum_{P\in S_n} a^{\mu_{P(1)}\cdots\nu_{P(n)}}. \end{aligned} \tag{A.4}$$

# B Spectral decomposition of correlators

Definition of considered correlators:

$$C_{2\mathrm{pt}}(\vec{p},t) = \langle 0|\mathcal{J}(\vec{p},t)\,\overline{\mathcal{J}}(\vec{p},0)|0\rangle = \sum_n \frac{\langle 0|\mathcal{J}(0)|n,\vec{p}\rangle\ \langle n,\vec{p}|\overline{\mathcal{J}}(0)|0\rangle}{2E_n(\vec{p})}\, e^{-E_n(\vec{p})t}. \tag{B.1}$$

$$\begin{aligned} C_{3\mathrm{pt}}(\vec{p},t,\tau) &= \langle 0|\mathcal{J}(\vec{p},t)\,O(\tau)\,\overline{\mathcal{J}}(\vec{p},0)|0\rangle \\ &= \sum_{n,k} \frac{\langle 0|\mathcal{J}|n,\vec{p}\rangle\ \langle n,\vec{p}|O|k,\vec{p}\rangle\ \langle k,\vec{p}|\overline{\mathcal{J}}|0\rangle}{4E_n(\vec{p})\,E_k(\vec{p})}\ e^{-E_n(\vec{p})(t-\tau)}e^{-E_k(\vec{p})\tau}. \end{aligned} \tag{B.2}$$

$$\begin{aligned} C_{4\mathrm{pt}}(\vec{p};t,\tau_2,\tau_1) = \sum_{n,m,k} &\frac{\langle 0|\mathcal{J}|n,\vec{p}\rangle\ \langle n,\vec{p}|O_2|m,\vec{p}\rangle\ \langle m,\vec{p}|O_1|k,\vec{p}\rangle\ \langle k,\vec{p}|\overline{\mathcal{J}}|0\rangle}{8\,E_n(\vec{p})\,E_m(\vec{p})\,E_k(\vec{p})} \\ &\times e^{-E_n(\vec{p})(t-\tau_2)}e^{-E_m(\vec{p})(\tau_2-\tau_1)}e^{-E_k(\vec{p})\,\tau_1}. \end{aligned} \tag{B.3}$$

$$C_{4\mathrm{pt}}(\vec{p};t,\tau) = \sum_{n,k} \frac{\langle 0|\mathcal{J}|n,\vec{p}\rangle\ \langle n,\vec{p}|O_2\,O_1|k,\vec{p}\rangle\ \langle k,\vec{p}|\overline{\mathcal{J}}|0\rangle}{4\,E_n(\vec{p})\,E_k(\vec{p})}\ e^{-E_n(\vec{p})(t-\tau)}e^{-E_k(\vec{p})\,\tau}. \tag{B.4}$$

$C_{4\mathrm{pt}}$ with $\tau_1 = \tau_2$ can be treated like $C_{3pt}$, thus we perform the truncation of the spectral decomposition at leading excited states only for $C_{2pt}$ and $C_{3pt}$.

$$\begin{aligned} C_2(\vec{p},t) &\approx \frac{\langle 0|\mathcal{J}|0\rangle\langle 0|\overline{\mathcal{J}}|0\rangle}{2E_0}e^{-E_0t}\ +\ \frac{\langle 0|\mathcal{J}|1\rangle\langle 1|\overline{\mathcal{J}}|0\rangle}{2E_1}e^{-E_1t} \\ &\equiv A_0\,e^{-E_0t} + A_1\,e^{-E_1t} = A_0\,e^{-E_0t}\left[1+\frac{A_1}{A_0}\,e^{-\Delta Et}\right] \end{aligned} \tag{B.5}$$

$$\begin{aligned} C_3(\vec{p},t,\tau) \approx\ & \frac{\langle 0|\mathcal{J}|0\rangle\langle 0|O|0\rangle\langle 0|\overline{\mathcal{J}}|0\rangle}{4E_0^2}\,e^{-E_0t} \\ &+ \frac{\langle 0|\mathcal{J}|0\rangle\langle 0|O|1\rangle\langle 1|\overline{\mathcal{J}}|0\rangle}{4E_0E_1}\,e^{-E_0(t-\tau)}e^{-E_1\tau} + \frac{\langle 0|\mathcal{J}|1\rangle\langle 1|O|0\rangle\langle 0|\overline{\mathcal{J}}|0\rangle}{4E_1E_0}\,e^{-E_1(t-\tau)}e^{-E_0\tau} \end{aligned}$$

$$
\begin{aligned}
&+ \frac{\langle 0|\mathcal{J}|1\rangle\langle 1|O|1\rangle\langle 1|\overline{\mathcal{J}}|0\rangle}{4E_1^2}\, e^{-E_1 t} \\
&= A_0 \frac{\langle 0|O|0\rangle}{2E_0}\, e^{-E_0 t} + B_{01}\, e^{-E_0(t-\tau)} e^{-E_1 \tau} + B_{10}\, e^{-E_1(t-\tau)} e^{-E_0 \tau} + B_{11}\, e^{-E_1 t} \\
&= A_0\, e^{-E_0 t} \left[ \frac{\langle 0|O|0\rangle}{2E_0} + \frac{B_{01}}{A_0} \left( e^{-\Delta E \tau} + e^{-\Delta E t} e^{\Delta E \tau} \right) + \frac{B_{11}}{A_0}\, e^{-\Delta E t} \right] \\
&= A_0\, e^{-E_0 t} \left[ \frac{\langle 0|O|0\rangle}{2E_0} + \frac{B_{01}}{A_0}\, e^{-\Delta E \frac{t}{2}} \left( e^{-\Delta E \left(\tau - \frac{t}{2}\right)} + e^{\Delta E \left(\tau - \frac{t}{2}\right)} \right) + \frac{B_{11}}{A_0}\, e^{-\Delta E t} \right] \\
&= A_0\, e^{-E_0 t} \left[ \frac{\langle 0|O|0\rangle}{2E_0} + 2\frac{B_{01}}{A_0}\, e^{-\Delta E \frac{t}{2}} \cosh\left( \Delta E \left( \tau - \frac{t}{2} \right) \right) + \frac{B_{11}}{A_0}\, e^{-\Delta E t} \right]
\end{aligned}
\tag{B.6}
$$

We combine the results of $C_{2pt}$ and $C_{3pt}$ to obtain a approximate functional form for the ratio $R(\vec{p}, t, \tau)$:

$$
\begin{aligned}
R(\vec{p}, t, \tau) = \frac{C_3(\vec{p}, t, \tau)}{C_2(\vec{p}, t)} &\approx \frac{A_0\, e^{-E_0 t} \left[ \frac{\langle 0|O|0\rangle}{2E_0} + 2\frac{B_{01}}{A_0}\, e^{-\Delta E \frac{t}{2}} \cosh\left( \Delta E \left( \tau - \frac{t}{2} \right) \right) + \frac{B_{11}}{A_0}\, e^{-\Delta E t} \right]}{A_0\, e^{-E_0 t} \left[ 1 + \frac{A_1}{A_0}\, e^{-\Delta E t} \right]} \\
&= \frac{\frac{\langle 0|O|0\rangle}{2E_0} + 2\frac{B_{01}}{A_0}\, e^{-\Delta E \frac{t}{2}} \cosh\left( \Delta E \left( \tau - \frac{t}{2} \right) \right) + \frac{B_{11}}{A_0}\, e^{-\Delta E t}}{1 + \frac{A_1}{A_0}\, e^{-\Delta E t}} \\
&\equiv \frac{c_0 + c_1\, e^{-\Delta E \frac{t}{2}} \cosh\left( \Delta E \left( \tau - \frac{t}{2} \right) \right) + c_2\, e^{-\Delta E t}}{1 + c_3\, e^{-\Delta E t}}
\end{aligned}
\tag{B.7}
$$

This can be used as a fitting ansatz. obtaining $\Delta E$ and $c_3$ initial values from the truncated decomposition of $C_{2pt}$ allows them to be either fixed or used as priors in the fit.

# C Euclidean correlation functions with open boundary conditions

The discretized partition function for general boundary states $\langle B_f|$ and $|B_i\rangle$, separated by time $T = Na$, takes the form:

$$Z_E = \int \mathcal{D}\left[B_i\right] \mathcal{D}\left[B_f\right] \mathcal{D}\left[\phi_{N-1}\right] \cdots \mathcal{D}\left[\phi_1\right] \langle B_f| \, e^{-aH} \, |\phi_{N-1}\rangle \cdots \langle \phi_1| \, e^{-aH} \, |B_i\rangle \ . \tag{C.1}$$

Resolving the unities $\mathbb{1} = \int \mathcal{D}\left[\phi_i\right] |\phi_i\rangle \langle \phi_i|$, we get:

$$Z_E = \int \mathcal{D}\left[B_i\right] \mathcal{D}\left[B_f\right] \langle B_f| \, e^{-TH} \, |B_i\rangle \ . \tag{C.2}$$

If we have periodic boundary conditions, i.e. $\langle B_f|B_i\rangle = 1$, this reduces to the known expression

$$Z_E = \int \mathcal{D}\left[\phi\right] \langle \phi| \, e^{-TH} \, |\phi\rangle = \mathrm{tr}\left(e^{-TH}\right) \ , \tag{C.3}$$

producing the spectral decomposition given in (4.6). For open boundary conditions (OBCs), we have to take the boundary states into account:

$$Z_{\mathrm{OBC}} = \sum_{i,f} \langle f| \, e^{-TH} \, |i\rangle \ , \tag{C.4}$$

where we switched to eigenstates of the Hamiltonian $H\,|s\rangle = E_s\,|s\rangle$. For the two-point correlation function, this implies

$$\langle O_2(t_2) O_1(t_1)\rangle_{\mathrm{OBC}} = \sum_{i,f} \frac{\langle f| \, e^{-(T-t_2)H} \, O_2(0) \, e^{-t_2 H} \, e^{t_1 H} \, O_1(0) \, e^{-t_1 H} \, |i\rangle}{\langle f| \, e^{-TH} \, |i\rangle}. \tag{C.5}$$

Inserting three complete sets of energy eigenstates $\mathbb{1} = \sum_n |n\rangle \langle n|$, one obtains a modified spectral representation

$$\begin{aligned} &\langle O_2(t_2) O_1(t_1)\rangle_{\mathrm{OBC}} \\ &= Z_{\mathrm{OBC}}^{-1} \sum_{i,f,n,m,l} \langle f\,|n\rangle \, \langle n|\, O_2(0)\,|m\rangle \, \langle m|\, O_1(0)\,|l\rangle \, \langle l\,|i\rangle \ e^{-E_n(T-t_2)} e^{-E_m(t_2-t_1)} e^{-E_l t_1}. \end{aligned} \tag{C.6}$$

This expression contains more spectral sums than the PBC case, reflecting the presence of boundary states. In the bulk region of the lattice, where $t_1 \gg a$ and $T - t_2 \gg a$,

the Euclidean time evolution factors

$$e^{-E_l t_1}, \qquad e^{-E_n (T-t_2)} \tag{C.7}$$

lead to an exponential suppression of all contributions with $E_l > 0$ and $E_n > 0$, such that the boundary states are effectively projected onto the vacuum, as $\langle f|0\rangle = \delta_{f0}$ implies that only $f = 0$ contributes (analogous for the initial state). The correlation function then recovers the spectral decomposition (4.6) for $T \to \infty$:

$$\langle O_2(t_2) O_1(t_1)\rangle_{\mathrm{OBC}} \xrightarrow[\text{bulk}]{} \sum_m \langle 0|\, O_2(0)\, |m\rangle \, \langle m|\, O_1(0)\, |0\rangle \; e^{-E_m (t_2 - t_1)}\,, \tag{C.8}$$

where we used $Z_{\mathrm{OBC}} \to 1$ for $T \to \infty$.

# Bibliography


[1] E. Rutherford. "The scattering of alpha and beta particles by matter and the structure of the atom". In: *Phil. Mag. Ser. 6* 21 (1911), pp. 669–688.

[2] R. Hofstadter, H. R. Fechter, and J. A. McIntyre. "High-Energy Electron Scattering and Nuclear Structure Determinations". In: *Phys. Rev.* 92.4 (1953), p. 978.

[3] L. I. Schiff. "Interpretation of Electron Scattering Experiments". In: *Phys. Rev.* 92 (1953). [Erratum: Phys.Rev. 93, 1434–1434 (1954)], pp. 988–993.

[4] Murray Gell-Mann. "A Schematic Model of Baryons and Mesons". In: *Phys. Lett.* 8 (1964), pp. 214–215.

[5] G. Zweig. "An SU(3) model for strong interaction symmetry and its breaking. Version 1". In: (Jan. 1964).

[6] J. Prentki and J. Steinberger, eds. *Proceedings, 14th International Conference on High-Energy Physics (ICHEP 68): Vienna, Austria, 28 Aug-5 Sep, 1968*. Geneva: CERN, 1968.

[7] J. D. Bjorken and Emmanuel A. Paschos. "Inelastic Electron Proton and gamma Proton Scattering, and the Structure of the Nucleon". In: *Phys. Rev.* 185 (1969), pp. 1975–1982.

[8] Richard P. Feynman. "Very high-energy collisions of hadrons". In: *Phys. Rev. Lett.* 23 (1969). Ed. by L. M. Brown, pp. 1415–1417.

[9] S. D. Drell and Tung-Mow Yan. "Massive Lepton Pair Production in Hadron-Hadron Collisions at High-Energies". In: *Phys. Rev. Lett.* 25 (1970). [Erratum: Phys.Rev.Lett. 25, 902 (1970)], pp. 316–320.

[10] T. Akesson et al. "Double Parton Scattering in $pp$ Collisions at $\sqrt{s} = 63$ GeV". In: *Z. Phys. C* 34 (1987), p. 163.

[11] J. Alitti et al. "A Study of multi-jet events at the CERN $\bar{p}p$ collider and a search for double parton scattering". In: *Phys. Lett. B* 268 (1991), pp. 145–154.

[12] F. Abe et al. "Study of four jet events and evidence for double parton interactions in $p\bar{p}$ collisions at $\sqrt{s} = 1.8$ TeV". In: *Phys. Rev. D* 47 (1993), pp. 4857–4871.

[13] F. Abe et al. "Double parton scattering in $\bar{p}p$ collisions at $\sqrt{s} = 1.8$ TeV". In: *Phys. Rev. D* 56 (1997), pp. 3811–3832.

[14] F. Abe et al. "Double parton scattering in $\bar{p}p$ collisions at $\sqrt{s} = 1.8$TeV". In: *Phys. Rev. D* 56 (1997), pp. 3811–3832.

[15] "Study of hard double parton scattering in four-jet events in *pp* collisions at $\sqrt{s} = 7$ TeV with the ATLAS experiment at the LHC". In: (Nov. 2015). Ed. by Hannes Jung et al.

[16] Roel Aaij et al. "Measurement of the J/$\psi$ pair production cross-section in pp collisions at $\sqrt{s} = 13$ TeV". In: *JHEP* 06 (2017). [Erratum: JHEP 10, 068 (2017)], p. 047. arXiv: 1612.07451 [hep-ex].

[17] Albert M Sirunyan et al. "Constraints on the double-parton scattering cross section from same-sign W boson pair production in proton-proton collisions at $\sqrt{s} = 8$ TeV". In: *JHEP* 02 (2018), p. 032. arXiv: 1712.02280 [hep-ex].

[18] Victor Mukhamedovich Abazov et al. "Observation and Studies of Double $J/\psi$ Production at the Tevatron". In: *Phys. Rev. D* 90.11 (2014), p. 111101. arXiv: 1406.2380 [hep-ex].

[19] Victor Mukhamedovich Abazov et al. "Evidence for simultaneous production of $J/\psi$ and $\Upsilon$ mesons". In: *Phys. Rev. Lett.* 116.8 (2016), p. 082002. arXiv: 1511.02428 [hep-ex].

[20] Morad Aaboud et al. "Measurement of the prompt J/ $\psi$ pair production cross-section in pp collisions at $\sqrt{s} = 8$ TeV with the ATLAS detector". In: *Eur. Phys. J. C* 77.2 (2017), p. 76. arXiv: 1612.02950 [hep-ex].

[21] Morad Aaboud et al. "Study of the hard double-parton scattering contribution to inclusive four-lepton production in *pp* collisions at $\sqrt{s} = 8$ TeV with the ATLAS detector". In: *Phys. Lett.* 790 (2019), p. 595. arXiv: 1811.11094 [hep-ex].

[22] Albert M Sirunyan et al. "Evidence for WW production from double-parton interactions in proton–proton collisions at $\sqrt{s} = 13\,\text{TeV}$". In: *Eur. Phys. J. C* 80.1 (2020), p. 41. arXiv: 1909.06265 [hep-ex].

[23] Armen Tumasyan et al. "Observation of triple J/$\psi$ meson production in proton-proton collisions". In: *Nature Phys.* 19.3 (2023). [Erratum: Nature Phys. 19, (2023)], pp. 338–350. arXiv: 2111.05370 [hep-ex].

[24] Armen Tumasyan et al. "Observation of same-sign WW production from double parton scattering in proton-proton collisions at $\sqrt{s} = 13$ TeV". In: *Phys. Rev. Lett.* 131 (2023), p. 091803. arXiv: 2206.02681 [hep-ex].

[25] Georges Aad et al. "Observation of double parton scattering in same-sign W boson pair production in pp collisions at s=13 TeV with the ATLAS detector". In: *Phys. Lett. B* 870 (2025), p. 139892. arXiv: 2505.08313 [hep-ex].

[26] Mieczyslaw Witold Krasny and Wieslaw Placzek. "On the contribution of the double Drell-Yan process to WW and ZZ production at the LHC". In: *Acta Phys. Polon. B* 47 (2016), pp. 1045–1056. arXiv: 1501.04569 [hep-ph].

[27] N. Paver and D. Treleani. "Multi-Parton Processes and the Drell-Yan Cross Section at Collider Energies". In: *Nuovo Cim. A* 70 (1982), pp. 215–236.

[28] Jonathan R. Gaunt et al. "Same-sign W pair production as a probe of double parton scattering at the LHC". In: *Eur. Phys. J. C* 69 (2010), pp. 53–65. arXiv: 1003.3953 [hep-ph].

[29] Markus Diehl et al. "Two-loop splitting in double parton distributions". In: *SciPost Phys.* 7.2 (2019), p. 017. arXiv: 1902.08019 [hep-ph].

[30] Markus Diehl, Daniel Ostermeier, and Andreas Schäfer. "Elements of a theory for multiparton interactions in QCD". In: *JHEP* 03 (2012). [Erratum: JHEP 03, 001 (2016)], p. 089. arXiv: 1111.0910 [hep-ph].

[31] Gunnar S. Bali et al. "Double parton distributions in the nucleon from lattice QCD". In: *Journal of High Energy Physics* 2021.9 (Sept. 2021). ISSN: 1029-8479. URL: http://dx.doi.org/10.1007/JHEP09(2021)106.

[32] Daniel Reitinger et al. "Double parton distributions with flavor interference from lattice QCD". In: *JHEP* 04 (2024), p. 087. arXiv: 2401.14855 [hep-lat].

[33] Keh-Fei Liu and Shao-Jing Dong. "Origin of difference between anti-d and anti-u partons in the nucleon". In: *Phys. Rev. Lett.* 72 (1994), pp. 1790–1793. arXiv: hep-ph/9306299.

[34] William Detmold and C. J. David Lin. "Deep-inelastic scattering and the operator product expansion in lattice QCD". In: *Phys. Rev. D* 73 (2006), p. 014501. arXiv: hep-lat/0507007.

[35] V. Braun and Dieter Müller. "Exclusive processes in position space and the pion distribution amplitude". In: *Eur. Phys. J. C* 55 (2008), pp. 349–361. arXiv: 0709.1348 [hep-ph].

[36] Zohreh Davoudi and Martin J. Savage. "Restoration of Rotational Symmetry in the Continuum Limit of Lattice Field Theories". In: *Phys. Rev. D* 86 (2012), p. 054505. arXiv: 1204.4146 [hep-lat].

[37] Xiangdong Ji. "Parton Physics on a Euclidean Lattice". In: *Phys. Rev. Lett.* 110 (2013), p. 262002. arXiv: 1305.1539 [hep-ph].

[38] A. V. Radyushkin. "Quasi-parton distribution functions, momentum distributions, and pseudo-parton distribution functions". In: *Phys. Rev. D* 96.3 (2017), p. 034025. arXiv: 1705.01488 [hep-ph].

[39] Yan-Qing Ma and Jian-Wei Qiu. "Exploring Partonic Structure of Hadrons Using ab initio Lattice QCD Calculations". In: *Phys. Rev. Lett.* 120.2 (2018), p. 022003. arXiv: 1709.03018 [hep-ph].

[40] A. J. Chambers et al. "Nucleon Structure Functions from Operator Product Expansion on the Lattice". In: *Phys. Rev. Lett.* 118.24 (2017), p. 242001. arXiv: 1703.01153 [hep-lat].

[41] Andrea Shindler. "Moments of parton distribution functions of any order from lattice QCD". In: *Phys. Rev. D* 110.5 (2024), p. L051503. arXiv: 2311.18704 [hep-lat].

[42] Xiang-Dong Ji. "Off forward parton distributions". In: *J. Phys. G* 24 (1998), pp. 1181–1205. arXiv: hep-ph/9807358.

[43] Krzysztof Cichy and Martha Constantinou. "A guide to light-cone PDFs from Lattice QCD: an overview of approaches, techniques and results". In: *Adv. High Energy Phys.* 2019 (2019), p. 3036904. arXiv: 1811.07248 [hep-lat].

[44] Yu-Sheng Liu et al. "Unpolarized isovector quark distribution function from lattice QCD: A systematic analysis of renormalization and matching". In: *Phys. Rev. D* 101.3 (2020), p. 034020. arXiv: 1807.06566 [hep-lat].

[45] Jian-Hui Zhang et al. "Accessing Gluon Parton Distributions in Large Momentum Effective Theory". In: *Phys. Rev. Lett.* 122.14 (2019), p. 142001. arXiv: 1808.10824 [hep-ph].

[46] Zhou-You Fan et al. "Gluon Quasi-Parton-Distribution Functions from Lattice QCD". In: *Phys. Rev. Lett.* 121.24 (2018), p. 242001. arXiv: 1808.02077 [hep-lat].

[47] Taku Izubuchi et al. "Valence parton distribution function of pion from fine lattice". In: *Phys. Rev. D* 100.3 (2019), p. 034516. arXiv: 1905.06349 [hep-lat].

[48] Yahui Chai et al. "Parton distribution functions of $\Delta^+$ on the lattice". In: *Phys. Rev. D* 102.1 (2020), p. 014508. arXiv: 2002.12044 [hep-lat].

[49] Xiangdong Ji et al. "A hybrid renormalization scheme for quasi light-front correlations in large-momentum effective theory". In: *Nucl. Phys. B* 964 (2021), p. 115311. arXiv: 2008.03886 [hep-ph].

[50] Huey-Wen Lin et al. "Valence-Quark Distribution of the Kaon and Pion from Lattice QCD". In: *Phys. Rev. D* 103.1 (2021), p. 014516. arXiv: 2003.14128 [hep-lat].

[51] Zhouyou Fan et al. "Isovector parton distribution functions of the proton on a superfine lattice". In: *Phys. Rev. D* 102.7 (2020), p. 074504. arXiv: 2005.12015 [hep-lat].

[52] Xiang Gao et al. "Lattice QCD Determination of the Bjorken-x Dependence of Parton Distribution Functions at Next-to-Next-to-Leading Order". In: *Phys. Rev. Lett.* 128.14 (2022), p. 142003. arXiv: 2112.02208 [hep-lat].

[53] Yushan Su et al. "Resumming quark's longitudinal momentum logarithms in LaMET expansion of lattice PDFs". In: *Nucl. Phys. B* 991 (2023), p. 116201. arXiv: 2209.01236 [hep-ph].

[54] Jun Hua et al. "Pion and Kaon Distribution Amplitudes from Lattice QCD". In: *Phys. Rev. Lett.* 129.13 (2022), p. 132001. arXiv: 2201.09173 [hep-lat].

[55] Fei Yao and others (Lattice Parton collaboration). "Nucleon Transversity Distribution in the Continuum and Physical Mass Limit from Lattice QCD". In: *Phys. Rev. Lett.* 131.26 (2023), p. 261901. arXiv: 2208.08008 [hep-lat].

[56] Xue-Ying Han and others (Lattice Parton Collaboration (LPC)). "Calculation of heavy meson light-cone distribution amplitudes from lattice QCD". In: *Phys. Rev. D* 111.3 (2025), p. 034503. arXiv: 2410.18654 [hep-lat].

[57] Xiang Gao et al. "Unpolarized proton PDF at NNLO from lattice QCD with physical quark masses". In: *Phys. Rev. D* 107.7 (2023), p. 074509. arXiv: 2212.12569 [hep-lat].

[58] Xiang Gao et al. "Transversity PDFs of the proton from lattice QCD with physical quark masses". In: *Phys. Rev. D* 109.5 (2024), p. 054506. arXiv: 2310.19047 [hep-lat].

[59] Chen Chen et al. "Parton distribution function of a deuteronlike dibaryon system from lattice QCD". In: *Phys. Rev. D* 111.7 (2025), p. 074506. arXiv: 2408.12819 [hep-lat].

[60] Jack Holligan and Huey-Wen Lin. "Pion valence quark distribution at physical pion mass of N $_f = 2 + 1 + 1$ lattice QCD". In: *J. Phys. G* 51.6 (2024), p. 065101. arXiv: 2404.14525 [hep-lat].

[61] Jack Holligan and Huey-Wen Lin. "Nucleon helicity parton distribution function in the continuum limit with self-renormalization". In: *Phys. Lett. B* 854 (2024), p. 138731. arXiv: 2405.18238 [hep-lat].

[62] Xiangdong Ji et al. "Effects of threshold resummation for large-x PDF in large momentum effective theory". In: *JHEP* 03 (2025), p. 045. arXiv: 2410.12910 [hep-ph].

[63] Kuan Zhang et al. "Impact of gauge fixing precision on the continuum limit of nonlocal quark-bilinear lattice operators". In: *Phys. Rev. D* 110.7 (2024), p. 074505. arXiv: 2405.14097 [hep-lat].

[64] Talal Ahmed Chowdhury et al. "Polarized and unpolarized gluon PDFs: Generative machine learning applications for lattice QCD matrix elements at short distance and large momentum". In: *Phys. Rev. D* 111.7 (2025), p. 074509. arXiv: 2409.17234 [hep-lat].

[65] Chen Chen et al. "Unpolarized gluon PDF of the nucleon from lattice QCD in the continuum limit". In: (Oct. 2025). arXiv: 2510.26425 [hep-lat].

[66] Alex NieMiera et al. "Systematic Study of the Self-Renormalized Nucleon Gluon PDF in Large-Momentum Effective Theory". In: (Nov. 2025). arXiv: 2511.14708 [hep-lat].

[67] Ian Cloet et al. "Lattice QCD calculation of x-dependent meson distribution amplitudes at physical pion mass with threshold logarithm resummation". In: *Phys. Rev. D* 110.11 (2024), p. 114502. arXiv: 2407.00206 [hep-lat].

[68] Rui Zhang et al. "Kinematically enhanced interpolating operators for boosted hadrons". In: *Phys. Rev. D* 112.5 (2025), p. L051502. arXiv: 2501.00729 [hep-lat].

[69] Markus Diehl et al. “Extracting Mellin moments of double parton distributions from lattice data”. In: (Nov. 2025). arXiv: 2511.15546 [hep-lat].

[70] Daniel Reitinger et al. “Kinematic enhancement for nucleon interpolators”. In: (June 2026). arXiv: 2606.02447 [hep-lat].

[71] Michael E. Peskin and Daniel V. Schroeder. *An Introduction to quantum field theory*. Reading, USA: Addison-Wesley, 1995. ISBN: 978-0-201-50397-5, 978-0-429-50355-9, 978-0-429-49417-8.

[72] John Collins. *Foundations of Perturbative QCD*. Vol. 32. Cambridge University Press, 2011. ISBN: 978-1-009-40184-5, 978-1-009-40183-8, 978-1-009-40182-1.

[73] Markus Diehl, Daniel Ostermeier, and Andreas Schäfer. “Elements of a theory for multiparton interactions in QCD”. In: *Journal of High Energy Physics* 2012.3 (Mar. 2012). ISSN: 1029-8479. URL: http://dx.doi.org/10.1007/JHEP03(2012)089.

[74] Markus Diehl and Jonathan R. Gaunt. *Double parton scattering theory overview*. 2017. arXiv: 1710.04408 [hep-ph]. URL: https://arxiv.org/abs/1710.04408.

[75] David J. Gross and Frank Wilczek. “Ultraviolet Behavior of Nonabelian Gauge Theories”. In: *Phys. Rev. Lett.* 30 (1973), pp. 1343–1346.

[76] H. David Politzer. “Reliable Perturbative Results for Strong Interactions?” In: *Phys. Rev. Lett.* 30 (1973), pp. 1346–1349.

[77] John C. Collins, Davison E. Soper, and George F. Sterman. “Factorization of Hard Processes in QCD”. In: *Adv. Ser. Direct. High Energy Phys.* 5 (1989), pp. 1–91. arXiv: hep-ph/0409313.

[78] T. Åkesson et al. “Double Parton Scattering in $pp$ Collisions at $\sqrt{s} = 63$ GeV”. In: *Z. Phys. C* 34 (1987), p. 163.

[79] J. Alitti et al. “A Study of multi-jet events at the CERN $\bar{p}p$ collider and a search for double parton scattering”. In: *Phys. Lett. B* 268 (1991), pp. 145–154.

[80] F. Abe et al. “Study of four-jet events and evidence for double parton interactions in $p\bar{p}$ collisions at $\sqrt{s} = 1.8$ TeV”. In: *Phys. Rev. D* 47 (1993), pp. 4857–4871.

[81] F. Abe et al. “Double parton scattering in $\bar{p}p$ collisions at $\sqrt{s} = 1.8$TeV”. In: *Phys. Rev. D* 56 (1997), pp. 3811–3832.

[82] G. Aad et al. “Measurement of hard double-parton interactions in $W(\rightarrow l\nu) + 2$ jet events at $\sqrt{s} = 7$ TeV with the ATLAS detector”. In: *New J. Phys.* 15 (2013), p. 033038. arXiv: 1301.6872 [hep-ex].

[83] Victor Mukhamedovich Abazov et al. “Double Parton Interactions in $\gamma + 3$ Jet and $\gamma + b/cjet + 2$ Jet Events in $p\bar{p}$ Collisions at $\sqrt{s} = 1.96$ TeV”. In: *Phys. Rev. D* 89.7 (2014), p. 072006. arXiv: 1402.1550 [hep-ex].

[84] S. Chatrchyan et al. "Study of double parton scattering using $W$ + 2-jet events in proton-proton collisions at $\sqrt{s} = 7$ TeV". In: *JHEP* 03 (2014), p. 032. arXiv: 1312.5729 [hep-ex].

[85] Victor Mukhamedovich Abazov et al. "Study of double parton interactions in diphoton + dijet events in $p\bar{p}$ collisions at $\sqrt{s} = 1.96$ TeV". In: *Phys. Rev. D* 93.5 (2016), p. 052008. arXiv: 1512.05291 [hep-ex].

[86] Morad Aaboud et al. "Study of hard double-parton scattering in four-jet events in pp collisions at $\sqrt{s} = 7$ TeV with the ATLAS experiment". In: *JHEP* 11 (2016), p. 110. arXiv: 1608.01857 [hep-ex].

[87] Roel Aaij et al. "Production of associated Y and open charm hadrons in pp collisions at $\sqrt{s} = 7$ and 8 TeV via double parton scattering". In: *JHEP* 07 (2016), p. 052. arXiv: 1510.05949 [hep-ex].

[88] Morad Aaboud et al. "Measurement of the prompt J/ $\psi$ pair production cross-section in pp collisions at $\sqrt{s} = 8$ TeV with the ATLAS detector". In: *Eur. Phys. J. C* 77.2 (2017), p. 76. arXiv: 1612.02950 [hep-ex].

[89] Roel Aaij et al. "Measurement of the J/$\psi$ pair production cross-section in pp collisions at $\sqrt{s} = 13$ TeV". In: *JHEP* 06 (2017). [Erratum: JHEP 10, 068 (2017)], p. 047. arXiv: 1612.07451 [hep-ex].

[90] Jean-Philippe Lansberg, Hua-Sheng Shao, and Nodoka Yamanaka. "Indication for double parton scatterings in $W+$ prompt $J/\psi$ production at the LHC". In: *Phys. Lett. B* 781 (2018), pp. 485–491. arXiv: 1707.04350 [hep-ph].

[91] Albert M Sirunyan et al. "Constraints on the double-parton scattering cross section from same-sign W boson pair production in proton-proton collisions at $\sqrt{s} = 8$ TeV". In: *JHEP* 02 (2018), p. 032. arXiv: 1712.02280 [hep-ex].

[92] Armen Tumasyan et al. "Measurement of double-parton scattering in inclusive production of four jets with low transverse momentum in proton-proton collisions at $\sqrt{s} = 13$ TeV". In: *JHEP* 01 (2022), p. 177. arXiv: 2109.13822 [hep-ex].

[93] Alessandro Lovato et al. *Momentum fraction and hard scale dependence of double parton scattering in heavy-ion collisions.* arXiv:2603.04510 [hep-ph]. 2025. arXiv: 2603.04510 [hep-ph].

[94] Tiancai Peng et al. "Double parton distributions of the proton from basis light-front quantization". In: *Phys. Rev. D* 112 (2025), p. 014018. arXiv: 2410.11574 [hep-ph].

[95] Jonathan R. Gaunt and W. James Stirling. "Double Parton Distributions Incorporating Perturbative QCD Evolution and Momentum and Quark Number Sum Rules". In: *JHEP* 03 (2010), p. 005. arXiv: 0910.4347 [hep-ph].

[96] Markus Diehl and Peter Plößl. *A quantitative study of two-loop splitting in double parton distributions.* arXiv:2602.18233 [hep-ph]. 2026. arXiv: 2602.18233 [hep-ph].

[97] Matthias Burkardt. "Light front quantization". In: *Adv. Nucl. Phys.* 23 (1996), pp. 1–74. arXiv: hep-ph/9505259.

[98] Markus Diehl and Thierry Gousset. "Time ordering in off diagonal parton distributions". In: *Phys. Lett. B* 428 (1998), pp. 359–370. arXiv: hep-ph/9801233.

[99] John C. Collins. "Leading twist single transverse-spin asymmetries: Drell-Yan and deep inelastic scattering". In: *Phys. Lett. B* 536 (2002), pp. 43–48. arXiv: hep-ph/0204004.

[100] M. Diehl. "Generalized parton distributions". In: *Phys. Rept.* 388 (2003), pp. 41–277. arXiv: hep-ph/0307382.

[101] Jun John Sakurai and Jim Napolitano. *Modern Quantum Mechanics*. 3rd ed. Quantum physics, quantum information and quantum computation. Cambridge University Press, Oct. 2020. ISBN: 978-0-8053-8291-4, 978-1-108-52742-2, 978-1-108-58728-0.

[102] Yuri L. Dokshitzer. "Calculation of the Structure Functions for Deep Inelastic Scattering and $e^+e^-$ Annihilation by Perturbation Theory in Quantum Chromodynamics". In: *Sov. Phys. JETP* 46 (1977). Zh. Eksp. Teor. Fiz. 73 (1977) 1216, pp. 641–653.

[103] V. N. Gribov and L. N. Lipatov. "Deep inelastic *ep* scattering in perturbation theory". In: *Sov. J. Nucl. Phys.* 15 (1972), pp. 438–450.

[104] Guido Altarelli and Giorgio Parisi. "Asymptotic Freedom in Parton Language". In: *Nucl. Phys. B* 126 (1977), pp. 298–318.

[105] Markus Diehl and Andreas Schafer. "Theoretical considerations on multiparton interactions in QCD". In: *Phys. Lett. B* 698 (2011), pp. 389–402. arXiv: 1102.3081 [hep-ph].

[106] Gunnar S. Bali et al. "Double parton distributions in the pion from lattice QCD". In: *JHEP* 02 (2021), p. 067. arXiv: 2006.14826 [hep-lat].

[107] Jonathan Gaunt. "Double parton scattering in proton-proton collisions". PhD thesis. Cambridge U., Oct. 2012.

[108] Markus Diehl, P. Plößl, and A. Schäfer. "Proof of sum rules for double parton distributions in QCD". In: *Eur. Phys. J. C* 79.3 (2019), p. 253. arXiv: 1811.00289 [hep-ph].

[109] Markus Diehl et al. "Cancellation of Glauber gluon exchange in the double Drell-Yan process". In: *JHEP* 01 (2016), p. 076. arXiv: 1510.08696 [hep-ph].

[110] Ted C. Rogers and Piet J. Mulders. "No Generalized TMD-Factorization in Hadro-Production of High Transverse Momentum Hadrons". In: *Phys. Rev. D* 81 (2010), p. 094006. arXiv: 1001.2977 [hep-ph].

[111] Aneesh V. Manohar and Wouter J. Waalewijn. "A QCD Analysis of Double Parton Scattering: Color Correlations, Interference Effects and Evolution". In: *Phys. Rev. D* 85 (2012), p. 114009. arXiv: 1202.3794 [hep-ph].

[112] Markus Diehl, Florian Fabry, and Peter Ploessl. "Evolution of colour correlated double parton distributions: a quantitative study". In: *JHEP* 02 (2024), p. 229. arXiv: 2310.16432 [hep-ph].

[113] Alexey Vladimirov. "Soft factors for double parton scattering at NNLO". In: *JHEP* 12 (2016), p. 038. arXiv: 1608.04920 [hep-ph].

[114] Markus Diehl, Jonathan R. Gaunt, and Kay Schönwald. "Double hard scattering without double counting". In: *JHEP* 06 (2017), p. 083. arXiv: 1702.06486 [hep-ph].

[115] Christof Gattringer and Christian B. Lang. *Quantum chromodynamics on the lattice*. Vol. 788. Berlin: Springer, 2010. ISBN: 978-3-642-01849-7, 978-3-642-01850-3.

[116] Martin Luscher and Stefan Schaefer. "Lattice QCD without topology barriers". In: *JHEP* 07 (2011), p. 036. arXiv: 1105.4749 [hep-lat].

[117] Holger Bech Nielsen and M. Ninomiya. "Absence of Neutrinos on a Lattice. 1. Proof by Homotopy Theory". In: *Nucl. Phys. B* 185 (1981). Ed. by J. Julve and M. Ramón-Medrano. [Erratum: Nucl.Phys.B 195, 541 (1982)], p. 20.

[118] B. Sheikholeslami and R. Wohlert. "Improved Continuum Limit Lattice Action for QCD with Wilson Fermions". In: *Nucl. Phys. B* 259 (1985), p. 572.

[119] John Bulava and Stefan Schaefer. "Improvement of $N_f = 3$ lattice QCD with Wilson fermions and tree-level improved gauge action". In: *Nucl. Phys. B* 874 (2013), pp. 188–197. arXiv: 1304.7093 [hep-lat].

[120] M. Luscher and P. Weisz. "On-shell improved lattice gauge theories". In: *Commun. Math. Phys.* 98.3 (1985). [Erratum: Commun.Math.Phys. 98, 433 (1985)], p. 433.

[121] Daniel Mohler and Stefan Schaefer. "Remarks on strange-quark simulations with Wilson fermions". In: *Phys. Rev. D* 102.7 (2020), p. 074506. arXiv: 2003.13359 [hep-lat].

[122] Martin Luscher and Filippo Palombi. "Fluctuations and reweighting of the quark determinant on large lattices". In: *PoS* LATTICE2008 (2008). Ed. by Christopher Aubin et al., p. 049. arXiv: 0810.0946 [hep-lat].

[123] Martin Luscher and Stefan Schaefer. "Lattice QCD with open boundary conditions and twisted-mass reweighting". In: *Comput. Phys. Commun.* 184 (2013), pp. 519–528. arXiv: 1206.2809 [hep-lat].

[124] S. Duane et al. "Hybrid Monte Carlo". In: *Phys. Lett. B* 195 (1987), pp. 216–222.

[125] Stefan Schaefer, Rainer Sommer, and Francesco Virotta. "Critical slowing down and error analysis in lattice QCD simulations". In: *Nucl. Phys. B* 845 (2011), pp. 93–119. arXiv: 1009.5228 [hep-lat].

[126] Martin Hasenbusch. "Speeding up the hybrid Monte Carlo algorithm for dynamical fermions". In: *Phys. Lett. B* 519 (2001), pp. 177–182. arXiv: hep-lat/0107019.

[127] Martin Hasenbusch. "Full QCD algorithms towards the chiral limit". In: *Nucl. Phys. B Proc. Suppl.* 129 (2004). Ed. by S. Aoki et al., pp. 27–33. arXiv: hep-lat/0310029.

[128] A. D. Kennedy, Ivan Horvath, and Stefan Sint. "A New exact method for dynamical fermion computations with nonlocal actions". In: *Nucl. Phys. B Proc. Suppl.* 73 (1999). Ed. by Thomas A. DeGrand et al., pp. 834–836. arXiv: hep-lat/9809092.

[129] M. A. Clark and A. D. Kennedy. "Accelerating dynamical fermion computations using the rational hybrid Monte Carlo (RHMC) algorithm with multiple pseudofermion fields". In: *Phys. Rev. Lett.* 98 (2007), p. 051601. arXiv: hep-lat/0608015.

[130] Simon Kuberski. "Low-mode deflation for twisted-mass and RHMC reweighting in lattice QCD". In: *Comput. Phys. Commun.* 300 (2024), p. 109173. arXiv: 2306.02385 [hep-lat].

[131] Mattia Bruno et al. "Simulation of QCD with $N_f = 2 + 1$ flavors of non-perturbatively improved Wilson fermions". In: *JHEP* 02 (2015), p. 043. arXiv: 1411.3982 [hep-lat].

[132] Daniel Mohler, Stefan Schaefer, and Jakob Simeth. "CLS 2+1 flavor simulations at physical light- and strange-quark masses". In: *EPJ Web Conf.* 175 (2018). Ed. by M. Della Morte et al., p. 02010. arXiv: 1712.04884 [hep-lat].

[133] Gunnar S. Bali et al. "Lattice simulations with $N_f = 2 + 1$ improved Wilson fermions at a fixed strange quark mass". In: *Phys. Rev. D* 94.7 (2016), p. 074501. arXiv: 1606.09039 [hep-lat].

[134] Christian Zimmermann. "Double Parton Distributions in the Nucleon on the Lattice". PhD thesis. Regensburg U., 2020.

[135] Justin Foley et al. "Practical all-to-all propagators for lattice QCD". In: *Comput. Phys. Commun.* 172 (2005), pp. 145–162. arXiv: hep-lat/0505023.

[136] G. Martinelli and C. T. Sachrajda. "A lattice study of nucleon structure". In: *Nucl. Phys. B* 316 (1989), pp. 355–372.

[137] Gunnar S. Bali et al. "Novel quark smearing for hadrons with high momenta in lattice QCD". In: *Physical Review D* 93.9 (May 2016). ISSN: 2470-0029. URL: http://dx.doi.org/10.1103/PhysRevD.93.094515.

[138] S. Gusken et al. "Nonsinglet Axial Vector Couplings of the Baryon Octet in Lattice QCD". In: *Phys. Lett. B* 227 (1989), pp. 266–269.

[139] M. Albanese et al. "Glueball masses and string tension in lattice QCD". In: *Physics Letters B* 192.1 (1987), pp. 163–169. ISSN: 0370-2693. URL: https://www.sciencedirect.com/science/article/pii/0370269387911609.

[140] G. Parisi. "The Strategy for Computing the Hadronic Mass Spectrum". In: *Phys. Rept.* 103 (1984). Ed. by C. Itzykson, Y. Pomeau, and N. Sourlas, pp. 203–211.

[141] G. Peter Lepage. "The Analysis of Algorithms for Lattice Field Theory". In: *Theoretical Advanced Study Institute in Elementary Particle Physics*. June 1989.

[142] Frank X. Lee and Derek B. Leinweber. "Negative parity baryon spectroscopy". In: *Nucl. Phys. B Proc. Suppl.* 73 (1999). Ed. by Thomas A. DeGrand et al., pp. 258–260. arXiv: hep-lat/9809095.

[143] Finn M. Stokes et al. "Electromagnetic Form Factors of Excited Nucleons via Parity-Expanded Variational Analysis". In: *PoS* LATTICE2016 (2016), p. 161. arXiv: 1701.07177 [hep-lat].

[144] Jialu Zhang et al. "Parton Distribution Functions from Large Momentum Expansion of Current-Current Correlators". In: (May 2026). arXiv: 2605.03234 [hep-ph].

[145] Konstantin Ottnad. "Excited states in nucleon structure calculations". In: *Eur. Phys. J. A* 57.2 (2021), p. 50. arXiv: 2011.12471 [hep-lat].

[146] Hans Dembinski and Piti Ongmongkolkul et al. "scikit-hep/iminuit". In: (Dec. 2020). URL: https://doi.org/10.5281/zenodo.3949207.

[147] F. James and M. Roos. "Minuit: A System for Function Minimization and Analysis of the Parameter Errors and Correlations". In: *Comput. Phys. Commun.* 10 (1975), pp. 343–367.

[148] Constantia Alexandrou et al. "Pion and kaon <x3> from lattice QCD and PDF reconstruction from Mellin moments". In: *Phys. Rev. D* 104.5 (2021), p. 054504. arXiv: 2104.02247 [hep-lat].

[149] Anthony Francis et al. "Probing higher moments of pion parton distribution functions". In: *PoS* LATTICE2024 (2025), p. 336. arXiv: 2412.01750 [hep-lat].

[150] Anthony Francis et al. "Moments of parton distributions functions of the pion from lattice QCD using gradient flow". In: (Oct. 2025). arXiv: 2510.26738 [hep-lat].

[151] Zhuoyi Pang, Jian-Hui Zhang, and Dian-Jun Zhao. "Moments from momentum derivatives in lattice QCD*". In: *Chin. Phys.* 49.10 (2025), p. 101001. arXiv: 2412.19862 [hep-lat].

[152] M. Gockeler et al. "Nonperturbative renormalization of composite operators in lattice QCD". In: *Nucl. Phys. B* 544 (1999), pp. 699–733. arXiv: hep-lat/9807044.

[153] G. Martinelli et al. "A general method for non-perturbative renormalization of lattice operators". In: *Nucl. Phys. B* 445 (1995), pp. 81–108. arXiv: hep-lat/9411010.

[154] G. S. Bali et al. "Nonperturbative renormalization in lattice QCD with three flavors of clover fermions: Using periodic and open boundary conditions". In: *Physical Review D* 103.9 (May 2021). ISSN: 2470-0029. URL: http://dx.doi.org/10.1103/PhysRevD.103.094511.

[155] Gunnar S. Bali et al. “Double parton distributions in the nucleon from lattice QCD”. In: *JHEP* 09 (2021), p. 106. arXiv: 2106.03451 [hep-lat].

[156] Taku Izubuchi et al. “Factorization Theorem Relating Euclidean and Light-Cone Parton Distributions”. In: *Phys. Rev. D* 98.5 (2018), p. 056004. arXiv: 1801.03917 [hep-ph].

[157] Xiaonu Xiong et al. “One-loop matching for parton distributions: Nonsinglet case”. In: *Phys. Rev. D* 90.1 (2014), p. 014051. arXiv: 1310.7471 [hep-ph].

[158] Long-Bin Chen, Wei Wang, and Ruilin Zhu. “Next-to-Next-to-Leading Order Calculation of Quasiparton Distribution Functions”. In: *Phys. Rev. Lett.* 126.7 (2021), p. 072002. arXiv: 2006.14825 [hep-ph].

[159] Xiang Gao et al. “Origin and resummation of threshold logarithms in the lattice QCD calculations of PDFs”. In: *Phys. Rev. D* 103.9 (2021), p. 094504. arXiv: 2102.01101 [hep-ph].

[160] Jack Holligan and Huey-Wen Lin. “Systematic improvement of x-dependent unpolarized nucleon generalized parton distributions in lattice-QCD calculation”. In: *Phys. Rev. D* 110.3 (2024), p. 034503. arXiv: 2312.10829 [hep-lat].

[161] Rui Zhang et al. “Leading power accuracy in lattice calculations of parton distributions”. In: *Phys. Lett. B* 844 (2023), p. 138081. arXiv: 2305.05212 [hep-lat].

[162] Xiang Gao et al. “Nucleon Parton Distribution Functions from Boosted Correlations in the Coulomb gauge”. In: (Feb. 2026). arXiv: 2602.11283 [hep-lat].

[163] Joshua Miller et al. “Pion and Kaon PDFs from Lattice QCD with Complementary Approaches”. In: (Dec. 2025). arXiv: 2512.06121 [hep-lat].

[164] Jiunn-Wei Chen et al. “Symmetry properties of nonlocal quark bilinear operators on a Lattice”. In: *Chin. Phys. C* 43.10 (2019), p. 103101. arXiv: 1710.01089 [hep-lat].

[165] Xiangdong Ji et al. “A Hybrid Renormalization Scheme for Quasi Light-Front Correlations in Large-Momentum Effective Theory”. In: *Nucl. Phys. B* 964 (2021), p. 115311. arXiv: 2008.03886 [hep-ph].

[166] Kostas Orginos et al. “Lattice QCD exploration of parton pseudo-distribution functions”. In: *Phys. Rev. D* 96.9 (2017), p. 094503. arXiv: 1706.05373 [hep-ph].

[167] Anatoly V. Radyushkin. “One-loop evolution of parton pseudo-distribution functions on the lattice”. In: *Phys. Rev. D* 98.1 (2018), p. 014019. arXiv: 1801.02427 [hep-ph].

[168] Yi-Kai Huo et al. “Self-renormalization of quasi-light-front correlators on the lattice”. In: *Nucl. Phys. B* 969 (2021), p. 115443. arXiv: 2103.02965 [hep-ph].

[169] Yi-Kai Huo and others (Lattice Parton Collaboration (LPC)). “Self-renormalization of quasi-light-front correlators on the lattice”. In: *Nucl. Phys. B* 969 (2021), p. 115443. arXiv: 2103.02965 [hep-lat].

[170] Christian Zimmermann et al. “The hadronic tensor from four-point functions on the lattice”. In: *42th International Symposium on Lattice Field Theory*. Feb. 2026. arXiv: 2602.22379 [hep-lat].

[171] Daniel Reitinger, Christian Zimmermann, and Andreas Schäfer. “Double Parton Distributions in the nucleon: Lattice parameter dependence”. In: (Sept. 2026). arXiv: 2609.02752 [hep-lat].

[172] Gunnar S. Bali et al. “Two-current correlations in the pion on the lattice”. In: *JHEP* 12 (2018), p. 061. arXiv: 1807.03073 [hep-lat].

[173] Gunnar S. Bali et al. “Scale setting and the light baryon spectrum in Nf = 2 + 1 QCD with Wilson fermions”. In: *Journal of High Energy Physics* 2023.5 (May 2023). ISSN: 1029-8479. URL: http://dx.doi.org/10.1007/JHEP05(2023)035.

[174] Gunnar S. Bali et al. “Novel quark smearing for hadrons with high momenta in lattice QCD”. In: *Phys. Rev. D* 93.9 (2016), p. 094515. arXiv: 1602.05525 [hep-lat].

[175] Robert G. Edwards and Balint Joo. “The Chroma software system for lattice QCD”. In: *Nucl. Phys. B Proc. Suppl.* 140 (2005). Ed. by Geoffrey T. Bodwin et al., p. 832. arXiv: hep-lat/0409003.

[176] Daniel Reitinger et al. “Double parton distributions with flavor interference from lattice QCD”. In: *Journal of High Energy Physics* 2024.4 (Apr. 2024). ISSN: 1029-8479. URL: http://dx.doi.org/10.1007/JHEP04(2024)087.

[177] Gunnar S. Bali et al. “Double parton distributions in the pion from lattice QCD”. In: *Journal of High Energy Physics* 2021.2 (Feb. 2021). ISSN: 1029-8479. URL: http://dx.doi.org/10.1007/JHEP02(2021)067.

[178] Gunnar S. Bali et al. “Two-current correlations in the pion on the lattice”. In: *Journal of High Energy Physics* 2018.12 (Dec. 2018). ISSN: 1029-8479. URL: http://dx.doi.org/10.1007/JHEP12(2018)061.

[179] Gunnar S. Bali et al. “Pion distribution amplitude from Euclidean correlation functions”. In: *Eur. Phys. J. C* 78.3 (2018). Ed. by M. Della Morte et al., p. 217. arXiv: 1709.04325 [hep-lat].

[180] Gunnar S. Bali et al. “Pion distribution amplitude from Euclidean correlation functions: Exploring universality and higher-twist effects”. In: *Phys. Rev. D* 98.9 (2018), p. 094507. arXiv: 1807.06671 [hep-lat].

[181] Gunnar S. Bali et al. “Scale setting and the light baryon spectrum in $N_f = 2 + 1$ QCD with Wilson fermions”. In: *JHEP* 05 (2023), p. 035. arXiv: 2211.03744 [hep-lat].

[182] Alessandro Conigli et al. “Precision lattice calculation of the hadronic contribution to the running of the electroweak gauge couplings”. In: (Nov. 2025). arXiv: 2511.01623 [hep-lat].

[183] G. S. Bali et al. "Nonperturbative Renormalization in Lattice QCD with three Flavors of Clover Fermions: Using Periodic and Open Boundary Conditions". In: *Phys. Rev. D* 103.9 (2021). [Erratum: Phys.Rev.D 107, 039901 (2023)], p. 094511. arXiv: 2012.06284 [hep-lat].

[184] A. V. Radyushkin. "Nonforward parton distributions". In: *Phys. Rev. D* 56 (1997), pp. 5524–5557. arXiv: hep-ph/9704207.

[185] Xiang Gao, Wei-Yang Liu, and Yong Zhao. "Parton distributions from boosted fields in the Coulomb gauge". In: *Phys. Rev. D* 109.9 (2024), p. 094506. arXiv: 2306.14960 [hep-ph].

[186] Yong Zhao. "Transverse Momentum Distributions from Lattice QCD without Wilson Lines". In: *Phys. Rev. Lett.* 133.24 (2024), p. 241904. arXiv: 2311.01391 [hep-ph].

[187] Jack Holligan et al. "Resummation for lattice QCD calculation of generalized parton distributions at nonzero skewness". In: *JHEP* 207 (2025), p. 241. arXiv: 2501.19225 [hep-ph].

[188] Dennis Bollweg et al. "Transverse-momentum-dependent pion structures from lattice QCD: Collins-Soper kernel, soft factor, TMDWF, and TMDPDF". In: *Phys. Rev. D* 112.3 (2025), p. 034501. arXiv: 2504.04625 [hep-lat].

[189] Jin-Xin Tan et al. "Lattice QCD determination of the Collins-Soper kernel in the continuum and physical mass limits". In: *Phys. Rev. D* 113.5 (2026), p. 054505. arXiv: 2511.22547 [hep-lat].

[190] Dian-Jun Zhao et al. "Total Gluon Helicity Contribution to the Proton Spin from Lattice QCD". In: (Dec. 2025). arXiv: 2512.24315 [hep-lat].

[191] M.A. Clark et al. "Solving lattice QCD systems of equations using mixed precision solvers on GPUs". In: *Computer Physics Communications* 181.9 (Sept. 2010), pp. 1517–1528. ISSN: 0010-4655. URL: http://dx.doi.org/10.1016/j.cpc.2010.05.002.

[192] R. Babich et al. "Scaling lattice QCD beyond 100 GPUs". In: *Proceedings of 2011 International Conference for High Performance Computing, Networking, Storage and Analysis*. SC '11. ACM, Nov. 2011, pp. 1–11. URL: http://dx.doi.org/10.1145/2063384.2063478.

[193] Xiangyu Jiang et al. *Use QUDA for lattice QCD calculation with Python*. 2024. arXiv: 2411.08461 [hep-lat]. URL: https://arxiv.org/abs/2411.08461.

[194] Jack Holligan and Huey-Wen Lin. "Systematic improvement of $x$-dependent unpolarized nucleon generalized parton distributions in lattice-QCD calculation". In: *Phys. Rev. D* 110 (2024), p. 034503. arXiv: 2312.10829 [hep-lat].

[195] Alex NieMiera et al. "First Self-Renormalized Gluon PDF of Nucleon from Large-Momentum Effective Theory in the Continuum Limit". In: *arXiv preprint* (2025). submitted Oct. 20, 2025; uses hybrid renormalization with self-renormalization to obtain the LaMET gluon PDF continuum limit. arXiv: 2510.17758 [hep-lat].

[196] Jack Holligan and Huey-Wen Lin. "Nucleon helicity parton distribution function in the continuum limit with self-renormalization". In: *Physics Letters B* 854 (July 2024), p. 138731. ISSN: 0370-2693. URL: http://dx.doi.org/10.1016/j.physletb.2024.138731.

[197] Haoyang Bai and others (Lattice Parton Collaboration (LPC)). "Hybrid renormalization for distribution amplitude of a light baryon in large momentum effective theory". In: *Phys. Rev. D* 112.11 (2025), p. 114515. arXiv: 2508.08971 [hep-lat].

[198] Yi-Kai Huo et al. "Self-renormalization of quasi-light-front correlators on the lattice". In: *Nucl. Phys. B* 969 (2021), p. 115443. arXiv: 2103.02965 [hep-lat].

[199] Jack Holligan et al. "Precision control in lattice calculation of x-dependent pion distribution amplitude". In: *Nucl. Phys. B* 993 (2023), p. 116282. arXiv: 2301.10372 [hep-lat].

[200] Max Jaarsma, Rudi Rahn, and Wouter J. Waalewijn. "Towards double parton distributions from first principles using Large Momentum Effective Theory". In: *JHEP* 12 (2023), p. 014. arXiv: 2305.09716 [hep-ph].

# Acknowledgments

During my time as a student, I was lucky to be surrounded by a great many people who not only advanced my understanding of physics, but also considerably enhanced my quality of life and enjoyment thereof.

I am deeply indebted to my supervisor Andreas Schäfer, who has been my mentor in physics ever since my time as an undergraduate. Not only has he been a great teacher in particle physics, he has also always been very understanding about all the things I knew nothing about. Besides introducing me to many great physicists and topics, his insights into the field were invaluable. I am especially grateful for all the support he has offered over the past 8 years, such as securing the Deutsche Forschungsgemeinschaft (DFG) grant SCHA 458/23, which allowed me to work on all the topics presented in this work and more.

I sincerely thank Markus Diehl, both as a long-term collaborator and second referee for this thesis. Without his insights, particularly into the phenomenological aspects of multiparton interactions, my research and understanding of the field would not be the same.

I would furthermore like to thank Juan Diego Urbina and Sascha Schäfer for serving on my committee, especially on such short notice.

My thanks also go to Christian Zimmermann, who has been a close collaborator on all things four-point ever since my master's thesis. His guidance in computational matters was - and remains - greatly appreciated. Likewise, I would like to thank my collaborators Tobias Sizmann, Oskar Grocholski, Rui Zhang and Yong Zhao for all our shared projects and efforts. I want to thank Wolfgang Söldner in particular for providing vital knowledge and files, especially towards the end of the thesis.

Many thanks to my colleagues and fellow members of the physics department at the University of Regensburg, who created just the right mix of pleasant, entertaining, and serious working atmosphere. May your coffee breaks remain as insightful.

I would particularly like to thank Julian, Valentin and Christian for proofreading my thesis, finding countless typos I overlooked and providing insightful comments about the difficulties in understanding my deliberations, most prominently "was?".

My sincere thanks go to my friends for their encouragement and companionship throughout my time as a student. I consider myself lucky that there are so many of them and that I could spend many long hours with them, including Andrea, Andreas, Bastiaan, Benjamin, Caspar, Charlotte, Christian, Christina, Clemens, Constantin, Daniel, Daniela, Elia, Gloria, Hannah, Hardy, Hengameh, Isabella, Johannes, Jonathan, Julian, Katrin, Ludwig, Marc, Marcel, Markus, Martina, Matthias, Max, Moff, Nicholas, Nils, Paul, Pavel, Polina, Reza, Simon, Susanne, Theresa, Torsten, Valentin and Viktoria.

Finally, I would like to thank my family, my parents Alfred and Michaela as well as my sister Angela, and my grandparents Peter and Brigitte, for their unconditional love and support over the past 28 years, without which none of this would have been possible. I have also been very fortunate to call Josie my girlfriend, whose undying love I cherish every day, and I am deeply grateful for the wonderful years we have shared together. May they continue to be as amazing.